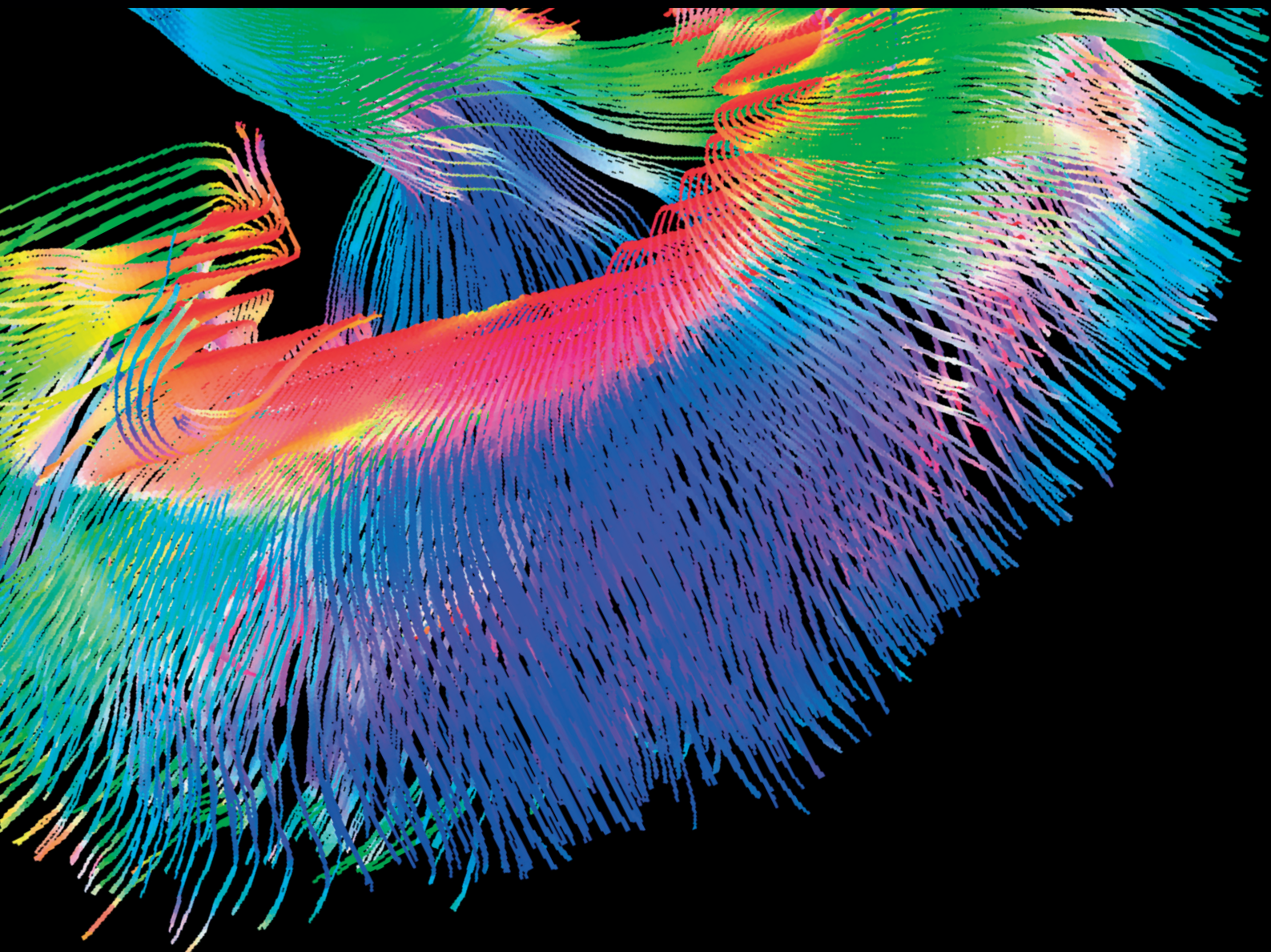


Contrast Media & Molecular Imaging

# Molecular Imaging: *In Vivo* Agents for the Diagnosis and Treatment of Cancer

Lead Guest Editor: Daniela Haeusler

Guest Editors: Clemens Decristoforo, James Frost, Sundaresan Gobalakrishnan, and Ya-Yao Huang



---

**Molecular Imaging: *In Vivo* Agents for  
the Diagnosis and Treatment of Cancer**

Contrast Media & Molecular Imaging

---

**Molecular Imaging: *In Vivo* Agents for  
the Diagnosis and Treatment of Cancer**

Lead Guest Editor: Daniela Haeusler

Guest Editors: Clemens Decristoforo, James Frost,  
Sundaresan Gobalakrishnan, and Ya-Yao Huang



---

Copyright © 2018 Hindawi. All rights reserved.

This is a special issue published in “Contrast Media & Molecular Imaging.” All articles are open access articles distributed under the Creative Commons Attribution License, which permits unrestricted use, distribution, and reproduction in any medium, provided the original work is properly cited.

---

## Editorial Board

Ali Azhdarinia, USA  
Peter Bannas, Germany  
Giorgio Biasiotto, Italy  
A. L. B. de Barros, Brazil  
Dinesh K. Deelchand, USA  
Paul Edison, UK  
Michael J. Evans, USA  
Samer Ezziddin, Germany  
G. Ferro-Flores, Mexico  
Filippo Galli, Italy  
M. L. García-Martín, Spain

Alexander R. Haug, Germany  
Hao Hong, USA  
Alexey P. Kostikov, Canada  
F. Kraeber-Bodéré, France  
Kuo-Shyan Lin, Canada  
Gaurav Malviya, UK  
Barbara Palumbo, Italy  
Giancarlo Pascali, Australia  
Maria Joao Ribeiro, France  
Laurent M. Riou, France  
Anne Roivainen, Finland

Pedro Rosa-Neto, Canada  
Giuseppe Rubini, Italy  
Barbara Salvatore, Italy  
Ralf Schirmacher, Canada  
Giorgio Treglia, Switzerland  
Reza Vali, Canada  
Mattia Veronese, UK  
Changning Wang, USA  
Habib Zaidi, Switzerland  
Luc Zimmer, France

## Contents

### **Molecular Imaging: *In Vivo* Agents for the Diagnosis and Treatment of Cancer**

D. Haeusler , C. Decristoforo , J. Frost, S. Gobalakrishnan, and Y. Y. Huang   
Editorial (2 pages), Article ID 8541915, Volume 2018 (2018)

### ***In Vivo* Molecular Ultrasound Assessment of Glioblastoma Neovasculature with Endoglin-Targeted Microbubbles**

Cheng Liu , Fei Yan , Yajie Xu, Hairong Zheng , and Lei Sun   
Research Article (10 pages), Article ID 8425495, Volume 2018 (2018)

### **Targeted Optical Imaging Agents in Cancer: Focus on Clinical Applications**

Bishnu P. Joshi  and Thomas D. Wang   
Review Article (19 pages), Article ID 2015237, Volume 2018 (2018)

### **Measuring Tumor Metabolism in Pediatric Diffuse Intrinsic Pontine Glioma Using Hyperpolarized Carbon-13 MR Metabolic Imaging**

Adam W. Autry, Rintaro Hashizume, C. David James, Peder E. Z. Larson, Daniel B. Vigneron, and Ilwoo Park   
Research Article (6 pages), Article ID 3215658, Volume 2018 (2018)

### **Comparative Evaluation of Radioiodine and Technetium-Labeled DARPIn 9\_29 for Radionuclide Molecular Imaging of HER2 Expression in Malignant Tumors**

Anzhelika Vorobyeva , Olga Bragina, Mohamed Altai, Bogdan Mitran , Anna Orlova , Alexey Shulga, Galina Proshkina, Vladimir Chernov, Vladimir Tolmachev , and Sergey Deyev  
Research Article (11 pages), Article ID 6930425, Volume 2018 (2018)

### **Evaluation of $^{99m}\text{Tc}$ -HYNIC-VCAM-1<sub>scFv</sub> as a Potential Qualitative and Semiquantitative Probe Targeting Various Tumors**

Xiao Zhang, Fan Hu , Chunbao Liu, Lianglan Yin , Yingying Zhang , Yongxue Zhang , and Xiaoli Lan   
Research Article (8 pages), Article ID 7832805, Volume 2018 (2018)

### **Thallium Labeled Citrate-Coated Prussian Blue Nanoparticles as Potential Imaging Agent**

Krisztián Szigeti , Nikolett Hegedűs , Kitti Rácz, Ildikó Horváth, Dániel S. Veres, Dávid Szöllősi, Ildikó Futó, Károly Módos, Tamás Bozó, Kinga Karlinger, Noémi Kovács, Zoltán Varga , Magor Babos, Ferenc Budán, Parasuraman Padmanabhan , Balázs Gulyás, and Domokos Máthé   
Research Article (10 pages), Article ID 2023604, Volume 2018 (2018)

### **Exploiting the Concept of Multivalency with $^{68}\text{Ga}$ - and $^{89}\text{Zr}$ -Labelled Fusarinine C-Minigastrin Bioconjugates for Targeting CCK2R Expression**

Dominik Summer, Christine Rangger , Maximilian Klingler, Peter Laverman, Gerben M. Franssen, Beatrix E. Lechner, Thomas Orasch, Hubertus Haas, Elisabeth von Guggenberg, and Clemens Decristoforo   
Research Article (12 pages), Article ID 3171794, Volume 2018 (2018)

**Tumor-Shed Antigen Affects Antibody Tumor Targeting: Comparison of Two <sup>89</sup>Zr-Labeled Antibodies Directed against Shed or Nonshed Antigens**

Jae-Ho Lee , Heejung Kim , Zhengsheng Yao, Lawrence P. Szajek, Luigi Grasso, Insook Kim, and Chang H. Paik 

Research Article (12 pages), Article ID 2461257, Volume 2018 (2018)

**Construction and Evaluation of the Tumor-Targeting, Cell-Penetrating Multifunctional Molecular Probe iCREKA**

Li-juan Wang, Hong-sheng Li, Quan-shi Wang , Hu-bing Wu, Yan-jiang Han, Wen-lan Zhou, Meng Wang, and Shun Huang

Research Article (11 pages), Article ID 7929617, Volume 2018 (2018)

**Preclinical *In Vitro* and *In Vivo* Evaluation of [<sup>18</sup>F]FE@SUPPY for Cancer PET Imaging: Limitations of a Xenograft Model for Colorectal Cancer**

T. Balber, J. Singer, N. Berroterán-Infante, M. Dumanic, L. Fetty, J. Fazekas-Singer , C. Vraka, L. Nics, M. Bergmann, K. Pallitsch, H. Spreitzer, W. Wadsak , M. Hacker, E. Jensen-Jarolim, H. Viernstein, and M. Mitterhauser 

Research Article (9 pages), Article ID 1269830, Volume 2018 (2018)

**Fluorine-19 Magnetic Resonance Imaging and Positron Emission Tomography of Tumor-Associated Macrophages and Tumor Metabolism**

Soo Hyun Shin, Sang Hyun Park, Se Hun Kang, Seung Won Kim, Minsun Kim, and Daehong Kim

Research Article (8 pages), Article ID 4896310, Volume 2017 (2018)

## Editorial

# Molecular Imaging: *In Vivo* Agents for the Diagnosis and Treatment of Cancer

D. Haeusler <sup>1</sup>, C. Decristoforo <sup>2</sup>, J. Frost,<sup>3</sup> S. Gobalakrishnan,<sup>4</sup> and Y. Y. Huang <sup>5</sup>

<sup>1</sup>WISIA-Women in Science-an Interdisciplinary Association, Vienna, Austria

<sup>2</sup>Medical University of Innsbruck, Innsbruck, Austria

<sup>3</sup>Johns Hopkins University, Baltimore, MD, USA

<sup>4</sup>Virginia Commonwealth University, Richmond, VA, USA

<sup>5</sup>National Taiwan University Hospital, Taipei, Taiwan

Correspondence should be addressed to D. Haeusler; [daniela.barbara.haeusler@gmail.com](mailto:daniela.barbara.haeusler@gmail.com)

Received 20 September 2018; Accepted 20 September 2018; Published 22 October 2018

Copyright © 2018 D. Haeusler et al. This is an open access article distributed under the Creative Commons Attribution License, which permits unrestricted use, distribution, and reproduction in any medium, provided the original work is properly cited.

Molecular imaging continues to advance the goal of improving diagnosis and treatment in cancer. This special issue examines a cross section of the current basic and clinical research across imaging modalities, probes, and molecular targets. The issue articles permit comparison of the advantages and limitations of varied modalities, including PET, SPECT, CT, MRI, ultrasound imaging, and fluorescence imaging. The corresponding agents in development are able to interact with many targets of relevance to cancer. Highly sensitive and specific *in vivo* agents permit visualization of receptor systems, enzymes, and proteins involved in cancer initiation, maintenance, and spread. As another dimension of cancer targeting, molecular probes for the tumor microenvironment, including stromal, endothelial, and immune cells, are increasingly recognized as key factors in attacking cancer.

The kaleidoscope of targets and methods available to achieve these goals is exemplified in this special issue. The topics cover the development of molecular imaging agents targeting the cholecystokinin 2 receptor (CCK2R), the adenosine A3 receptor (A3R), and the human epidermal growth factor receptor 2 (HER2). Cancer stroma targeting is addressed with molecular probes for the vascular cell adhesion molecule 1 (VCAM-1) and endoglin (CD105), a proangiogenic growth factor, which are both overexpressed in a variety of malignancies.

The tools used in the selection of displayed articles were molecules, small peptides, engineered proteins, intact

antibodies and antibody fragments, nanoparticles, and microbubbles, demonstrating the breadth of targeting scaffolds currently to investigators and soon to cancer clinicians.

Each paper included in this special issue approaches the challenge of molecular imaging in diagnosis and treatment of cancer in a different way, focusing on new molecules, innovative labelling strategies, and characterization in disease models. Each contribution stands on its own as a marker for the next advances in cancer understanding and patient care.

The editors have endeavored to have the authors clearly point up the advantages of the current technologies and demonstrate the needs for advancement to the next stages of development. We hope this effort will stimulate the reader to think hard about their own research and how the community of cancer imaging investigators can continue progress from proof of concept to clinical use.

Finally, we would like to acknowledge the strong efforts of all the reviewers who supported this special issue through their careful, insightful, and timely reviews.

This issue was edited by a group of researchers across the world who shared the aim to shed more light on the omnipresent unsolved cancer problem. Apart from our own research in the field of molecular imaging and cancer, it was a pleasure to conceive, organize, and edit this special issue. Last but not least, we conclude that, in molecular imaging of cancer, highly promising tools are being evaluated; as a next step, we need to use them in clinical practice.

**Conflicts of Interest**

The editors declare that they have no conflicts of interest regarding the publication of this special issue.

*D. Haeusler*  
*C. Decristoforo*  
*J. Frost*  
*S. Gobalakrishnan*  
*Y. Y. Huang*

## Research Article

# In Vivo Molecular Ultrasound Assessment of Glioblastoma Neovasculature with Endoglin-Targeted Microbubbles

Cheng Liu <sup>1</sup>, Fei Yan <sup>2</sup>, Yajie Xu,<sup>1</sup> Hairong Zheng <sup>2</sup> and Lei Sun <sup>1</sup>

<sup>1</sup>Department of Biomedical Engineering, The Hong Kong Polytechnic University, Hong Kong SAR, China

<sup>2</sup>Paul C. Lauterbur Research Center for Biomedical Imaging, Shenzhen Institutes of Advanced Technology, Chinese Academy of Sciences, Shenzhen, China

Correspondence should be addressed to Lei Sun; lei.sun@polyu.edu.hk

Received 26 January 2018; Revised 16 May 2018; Accepted 20 September 2018; Published 18 October 2018

Guest Editor: Sundaresan Gobalakrishnan

Copyright © 2018 Cheng Liu et al. This is an open access article distributed under the Creative Commons Attribution License, which permits unrestricted use, distribution, and reproduction in any medium, provided the original work is properly cited.

**Objectives.** Glioblastoma, as one of the most malignant cancer in the world, usually shows substantially increased angiogenesis. Endoglin (CD105), which is an alternative proangiogenic growth factor, has been remarkably upregulated on the proliferating glioblastoma neovasculature. However, little is known on the noninvasive assessment of the expression levels of CD105 during glioblastoma progression. Herein, we investigated the potential of the molecular ultrasound imaging for the noninvasive assessment of the expression levels of the biomarker CD105 during the glioblastoma progression. **Materials and Methods.** The CD105-targeted perfluorocarbon-containing lipid-shelled microbubbles (MBs) were prepared. A parallel flow chamber was employed, in which the CD105-targeted and non-targeted MBs were tested across the CD105  $\pm$  expression cell lines. **In vivo** molecular US imaging was conducted based on a subcutaneous xenograft tumor model ( $n = 9$ ). Finally, the statistical analysis was conducted to quantitatively correlate the attachment numbers of MBs in the parallel flow chamber test with the CD105 expression levels of the cells in the flow cytometry test and the *in vivo* molecular ultrasound signals with the *ex vivo* expression levels of CD105 in the immunohistochemical test. **Results and Discussion.** The attachment numbers of the CD105-targeted MBs significantly correlated with the CD105 expression levels of the cells in the parallel flow chamber test. There was a good correlation between the *in vivo* molecular ultrasound signals with the CD105-targeted MBs and the *ex vivo* expression levels of CD105 in the immunohistochemical test. The results indicate that the molecular US imaging is much potential to assess the progression of the glioblastoma neovasculature noninvasively.

## 1. Introduction

Glioblastoma, which is one of the most malignant cancer types of the central nervous system, continues to cause high morbidity and mortality rates in the world [1]. Although significant development has been made in the glioblastoma management, various challenges still remain, such as diagnosis at the early stage [2]. At the early progression stage of glioblastoma, the production of neovasculature (blood vessels) from the preexisting vessels (mature) or microvessels is essential to the pathological processes, which provides the oxygen and nutrients to the malignant cells for rapid growth. Typically, after reaching a certain size, the malignant cells enter the exponential growth phase, during

which the realignment and distributions of the endothelial cells lead to the neovasculatures around and within the malignant cells [3].

The formation of neovasculature is a complicated process with multiple steps, which is promoted by a series of proangiogenic growth factors (e.g., VEGF) [4]. These proangiogenic growth factors can work as the biomarkers of molecular imaging for the noninvasive assessment of the tumor progression. Among those proangiogenic biomarkers, endoglin (CD105) has been shown to be remarkably upregulated on highly proliferating endothelial cells (neovasculature wall), instead of the normal endothelial cells or mature vessels [5, 6]. In clinic, it is reported that the outcome of the anticancer therapies targeting VEGF have

not met the high expectation, which could be due to the over expression of the alternative proangiogenic growth factor (e.g., endoglin (CD105)). Besides, pathologists have been using endoglin as an independent prognostic target for the assessment of the aggressiveness of most solid tumor types [7, 8]. Thus, the endoglin (CD105) has drawn a lot of attention as a novel alternative biomarker for the tumor diagnosis, prognosis, and therapy. Several preliminary studies have indicated endoglin (CD105) as a potential biomarker for different molecular imaging strategies, such as single-photon emission computed tomography (SPECT) [9], magnetic resonance imaging (MRI) [10], near-infrared fluorescence imaging [11], and ultrasound imaging [12]. However, little is known on the assessment of the expression levels of endoglin (CD105) during the glioblastoma progression *in vivo*. Understanding of the temporal and spatial expression levels of endoglin (CD105) *in vivo* could potentially contribute greatly to both the early diagnosis and anticancer therapy of glioblastoma.

Ultrasound imaging (US) is a popular imaging tool that utilizes unique acoustic-tissue interface behavior of the sound waves as it passes through a biological organ or tissue of interest. Ultrasound imaging is widely used due to its uniqueness that can be used for applications both in the diagnosis and therapy [13, 14]. Conventional ultrasound imaging has been well accepted as an imaging modality specialized for the morphological and functional imaging. While molecular ultrasound imaging, which employs functionalized contrast agents, is potentially capable to assess the tumor angiogenesis noninvasively and quantitatively *in vivo* [15]. Recently, microbubbles (MBs), which are liquid shell emulsions filled with gas (e.g., perfluorocarbon, nitrogen, sulfur hexafluoride, or air), have been used as contrast agents for molecular ultrasound imaging [16]. The shells of the microbubbles are usually composed of materials with good biocompatibility (e.g., lipid, protein, and polymers). The structure of MBs makes it unique in resonating and sending back high nonlinear harmonic and sub-harmonic ultrasound signals when exposed in the ultrasound mechanical waves, which would bring about high contrast-to-background ratio [17]. Importantly, the size of microbubbles usually in 1~4  $\mu\text{m}$  in diameter would limit them from going extravascularly from the blood vessels, that makes them quite suitable for the vasculature-related applications *in vivo* [18].

Microbubbles (MBs) are usually functionalized with ligands such as antibodies or peptides that bind the biomarkers of interest with high affinity [15]. Several studies have validated the use of MBs to detect the tumor angiogenesis in animal models by targeting to the proangiogenic growth biomarkers [19–21]. It is shown that targeted MBs could accumulate more in the tumor regions than the nontargeted MBs, which would significantly increase the ultrasound response strength. The aim of this study is to develop the CD105-targeted MBs and investigate the potential of molecular US for the noninvasive assessment of the expression levels of endoglin (CD105) during glioblastoma progression from small to large sizes *in vivo*, as illustrated in Figure 1.

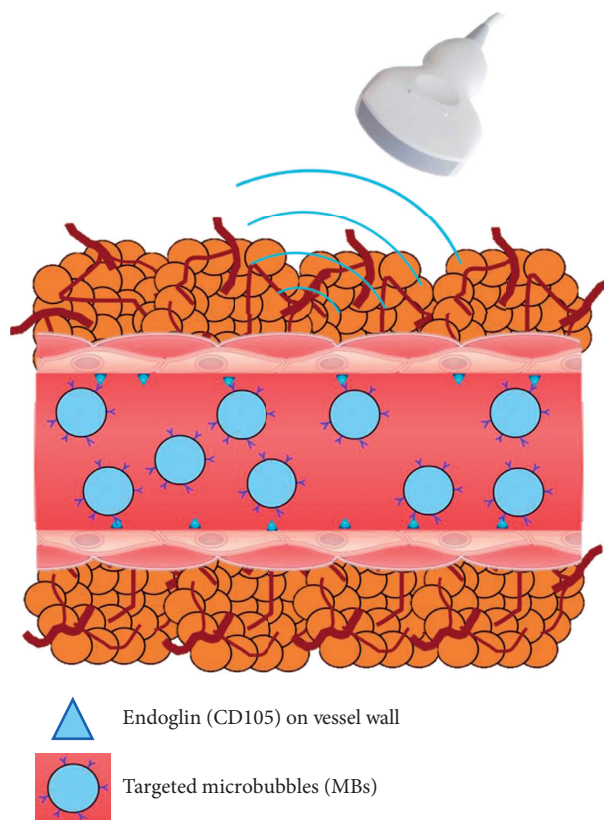


FIGURE 1: Illustration of the molecular ultrasound imaging strategy. Noninvasive assessment of the expression levels of the alternative proangiogenic growth factor endoglin (CD105) on the vessel wall by using the CD105-targeted microbubbles (MBs) with 1~4  $\mu\text{m}$  in diameter.

## 2. Materials and Methods

### 2.1. Synthesis and Characterization of CD105-Targeted MBs.

Two types of microbubbles (MBs), including (1) CD105-targeted MBs and (2) nontargeted MBs with an isotype-matched control immunoglobulin G antibody, were prepared by using streptavidin-biotin binding chemistry according to a reported protocol [22, 23]. The perfluorocarbon-containing lipid-shelled MBs-containing streptavidin moieties in the lipid shell were reconstituted in 1 mL sterile saline (0.9% sodium chloride), which are abbreviated as MB-biotin in Figure 2. For targeting the MBs-biotin, 5  $\mu\text{g}$  of the following two types of 1<sup>st</sup> antibodies were incubated with  $5 \times 10^7$  avidin-conjugated MBs-biotin for 10 mins at room temperature, respectively: (1) biotinylated rat antimouse CD105 monoclonal antibodies (eBioscience), which has been reported for use in flow cytometry analysis/cell sorting for specific targeting with the mouse endoglin (CD105) molecule [24, 25] and (2) biotinylated rat control immunoglobulin G antibodies (IgG) (eBioscience). The 2<sup>nd</sup> antibodies, which were fluorescein-conjugated anti-biotin antibodies (Jackson ImmunoResearch), were used to confirm the affinity of the 1<sup>st</sup> antibodies on the shell of MBs through the specific biotin-avidin binding chemistry, as shown in Figure 2. The free avidin and antibodies were removed by washing with PBS. The mean and standard deviation of the MBs' diameter

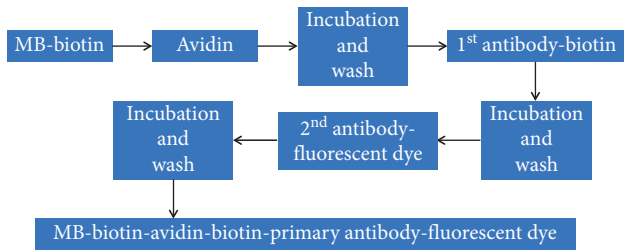


FIGURE 2: Preparation procedures of the microbubbles (MBs). Two types of MBs were prepared: (1) CD105-targeted MBs as MBs-biotin-avidin-biotin-CD105-biotin and (2) control nontargeted MBs as MBs-biotin-avidin-biotin-IgG-biotin. Biotinylated rat antimouse CD105 monoclonal antibodies (eBioscience) and biotinylated rat immunoglobulin G antibodies (IgG) were used as 1<sup>st</sup> antibodies for the CD105-targeted MBs and the control nontargeted MBs, respectively. The 2<sup>nd</sup> antibodies, which were fluorescein-conjugated anti-biotin antibodies (Jackson ImmunoResearch), were used to confirm the affinity of the 1<sup>st</sup> antibodies on the shell of MBs through the specific biotin-avidin conjugation.

were assessed by an optical particle counter with a 0.5 mm diameter detection limit (AccuSizer 780; Particle Sizing Systems, Santa Barbara, CA, USA).

**2.2. Parallel Flow Chamber Test.** To assess the binding specificity of the CD105-targeted MBs to the biomarker CD105, the parallel flow chamber test was performed, according to a reported protocol [26].

Two types of cell lines, mouse endothelial cell line MS1 and mouse breast cancer cell line 4T1, were selected as the cell lines with high and low CD105 expression levels, respectively. Both the MS1 and 4T1 cell lines were purchased from the National Infrastructure of Cell Line Resource (Chinese Academy of Science, Shanghai, China). For the MS1 cells, the culture medium was ATCC-formulated Dulbecco's modified Eagle medium (ATCC) with 5% fetal bovine serum and 1% penicillin-streptomycin. For the 4T1 cells, they were cultured in ATCC-formulated RPMI-1640 medium with 10% fetal bovine serum and 1% penicillin-streptomycin. Both cell lines were cultured in sterilized environment with 5% CO<sub>2</sub> humidified condition and 37°C air atmosphere.

The cell culture dishes were pretreated with 50 µg/ml collagen (type 1, rat tail, BD Biosciences, Bedford, MA) in 0.02 M acetic acid for 1 hr, aspirated and rinsed with sterile DPBS prior to the cell coating. Two million MS1 cells and two million 4T1 cells were coated on different cell culture dishes, respectively. The dishes would then be tested on the parallel flow chamber, as shown in Figure 3. The solutions would be passed over the two types of cells in the parallel flow chamber in the following order: (a) PBS, (b) 5 × 10<sup>7</sup> of CD105-targeted MBs and control MBs in PBS, and (c) PBS. Afterwards, the dishes would then be imaged immediately with dark-field microscopy. Six random optical fields of view per dish would be selected for the quantification of the number of attached MBs per cell. In order to further confirm the binding specificity of the CD105-targeted MBs, another two groups of cells, including MS1 and 4T1, were incubated

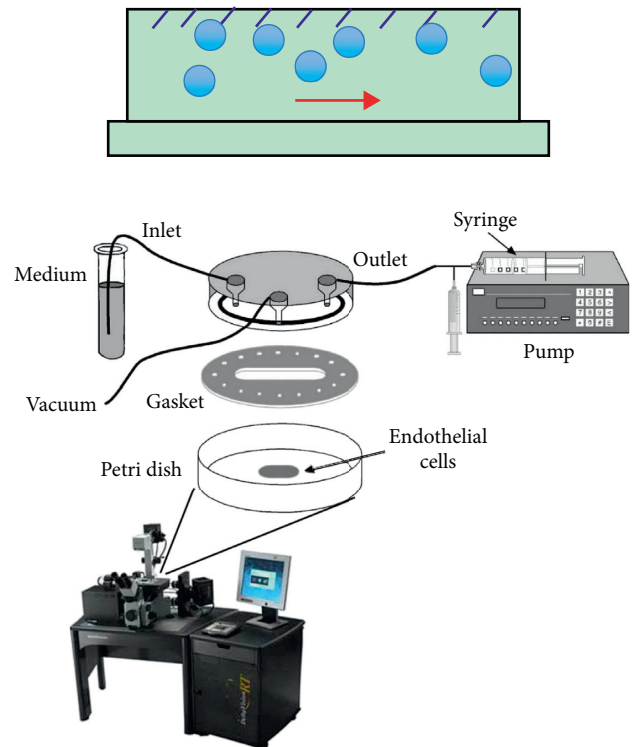


FIGURE 3: Illustration of the parallel flow chamber test. The cells were coated on the bottom of Petri dish, while the MBs would flow through the chamber as the red arrow shows. Two types of cell lines, including MS1 and 4T1, were selected as cell lines with high and low CD105 expressing levels, respectively. The CD105-targeted MBs and nontargeted MBs would be used to test the attachment specificity in the absence and presence of blocking antibodies.

with antimouse CD105 monoclonal antibodies to block the CD105 receptor in prior, followed by the parallel flow chamber test. Triplicate repetitions were performed.

**2.3. Subcutaneous Tumor Model.** All procedures using laboratory animals were approved by the Department of Health, the Government of the Hong Kong Special Administrative Region, and the Hong Kong Polytechnic University Animal Subjects Ethics Sub-Committee. Tumors were established by subcutaneous injection of 5 × 10<sup>6</sup> U-87 MG glioblastoma cells dissolved in 50 µL suspension (National Infrastructure of Cell Line Resource, Chinese Academy of Science, Shanghai, China) into the right hind limb of 6–8-week old female nude mice [27]. A total of 9 pieces of tumors were produced and used in this study. Tumor volumes of each mouse were measured and recorded daily with B-mode ultrasound imaging. According to the tumor volumes, the mice were divided into 3 groups: 50–150 mm<sup>3</sup> as small group, 151–250 mm<sup>3</sup> as medium group, and larger than 250 mm<sup>3</sup> as large group. All tumors were scanned using Vevo2100 high-frequency ultrasound system (FUJIFILM VisualSonics, Toronto, Canada) with an LZ-250 linear array transducer (center frequency at 21 MHz, 256 elements, lateral and axial resolution of 165 and ~75 µm, respectively, maximum imaging depth of 20 mm).

**2.4. In Vivo Molecular Ultrasound Imaging Experiment.** All the mice would be kept under anesthesia with 2% isoflurane in room air during the experiment, and all the imaging experiment settings would be kept constant throughout the imaging experiment. Molecular ultrasound imaging was performed using Vevo2100 high-frequency ultrasound system (FUJIFILM VisualSonics, Toronto, Canada) with an LZ-250 linear array transducer. The central planes of those tumors would be aligned by the guidance of the B-mode ultrasound imaging.

Since the ultrasound signal contribution from the attached CD105-targeted MBs also would depend on the regional MBs perfusion, the results representing the attached CD105-targeted MBs would need to be normalized to the blood flow perfusion reference condition measured by using the nontargeted MBs in the same animal before the CD105-targeted MBs imaging session, with the same imaging conditions, for all mice [28]. To allow full clearance of the nontargeted MBs from the previous imaging session, a 40 min interval was applied before the CD105-targeted MBs-imaging session to avoid any interference between the two sessions. This interval period of time between the two MBs injection was chosen according to a previously reported protocol [29]. It was demonstrated that most of the MBs would be cleared from the vasculature in 40 mins after I.V. injection. In all mice, data acquisitions were performed by injecting the two types of MBs in the following order: (1) control nontargeted MBs and (2) CD105-targeted MBs, into the same animal with an interval time of 40 mins, as shown in Figure 4.

After injection of the microbubbles (MBs), molecular ultrasound imaging based on the ultrasound burst-and-replenish technique would be performed according to a reported protocol [30, 31]: 3 mins after the MBs injection, both B-mode ultrasound imaging and nonlinear contrast ultrasound imaging frames would be acquired and overlaid over a 10-second period for 250 frames. After that, a destruction burst (10 MHz; mechanical index, approximately 0.235) would be applied for 5 seconds to destroy all the MBs in the tumor region. After the destruction burst, another 250 frames would be acquired to record the replenishment procedure of the floating-in MBs, as shown in Figure 5(a). The regions of interest (ROI) within the tumors would be selected by an experienced reader. The molecular ultrasound signals from the CD105-targeted MBs would be calculated by averaging the predestruction and postdestruction imaging signals and subtracting the postdestruction signal average from the predestruction signal average, which was defined as differential targeted enhancement (dTE), as shown in Figure 5(b). This factor would be used to represent the molecular signal which is contributed by attached MBs. The molecular US images representing the attached MBs would be combined with the B-mode ultrasound anatomic images. Finally, the quantitative molecular US signals would be correlated with the result of *ex vivo* immunohistochemistry analysis (e.g., CD31 and CD105).

**2.5. Statistical Analysis.** The data would be analyzed and output as means  $\pm$  standard deviations. For the parallel

flow chamber test, a paired Wilcoxon test would be applied to compare the attachment number of CD105-targeted MBs with control non-targeted MBs, which passed over the two cell lines, including MS1 and 4T1. The different attachment numbers before and after the blocking with antibody would be tested with a paired Wilcoxon test. Also, a Spearman rank correlation ( $\rho$  values) would be used to test the correlation between the CD105 expression levels of the two types of cell lines assessed by the flow cytometry test and the attachment numbers of MBs in the parallel flow chamber test. Spearman rank correlation was applied to test the *in vivo* CD105-targeted US imaging results with the *ex vivo* immunofluorescence results in the three tumor groups.  $P < 0.05$  would be considered to be a statistically significant difference.

### 3. Results and Discussion

**3.1. Parallel Flow Chamber Test of CD105-Targeted MBs In Vitro.** The morphology and size distribution of CD105-targeted MBs are shown in Figure 6. The fluorescence microscope imaging confirmed that the antimouse CD105 monoclonal antibodies were successfully bound to the shell of the MBs.

The attachment number of the CD105-targeted MBs to MS1 cells (CD105 positive) was significantly ( $P = 0.005$ ) higher than that to 4T1 cells (CD105 negative), as shown in Figure 7. And, the attachment number of nontargeted MBs to MS1 cells was significantly ( $P = 0.025$ ) lower in comparison with the CD105-targeted MBs, as shown in Figure 7. Furthermore, the MS1 cells with the blocking treatment would result in a significant ( $P = 0.015$ ) reduction in the attachment number of the CD105-targeted MBs, as shown in Figure 7, which could confirm the attachment specificity of the CD105-targeted MBs to the specific biomarker in the parallel flow chamber test. Furthermore, the analysis between the attachment numbers of CD105-targeted MBs and the expression levels of CD105 in two types of cells as assessed by the flow cytometry test showed a significant positive correlation ( $\rho = 0.76$ ,  $P < 0.032$ ).

**3.2. In Vivo Assessment of Endoglin Expression Levels.** There was a good positive correlation between the *in vivo* molecular US signal and *ex vivo* expression levels of CD105 as assessed with the immunofluorescence test ( $\rho = 0.86$ ,  $P < 0.001$ ), as shown in Figure 8. Additionally, the immunofluorescence test confirmed that the expressions of both CD105 and CD31 were colocalized on the endothelial cells, as shown in Figure 8, which demonstrated that the *in vivo* molecular US signals specifically came from those attached CD105-targeted MBs on the endothelial cells. In the subcutaneous tumor model, the expression levels of endoglin (CD105) in small and medium size tumors were significantly higher ( $P < 0.032$ ) in comparison with CD31. In large size tumors, the expression levels of endoglin (CD105) was significantly lower ( $P < 0.023$ ) than those of CD31, as shown in Figure 8.

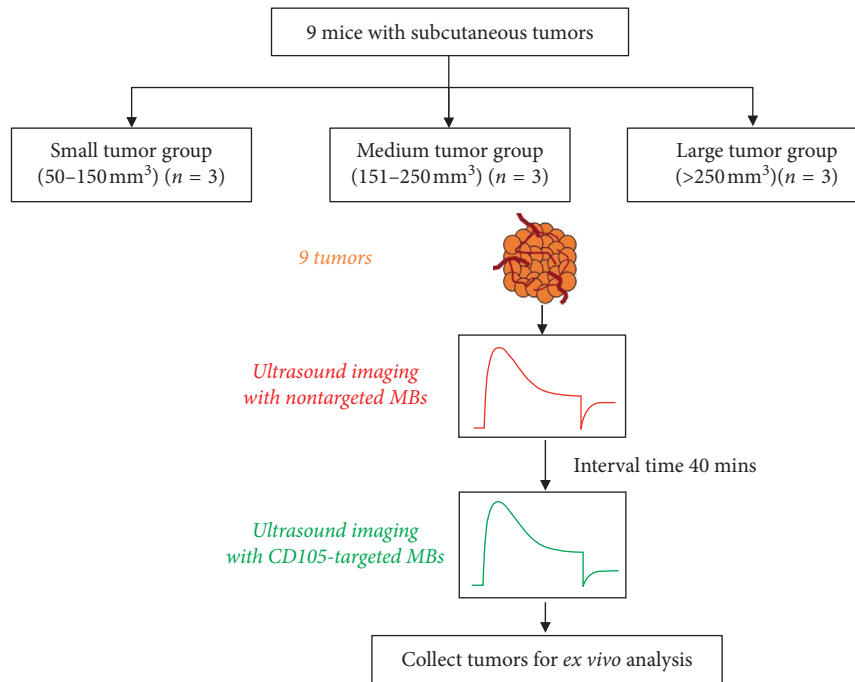


FIGURE 4: The experiment design of *in vivo* molecular US imaging experiment. Subcutaneous tumor models were established for the assessment of CD105 expression levels during tumor progression from small to large size. The nontargeted MBs were injected and measured as the control, and the CD105-targeted MBs were injected with a 40 min interval after the injection of nontargeted MBs. The US signals from the CD105-targeted MBs would be calculated by averaging predestruction and postdestruction imaging signals and subtracting the postdestruction signal average from the predestruction signal average.

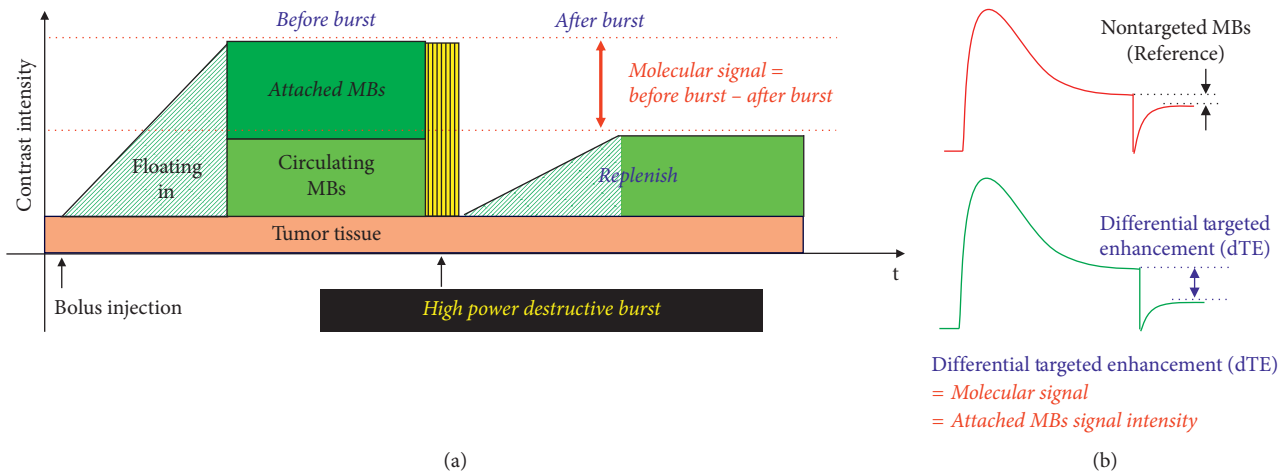


FIGURE 5: Principal of the quantitative assessment of molecular US signals. (a) Burst-and-replenishment technique for the quantitative assessment of the attached MBs; (b) the differential targeted enhancement (dTE) would be used to indicate the molecular US signal which is contributed by attached MBs only. The nontargeted MBs were used as a reference for the CD105-targeted MBs.

3.3. *Discussion.* Ultrasound imaging is a popular imaging tool that utilizes unique acoustic-tissue interface behavior of sound waves at high frequency as it passes through a biological organ or tissue of interest. Ultrasound is widely used due to its uniqueness that can be used for applications in both diagnosis and therapy. Conventional ultrasound has been well accepted as an imaging modality specialized for morphological imaging. The advantages of ultrasound include, but not limited to, economic cost, availability,

portability, high temporal resolution, ionizing radiation free, and high sensitivity. However, ultrasound imaging is not competent in imaging structures containing bone or air, because ultrasound waves could not transmit bone or air.

Molecular ultrasound imaging, which employs functionalized ultrasound contrast agent, is potentially able to assess tumor angiogenesis noninvasively and quantitatively. Recently, ultrasound contrast agents are based on microbubbles (MBs), which are liquid shell emulsions filled with

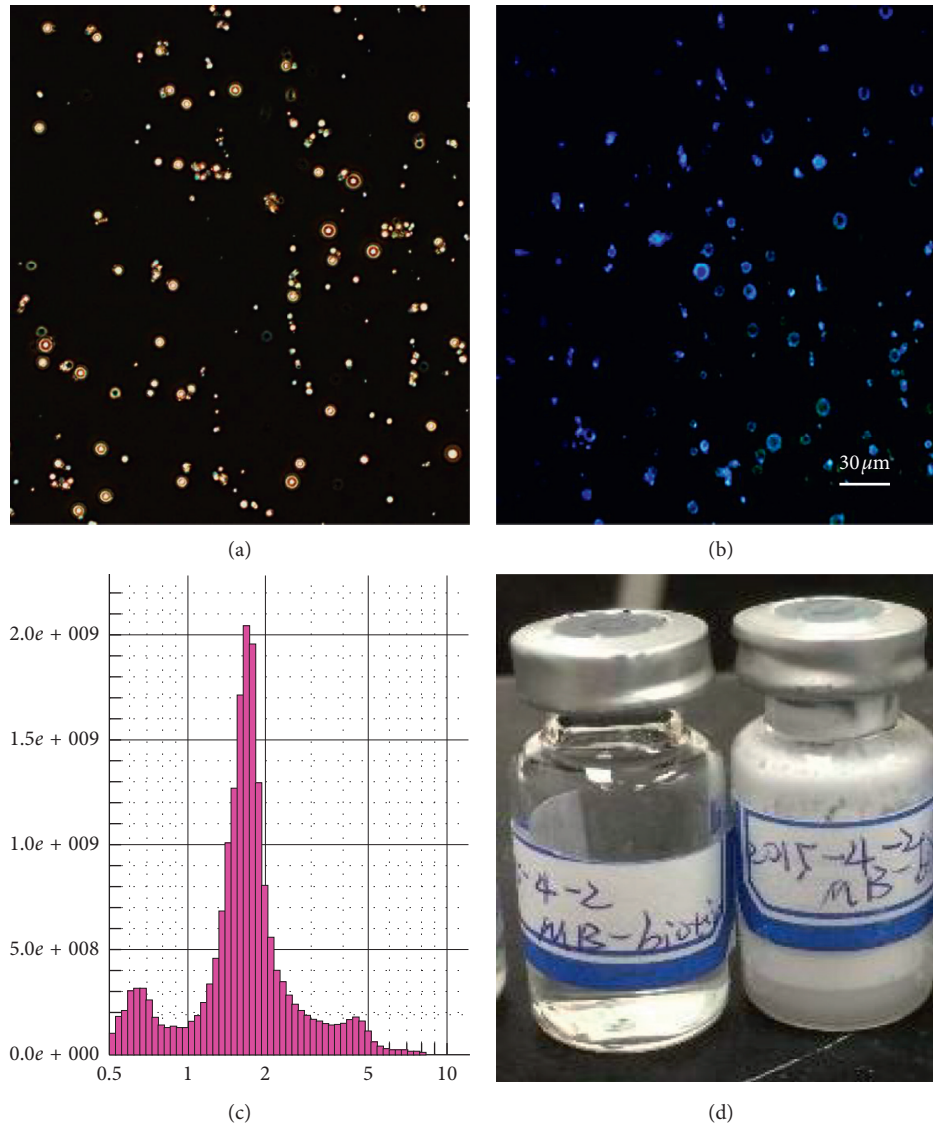


FIGURE 6: *In vitro* characterization of CD105-targeted MBs (MBs-biotin-avidin-biotin-anti-CD105-FITC). (a) The dark-field microscope image; (b) the fluorescence microscope image; (c) the size distribution of MBs, mean diameter in 2–3  $\mu\text{m}$ ; (d) the photograph of prepared MBs kept in vials.

gas, such as perfluorocarbon, sulfur hexafluoride, and nitrogen. The structure of microbubbles (MBs) makes it unique in very high echogenic response when exposed in ultrasound mechanical waves. On the one hand, this mechanical echogenic response would bring about high contrast-to-background ratio. On the other hand, the size of microbubbles usually 1~4  $\mu\text{m}$  in diameter could limit them from going to extravascular regions. Overall, molecular ultrasound imaging with the aid of MBs is quite potential for detecting biomarkers that are overexpressed on the vessel wall. Among all the contrast agent-centered imaging modalities, US molecular imaging is a recently emerging one in the preclinical translation phase, whose clinical potential might be fully exploited in the next decade.

In this study, the expression levels of CD105, which are highly relevant to the growth of glioblastoma neovasculature, have been assessed by the molecular US imaging *in vivo* based

on a subcutaneous tumor model. The *in vivo* US signals from the CD105-targeted MBs have shown that the expression levels of CD105 decreased when the tumor progressed to a larger size which was correlated with the histology result (costaining CD105/CD31) *ex vivo*. The *in vitro* binding test showed that the CD105-targeted MBs could target to a specific biomarker (CD105) on the positive CD105 expression cells. In this study, two types of cell lines (MS1 and 4T1) were selected as the CD105  $\pm$  expression cells for the assessment of the expression levels of CD105 in the parallel flow chamber test. The *in vitro* parallel flow chamber test was used as a mimic situation for the *in vivo* blood flow environment, which could be used to test the binding affinity of the CD105-targeted MBs *in vitro*. The parallel flow chamber test showed that the binding affinity and specificity were adequate for *in vivo* applications. And, the successful binding of avidin-biotin conjugate was tested using the fluorescein-conjugated anti-biotin antibodies under the

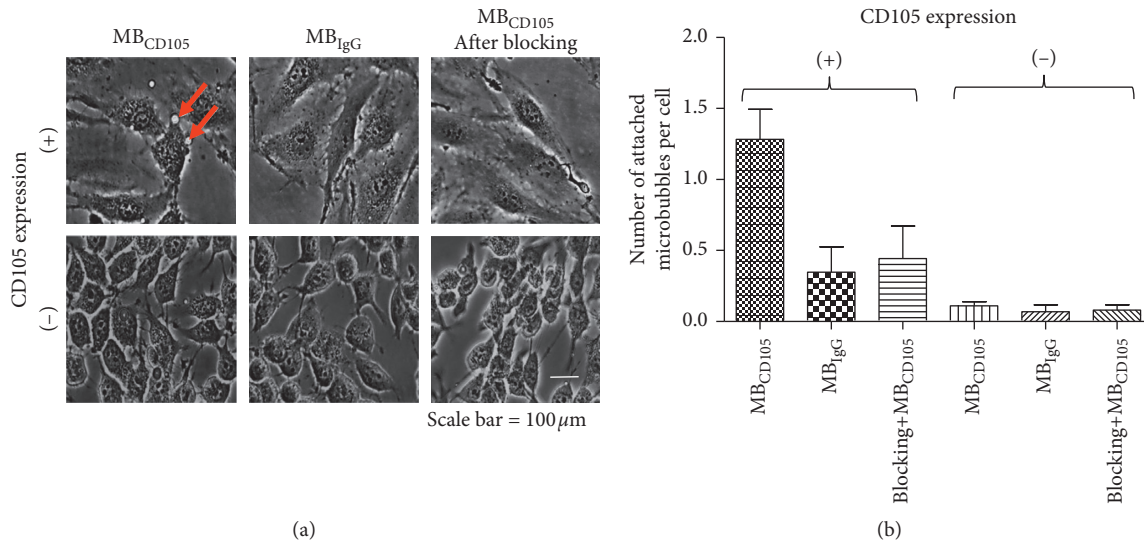


FIGURE 7: The parallel flow chamber test results. (a) Bright-field microscope images of the parallel flow chamber test. Two types of cell lines were used: endothelial cell MS1 with CD105 high expression level and 4T1 cells with CD105 low expression level. The CD105-targeted MBs and nontargeted MBs were used as control, while the anti-CD105 monoclonal antibody was used as the blocking control for CD105 high expressing cells. The red arrow indicates the location of the attached CD105-targeted MBs. The round small spots under the bright-field microscopy were MBs that were in contact with the membrane of cells without free floating movement. (b) The quantitative attachment results of the parallel flow chamber test. The attachment of the control nontargeted MBs to the MS1 cells was significantly ( $P = 0.025$ ) lower in comparison with the CD105-targeted MBs; The MS1 cells (CD105 positive) with blocking treatment would result in a significant ( $P = 0.015$ ) reduction in the attachment number of the CD105-targeted MBs, which could confirm the attachment specificity of the CD105-targeted MBs to the specific biomarker in the parallel flow chamber test.

visualization of fluorescence microscope. Overall, the molecular US imaging as a preclinical research tool was used to evaluate the expression levels of neovascularization-related endoglin (CD105) *in vivo* on the glioblastoma subcutaneous xenograft model. The statistical results *in vivo* and the *in vitro* parallel flow chamber test together have validated this strategy as a noninvasive method to assess the progression of neovascularization for glioblastoma *in vivo*.

The assessment of tumor angiogenesis is one of the most popular applications of molecular US imaging. Among all the proangiogenic growth factors, vascular endothelial growth factor (VEGF) is the best-studied one and has gained much expectation for clinical translation. Besides VEGF, endoglin (CD105) acts as an alternative proangiogenic growth factor. In clinic, the endoglin (CD105)-based immunohistochemistry test is accepted as a standard test to assess the tumor angiogenesis by quantifying the microvessel density (MVD) for many types of solid tumors [32, 33]. It has been approved that endoglin (CD105) could be selectively expressed on the highly proliferating endothelial cells rather than the normal and mature endothelial cells. However, the studies of molecular US imaging that are relevant to the alternative proangiogenic growth factor endoglin (CD105) are still in the developing phase according to the literature [34].

The noninvasive molecular US imaging and assessment of endoglin (CD105) are potential to act as an alternative strategy for monitoring tumor angiogenesis. Therefore, we are motivated to develop the CD105-targeted molecular US imaging strategy for the assessment of glioblastoma

neovascularization. The CD105-targeted US contrast agent (microbubbles) has been investigated in solution, *in vitro* parallel flow chamber test, and *in vivo* subcutaneous tumor model. Noteworthy, the micrometer size microbubbles would be limited within the blood lumen, which are quite suitable for applications to the intravascular biomarkers. The targeted microbubbles, when decorated with the functional ligands, could actively bind to the highly expressed endoglin (CD105) on the tumor neovascularization. Because the US signal intensity and harmonic components from the MBs are substantially higher and richer than the signals from the surrounding tissues, the targeted MBs that are accumulated in the neovascularization can be identified and visualized with the molecular US imaging with high sensitivity. Although the image resolution of molecular US image was limited to delineate the morphology of the biomarker CD105 expression *in vivo*, the quantitative molecular US signals were demonstrated to be correlated with the IHC analysis *ex vivo*. In addition, the molecular US images representing the attached MBs to biomarker CD105 in the molecular level could be combined with the complementary B-mode ultrasound anatomic images *in vivo*.

#### 4. Conclusions

Among all the contrast agent-centered imaging modalities, molecular ultrasound imaging is a recently emerging one in the preclinical translation phase, whose clinical potential could be fully exploited in the next decade. Endoglin (CD105), as an alternative angiogenic factor on the luminal

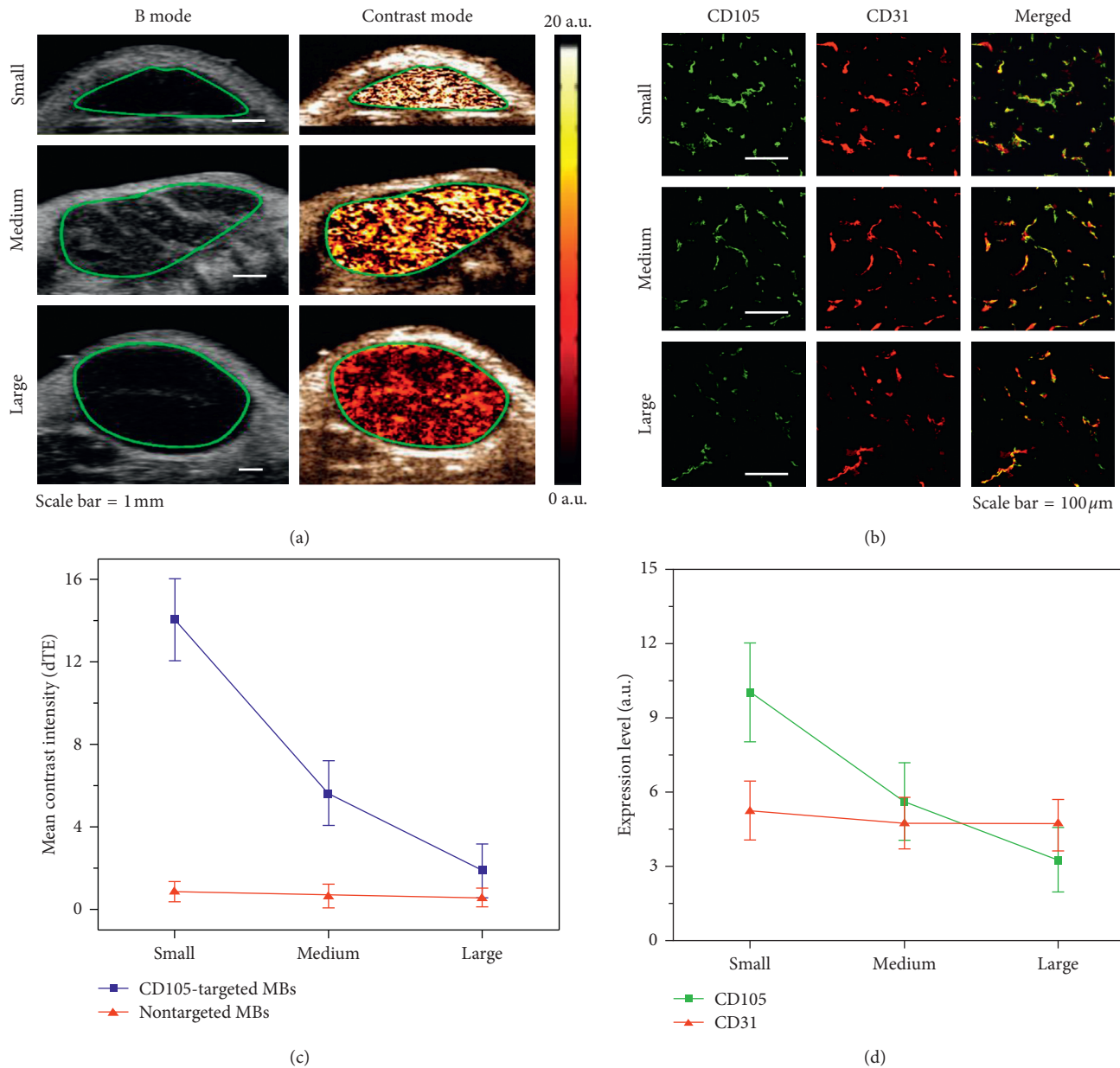


FIGURE 8: The *in vivo* assessment of the CD105 expression levels in the subcutaneous glioblastoma xenograft tumors (small, medium, and large sizes). (a) The dual-mode US imaging (B-mode and contrast mode) of tumors by using the CD105-targeted MBs, scale bar = 1 mm; (b) the *ex vivo* immunohistochemistry (IHC) test (e.g., CD105 and CD31) of the tumor tissues. CD105 was confirmed to be expressed on the endothelial cells; (c) the differential targeted enhancement (dTE) measured in the small, medium, and large glioblastoma tumor groups by using the CD105-targeted MBs and nontargeted MBs; (d) the qualification of the expression levels of CD105 and CD31 in tumor tissues assessed by *ex vivo* immunohistochemistry (IHC). The statistical results indicated that the expression levels of endoglin (CD105) in the small and medium size tumors were significantly higher ( $P < 0.032$ ) in comparison with CD31. And in large size tumors, the expression levels of endoglin (CD105) were significantly lower ( $P < 0.023$ ) than those of CD31.

surface of glioblastoma neovasculature, is suitable to work as the binding target of ultrasound contrast agent. Molecular US imaging with the aid of targeted MBs is suitable for assessing the neovasculature progression of glioblastoma at the early stage by visualization of the proangiogenic biomarker endoglin (CD105), which is highly expressed on the neovasculature wall. This study is a proof of concept work which may develop towards preclinical translation in the future.

### Data Availability

The data used to support the findings of this study are available from the corresponding author upon request.

### Conflicts of Interest

There are no conflicts of interest that the authors should disclose.

## Acknowledgments

This work was supported financially by the Health and Medical Research Fund of Food and Health Bureau of Hong Kong (01121836 and 03144266), the National Natural Science Foundations of China (61372026 and 11674271), the Hong Kong Innovation and Technology Fund (GHP/009/14SZ), the Shenzhen Science, Technology and Innovation Commission research grant (SGLH20150216172854731), and the Hong Kong Polytechnic University internal grant (4-BCAP and 4-BCDP). The authors acknowledge the use of the University Research Facility in Life Sciences (ULS).

## Supplementary Materials

Video of in vivo “burst-and-replenishment” experiment for quantitative assessment of the CD105 expression level with CD105-targeted MBs. (*Supplementary Materials*)

## References

- [1] J. P. Thakkar, T. A. Dolecek, C. Horbinski et al., “Epidemiologic and molecular prognostic review of glioblastoma,” *Cancer Epidemiology and Prevention Biomarkers*, vol. 23, no. 10, pp. 1985–1996, 2014.
- [2] A. Omuro and L. M. DeAngelis, “Glioblastoma and other malignant gliomas: a clinical review,” *JAMA*, vol. 310, no. 17, pp. 1842–1850, 2013.
- [3] S. Das and P. A. Marsden, “Angiogenesis in glioblastoma,” *New England Journal of Medicine*, vol. 369, no. 16, pp. 1561–1563, 2013.
- [4] Y. Soda, C. Myskiw, A. Rommel, and I. M. Verma, “Mechanisms of neovascularization and resistance to anti-angiogenic therapies in glioblastoma multiforme,” *Journal of Molecular Medicine*, vol. 91, no. 4, pp. 439–448, 2013.
- [5] L. S. Rosen, M. S. Gordon, F. Robert, and D. E. Matei, “Endoglin for targeted cancer treatment,” *Current Oncology Reports*, vol. 16, no. 2, pp. 365, 2014.
- [6] S. E. Duff, C. Li, J. M. Garland, and S. Kumar, “CD105 is important for angiogenesis: evidence and potential applications,” *The FASEB Journal*, vol. 17, no. 9, pp. 984–992, 2003.
- [7] M. Paauwe, P. Ten Dijke, and L. J. Hawinkels, “Endoglin for tumor imaging and targeted cancer therapy,” *Expert Opinion on Therapeutic Targets*, vol. 17, no. 4, pp. 421–435, 2013.
- [8] F. Nassiri, M. D. Cusimano, B. W. Scheithauer et al., “Endoglin (CD105): a review of its role in angiogenesis and tumor diagnosis, progression and therapy,” *Anticancer Research*, vol. 31, no. 6, pp. 2283–2290, 2011.
- [9] S. Bredow, M. Lewin, B. Hofmann, E. Marecos, and R. Weissleder, “Imaging of tumour neovasculature by targeting the TGF- $\beta$  binding receptor endoglin,” *European Journal of Cancer*, vol. 36, no. 5, pp. 675–681, 2000.
- [10] D. Zhang, X.-Y. Feng, T. D. Henning et al., “MR imaging of tumor angiogenesis using sterically stabilized Gd-DTPA liposomes targeted to CD105,” *European Journal of Radiology*, vol. 70, no. 1, pp. 180–189, 2009.
- [11] Y. Yang, Y. Zhang, H. Hong, G. Liu, B. R. Leigh, and W. Cai, “In vivo near-infrared fluorescence imaging of CD105 expression during tumor angiogenesis,” *European Journal of Nuclear Medicine and Molecular Imaging*, vol. 38, no. 11, pp. 2066–2076, 2011.
- [12] G. Korpanty, J. G. Carbon, P. A. Grayburn, J. B. Fleming, and R. A. Brekken, “Monitoring response to anticancer therapy by targeting microbubbles to tumor vasculature,” *Clinical Cancer Research*, vol. 13, no. 1, pp. 323–330, 2007.
- [13] A. K. Wood and C. M. Sehgal, “A review of low-intensity ultrasound for cancer therapy,” *Ultrasound in Medicine & Biology*, vol. 41, no. 4, pp. 905–928, 2015.
- [14] F. Yan, X. Li, Q. Jin et al., “Therapeutic ultrasonic microbubbles carrying paclitaxel and LyP-1 peptide: preparation, characterization and application to ultrasound-assisted chemotherapy in breast cancer cells,” *Ultrasound in Medicine & Biology*, vol. 37, no. 5, pp. 768–779, 2011.
- [15] F. Kiessling, S. Fokong, P. Koczera, W. Lederle, and T. Lammers, “Ultrasound microbubbles for molecular diagnosis, therapy, and theranostics,” *Journal of Nuclear Medicine*, vol. 53, no. 3, pp. 345–348, 2012.
- [16] F. Kiessling, J. Huppert, and M. Palmowski, “Functional and molecular ultrasound imaging: concepts and contrast agents,” *Current Medicinal Chemistry*, vol. 16, no. 5, pp. 627–642, 2009.
- [17] N. Deshpande, A. Needles, and J. K. Willmann, “Molecular ultrasound imaging: current status and future directions,” *Clinical Radiology*, vol. 65, no. 7, pp. 567–581, 2010.
- [18] K. Ferrara, R. Pollard, and M. Borden, “Ultrasound microbubble contrast agents: fundamentals and application to gene and drug delivery,” *Annual Review of Biomedical Engineering*, vol. 9, no. 1, pp. 415–447, 2007.
- [19] I. Tardy, S. Pochon, M. Theraulaz et al., “Ultrasound molecular imaging of VEGFR2 in a rat prostate tumor model using BR55,” *Investigative Radiology*, vol. 45, no. 10, pp. 573–578, 2010.
- [20] G. E. Weller, M. K. Wong, R. A. Modzelewski et al., “Ultrasonic imaging of tumor angiogenesis using contrast microbubbles targeted via the tumor-binding peptide arginine-arginine-leucine,” *Cancer Research*, vol. 65, no. 2, pp. 533–539, 2005.
- [21] H. Leong-Poi, J. Christiansen, A. L. Klibanov, S. Kaul, and J. R. Lindner, “Noninvasive assessment of angiogenesis by ultrasound and microbubbles targeted to a v-integrins,” *Circulation*, vol. 107, no. 3, pp. 455–460, 2003.
- [22] F. Yan, X. Li, Q. Jin et al., “Ultrasonic imaging of endothelial CD81 expression using CD81-targeted contrast agents in vitro and in vivo studies,” *Ultrasound in Medicine & Biology*, vol. 38, no. 4, pp. 670–680, 2012.
- [23] Y. He, B. Zhang, Y. Chen et al., “Image-guided hydrogen gas delivery for protection from myocardial ischemia-reperfusion injury via microbubbles,” *ACS Applied Materials & Interfaces*, vol. 9, no. 25, pp. 21190–21199, 2017.
- [24] S. Yuan, S. Pardue, X. Shen, J. S. Alexander, A. W. Orr, and C. G. Kevil, “Hydrogen sulfide metabolism regulates endothelial solute barrier function,” *Redox Biology*, vol. 9, pp. 157–166, 2016.
- [25] C. Böiers, N. Buza-Vidas, C. T. Jensen et al., “Expression and role of FLT3 in regulation of the earliest stage of normal granulocyte-monocyte progenitor development,” *Blood*, vol. 115, no. 24, pp. 5061–5068, 2010.
- [26] M. A. Pysz, K. Foygel, J. Rosenberg, S. S. Gambhir, M. Schneider, and J. K. Willmann, “Antiangiogenic cancer therapy: monitoring with molecular US and a clinically translatable contrast agent (BR55),” *Radiology*, vol. 256, no. 2, pp. 519–527, 2010.
- [27] R. K. Jain, “Determinants of tumor blood flow: a review,” *Cancer Research*, vol. 48, no. 10, pp. 2641–2658, 1988.
- [28] J. J. Rychak, J. Graba, A. M. Cheung et al., “Microultrasound molecular imaging of vascular endothelial growth factor receptor 2 in a mouse model of tumor angiogenesis,” *Molecular Imaging*, vol. 6, no. 5, article 7290.2007.00024, 2007.

- [29] N. Deshpande, Y. Ren, K. Foygel, J. Rosenberg, and J. K. Willmann, "Tumor angiogenic marker expression levels during tumor growth: longitudinal assessment with molecularly targeted microbubbles and US imaging," *Radiology*, vol. 258, no. 3, pp. 804–811, 2011.
- [30] D. B. Ellegala, H. Leong-Poi, J. E. Carpenter et al., "Imaging tumor angiogenesis with contrast ultrasound and microbubbles targeted to  $\alpha_v\beta_3$ ," *Circulation*, vol. 108, no. 3, pp. 336–341, 2003.
- [31] J. K. Willmann, R. Paulmurugan, K. Chen et al., "US imaging of tumor angiogenesis with microbubbles targeted to vascular endothelial growth factor receptor type 2 in mice," *Radiology*, vol. 246, no. 2, pp. 508–518, 2008.
- [32] E. Fonsatti, H. J. Nicolay, M. Altomonte, A. Covre, and M. Maio, "Targeting cancer vasculature via endoglin/CD105: a novel antibody-based diagnostic and therapeutic strategy in solid tumours," *Cardiovascular Research*, vol. 86, no. 1, pp. 12–19, 2009.
- [33] E. Fonsatti, L. Sigalotti, P. Arslan, M. Altomonte, and M. Maio, "Emerging role of endoglin (CD105) as a marker of angiogenesis with clinical potential in human malignancies," *Current Cancer Drug Targets*, vol. 3, no. 6, pp. 427–432, 2003.
- [34] Y. Zhang, Y. Yang, H. Hong, and W. Cai, "Multimodality molecular imaging of CD105 (Endoglin) expression," *International Journal of Clinical and Experimental Medicine*, vol. 4, no. 1, pp. 32–42, 2011.

## Review Article

# Targeted Optical Imaging Agents in Cancer: Focus on Clinical Applications

**Bishnu P. Joshi** <sup>1</sup> and **Thomas D. Wang** <sup>1,2,3</sup>

<sup>1</sup>*Division of Gastroenterology, Department of Internal Medicine, School of Medicine, University of Michigan, 109 Zina Pitcher Place, BSRB 1722, Ann Arbor, MI 48109, USA*

<sup>2</sup>*Department of Biomedical Engineering, University of Michigan, Ann Arbor, MI 48109, USA*

<sup>3</sup>*Department of Mechanical Engineering, University of Michigan, Ann Arbor, MI 48109, USA*

Correspondence should be addressed to Thomas D. Wang; [thomaswa@umich.edu](mailto:thomaswa@umich.edu)

Received 26 January 2018; Revised 27 May 2018; Accepted 4 July 2018; Published 27 August 2018

Academic Editor: Daniela Haeusler

Copyright © 2018 Bishnu P. Joshi and Thomas D. Wang. This is an open access article distributed under the Creative Commons Attribution License, which permits unrestricted use, distribution, and reproduction in any medium, provided the original work is properly cited.

Molecular imaging is an emerging strategy for in vivo visualization of cancer over time based on biological mechanisms of disease activity. Optical imaging methods offer a number of advantages for real-time cancer detection, particularly in the epithelium of hollow organs and ducts, by using a broad spectral range of light that spans from visible to near-infrared. Targeted ligands are being developed for improved molecular specificity. These platforms include small molecule, peptide, affibody, activatable probes, lectin, and antibody. Fluorescence labeling is used to provide high image contrast. This emerging methodology is clinically useful for early cancer detection by identifying and localizing suspicious lesions that may not otherwise be seen and serves as a guide for tissue biopsy and surgical resection. Visualizing molecular expression patterns may also be useful to determine the best choice of therapy and to monitor efficacy. A number of these imaging agents are overcoming key challenges for clinical translation and are being validated in vivo for a wide range of human cancers.

## 1. Introduction

Cancer is a worldwide health-care concern that is steadily growing. By 2030, an annual incidence and mortality of 21.7 and 13 million cases, respectively, are expected [1]. This increase is attributed to an aging population, greater prevalence of obesity, adoption of western diets by developing countries, and environmental factors [2–4]. Many cancers arise from the epithelium of hollow organs and ducts, including breast, colon, esophagus, head and neck, lung, pancreas, and stomach [5–11]. This thin layer of highly metabolic tissue can be thoroughly and rapidly evaluated in the clinic using methods of optical imaging. Many cancer surveillance guidelines recommend random biopsies, an approach that is inefficient, time consuming, and not widely practiced [12–18]. Targeted optical contrast agents have the potential to provide a molecular mechanism to complement the anatomical view of cancer provided by conventional

imaging platforms. They can be administered via different routes, including topically and systemically, to infiltrate the epithelium for effective binding to achieve high contrast images. Malignant and premalignant lesions that may not otherwise be seen can then be detected to guide either diagnostic biopsy or intraoperative surgical resection. Imaging systems should be portable, electrically isolated, and easy to position while providing fluorescence images with micron resolution over a field of view of several centimeters. Progress in this emerging direction requires identification of highly specific targets paired with robust clinical validation.

Molecular imaging is an integrated approach that combines advances in instrumentation with progress in probe chemistries. This methodology promises to advance precision medicine by improving diagnostic performance for early cancer detection, tumor staging, risk stratification, and guidance of therapy. Rapid progress has been made in the technical performance of whole-body imaging systems,

including computed tomography (CT), magnetic resonance imaging (MRI), and ultrasound (US) [19–23]. While these platforms provide detailed images of tumor anatomy, they reveal little about the biology that drives cancer progression. Nuclear methods, such as positron emission tomography (PET) and single-photon emission computed tomography (SPECT), visualize and measure physiological processes using radiotracers. For example, 2-deoxy-2-<sup>18</sup>F-fluoro-D-glucose (<sup>18</sup>FDG) is used routinely with PET in clinical practice for cancer staging [24–26]. While both modalities have the capability to image multiple targets using affinity probes labeled with different radioisotopes, this approach is limited by high cost, lack of widespread radiotracer availability, and radiotracer stability. Furthermore, there are limited data to justify use of whole-body PET for cancer screening.

Optical imaging is an alternative modality that detects light emitted from fluorophores attached to ligands that bind specifically to molecular targets overexpressed in cancer. Light is nondestructive, nonionizing, real time, and information rich and can be used over a wide spectral range spanning from visible to near-infrared (NIR). This breadth allows for multiplexing to be performed whereby two or more targets can be visualized simultaneously and is relevant to detection of genetically heterogeneous tumors. Probe platforms are being developed for optical imaging that include small molecule, peptide, affibody, activatable, lectin, and antibody. These ligands range considerably in size from nanoparticles to large macromolecules [27–34]. Tracers used in the clinic for hybrid and theranostic applications have been reviewed previously and are not included in this current review [28]. Chemistries for fluorescence labeling and long-term stability monitoring of these molecules are fairly well developed [22, 35–38]. Clinical translation of these targeted contrast agents is challenging and can be affected by the photophysical properties, stability, pharmacokinetics (PK), and dose. Often, a multidisciplinary team is required [36]. Regulatory expertise is needed to prepare the Investigational New Drug (IND) application. Study objectives for “first-in-human” clinical studies include establishing a safety profile, identifying optimal dosage, determining time course for probe uptake, and validating target expression.

## 2. Nonspecific Optical Imaging Agents

The first optical contrast agents developed for clinical use are nonspecific. Chromoendoscopy employs the use of intravital dyes, such as methylene blue and indigo carmine [39, 40]. These dyes are topically administered and have absorptive properties that highlight mucosal surface patterns. Physician looks for areas with abnormal appearance to guide endoscopic resection of premalignant lesions. This procedure has been recommended by leading medical societies and international experts for use as an adjunct to conventional white light colonoscopy for colorectal cancer (CRC) surveillance in patients with inflammatory bowel disease (IBD), including ulcerative colitis and Crohn’s disease [41, 42]. However, the images generated by these dyes are low in

contrast, subjective in appearance, difficult to interpret without substantial training, and prone to inter- and intraobserver variability.

By comparison, fluorescence produces high image contrast that can be used for real-time clinical inspection. Fluorophores with a large molar extinction coefficient, safe toxicity profile, low molecular weight ( $\leq 1$  kD), and minimal nonspecific binding to normal tissues are best suited for this application. Also, low cost, ready availability, and well-developed labeling protocols are desirable. These contrast agents can be used to localize cancer either intra- or extracellularly based on their size and charge distribution. Delivery can be performed either topically or intravenously (iv) depending on the clinical application. Fluorescein isothiocyanate (FITC), a fluorescein derivative that is FDA-approved for human use, is one of the first optical imaging agents used in the clinic [43]. However, the peak absorbance of FITC is near that of hemoglobin, resulting in limited imaging depth and contrast and high autofluorescence background. Also, FITC is sensitive to photobleaching, which limits the time available for imaging.

5-Aminolevulinic acid (5-ALA) is an endogenous substrate that emits no fluorescence in its native state. Metabolically active tumor cells preferentially take up 5-ALA for heme synthesis (Figure 1(a)). Protoporphyrin IX (PpIX,  $\lambda_{\text{ex}} = 380$  nm;  $\lambda_{\text{em}} = 637$  nm) is a downstream substrate that is highly fluorescent (Figure 1(b)). Clinical studies using topical, oral, and intravesical administration have been conducted for a variety of diseases, including glioma, bladder, esophageal, and squamous cell carcinoma. Fluorescence has been collected with a systemic injection of 0.2, 2, and 20 mg/kg in clinical studies of dose escalation. The dose of 20 mg/kg has been found to produce the strongest fluorescence signal from tumor, and margins based on visual and spectroscopic assessment have correlated well with histology. In the clinic, 5-ALA has also been administered orally 6 hours in advance of imaging for detection of bladder cancer and glioblastoma [44–46]. However, studies have shown that 5-ALA and PpIX can accumulate in non-malignant tissues as well as in tumor, including brain parenchyma, subependymal zone, and choroid plexus [47, 48]. Other studies have shown that use of this nonspecific contrast agent can generate fluorescence in a heterogeneous spatial pattern that may not correlate with the tumor grade [49–53].

Indocyanine green (ICG,  $\lambda_{\text{ex}} = 783$  nm;  $\lambda_{\text{em}} = 813$  nm) is another nonspecific contrast agent that is FDA-approved for human use (Figure 1(c)). ICG offers several advantages, including low toxicity ( $\text{LD}_{50}$  of 50–80 mg/kg in animals) and rapid excretion into bile, and is used routinely in the clinic as iv contrast for angiography and evaluation of cardiac and liver functions [54]. ICG produces NIR fluorescence with peak emission near 800 nm. In this spectral regime, sensitivity to hemoglobin absorption, tissue scattering, and tissue autofluorescence is low, and light penetration depth is high. ICG binds rapidly to albumin in circulation and results in 5–10 nm complexes that accumulate in tumors via the enhanced permeability and retention (EPR) effect (Figure 1(d)) [55–57]. ICG has been used clinically to guide surgical

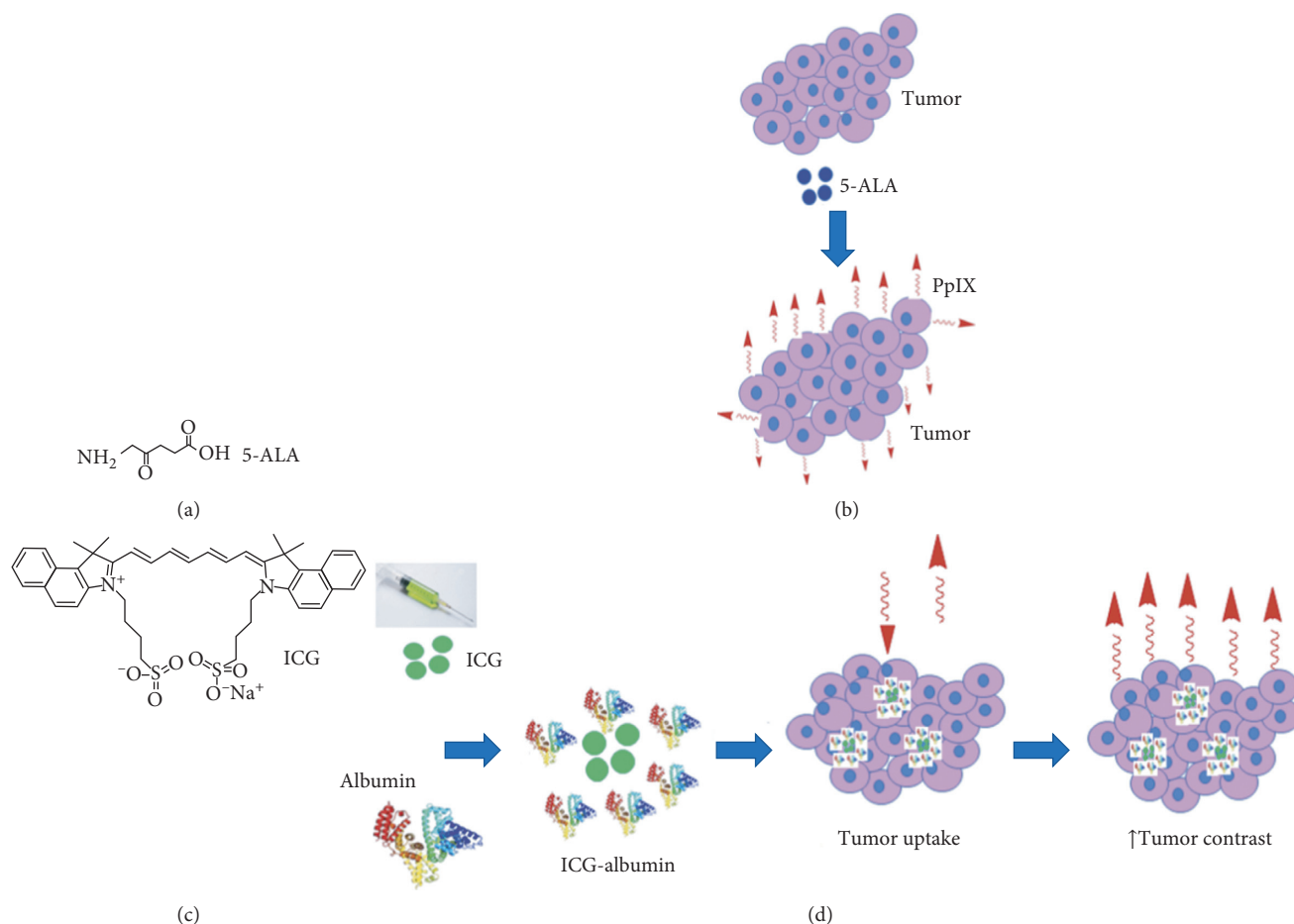


FIGURE 1: Nonspecific optical imaging agents. (a) Chemical structure of 5-ALA. (b) 5-ALA is taken up by tumor cells and used for synthesis of PpIX (abs = 405 nm, em = 635 nm). (c) Chemical structure of ICG (abs = 783 nm, em = 813 nm). (d) ICG binds to albumin and forms a complex that accumulates in tumor cells to enhance image contrast.

resection of cancer, including breast, CRC, and hepatocellular carcinoma [58]. Liberale et al. evaluated the role of fluorescence imaging using an intraoperative injection of free ICG for detection of peritoneal metastases from CRC. Free ICG at 0.25 mg/kg was iv injected, and the mean tumor-to-background ratio (TBR) was  $1.92 \pm 0.67$  in malignant and  $1.02 \pm 0.06$  in benign nodules ( $P = 0.0099$ ) in  $n = 42$  nodules from  $n = 9$  patients with nonmucinous adenocarcinoma [57]. However, nonspecific dye retention can reduce diagnostic performance for ICG, and clinical utility is limited by high levels of binding to plasma proteins (98%), low stability in aqueous media, and concentration dependent shifts in wavelength [59].

### 3. Targeted Optical Imaging Agents

By comparison, molecular probes that either bind or are activated by enzymes unique to cancer targets provide specific detection. In general, these contrast agents consist of a ligand, fluorescence signaling moiety, and carrier molecule. Different types of ligands include small molecule, peptide, affibody, activatable, lectin, and antibody (Figure 2 (A)–(F)). Clinical studies are being performed to evaluate

specific agents in various types of cancer (Figure 2(G)). The probes best suited for clinical imaging have good binding affinity, specific uptake, high cancer retention, and rapid clearance from nontarget tissues. These properties produce high in vivo TBR. In general, molecules with smaller size have a favorable pharmacokinetic profile with faster clearance that allow for imaging to be performed at earlier time points after administration. Long-term stability, in vivo integrity, ease of preparation, and safety are also important features. Table 1 summarizes clinical trials that use each class of imaging agent and are either ongoing or have been completed and are registered online at Clinicaltrials.gov.

**3.1. Small Molecule.** Folate is a small molecule that binds specifically to the folate receptor alpha (FR- $\alpha$ ). This target is overexpressed in ovarian cancer in up to 95% of patients. Moreover, FR- $\alpha$  is minimally expressed in normal cells and thus has potential to generate high image contrast. Folate has been labeled with FITC (EC17,  $\lambda_{ex} = 490$  nm;  $\lambda_{em} = 520$  nm) and ICG (OTL38) to target FR- $\alpha$  for real-time cancer detection (Figures 3(a) and 3(b)) [60]. In a clinical study of  $n = 12$  patients with ovarian cancer undergoing exploratory laparotomy, high uptake of EC17 was found in FR- $\alpha$  positive

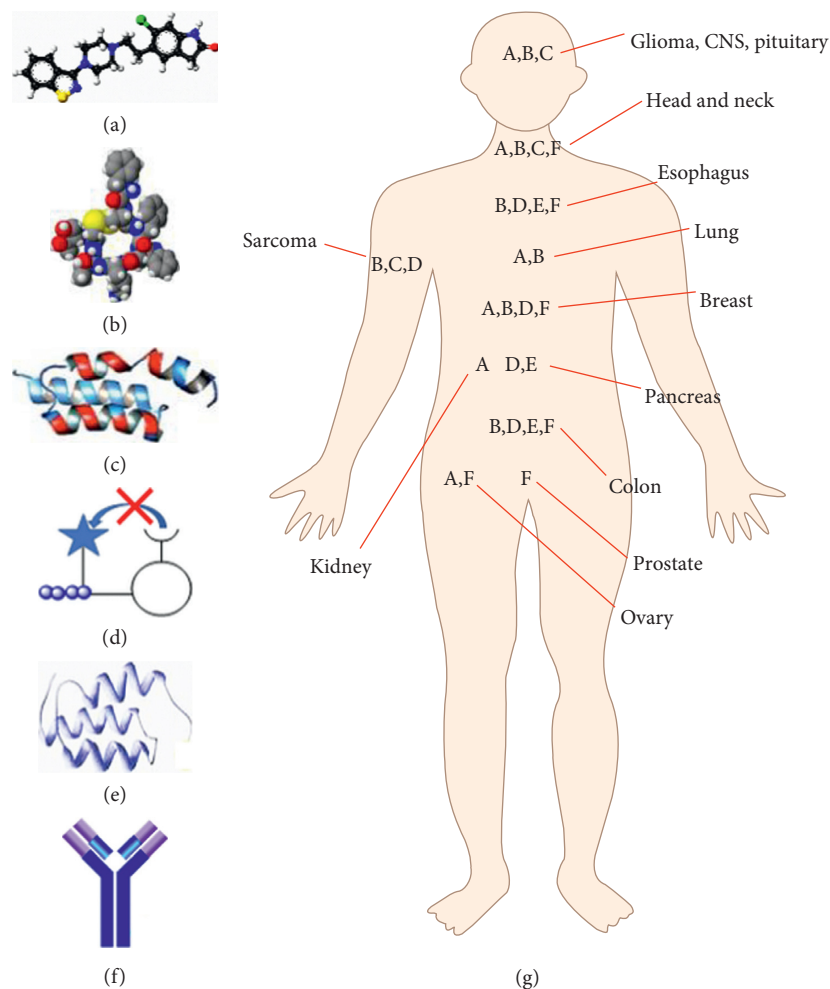


FIGURE 2: Molecular probe platforms. Targeted contrast agents being developed for optical imaging include (A) small molecule, (B) peptide, (C) affibody, (D) activatable, (E) lectin, and (F) antibody. (G) Clinical studies are being performed using each platform in a wide range of cancers.

tumors and metastases during laparoscopy (Figures 3(c) and 3(d)) [61]. The iv injected formulation for both EC17 and OTL38 appeared to be safe. The fluorescence intensity was found to peak within the range of 2–8 hours postinjection. All patients completed the study, and no serious adverse events (SAEs) were reported. The mean TBR was 3.1 and 4.4 for EC17 and OTL38, respectively, at the injected doses of 0.3 mg/kg for EC17 and 0.05 mg/kg for OTL38. Surgeons were able to find and resect an additional 29% of malignant lesions that were not identified using conventional white light. Based on the preclinical imaging and biodistribution experiments performed with TC1-implanted murine lung cancer cells, the majority of EC17 and OTL38 accumulated in the digestive system, mostly localized in the stomach and small and large intestines. There was significant fluorescence in tumors, and no signal was found in the lung, heart, spleen, muscle, bone, fat, or liver. OTL38 was fluorescent in the kidneys, whereas EC17 was not. There were no signs of acute toxicity in any of the animals. Use of fluorescence did not interfere with the surgeon's ability to perform the procedure. This "first-in-human" study demonstrates potential for use of small molecules to target ovarian cancer, guide radical

cytoreductive surgery, and improve methods for intra-operative staging [62–69].

PARPi-FL is a small-molecule inhibitor that binds to the DNA repair enzyme poly(ADP-ribose) polymerase 1 (PARP1) and is fluorescently labeled with boron-dipyrromethene (BODIPY,  $\lambda_{ex} = 507$  nm;  $\lambda_{em} = 525$  nm) (Figure 4(a)). PARPi-FL has potential to improve diagnostic performance and guide surgical resection of oropharyngeal squamous cell cancer (OSCC) (Figures 4(c) and 4(d)) [70]. The incidence of this disease has increased steadily as a result of chronic infection with the human papillomavirus (HPV). PARP1 expression is increased by ~8-fold in OSCC relative to normal oral mucosa. In the preclinical study performed in an orthotopic tongue tumor model of OSCC (FaDu cells), iv injection of 75 nmol PARPi-FL per animal provided a maximum uptake at 90 minutes postinjection. Fluorescence imaging showed strong PARPi-FL accumulation in parts of the tongue that were visibly affected by OSCC, whereas no signal accumulation was observed in regions without tumors after injection of either PARPi-FL or vehicle. When compared with vehicle, the average signal intensity from tumor-bearing mice was significantly higher ( $35.4 \pm 8.6$  versus  $15.2 \pm 5.0$  AU,

TABLE 1: Clinical studies of targeted imaging agents. A summary of the ongoing or completed clinical trials, as described online at Clinicaltrials.gov organized by each class of molecular probe.

| NCT#                  | Dates           | Cancer                     | Ligand/target                           | Fluorophore | Reference |
|-----------------------|-----------------|----------------------------|---|-------------|-----------|
| <i>Small molecule</i> |                 |                            |   |             |           |
| NCT02000778           | 11/2013–2/2018  | Ovary                      | EC17/Folate- $\alpha$                   | FITC        | [60, 61]  |
| NCT02769533           | 09/2015–9/2020  | Pituitary                  | OTL38/Folate- $\alpha$                  | ICG         | [62]      |
| NCT01778933           | 05/2013–2/2018  | Renal cell                 | EC17/Folate- $\alpha$                   | FITC        | [63]      |
| NCT01778920           | 04/2012–5/2016  | Lung                       | EC17/Folate- $\alpha$                   | FITC        | [64]      |
| NCT02602119           | 05/2015–8/2017  | Lung                       | OTL38/Folate- $\alpha$                  | ICG         | [65]      |
| NCT01994369           | 05/2014–2/2018  | Breast                     | EC17/Folate- $\alpha$                   | FITC        | [66]      |
| NCT02653612           | 01/2016–2/2020  | Lung                       | EC17/Folate- $\alpha$                   | FITC        | [67]      |
| NCT02645409           | 12/2015–4/2018  | Renal cell                 | OTL38/Folate- $\alpha$                  | ICG         | [68, 69]  |
| NCT03085147           | 03/2015/-3/2019 | Head & neck                | Olaparib/poly(ADP-ribose) polymerase 1  | BODIPY      | [70]      |
| NCT03333031           | 01/2018–2/2020  | Breast                     | HS-196/Hsp90                            | FITC        | [71]      |
| <i>Peptide</i>        |                 |                            |   |             |           |
| NCT02462629           | 06/2015–2/2016  | CNS                        | BLZ-100/a*                              | Cy5.5       | [72, 73]  |
| NCT02496065           | 07/2015–2/2016  | Breast                     | BLZ-100/a*                              | Cy5.5       | [74]      |
| NCT02464332           | 09/2015–5/2016  | Sarcoma                    | BLZ-100/a*                              | Cy5.5       | [75–77]   |
| NCT02234297           | 10/2014–2/2016  | Glioma                     | BLZ-100/a*                              | Cy5.5       | [72, 73]  |
| NCT02097875           | 12/2013–3/2015  | Basal/squamous cell        | BLZ-100/a*                              | Cy5.5       | [75–77]   |
| NCT03205501           | 02/2017–2/2018  | Esophagus                  | EMI-137/c-Met                           | Cy5         | [78]      |
| NCT03360461           | 12/2017–7/2018  | Colon                      | EMI-137/c-Met                           | Cy5         | [78]      |
| NCT02676050           | 02/2018–6/2018  | Lung                       | EMI-137, NAP/c-Met                      | Cy5         | [78]      |
| NCT02807597           | 12/2017–2/2020  | Breast                     | LS301/ $\alpha$ V $\beta$ III integrins | Cypate      | [79]      |
| NCT01722058           | 02/2013–8/2013  | Colon                      | VRPMLQ/b*                               | Fluorescein | [80]      |
| NCT02156557           | 06/2014–7/2016  | Colon                      | KCCFPAQ/c*                              | FITC        | [81]      |
| NCT01391208           | 02/2011–6/2012  | Esophagus                  | ASYNYDA/d*                              | FITC        | [82]      |
| NCT01630798           | 07/2012–9/2013  | Esophagus                  | ASYNYDA/d*                              | FITC        | [83]      |
| NCT02574858           | 11/2015–8/2016  | Esophagus                  | QRHKPRE/EGFR                            | Cy5         | [84]      |
| NCT03161418           | 06/2017–9/2017  | Esophagus                  | KSPNPRF/Her2                            | IRDye800    | [85]      |
| NCT03148119           | 03/2017–3/2018  | Colon                      | QRHKPRE/EGFR                            | Cy5         | [84]      |
| <i>Affibody</i>       |                 |                            |   |             |           |
| NCT02901925           | 12/2016–3/2018  | Glioma                     | ABY-029/EGFR                            | IRDye800    | [86–88]   |
| NCT03282461           | 10/2017–2/2018  | Head & neck                | ABY-029/EGFR                            | IRDye800    | [86–88]   |
| NCT03154411           | 08/2017–2/2018  | Sarcoma                    | ABY-029/EGFR                            | IRDye800    | [86–88]   |
| <i>Activatable</i>    |                 |                            |   |             |           |
| NCT02438358           | 06/2015–9/2016  | Breast                     | LUM015/Enzymes                          | Cy5         | [89]      |
| NCT01626066           | 06/2012–8/2015  | Sarcoma                    | LUM015/Enzymes                          | Cy5         | [89]      |
| NCT02584244           | 05/2016–3/2018  | Colon, pancreas, esophagus | LUM015/Enzymes                          | Cy5         | [89]      |
| <i>Lectin</i>         |                 |                            |   |             |           |
| NCT03070613           | 04/2017–3/2018  | Colon                      | Wisteria floribunda/e*                  | Fluorescein | [90]      |
| <i>Antibody</i>       |                 |                            |   |             |           |
| NCT02497599           | 06/2015/-8/2018 | Renal cell                 | Girentuximab/carbo-nic anhydrase IX     | IRDye800    | [91]      |
| NCT03134846           | 05/2017–1/2021  | Head & neck                | Cetuximab/EGFR                          | IRDye800    | [92]      |
| NCT02736578           | 07/2016/-4/2017 | Pancreas                   | Cetuximab/EGFR                          | IRDye800    | [92]      |
| NCT01987375           | 11/2015–2/2018  | Head & neck                | Cetuximab/EGFR                          | IRDye800    | [92]      |
| NCT02415881           | 04/2015–8/2017  | Head & neck                | Panitumumab/EGFR                        | IRDye800    | [92]      |
| NCT01372189           | 01/2011–7/2011  | Colon                      | anti-EGFR mAb                           | AF488       | [93]      |
| NCT02048150           | 03/2015–9/2016  | Prostate                   | MDX1201/PSMA                            | AF488       | [94]      |
| NCT02743975           | 09/2016–2/2017  | Pancreas                   | Bevacizumab/VEGF-A                      | IRDye800    | [95, 96]  |
| NCT01972373           | 10/2013–1/2017  | Rectum                     | Bevacizumab/VEGF-A                      | IRDye800    | [95, 96]  |
| NCT02583568           | 10/2015/-2/2017 | Breast                     | Bevacizumab/VEGF-A                      | IRDye800    | [95, 96]  |
| NCT02129933           | 04/2014–1/2016  | Esophagus                  | Bevacizumab/VEGF-A                      | IRDye800    | [95, 96]  |
| NCT02113202           | 03/2014–0/2015  | Colon                      | Bevacizumab/VEGF-A                      | IRDye800    | [95, 96]  |

a\*: multiple targets reported including matrix metalloproteinase-2 (MMP-2), membrane type-I MMP, and a transmembrane inhibitor of metalloproteinase-2 (TIMP2), ClC-3 chloride ion channels, and other proteins; b\*–d\*: peptide was screened using unbiased selection and target is unknown; e\*: disaccharides and other glycans.

resp.;  $P < 0.001$ ). There was no difference between the average signal intensity after PARPi-FL or vehicle injection in tongue and thigh muscle. Based on these promising preclinical

results, a Phase 1/2 clinical trial is being performed using PARPi-FL as a targeted contrast agent with topical administration for in vivo imaging (Table 1).

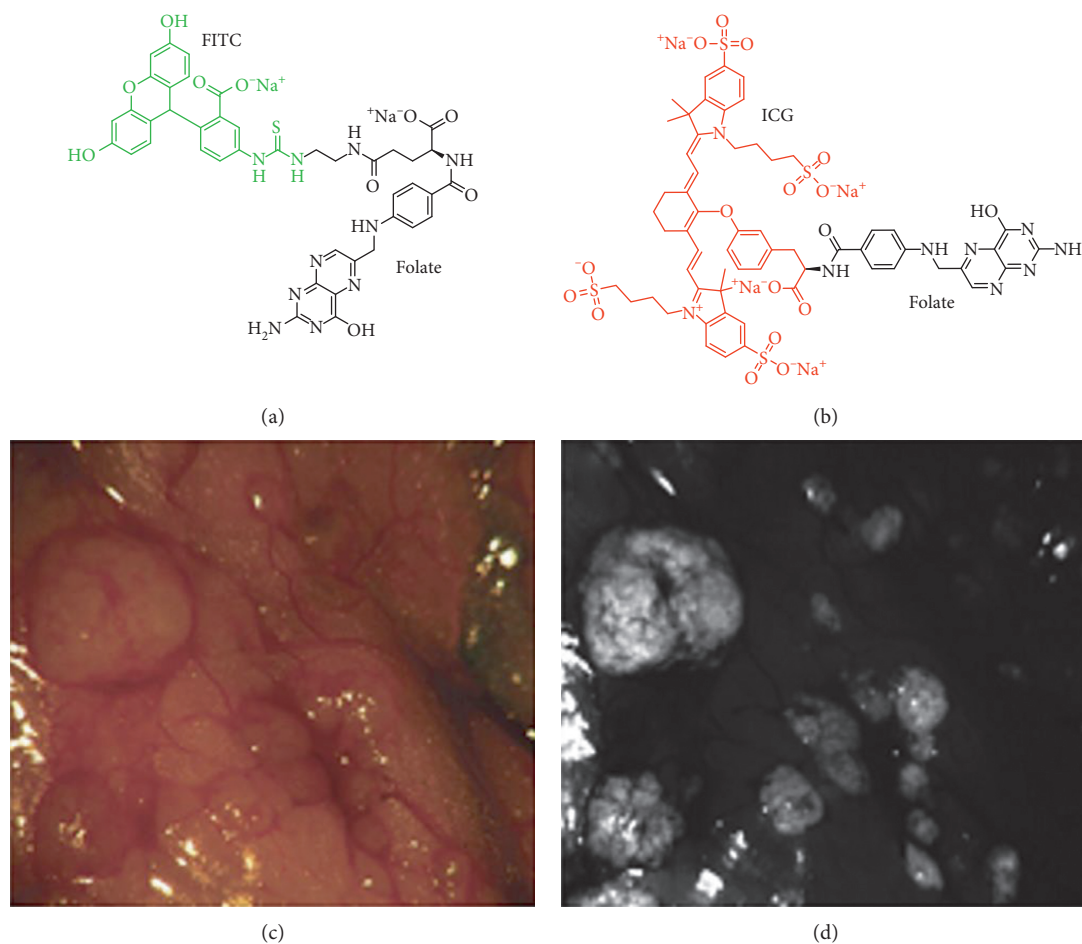


FIGURE 3: In vivo optical imaging with folate. Chemical structure is shown of folate labeled with (a) FITC (abs = 490 nm, em = 525 nm), known as EC17, and (b) ICG (abs = 783 nm, em = 813 nm), known as OTL38. (c) White light laparoscopic image of peritoneum in vivo and corresponding (d) fluorescence image show enhanced contrast from ovarian cancer metastases following systemic administration of EC17 ((c) and (d) reprinted with the permission from [60]).

Heat shock protein 90 (Hsp90) is a chaperone that aids in the folding, stabilization, and degradation of cellular proteins and is found in virtually all living organisms. Hsp90 expression is particularly high in cancer cells and may facilitate tumor invasion. HS-196 is a small molecule inhibitor that has been tethered to FITC via a PEG linker for optical imaging to target Hsp90 expressed ectopically in tumors (Figure 4(b)) [71]. Hsp90 has 3 structural domains including an *N*-terminal domain that contains an ATP binding site. Preclinical studies in breast cancer showed that these tethered inhibitors selectively recognize and are internalized by cells that overexpress Hsp90. High uptake of HS-196 was observed in vitro and in vivo in multiple breast cancer cell lines versus the Huh7 liver cancer cell. In vivo imaging of HS-196 with iv injection resulted quick and strong tumor accumulation and long retention. Pharmacokinetic studies show dose dependent uptake of either the visible or NIR forms, peak intensity within the tumor mass by 30 minutes, and a detectable signal for up to 72 hours. The TBR was calculated using flow cytometry, and ~3-fold greater uptake was observed in isolated tumor cells versus either splenocytes or hepatocytes. A clinical trial using iv

administration of HS-196 is planned for breast cancer patients (Table 1).

**3.2. Peptide.** Peptides bind a broad range of cell surface targets with high specificity and affinity. Their relatively small size (<5 kDa) facilitates delivery to overexpressed cancer targets for in vivo detection. Peptides exhibit rapid peak uptake, clear quickly to avoid toxicity, and minimize biodistribution to nontarget tissues. They bind within a few minutes, a timescale that is compatible with clinical use in high volume procedures, such as endoscopy. Peptides have low likelihood to elicit an immune response which allows for repeat use. Peptide analogs with good stability, binding properties, and pharmacokinetic behavior have been used clinically to image neuroendocrine tumors, adenocarcinomas, lymphomas, and melanomas [97–99]. Peptides can be labeled with a variety of fluorophores, including visible and NIR dyes. Recently, cyanine-based dyes that emit fluorescence in the NIR spectrum have been used in the clinic for greater imaging depth [22, 100, 101]. Chlorotoxin (CTX) is a naturally occurring 36-amino acid peptide with

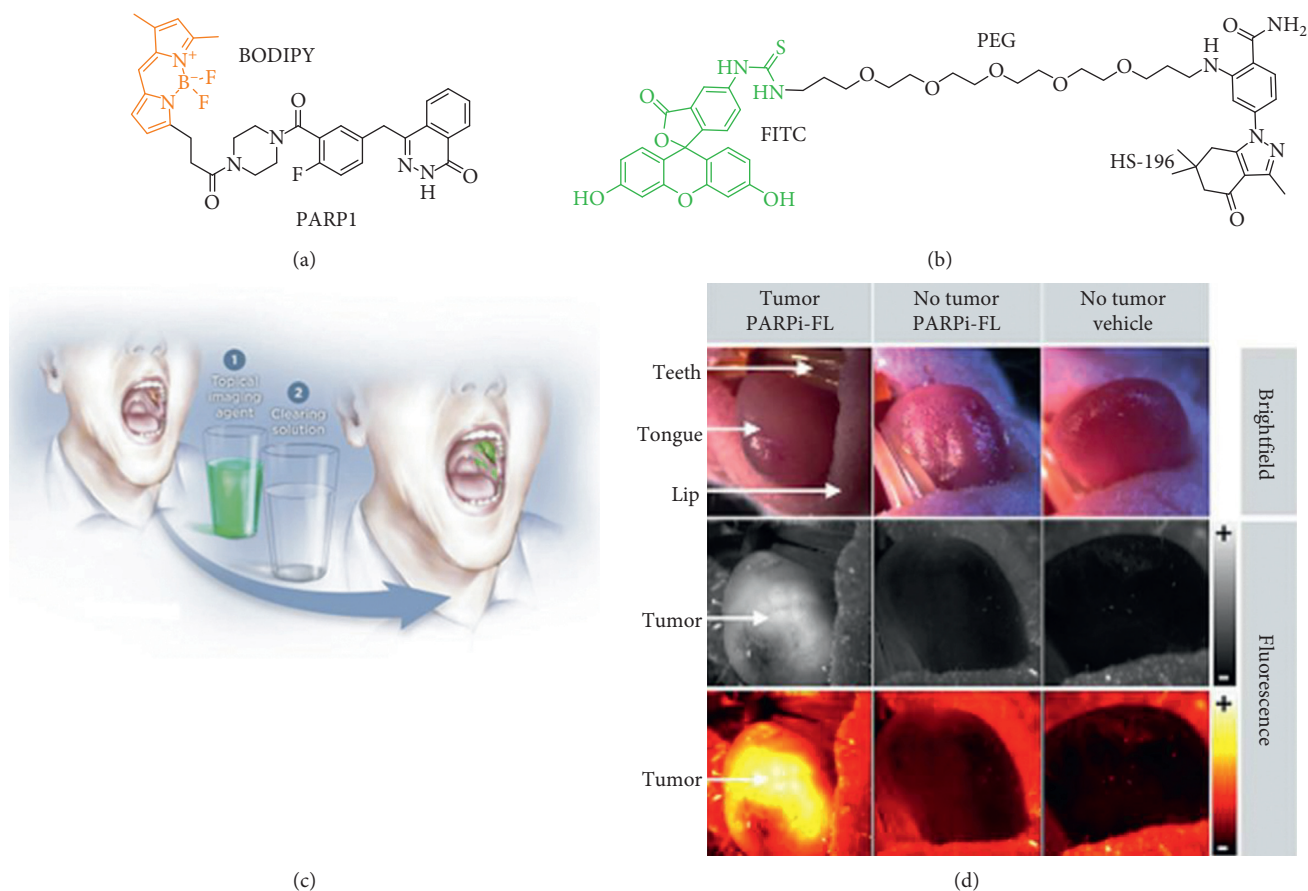


FIGURE 4: Small molecular inhibitors. Chemical structures of (a) PARP1 labeled with BODIPY ( $\text{abs} = 507 \text{ nm}$  and  $\text{em} = 525 \text{ nm}$ ) and (b) Hsp90 inhibitor HS-196 labeled with FITC. (c) Fluorescence imaging of the oral cavity is performed with topical application of PARPi-FL followed by an acetic acid rinse to remove any unbound contrast agent. (d) Detection of OSCC in mouse tongue in orthotopic xenograft model using fluorescence stereoscope ((c) and (d) reprinted with the permission from [70]).

4 disulfide bonds and is derived from the *Leiurus quinquestriatus* scorpion. CTX binds to a lipid raft-anchored complex that contains matrix metalloproteinase-2 (MMP-2), membrane type-I MMP, and a transmembrane inhibitor of metalloproteinase-2 (TIMP2), CIC-3 chloride ion channels, and other proteins [72–74]. This complex is internalized by cancer cells and eliminates functional chloride channels. CTX has been labeled with Cy5.5 ( $\lambda_{\text{ex}} = 675 \text{ nm}$ ;  $\lambda_{\text{em}} = 695 \text{ nm}$ ) using a side chain of lysine, denoted as BLZ-100, for use in Phase 1 clinical studies (Figure 5(a)) [75–77, 102, 103]. BLZ-100 is also known as “tumor paint” and was first used to image gliomas. The nonclinical safety and pharmacokinetic profile of BLZ-100 were evaluated in mice, rats, canines, and nonhuman primates (NHP). Single bolus iv administration of BLZ-100 was well tolerated and no-observed-adverse-effect-levels (NOAELs) included 7 mg (28 mg/kg) in rats and 60 mg (20 mg/kg) in NHP. In the most recent study, BLZ-100 was administered at different doses as a single iv bolus 6–31 hours prior to surgery in pediatric glioblastoma patients with either confirmed or suspected brain tumor. Tumor fluorescence was evaluated in situ and ex vivo using a synchronized infrared imaging system (SIRIS). TBR was not reported; however, tumor fluorescence was observed in 13/15 tumors including 5/7 low-grade gliomas.

Fluorescence intensity increased with the dose of BLZ-100. More recently, this targeted contrast agent has been used to detect a variety of other cancers, including the medulloblastoma, sarcoma, prostate, colon, breast, lung, and skin.

GE-137 is a 26-mer cyclic peptide, also known as EMI-137, which was developed using phage display screening for specific binding to c-Met (Figure 5(b)) [78]. c-Met is a protooncogene that encodes a transmembrane receptor tyrosine kinase to stimulate tumor progression and metastases. Based on the high prevalence of dysregulation noted in human tumors and its association with advanced disease, c-Met can also be used as a therapeutic target. The peptide was labeled with the NIR fluorophore Cy5 ( $\lambda_{\text{ex}} = 645 \text{ nm}$ ;  $\lambda_{\text{em}} = 665 \text{ nm}$ ) and was administered iv for optical imaging of colonic adenomas using a fiber-optic imaging bundle. The biodistribution and pharmacology/toxicity of this peptide were first evaluated in rats and cynomolgus monkeys, and a single iv dose of up to 0.36 mg/kg was felt to be safe in humans. This dose is twice that used for clinical imaging. A single dose (0.02–0.18 mg/kg) of peptide was then administered iv in both healthy volunteers and subjects at high risk of colorectal neoplasia (total  $n = 31$ ). The peptide was found to be well tolerated and safe and did not result in any clinically significant changes in symptoms, blood and

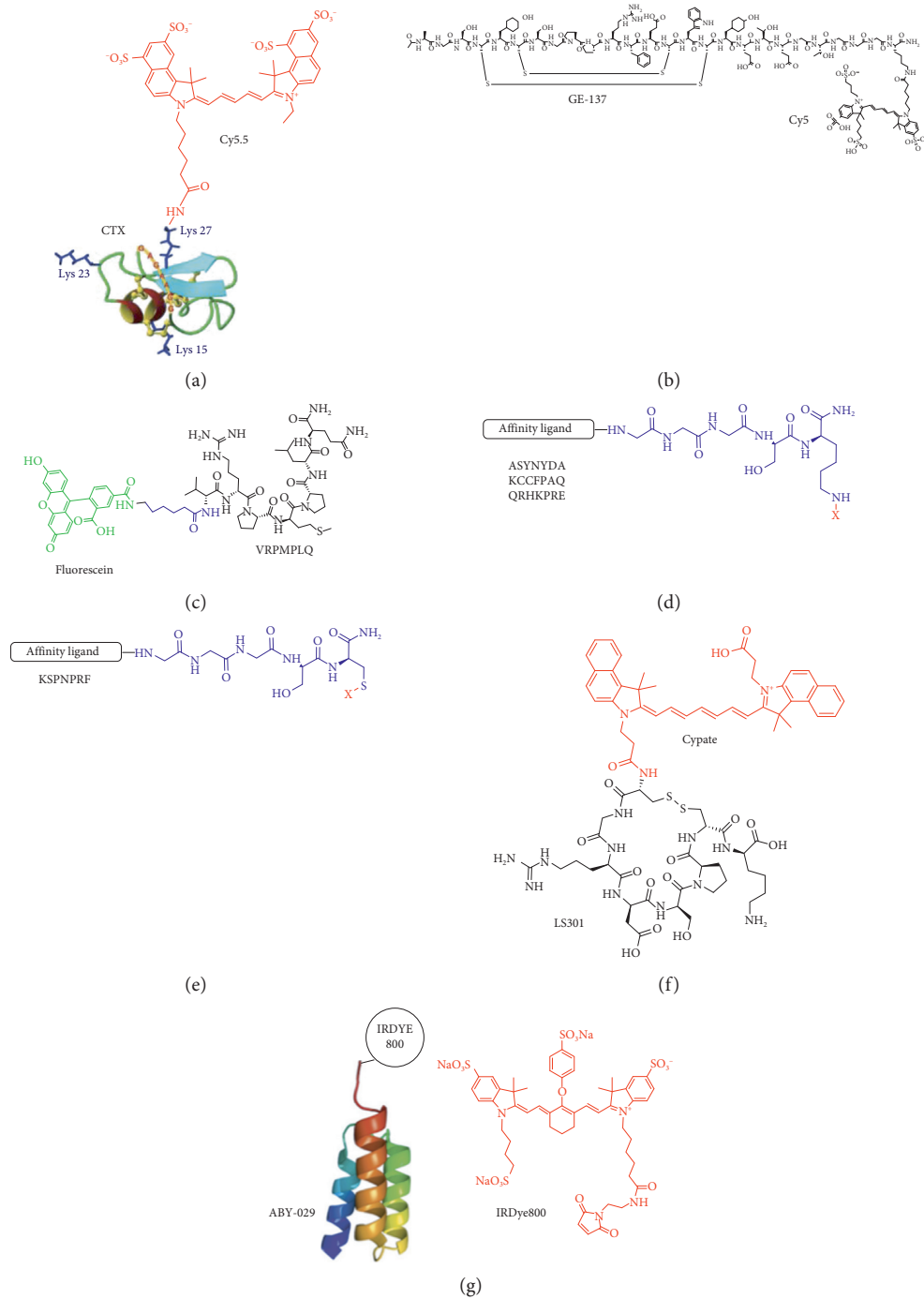


FIGURE 5: Peptides. (a) Chlorotoxin (CTX) is labeled with Cy5.5 (abs = 675 nm and em = 695 nm), also known as BLZ-100. (b) GE-137 is specific for c-Met and is labeled with Cy5 (abs = 645 nm and em = 665 nm), also known as EMI-137. (c) VRPMLQ is labeled with fluorescein (abs = 490 nm and em = 520 nm). (d) Peptides ASYNYDA, KCCFPAQ, and QRHKPRE are labeled with either FITC or Cy5 via a linker (X = FITC or CY5). (e) Peptide specific for Her2 is labeled with IRDye800 via a thiol-maleimide (X = IRDYE800). (f) Cyclic peptide LS301 specific for integrin is labeled with cypate (abs = 778 nm and em = 805 nm). (g) ABY-029 affibody specific for EGFR is labeled with IRDye800 ((a) reprinted and modified with the permission from [102] and (b) reprinted with the permission from [78]).

urinary lab parameters, vital signs, or EKG. Fluorescence measurements indicated a half-life of ~2 hour 30 minutes for the background to clear at all doses. From ex vivo images, ~2.3-fold higher fluorescence intensity was observed in the premalignant lesions versus normal colonic mucosa. This

imaging approach was demonstrated in vivo in  $n = 15$  patients and was found to improve the diagnostic yield of adenomas by 19%. Some premalignant lesions had either flat or subtle features on colonoscopy and were easily missed with conventional white light illumination.

Peptides have also been identified empirically using phage display by screening against cancer cells. This approach maximizes fluorescence signal needed for real time in vivo imaging; however knowledge of the target may be incomplete. The peptide VRPMLQ was labeled with fluorescein via an aminohexanoic acid linker (Figure 5(c)) and was found to bind preferentially to premalignant rather than normal colonic crypts using confocal endomicroscopy [80]. This peptide was applied topically at 100  $\mu$ M, and imaging was performed after 5 min postincubation. A TBR of  $17.9 \pm 4.2$  (SEM) in fluorescence intensity between adenomas and normal colonocytes was found with an average signal-to-noise ratio (SNR) of  $9.3 \pm 0.9$  (SEM) for  $n = 18$  adenomas. Contrast ranged between  $0.9 \pm 17.2$  (SD) and  $52.3 \pm 6.8$  (SD).

The peptide ASYNYDA was found to localize to regions of high-grade dysplasia and esophageal adenocarcinoma in patients with Barrett's esophagus using either confocal endomicroscopy or wide-field endoscopy (Figure 5(d)) [82, 83]. The pharmacology/toxicology study was performed in rats at 4 doses in escalation by oral gavage and showed no peptide-related acute adverse effects in clinical signs or chemistries or on necropsy up to 15 days after peptide administration up to 0.86 mg/kg. The receiver-operator characteristic (ROC) curve for in vivo imaging showed an optimum sensitivity of 75% (95% CI: 43%–95%) and specificity of 97% (95% CI: 85%–100%) at TBR = 4.2, with an area under curve (AUC) of 0.91. The performance of the peptide varied with threshold. At this TBR,  $n = 9$  true positives,  $n = 1$  false positive,  $n = 34$  true negatives, and  $n = 3$  false negatives for identifying neoplasia were found, resulting in a PPV of 90% and NPV of 92%.

The peptide KCCFPAQ was screened against human CRC cells that have a point mutation in the V600E locus of the BRAF gene, a characteristic of sessile serrated adenoma (SSA) but not tubular adenomas (Figure 5(d)) [81]. A rigorous pharmacology/toxicology study of GMP-synthesized peptide was performed in rats to provide an initial assessment of safety. Intracolonic administration with a volume of 10 mL/kg was performed in 4 groups of rats at 7 weeks of age, including vehicle (PBS) and at 0.0086 mg/kg, 0.026 mg/kg, and 0.86 mg/kg. No acute peptide-related adverse effects in clinical signs, labs, or necropsy were found in any of the animals. A Phase 1A safety study was performed in  $n = 25$  patients and showed no significant adverse events with the FITC-labeled peptide administered topically to colonic mucosa (Table 1). An optical imaging study was performed in the proximal colon of  $n = 38$  patients with suspected adenomas using tandem white light and fluorescence endoscopy, Table 1. SSAs were found to have significantly greater mean fluorescence intensity than normal colon. Fluorescence images were used to distinguish SSAs from normal mucosa with 89% sensitivity and 92% specificity at a TBR of 1.16 (Figures 6(a)–6(f)).

Peptides have also been developed that bind specifically to known cancer targets. QRHKPRE was labeled with Cy5.5 to detect epidermal growth factor receptor (EGFR) overexpressed in epithelial cancers (Figure 5(d) [84]). Use of this peptide for imaging has been demonstrated in several preclinical models of cancer, including colon and liver.

Clinical studies are under way for early cancer detection in patients at increased risk for colorectal cancer (Table 1). KSPNPRF was developed to bind specifically to epidermal growth factor receptor 2 (ErbB2), [85] also known as Her2, another member of the tyrosine kinase family. Her2 is overexpressed in many cancers including breast, colon, esophagus, and stomach. This peptide was labeled with IRDye800 ( $\lambda_{\text{ex}} = 775$  nm  $\lambda_{\text{em}} = 795$  nm) using thiol-maleimide chemistry (Figure 5(e)) and safety with topical administration was established in a Phase 1A clinical study (Table 1). Peptides targeting either EGFR or Her2 did not initiate downstream signaling following ligand-receptor binding to support safety for clinical imaging. Also, both peptides did not show any acute toxicity in rats.

LS301 is cyclic octapeptide (D-Cys-Gly-Arg-Asp-Ser-Pro-Cys)-Lys-OH that binds specifically to integrins expressed by tumor cells but not normal. D-cysteine is incorporated to prevent degradation by endogenous serum proteases. This peptide has been labeled with cypate ( $\lambda_{\text{ex}} = 778$  nm  $\lambda_{\text{em}} = 805$  nm), a hydrophobic NIR fluorophore, Figure 5(f). Tumor cells take up this targeted contrast agent via receptor-mediated endocytosis, and fluorescence images are visualized using special Cancer vision goggles (CVG). LS301 has shown promising results in vivo in preclinical studies [79].

Fluorescence images collected using LS301 identified all tumors in mice ( $n = 10$ ) with a mean TBR of  $1.21 \pm 0.1$  and was used to guide real-time resection. The fluorescence signal was significantly higher in tumors than in surrounding tissue ( $P < 0.05$ ) and correlated well with histology. A clinical study has been planned to evaluate use of this peptide in patients with breast cancer undergoing partial mastectomy and biopsy (Table 1). The study aims to use NIR fluorescence images to evaluate the ability of LS301 to predict the presence of positive cancer margins around the mastectomy site and to locate positive sentinel lymph nodes.

**3.3. Affibody.** Affibodies are nonimmunoglobulin, synthetic proteins (~7 kDa) that are generally larger in size than peptides but smaller than antibodies. Similar to peptides, affibodies exhibit rapid tumor uptake and fast clearance from normal tissues by comparison with antibodies. They also have good stability and binding affinity. The clinical utility of an affibody specific for Her2 has been demonstrated using nuclear imaging in breast cancer patients with recurring metastases [104]. ABY-029 is an affibody specific for EGFR that has been labeled with IRDye800 ( $\lambda_{\text{ex}} = 775$  nm  $\lambda_{\text{em}} = 795$  nm) for optical imaging (Figure 5(g)) [86, 87]. A microdose injection of ABY-029 was used to delineate human glioma xenograft tumors in nude rats. Optical imaging with ABY-029 outperformed 5-ALA for detection of orthotopically implanted gliomas [88]. ABY-029 has been synthesized for in vivo characterization and will be evaluated clinically in patients with recurrent glioma, head and neck cancer, and primary sarcoma, Table 1.

**3.4. Activatable.** Activatable probes are optically inactive in the native state and become highly fluorescent when cleaved

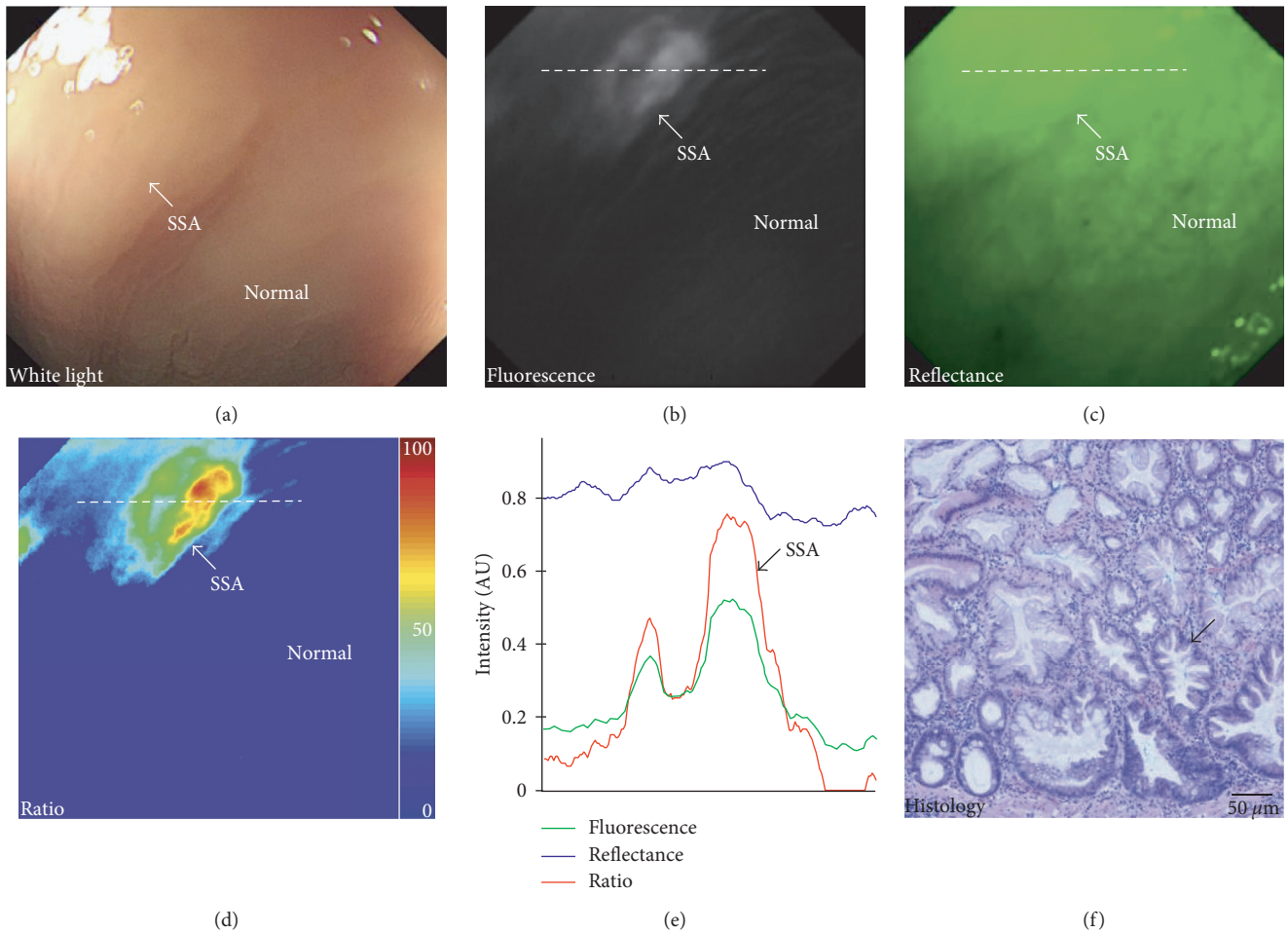


FIGURE 6: In vivo peptide image of human colonic adenoma. (a) SSA (arrow) with flat morphology collected with conventional white light is shown. (b) Fluorescence image following topical administration of peptide KCCFPAQ labeled with FITC shows increased contrast from lesion (arrow). (c) Reflectance and fluorescence images are combined as a (d) ratio to quantify image. (e) Image intensities along horizontal dashed line in (b–d) show a peak located at site of the SSA (arrow). (f) Corresponding histology of SSA shows serrated morphology (arrow) (reprinted with the permission from [81]).

by enzymes that are overexpressed in cancer. This class of targeted contrast agent has been demonstrated in preclinical optical imaging studies in a number of disease models, including cancer, atherosclerosis, rheumatoid arthritis, and thrombosis [34, 105–108]. Lum015 consists of a 22 kDa polyethylene glycol (PEG 450) and the NIR fluorophore Cy5 ( $\lambda_{\text{ex}} = 645 \text{ nm}$ ,  $\lambda_{\text{em}} = 665 \text{ nm}$ ) attached to a QSY21 ( $\lambda_{\text{ex}} = 660 \text{ nm}$ ,  $\lambda_{\text{em}} = 792 \text{ nm}$ ) quencher (Figure 7(a)). Cathepsins cleave the Gly-Gly-Arg-Lys (GGRK) recognition sequence to release fluorescence. Preclinical imaging results with LUM015 in various cancer types have been promising. No adverse effects have been found in either mice or canines with naturally occurring cancers following injection 6–24 hours prior to surgery. Biodistribution, pharmacokinetic profiles, and metabolism were similar in mice and human subjects. LUM015 was administered to  $n = 6$  patients at a dose of 0.5 and 1.0 mg/kg and  $n = 3$  patients at 1.5 mg/kg. Surgical removal of tumors immediately followed by ex vivo fluorescence imaging was done either the same day as probe injection (at ~6 hours) or the following day (at ~30 hours). LUM015 is currently in Phase 1 clinical studies for soft-tissue

sarcoma, breast cancer, and digestive tract cancers, including colon, esophagus, and pancreas (Table 1 [89]). Tissue specimens of cancer ( $n = 49$ ) imaged intraoperatively showed good correlation with pathology.

**3.5. Lectin.** Lectins are glycoproteins that bind to specific sugar residues (oligosaccharides) and have been developed to detect cell-surface glycans that are altered in cancer [90, 109]. Unlike other posttranslational modifications, glycosylation is highly specific in cancer and provides a promising biomarker for early cancer detection [110, 111]. Wheat germ agglutinin (WGA) is a lectin that has been fluorescein-labeled and topically administered to the epithelial surface of freshly resected specimens of whole human esophagus. Specific binding to high-grade dysplasia was visualized using a clinical fluorescence endoscope ex vivo. These lesions were flat in appearance and not likely to be detected with conventional white light endoscopy. Unlike the other targeting ligands, cancer progression is associated with reduced lectin binding.

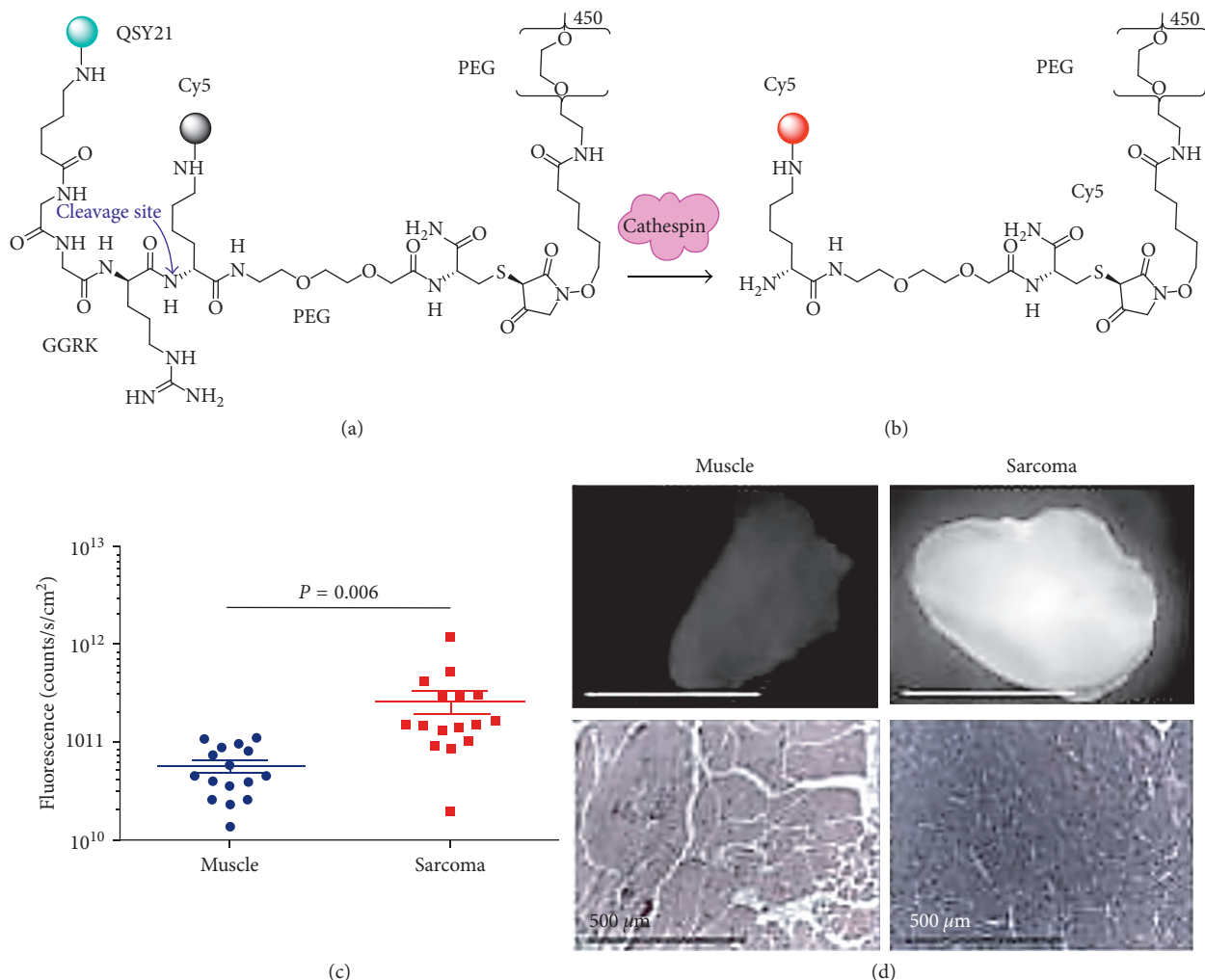


FIGURE 7: Activatable probe. (a) LUM015 consists of GGRK cleavage site. The Cy5 fluorophore is quenched by QSY21 in native state. (b) Proteolytic cleavage of the quencher by cathepsins activates fluorescence from Cy5. (c) Significantly increased signal is seen in a preclinical model of sarcoma. (d) Representative ex vivo fluorescence images of resected normal human muscle and sarcoma along with corresponding histology ((c) and (d) reprinted with the permission from [89]).

WGA labeled with Alexa Fluor 647 (AF647,  $\lambda_{ex} = 650$  nm  $\lambda_{em} = 668$  nm) showed significantly decreased binding in sections of human colonic adenomas ex vivo (Figure 8(a)) [90]. This targeted contrast agent could distinguish among normal epithelium, hyperplastic polyps, low-grade dysplasia, high-grade dysplasia, and adenocarcinoma with high sensitivity, specificity, and positive predictive value (Figures 8(b) and 8(c)). Another lectin, helix pomatia agglutinin (HPA) demonstrated comparable performance. Decreased binding of WGA and HPA to the epithelium in dysplasia suggests that these lectins may be used clinically with fluorescence colonoscopy for early cancer detection. However, this negative contrast strategy can be limited by false-positives when used in vivo because of overlying mucus, anatomic shadows, and mucosal folds. The fluorescein-labeled lectin wisteria floribunda is currently being evaluated in a Phase 1 clinical trial for early detection of colorectal cancer, Table 1.

3.6. *Antibody.* Antibodies are immunoglobulins developed originally for therapy and have been fluorescently labeled for

clinical use as targeted imaging agents [33, 91, 112–114]. Following systemic administration, antibodies can have a long in vivo circulation time that can last up to several days. The unbound probe must clear to reduce background before imaging. Cetuximab is a chimeric (human/mouse) monoclonal antibody (mAb), and panitumumab is a fully human mAb specific for EGFR. Both have been labeled with IRDye800 ( $\lambda_{ex} = 775$  nm  $\lambda_{em} = 795$  nm) and are being evaluated clinically (Table 1). Use of cetuximab-IRDye800 to guide intraoperative surgery of head & neck cancer has been demonstrated with NIR fluorescence imaging [92]. This imaging agent was found to be well tolerated and provided high contrast between tumor and normal mucosa in a dose- and time-dependent fashion. Wide-field fluorescence imaging was performed 3-4 days postinjection in  $n = 12$  patients with squamous cell carcinoma of the head & neck. High-contrast images were collected that could differentiate tumor from normal mucosa during resection. On immunofluorescence, the signal correlated with EGFR expression. In a separate study, an EGFR

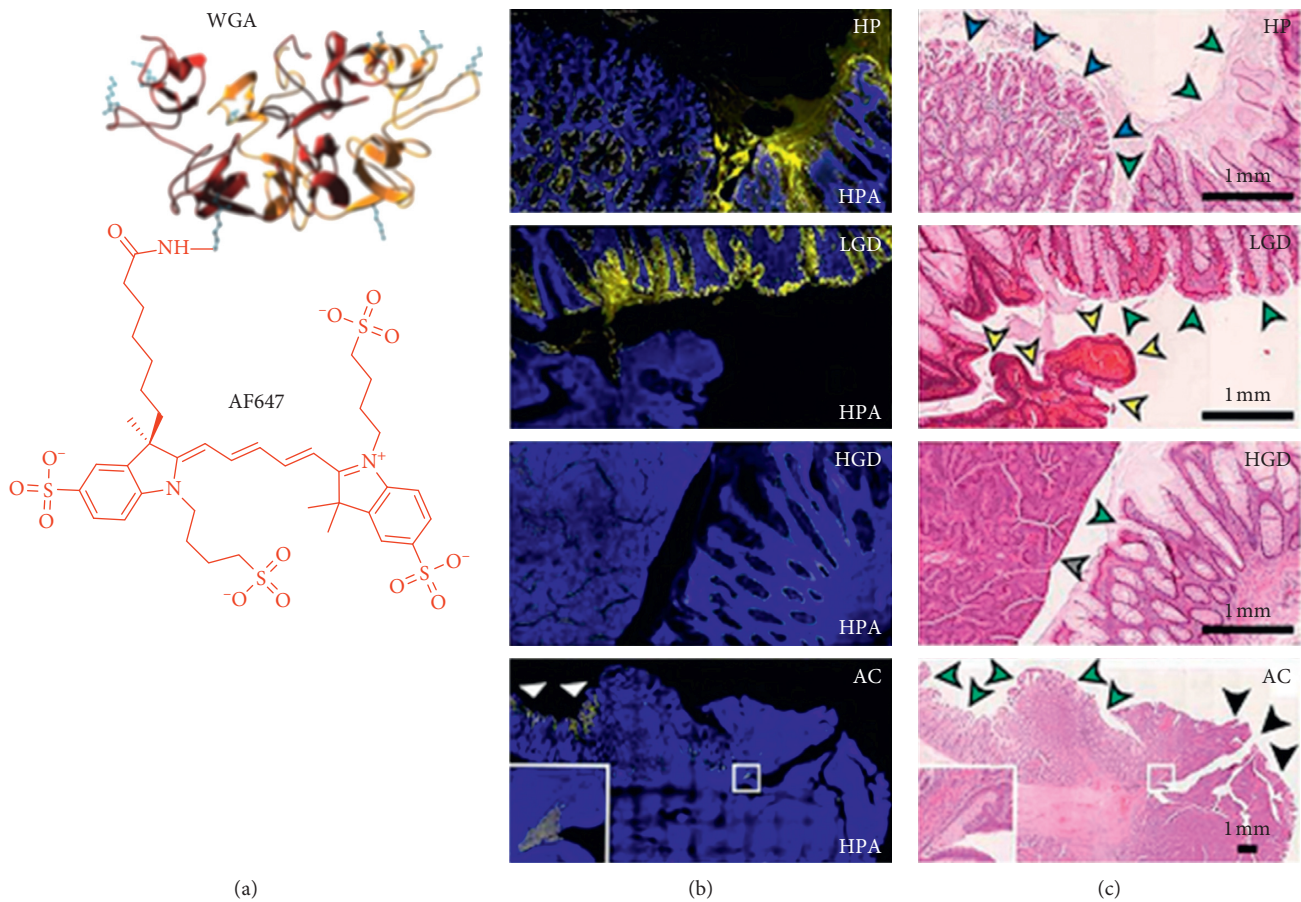


FIGURE 8: Lectin. (a) Chemical structure is shown of wheat germ agglutinin (WGA) labeled with AF647 (abs = 650 nm and em = 668 nm). (b) Immunofluorescence of human colon, including (HP), low-grade dysplasia (LGD), high grade dysplasia (HGD), and adenocarcinoma (AC), is shown stained with lectin *Helix pomatia* agglutinin (HPA) labeled with AF647. (c) Corresponding histology (H&E) ((a) reprinted and modified with the permission from [111] and (b) reprinted with the permission from [90]).

antibody was labeled with Alexa Fluor 488 (AF488) and topically administered in  $n = 40$  patients with colorectal neoplasia for imaging with confocal laser endomicroscopy [93]. Targeted biopsies were obtained from each site, and specific binding was found in 94.7% of adenocarcinomas and in 66.7% of adenomas when compared with histology and immunohistochemistry.

Bevacizumab is an mAb that is specific for vascular endothelial growth factor A (VEGF-A) and has been labeled with IRDye800 for in vivo optical imaging to guide surgical resection of breast and pancreatic cancer (Table 1). A Phase 1 clinical study is being performed using this targeted contrast agent to detect premalignant lesions endoscopically in patients with familial adenomatous polyposis (FAP), esophageal adenocarcinoma, and rectal cancer (Table 1). Systemic administration of bevacizumab-IRDye800 has been found to be safe in  $n = 20$  patients with breast cancer with good uptake at the tumor margin [95]. Fluorescence intensity in primary tumor was found to be higher than that at the tumor margin or in healthy breast. Also, VEGF-A expression with immunohistochemistry was found to correlate with fluorescence intensity. No tumor recurrence was found after surgery guided by bevacizumab-IRDye800

imaging. This molecular probe has also been used to detect premalignant lesions in patients with Barrett's esophagus undergoing endoscopic mucosal resection (EMR), Figures 9(a)–9(i) [96]. Topical and systemically administered bevacizumab-IRDye800 guided fluorescence endoscopy increased the rate of detection of Barrett's neoplasia by 25%. Many of these lesions were either focal or flat in appearance and were missed by conventional high-definition white-light endoscopy (WLE) and narrowband imaging (NBI). Using iv injection of bevacizumab-800CW, a proof-of-concept study was performed in FAP patients in 3 tracer-dose groups at 4.5, 10, and 25 mg. Patients underwent imaging with fluorescence endoscopy 3 days after injection. The fluorescence intensity was dose-dependent and the 25 mg dose provided a median TBR of 1.84. Bevacizumab-IRDye800CW had a good safety profile, and no tracer-related adverse events were observed.

MDX1201 is a human mAb labeled with AF488 ( $\lambda_{ex} = 488$  nm  $\lambda_{em} = 520$  nm) for specific binding to the extracellular domain of human prostate specific membrane antigen (PSMA). PSMA is a tumor-associated antigen and transmembrane protein that is overexpressed in the membrane of prostate epithelium. This molecular probe is currently being evaluated clinically for image-

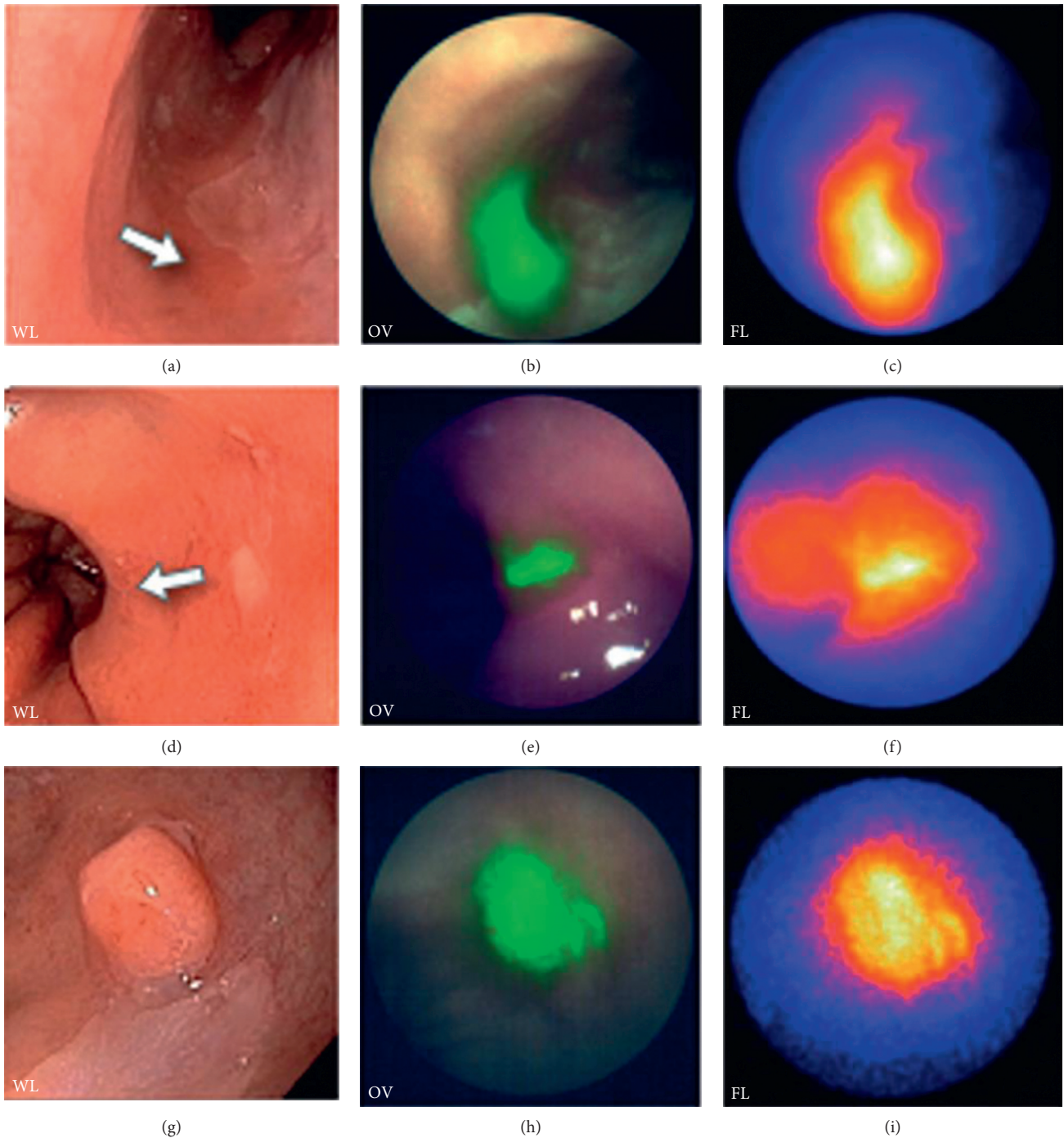


FIGURE 9: Antibody. Wide-field endoscopic images collected in vivo of human esophageal adenocarcinoma (EAC) following topical administration of bevacizumab labeled with IRDye800. (a) White light (WL), (b) overlay (OV), and (c) fluorescence (FL) image from nonfocal lesion (arrow) is shown. Similar set of images are shown for (d–f) flat and (g–i) protruding EAC (reprinted and modified with the permission from [96]).

guided surgery of prostate cancer (Table 1). Girentuximab is an mAb that specifically recognizes carbonic anhydrase IX overexpressed in renal cell carcinoma (Table 1). This dual modality molecular probe can be used for either optical or nuclear imaging [91].

Whole antibodies have been truncated to reduce probe size by forming antibody fragments, diabodies, and minibodies

for improved pharmacokinetics [115–119]. Because of their relatively smaller dimensions (<60 kDa), these ligands clear faster from the vasculature to facilitate more rapid visualization of cancer with higher image contrast. Improved serum stability has been achieved with recombinant proteins produced by *E. Coli*. After fluorophore conjugation, these ligands maintain the fluorophore closer to the target for

improved spatial resolution. Greater effort is being made to develop these antibody-based probes to overcome some of the limitations associated with use of full antibodies for clinical imaging.

#### 4. Summary and Outlook

Optical contrast agents that are specific for cancer targets are being developed to visualize molecular behavior in vivo. These fluorescently labeled ligands are being used with optical imaging instruments in the clinic to guide surveillance biopsy and surgical resection. A variety of probe platforms with unique pharmacokinetic properties are being developed to provide specific contrast. Each class of probe offers unique strengths for targeted imaging. Labeling can be achieved over a broad spectrum, and multiplexed detection can be performed to address heterogeneity in target expression. Clinical evaluation of a number of these molecular probes has either been demonstrated or is being planned. Despite the many challenges posed, significant progress has been made toward clinical translation, and continued advances are expected in the near future. Here, we discussed optical imaging agents currently in either clinical trial or development. Many of these agents are being evaluated at an early stage. Phase 2/3 results will determine the likely impact of these agents for the use in general patient population.

Molecularly targeted contrast agents must exhibit properties that include a safe toxicity profile, rapid tumor uptake, higher TBR, and long-term stability to be clinically useful. Complete tumor resection is essential for curative treatment, and evaluation of tumor margins can be challenging. TBR may differ in various clinical studies depending on tumor size, dose, and image acquisition time. The minimal TBR should be achieved to accurately discriminate the lesion from healthy tissues and avoid false positives. Methods to measure TBR should be standardized, and multicenter clinical studies are needed to validate diagnostic performance. Several molecular probes have already overcome key regulatory hurdles and have been FDA-approved for use in first-in-human clinical studies. Pre-operative biopsies may be needed to confirm expression of the intended target prior to intraoperative use. Rigorous confirmation of specific probe interaction with the target is imperative. Also, the cost associated with use of exogenous agents, and potential for reimbursement must be considered before widespread acceptance can be expected. Imaging instruments that are sensitive to the spectral response of the fluorophore must become commercially available and easy to obtain by the community physician.

Despite the opportunity for molecular contrast, optical imaging techniques can be limited by tissue penetration depth. Photoacoustic imaging (PAI) is an emerging optical method that is being developed to improve this performance parameter [120–126]. This technology is also sensitive to targeted molecular contrast agents and can be useful for staging of early cancers (T<sub>1a</sub> versus T<sub>1b</sub>) to guide the choice between local endoscopic versus conventional surgical resection. Preclinical images collected in small animals in vivo for a variety of diseases using small-molecule dyes, gold

and carbon nanostructures, and liposome encapsulations have also shown promise with PAI. However, considerable challenges such as the large size of nanostructures relative to physiological barriers, biological requirements, target-tissue retention, and safety profiles must be addressed prior to clinical application.

#### Abbreviations

|         |  |
|---------|--|
| 5-ALA:  | 5-aminolevulinic acid                      |
| BODIPY: | Boron dipyrromethene                       |
| CRC:    | Colorectal cancer                          |
| CT:     | Computed tomography                        |
| CTX:    | Chlorotoxin                                |
| CVG:    | Cancer vision goggles                      |
| EGFR:   | Epidermal growth factor receptor           |
| FAP:    | Familial adenomatous polyposis             |
| FITC:   | Fluorescein isothiocyanate                 |
| FDG:    | Fluoro-deoxy-glucose                       |
| FDA:    | Food and drug administration               |
| Her2:   | Human epidermal growth factor receptor 2   |
| HPA:    | Helix pomatia agglutinin                   |
| Hsp90:  | Heat shock protein 90                      |
| IND:    | Investigational new drug                   |
| IBD:    | Inflammatory bowel disease                 |
| mAb:    | Monoclonal antibody                        |
| iv:     | Intravenous                                |
| MRI:    | Magnetic resonance imaging                 |
| NBI:    | Narrowband imaging                         |
| NHP:    | Nonhuman primates                          |
| NIR:    | Near-infrared                              |
| NOAEL:  | No-observed-adverse-effect-levels          |
| NPV:    | Negative predictive value                  |
| OSCC:   | Oral squamous cell carcinoma               |
| PAI:    | Photoacoustic imaging                      |
| PET:    | Positron emission tomography               |
| PK:     | Pharmacokinetic                            |
| PPIX:   | Protoporphyrin IX                          |
| PPV:    | Positive predictive value                  |
| PSMA:   | Prostate specific membrane antigen         |
| SD:     | Standard deviation                         |
| SEM:    | Standard error of the mean                 |
| SNR:    | Signal-to-noise ratio                      |
| SPECT:  | Single-photon emission computed tomography |
| TBR:    | Tumor-to-background ratio                  |
| US:     | Ultrasound                                 |
| VEGF:   | Vascular endothelial growth factor         |
| WLE:    | White light endoscopy                      |
| WGA:    | Wheat germ agglutinin.                     |

#### Disclosure

The authors are inventors on patents owned by the University of Michigan on some of the peptides discussed.

#### Conflicts of Interest

The authors declare that they have no conflicts of interest.

## Acknowledgments

The authors thank A Pant for editing. Funding was provided in part by NIH U54 CA163059, R01 CA1933377, R01 CA200007, and U01 CA189291 (Thomas D. Wang).

## References

- [1] American Cancer Society, *Cancer Facts and Figures*, American Cancer Society, Atlanta, GA, USA, 2017.
- [2] F. Bray, A. Jemal, N. Grey, J. Ferlay, and D. Forman, "Global cancer transitions according to the human development Index (2008–2030): a population-based study," *The Lancet Oncology*, vol. 13, no. 8, pp. 790–801, 2012.
- [3] National Cancer Institute, *Surveillance, Epidemiology, and End Results (SEER) Program Research Data (1973-2014), DCCPS, Surveillance Research Program, released April 2017, based on the November 2016 Submission*, National Cancer Institute, Rockville, MD, USA, 2017, <http://www.seer.cancer.gov>.
- [4] N. Howlader, A. M. Noone, M. Krapcho et al., *SEER Cancer Statistics Review, 1975–2013*, National Cancer Institute, Bethesda, MD, USA, 2016.
- [5] S. Jain and S. Dhingra, "Pathology of esophageal cancer and Barrett's esophagus," *Annals of Cardiothoracic Surgery*, vol. 6, no. 2, pp. 99–109, 2017.
- [6] A. C. Chi, T. A. Day, and B. W. Neville, "Oral cavity and oropharyngeal squamous cell carcinoma—an update," *CA: A Cancer Journal for Clinicians*, vol. 65, no. 5, pp. 401–421, 2015.
- [7] L. Nguyen, E. I. Ager, J. Neo, and C. Christophi, "Regulation of colorectal cancer cell epithelial to mesenchymal transition by the renin-angiotensin system," *Journal of Gastroenterology and Hepatology*, vol. 31, no. 10, pp. 1773–1782, 2016.
- [8] H. Cao, E. Xu, H. Liu, L. Wan, and M. Lai, "Epithelial-mesenchymal transition in colorectal cancer metastasis: a system review," *Pathology-Research and Practice*, vol. 211, no. 8, pp. 557–569, 2015.
- [9] A. E. Sirica, M. H. Nathanson, G. J. Gores, and N. F. LaRusso, "Pathobiology of biliary epithelia and cholangiocarcinoma: proceedings of the Henry M. and Lillian Stratton basic research single-topic conference," *Hepatology*, vol. 48, no. 6, pp. 2040–2046, 2008.
- [10] R. J. Kurman and I. M. Shih, "The origin and pathogenesis of epithelial ovarian cancer— a proposed unifying theory," *American Journal of Surgical Pathology*, vol. 34, no. 3, pp. 433–443, 2010.
- [11] W. Yan, I. I. Wistuba, M. R. Emmert-Buck, and H. S. Erickson, "Squamous cell carcinoma—similarities and differences among anatomical sites," *American Journal of Cancer Research*, vol. 1, no. 3, pp. 275–300, 2011.
- [12] M. Shinozaki, K. Kobayashi, R. Kunisaki et al., "Surveillance for dysplasia in patients with ulcerative colitis: discrepancy between guidelines and practice," *Digestive Endoscopy*, vol. 29, no. 5, pp. 584–593, 2017.
- [13] S. Winawer, R. Fletcher, D. Rex et al., "Colorectal cancer screening and surveillance: clinical guidelines and rationale—update based on new evidence," *Gastroenterology*, vol. 124, no. 2, pp. 544–560, 2003.
- [14] M. Bajbouj, M. Vieth, T. Rösch et al., "Probe-based confocal laser endomicroscopy compared with standard four-quadrant biopsy for evaluation of neoplasia in Barrett's esophagus," *Endoscopy*, vol. 42, no. 6, pp. 435–440, 2010.
- [15] J. D. Horwhat, C. L. Maydonovitch, F. Ramos et al., "A randomized comparison of methylene blue-directed biopsy versus conventional four-quadrant biopsy for the detection of intestinal metaplasia and dysplasia in patients with long-segment Barrett's esophagus," *American Journal of Gastroenterology*, vol. 103, no. 3, pp. 546–554, 2008.
- [16] W. L. Curvers, R. Singh, L. M. Song et al., "Endoscopic trimodal imaging for detection of early neoplasia in Barrett's oesophagus: a multi-centre feasibility study using high-resolution endoscopy, autofluorescence imaging and narrow band imaging incorporated in one endoscopy system," *Gut*, vol. 57, no. 2, pp. 167–172, 2008.
- [17] J. A. Abrams, R. C. Kapel, G. M. Lindberg et al., "Adherence to biopsy guidelines for Barrett's esophagus surveillance in the community setting in the United States," *Clinical Gastroenterology and Hepatology*, vol. 7, no. 7, pp. 736–742, 2009.
- [18] V. Ballester and M. Cruz-Correa, "Endoscopic surveillance of gastrointestinal premalignant lesions: current knowledge and future directions," *Current Opinion in Gastroenterology*, vol. 30, no. 5, pp. 477–483, 2014.
- [19] R. Weissleder and M. J. Pittet, "Imaging in the era of molecular oncology," *Nature*, vol. 452, no. 7187, pp. 580–589, 2008.
- [20] R. Weissleder, C. Markus, S. S. Gambhir, and H. Hricak, "Imaging approaches to optimize molecular therapies," *Science Translational Medicine*, vol. 8, no. 355, article 355ps16, 2016.
- [21] C. M. Gomes, A. J. Abrunhosa, P. Ramos, and E. K. J. Pauwels, "Molecular imaging with SPECT as a tool for drug development," *Advanced Drug Delivery Reviews*, vol. 63, no. 7, pp. 547–554, 2011.
- [22] G. Hong, A. L. Antaris, and H. Dai, "Near-infrared fluorophores for biomedical imaging," *Nature Biomedical Engineering*, vol. 1, no. 1, p. 0010, 2017.
- [23] B. P. Joshi and T. D. Wang, "Gastrointestinal imaging in 2015: emerging trends in endoscopic imaging," *Nature Reviews Gastroenterology & Hepatology*, vol. 13, no. 2, pp. 72–73, 2016.
- [24] T. E. Peterson and H. C. Manning, "Molecular imaging: <sup>18</sup>F-FDG PET and a whole lot more," *Journal of Nuclear Medicine Technology*, vol. 37, no. 3, pp. 151–161, 2009.
- [25] J. R. Mercer, "Molecular imaging agents for clinical positron emission tomography in oncology other than fluorodeoxyglucose (FDG): applications, limitations and potential," *Journal of Pharmacy & Pharmaceutical Sciences*, vol. 10, no. 2, pp. 180–202, 2007.
- [26] R. Abgral, S. Querellou, G. Potard et al., "Does 18F-FDG PET/CT improve the detection of posttreatment recurrence of head and neck squamous cell carcinoma in patients negative for disease on clinical follow-up?," *Journal of Nuclear Medicine*, vol. 50, no. 1, pp. 24–29, 2009.
- [27] M. A. Miller, E. Kim, M. F. Cuccarese et al., "Near infrared imaging of Mer tyrosine kinase (MERTK) using MERi-SiR reveals tumor associated macrophage uptake in metastatic disease," *Chemical Communications*, vol. 54, no. 1, pp. 42–45, 2018.
- [28] F. W. van Leeuwen, J. C. Hardwick, and A. R. van Erkel, "Luminescence-based imaging approaches in the field of interventional molecular imaging," *Radiology*, vol. 276, no. 1, pp. 12–29, 2015.
- [29] X. Chen, P. S. Conti, and R. A. Moats, "In vivo near-infrared fluorescence imaging of Integrin  $\alpha\beta 3$  in brain tumor

- xenografts," *Cancer Research*, vol. 64, no. 21, pp. 8009–8014, 2004.
- [30] Z. Cheng, Y. Wu, Z. Xiong, S. S. Gambhir, and X. Chen, "Near-infrared fluorescent RGD peptides for optical imaging of Integrin  $\alpha v\beta 3$  expression in living mice," *Bioconjugate Chemistry*, vol. 16, no. 6, pp. 1433–1441, 2005.
- [31] M. Li, C. P. Anastassiades, B. P. Joshi et al., "Affinity peptide for targeted detection of dysplasia in Barrett's esophagus," *Gastroenterology*, vol. 139, no. 5, pp. 1472–1480, 2010.
- [32] R. T. Robertson, S. T. Levine, S. M. Haynes et al., "Use of labeled tomato lectin for imaging vasculature structures," *Histochemistry and Cell Biology*, vol. 143, no. 2, pp. 225–234, 2015.
- [33] M. Goetz, A. Ziebart, S. Foersch et al., "In vivo molecular imaging of colorectal cancer with confocal endomicroscopy of epidermal growth factor receptor," *Gastroenterology*, vol. 138, no. 2, pp. 435–446, 2010.
- [34] Y. Urano, M. Sakabe, N. Kosaka et al., "Rapid cancer detection by topically spraying a  $\gamma$ -glutamyltranspeptidase-activated fluorescent probe," *Science Translational Medicine*, vol. 3, no. 110, article 110ra119, 2011.
- [35] H. Kobayashi, M. Ogawa, R. Alford, P. L. Choyke, and Y. Urano, "New strategies for fluorescent probe design in medical diagnostic imaging," *Chemical Reviews*, vol. 110, no. 5, pp. 2620–2640, 2010.
- [36] F. W. B. van Leeuwen<sup>1</sup>, B. Cornelissen, F. Caobelli et al., "Generation of fluorescently labeled tracers-which features influence the translational potential?," *EJNMMI Radiopharmacy and Chemistry*, vol. 2, no. 1, p. 15, 2017.
- [37] B. P. Joshi and T. D. Wang, "Exogenous molecular probes for targeted imaging in cancer: focus on multi-modal imaging," *Cancers*, vol. 2, no. 2, pp. 1251–1287, 2010.
- [38] S. Luo, E. Zhang, Y. Su, T. Cheng, and C. Shi, "A review of NIR dyes in cancer targeting and imaging," *Biomaterials*, vol. 32, no. 29, pp. 7127–7138, 2011.
- [39] P. J. Trivedi and B. Braden, "Indications, stains and techniques in chromoendoscopy," *QJM*, vol. 106, no. 2, pp. 117–131, 2013.
- [40] P. D. Stevens, C. J. Lightdale, P. H. Green, L. M. Siegel, R. J. Garcia-Carrasquillo, and H. Rotterdam, "Combined magnification endoscopy with chromoendoscopy for the evaluation of Barrett's esophagus," *Gastrointestinal Endoscopy*, vol. 40, no. 6, pp. 747–749, 1994.
- [41] J. A. Barkin, D. A. Sussman, and M. T. Abreu, "Chromoendoscopy and advanced imaging technologies for surveillance of patients with IBD," *Gastroenterology & Hepatology*, vol. 8, no. 12, pp. 796–802, 2012.
- [42] S. Naymagon and T. A. Ullman, "Chromoendoscopy and dysplasia surveillance in inflammatory bowel disease: past, present, and future," *Gastroenterology & Hepatology*, vol. 11, no. 5, pp. 304–311, 2015.
- [43] M. B. Wallace, A. Meining, M. I. Canto et al., "The safety of intravenous fluorescein for confocal laser endomicroscopy in the gastrointestinal tract," *Alimentary Pharmacology and Therapeutics*, vol. 31, no. 5, pp. 548–552, 2010.
- [44] P. Mlkvy, H. Messmann, J. Regula et al., "Sensitization and photodynamic therapy (PDT) of gastrointestinal tumors with 5-aminolevulinic acid (ALA) induced protoporphyrin IX (PPIX): a pilot study," *Neoplasma*, vol. 42, no. 3, pp. 109–113, 1995.
- [45] A. de Boer, C. Kluft, J. M. Kroon et al., "Liver blood flow as a major determinant of the clearance of recombinant human tissue-type plasminogen activator," *Thrombosis and Haemostasis*, vol. 67, no. 1, pp. 83–87, 1992.
- [46] T. Lin, Y. Li, Q. Liu et al., "Novel theranostic nanoporphyryns for photodynamic diagnosis and trimodal therapy for bladder cancer," *Biomaterials*, vol. 104, pp. 339–351, 2016.
- [47] M. Olivo and B. C. Wilson, "Mapping ALA-induced PPIX fluorescence in normal brain and brain tumour using confocal fluorescence microscopy," *International Journal of Oncology*, vol. 25, no. 1, pp. 37–45, 2004.
- [48] T. Masubuchi, Y. Kajimoto, S. Kawabata et al., "Experimental study to understand nonspecific protoporphyrin IX fluorescence in brain tissues near tumors after 5-aminolevulinic acid administration," *Photomedicine and Laser Surgery*, vol. 31, no. 9, pp. 428–433, 2013.
- [49] J. C. Tonn and W. Stummer, "Fluorescence-guided resection of malignant gliomas using 5-aminolevulinic acid: practical use, risks, and pitfalls," *Clinical Neurosurgery*, vol. 55, pp. 20–26, 2008.
- [50] Y. Kajimoto, T. Kuroiwa, S. I. Miyatake et al., "Use of 5-aminolevulinic acid in fluorescence-guided resection of meningioma with high risk of recurrence," *Journal of Neurosurgery*, vol. 106, no. 6, pp. 1070–1074, 2007.
- [51] D. Coluccia, J. Fandino, M. Fujioka, S. Cordovi, C. Muroi, and H. Landolt, "Intraoperative 5-aminolevulinic-acid-induced fluorescence in meningiomas," *Acta Neurochirurgica*, vol. 152, no. 10, pp. 1711–1719, 2010.
- [52] W. J. Whitson, P. A. Valdes, B. T. Harris, K. D. Paulsen, and D. W. Roberts, "Confocal microscopy for the histological fluorescence pattern of a recurrent atypical meningioma: case report," *Neurosurgery*, vol. 68, no. 6, pp. E1768–E1773, 2011.
- [53] F. W. Floeth, M. Sabel, C. Ewelt et al., "Comparison of <sup>18</sup>F-FET PET and 5-ALA fluorescence in cerebral gliomas," *European Journal of Nuclear Medicine and Molecular Imaging*, vol. 38, no. 4, pp. 731–741, 2011.
- [54] J. S. Treger, M. F. Priest, R. Izzy, and F. Bezanilla, "Real-time imaging of electrical signals with an infrared FDA-approved dye," *Biophysical Journal*, vol. 107, no. 6, pp. L09–L12, 2014.
- [55] N. Kosaka, M. Mitsunaga, M. R. Longmire, P. L. Choyke, and H. Kobayashi, "Near infrared fluorescence-guided real-time endoscopic detection of peritoneal ovarian cancer nodules using intravenously injected indocyanine green," *International Journal of Cancer*, vol. 129, no. 7, pp. 1671–1677, 2011.
- [56] H. Maeda, H. Nakamura, and J. Fang, "The EPR effect for macromolecular drug delivery to solid tumors: improvement of tumor uptake, lowering of systemic toxicity, and distinct tumor imaging in vivo," *Advanced Drug Delivery Reviews*, vol. 65, no. 1, pp. 71–79, 2013.
- [57] G. Liberale, S. Vankerckhove, M. G. Caldón et al., "Fluorescence imaging after indocyanine green injection for detection of peritoneal metastases in patients undergoing cytoreductive surgery for peritoneal carcinomatosis from colorectal cancer: a pilot study," *Annals of Surgery*, vol. 264, no. 6, pp. 1110–1115, 2016.
- [58] B. E. Schaafsma, J. S. D. Mieog, M. Hutteman et al., "The clinical use of indocyanine green as a near-infrared fluorescent contrast agent for image-guided oncologic surgery," *Journal of Surgical Oncology*, vol. 104, no. 3, pp. 323–332, 2011.
- [59] B. Yuan, N. Chen, and Q. Zhu, "Emission and absorption properties of indocyanine green in intralipid solution," *Journal of Biomedical Optics*, vol. 9, no. 3, pp. 497–503, 2004.
- [60] G. M. Van Dam, G. Themelis, L. M. A. Crane et al., "Intraoperative tumor-specific fluorescence imaging in ovarian cancer by folate receptor- $\alpha$  targeting: first in-human

- results," *Nature Medicine*, vol. 17, no. 10, pp. 1315–1319, 2011.
- [61] C. E. Hoogstins, Q. R. Tummers, K. N. Gaarenstroom et al., "A novel tumor-specific agent for intraoperative near-infrared fluorescence imaging: a translational study in healthy volunteers and patients with ovarian cancer," *Clinical Cancer Research*, vol. 22, no. 12, pp. 2929–2938, 2016.
- [62] J. Y. K. Lee, S. S. Cho, R. Zeh et al., "Folate receptor overexpression can be visualized in real time during pituitary adenoma endoscopic transsphenoidal surgery with near-infrared imaging," *Journal of Neurosurgery*, vol. 129, no. 2, pp. 390–403, 2018.
- [63] T. J. Guzzo, J. Jiang, J. Keating et al., "Intraoperative molecular diagnostic imaging can identify renal cell carcinoma," *Journal of Urology*, vol. 195, no. 3, pp. 748–755, 2016.
- [64] O. T. Okusanya, E. M. DeJesus, J. X. Jiang et al., "Intraoperative molecular imaging can identify lung adenocarcinomas during pulmonary resection," *Journal of Thoracic and Cardiovascular Surgery*, vol. 150, no. 1, pp. 28.e1–35.e1, 2015.
- [65] J. D. Predina, A. D. Newton, C. Connolly et al., "Identification of a folate receptor-targeted near-infrared molecular contrast agent to localize pulmonary adenocarcinomas," *Molecular Therapy*, vol. 26, no. 2, pp. 390–403, 2018, In press.
- [66] Q. Tummers, C. E. S. Hoogstins, K. N. Gaarenstroom et al., "Intraoperative imaging of folate receptor alpha positive ovarian and breast cancer using the tumor specific agent EC17," *Oncotarget*, vol. 7, no. 22, pp. 32144–32155, 2016.
- [67] E. De Jesus, J. J. Keating, S. A. Kularatne et al., "Comparison of folate receptor targeted optical contrast agents for intraoperative molecular imaging," *International Journal of Molecular Imaging*, vol. 2015, Article ID 469047, 10 pages, 2015.
- [68] C. F. Shum, C. D. Bahler, P. S. Low et al., "Novel use of folate-targeted intraoperative fluorescence, OTL38, in robot-assisted laparoscopic partial nephrectomy: report of the first three cases," *Journal of Endourology Case Reports*, vol. 2, no. 1, pp. 189–197, 2016.
- [69] C. D. Bahler, V. Maniar, K. N. Marley, S. V. Kheyfets, C. F. Shum, and C. P. Sundaram, "OTL-38-guided fluorescent imaging in renal cell cancer robotic partial nephrectomy," *Videourology*, vol. 31, no. 3, 2017.
- [70] S. Kossatz, C. Brand, S. Gutiontov et al., "Detection and delineation of oral cancer with a PARP1 targeted optical imaging agent," *Scientific Reports*, vol. 6, no. 1, article 21371, 2016.
- [71] J. J. Barrott, P. F. Hughes, T. Osada et al., "Tethered Hsp90 inhibitors carrying optical or radioiodinated probes reveal selective internalization of ectopic Hsp90 in malignant breast tumor cells," *Chemistry & Biology*, vol. 20, no. 9, pp. 1187–1197, 2013.
- [72] J. Deshane, C. C. Garner, and H. Sontheimer, "Chlorotoxin inhibits glioma cell invasion via matrix metalloproteinase-2," *Journal of Biological Chemistry*, vol. 278, no. 6, pp. 4135–4144, 2003.
- [73] L. Soroceanu, Y. Gillespie, M. B. Khazaeli, and H. Sontheimer, "Use of chlorotoxin for targeting of primary brain tumors," *Cancer Research*, vol. 58, no. 21, pp. 4871–4879, 1998.
- [74] M. Veisoh, P. Gabikian, S. B. Bahrami et al., "Tumor paint: a chlorotoxin: Cy5.5 bioconjugate for intraoperative visualization of cancer foci," *Cancer Research*, vol. 67, no. 14, pp. 6882–6888, 2007.
- [75] J. Fidel, K. C. Kennedy, W. S. Dernel et al., "Preclinical validation of the utility of BLZ-100 in providing fluorescence contrast for imaging canine spontaneous solid tumors," *Cancer Research*, vol. 75, no. 20, pp. 4283–4291, 2015.
- [76] F. M. Baik, S. Hansen, S. E. Knoblauch et al., "Fluorescence identification of head and neck squamous cell carcinoma and high-risk oral dysplasia with BLZ-100, a chlorotoxin-indocyanine green conjugate," *JAMA Otolaryngology-Head & Neck Surgery*, vol. 142, no. 4, pp. 330–338, 2016.
- [77] P. V. Butte, A. Mamelak, J. Parrish-Novak et al., "Near-infrared imaging of brain tumors using the tumor paint BLZ-100 to achieve near-complete resection of brain tumors," *Neurosurgical Focus*, vol. 36, no. 2, p. E1, 2014.
- [78] J. Burggraaf, I. M. C. Kamerling, P. B. Gordon et al., "Detection of colorectal polyps in humans using an intravenously administered fluorescent peptide targeted against c-Met," *Nature Medicine*, vol. 21, no. 8, pp. 955–961, 2015.
- [79] S. B. Mondal, S. Gao, N. Zhu et al., "Binocular goggle augmented imaging and navigation system provides real-time fluorescence image guidance for tumor resection and sentinel lymph node mapping," *Scientific Reports*, vol. 5, no. 1, article 12117, 2015.
- [80] P. L. Hsiung, J. Hardy, S. Friedland et al., "Detection of colonic dysplasia in vivo using a targeted heptapeptide and confocal microendoscopy," *Nature Medicine*, vol. 14, no. 4, pp. 454–458, 2008.
- [81] B. P. Joshi, Z. Dai, Z. Gao et al., "Detection of sessile serrated adenomas in the proximal colon using wide-field fluorescence endoscopy," *Gastroenterology*, vol. 152, no. 5, pp. 1002.e9–1013.e9, 2017.
- [82] M. B. Sturm, B. P. Joshi, S. Lu et al., "Targeted imaging of esophageal neoplasia with a fluorescently labeled peptide: first-in-human results," *Science Translational Medicine*, vol. 5, no. 184, article 184ra61, 2013.
- [83] B. P. Joshi, X. Duan, R. Kwon et al., "Multimodal endoscope can quantify wide-field fluorescence detection of Barrett's neoplasia," *Endoscopy*, vol. 48, no. 2, pp. 1–15, 2016.
- [84] J. Zhou, B. P. Joshi, X. Duan et al., "EGFR overexpressed in colonic neoplasia can be detected on wide-field endoscopic imaging," *Clinical and Translational Gastroenterology*, vol. 6, no. 7, p. e101, 2015.
- [85] B. P. Joshi, J. Zhou, A. Pant et al., "Design and synthesis of near-infrared peptide for in vivo molecular imaging of HER2," *Bioconjugate Chemistry*, vol. 27, no. 2, pp. 481–494, 2016.
- [86] A. L. R. de Souza, K. Marra, J. Gunn et al., "Fluorescent affibody molecule administered In Vivo at a microdose level labels EGFR expressing glioma tumor regions," *Molecular Imaging and Biology*, vol. 19, no. 1, pp. 41–48, 2017.
- [87] K. S. Samkoe, J. R. Gunn, K. Marra et al., "Toxicity and pharmacokinetic profile for single-dose injection of ABY-029: a fluorescent anti-EGFR synthetic affibody molecule for human use," *Molecular Imaging and Biology*, vol. 19, no. 4, pp. 512–521, 2017.
- [88] J. T. Elliott, A. V. Dsouza, K. Marra, B. W. Pogue, D. W. Roberts, and K. D. Paulsen, "Microdose fluorescence imaging of ABY-029 on an operating microscope adapted by custom illumination and imaging modules," *Biomedical Optics Express*, vol. 7, no. 9, pp. 3280–3288, 2016.
- [89] M. J. Whitley, D. M. Cardona, A. L. Lazarides et al., "A mouse-human phase 1 co-clinical trial of a protease-activated fluorescent probe for imaging cancer," *Science Translational Medicine*, vol. 8, no. 320, article 320ra4, 2016.

- [90] J. C. Kuo, A. E. Ibrahim, S. Dawson et al., "Detection of colorectal dysplasia using fluorescently labelled lectins," *Scientific Reports*, vol. 6, no. 1, article 24231, 2016.
- [91] M. Hekman, M. Rijpkema, E. Oosterwijk et al., "Intra-operative dual-modality imaging in clear cell renal cell carcinoma using Indium-111-DOTA-girentuximab-IRDye800CW," *European Urology Supplements*, vol. 16, no. 3, article e1831, 2017.
- [92] E. L. Rosenthal, J. M. Warram, E. de Boer et al., "Safety and tumor specificity of cetuximab-IRDye800 for surgical navigation in head and neck cancer," *Clinical Cancer Research*, vol. 21, no. 16, pp. 3658–3666, 2015.
- [93] J. Liu, X. Zuo, C. Li et al., "In vivo molecular imaging of epidermal growth factor receptor in patients with colorectal neoplasia using confocal laser endomicroscopy," *Cancer Letters*, vol. 330, no. 2, pp. 200–207, 2013.
- [94] K. A. Touijer and J. A. Eastham, "The sentinel lymph node concept and novel approaches in detecting lymph node metastasis in prostate cancer," *European Urology*, vol. 70, no. 5, pp. 738–739, 2016.
- [95] L. E. Lamberts, M. Koch, J. S. de Jong et al., "Tumor-specific uptake of fluorescent bevacizumab-IRDye800CW microdosing in patients with primary breast cancer: a phase I feasibility study," *Clinical Cancer Research*, vol. 23, no. 11, pp. 2730–2741, 2017.
- [96] W. B. Nagengast, E. Hartmans, P. B. Garcia-Allende et al., "Near-infrared fluorescence molecular endoscopy detects dysplastic oesophageal lesions using topical and systemic tracer of vascular endothelial growth factor A," *Gut*, 2017.
- [97] A. Becker, C. Hessenius, K. Licha et al., "Receptor-targeted optical imaging of tumors with near-infrared fluorescent ligands," *Nature Biotechnology*, vol. 19, no. 4, pp. 327–331, 2001.
- [98] G. Kostenich, N. Livnah, T. A. Bonasera et al., "Targeting small cell lung cancer with novel fluorescent analogs of somatostatin," *Lung Cancer*, vol. 50, no. 3, pp. 319–328, 2005.
- [99] G. Kostenich, M. Oron-Herman, S. Kimel, N. Livnah, I. Tsarfaty, and A. Orenstein, "Diagnostic targeting of colon cancer using a novel fluorescent somatostatin conjugate in a mouse xenograft model," *International Journal of Cancer*, vol. 122, no. 9, pp. 2044–2049, 2008.
- [100] J. Klohs, A. Wunder, and K. Licha, "Near-infrared fluorescent probes for imaging vascular pathophysiology," *Basic Research in Cardiology*, vol. 103, no. 2, pp. 144–151, 2008.
- [101] K. Licha and C. Olbrich Optical, "Imaging in drug discovery and diagnostic applications," *Advanced Drug Delivery Reviews*, vol. 57, no. 8, pp. 1087–1108, 2005.
- [102] Z. L. Bergeron and J. P. Bingham, "Scorpion toxins specific for potassium (K<sup>+</sup>) channels: a historical overview of peptide bioengineering," *Toxins*, vol. 4, no. 11, pp. 1082–1119, 2012.
- [103] J. Parrish-Novak, K. Byrnes-Blake, N. Lalayeva et al., "Nonclinical profile of BLZ-100, a tumor-targeting fluorescent imaging agent," *International Journal of Toxicology*, vol. 36, no. 2, pp. 104–112, 2017.
- [104] R. P. Baum, V. Prasad, D. Muller et al., "Molecular imaging of HER2-expressing malignant tumors in breast cancer patients using synthetic <sup>111</sup>In- or <sup>68</sup>Ga-labeled antibody molecules," *Journal of Nuclear Medicine*, vol. 51, no. 6, pp. 892–897, 2010.
- [105] R. Weissleder, C. H. Tung, U. Mahmood, and A. Bogdanov, "In Vivo imaging of tumors with protease-activated near-infrared fluorescent probes," *Nature Biotechnology*, vol. 17, no. 4, pp. 375–378, 1999.
- [106] M. Ogawa, N. Kosaka, M. R. Longmire, Y. Urano, P. L. Choyke, and H. Kobayashi, "Fluorophore-quencher based activatable targeted optical probes for detecting In Vivo cancer metastases," *Molecular Pharmaceutics*, vol. 6, no. 2, pp. 386–395, 2009.
- [107] Y. Urano, D. Asanuma, Y. Hama et al., "Selective molecular imaging of viable cancer cells with pH-activatable fluorescence probes," *Nature Medicine*, vol. 15, no. 1, pp. 104–109, 2009.
- [108] S. Lee, J. Xie, and X. Chen, "Activatable molecular probes for cancer imaging," *Current Topics in Medicinal Chemistry*, vol. 10, no. 11, pp. 1135–1144, 2010.
- [109] E. L. Bird-Lieberman, A. A. Neves, P. Lao-Sirieix et al., "Molecular imaging using fluorescent lectins permits rapid endoscopic identification of dysplasia in Barrett's esophagus," *Nature Medicine*, vol. 18, no. 2, pp. 315–321, 2012.
- [110] S. S. Pinho and C. A. Reis, "Glycosylation in cancer: mechanisms and clinical implications," *Nature Reviews Cancer*, vol. 15, no. 9, pp. 540–555, 2015.
- [111] G. H. KleinJan, T. Buckle, D. M. van Willigen et al., "Fluorescent lectins for local in vivo visualization of peripheral nerves," *Molecules*, vol. 19, no. 7, pp. 9876–9892, 2014.
- [112] S. Folli, P. Westermann, D. Braichotte et al., "Antibody-indocyanin conjugates for immunophotodetection of human squamous cell carcinoma in nude mice," *Cancer Research*, vol. 54, no. 10, pp. 2643–2649, 1994.
- [113] C. M. Matter, P. K. Schuler, P. Alessi et al., "Molecular imaging of atherosclerotic plaques using a human antibody against the extra domain B of fibronectin," *Circulation Research*, vol. 95, no. 12, pp. 1225–1233, 2004.
- [114] S. Ke, X. Wen, M. Gurfinkel et al., "Near-infrared optical imaging of epidermal growth factor receptor in breast cancer xenografts," *Cancer Research*, vol. 63, no. 22, pp. 7870–7875, 2003.
- [115] R. M. Sharkey, T. M. Cardillo, E. A. Rossi et al., "Goldenberg signal amplification in molecular imaging by pretargeting a multivalent, bispecific antibody," *Nature Medicine*, vol. 11, no. 11, pp. 1250–1255, 2005.
- [116] M. Jain, G. Venkatraman, and S. K. Batra, "Optimization of radioimmunotherapy of solid tumors: biological impediments and their modulation," *Clinical Cancer Research*, vol. 13, no. 5, pp. 1374–1382, 2007.
- [117] P. Holliger and P. J. Hudson, "Engineered antibody fragments and the rise of single domains," *Nature Biotechnology*, vol. 23, no. 9, pp. 1126–1136, 2005.
- [118] A. L. Nelson and J. M. Reichert, "Development trends for therapeutic antibody fragments," *Nature Biotechnology*, vol. 27, no. 4, pp. 331–337, 2009.
- [119] S. Banta, K. Dooley, and O. Shur, "Replacing antibodies: engineering new binding proteins," *Annual Review of Biomedical Engineering*, vol. 15, no. 1, pp. 93–113, 2013.
- [120] L. V. Wang and J. A. Yao, "Practical guide to photoacoustic tomography in the life sciences," *Nature Methods*, vol. 13, no. 8, pp. 627–638, 2016.
- [121] A. Taruttis, G. M. van Dam, and V. Ntziachristos, "Mesoscopic and macroscopic photoacoustic imaging of cancer," *Cancer Research*, vol. 75, no. 8, pp. 1548–1559, 2015.
- [122] S. Zackrisson, V. van de, and S. S. Gambhir, "Light in and sound out: emerging translational strategies for photoacoustic imaging," *Cancer Research*, vol. 74, no. 4, pp. 979–1004, 2014.
- [123] Y. Lin, R. Weissleder, and C. H. Tung, "Novel near-infrared cyanine fluorochromes: synthesis, properties, and

- bioconjugation,” *Bioconjugate Chemistry*, vol. 13, no. 3, pp. 605–610, 2002.
- [124] D. Zhang, Y.-X. Zhao, Z.-Y. Qiao et al., “Nano-confined squaraine dye assemblies: new photoacoustic and near-infrared fluorescence dual-modular imaging probes in vivo,” *Bioconjugate Chemistry*, vol. 25, no. 11, pp. 2021–2029, 2014.
- [125] E. Huynh, C. S. Jin, B. C. Wilson, and G. Zheng, “Aggregate enhanced trimodal porphyrin shell microbubbles for ultrasound, photoacoustic, and fluorescence imaging,” *Bioconjugate Chemistry*, vol. 25, no. 4, pp. 796–801, 2014.
- [126] A de la Zerda, C. Zavaleta, S. Keren et al., “Carbon nanotubes as photoacoustic molecular imaging agents in living mice,” *Nature Nanotechnology*, vol. 3, no. 9, pp. 557–562, 2008.

## Research Article

# Measuring Tumor Metabolism in Pediatric Diffuse Intrinsic Pontine Glioma Using Hyperpolarized Carbon-13 MR Metabolic Imaging

Adam W. Autry,<sup>1</sup> Rintaro Hashizume,<sup>2</sup> C. David James,<sup>2</sup> Peder E. Z. Larson,<sup>1</sup>  
Daniel B. Vigneron,<sup>1</sup> and Ilwoo Park<sup>3,4</sup>

<sup>1</sup>Department of Radiology and Biomedical Imaging, University of California, San Francisco, CA, USA

<sup>2</sup>Department of Neurological Surgery and Biochemistry and Molecular Genetics, Northwestern University, Chicago, IL, USA

<sup>3</sup>Department of Radiology, Chonnam National University Medical School, Gwangju, Republic of Korea

<sup>4</sup>Department of Radiology, Chonnam National University Hospital, Gwangju, Republic of Korea

Correspondence should be addressed to Ilwoo Park; [ipark@jnu.ac.kr](mailto:ipark@jnu.ac.kr)

Received 26 January 2018; Revised 3 June 2018; Accepted 28 June 2018; Published 30 July 2018

Academic Editor: Daniela Haeusler

Copyright © 2018 Adam W. Autry et al. This is an open access article distributed under the Creative Commons Attribution License, which permits unrestricted use, distribution, and reproduction in any medium, provided the original work is properly cited.

**Objective.** The purpose of this study was to demonstrate the feasibility of using hyperpolarized carbon-13 (<sup>13</sup>C) metabolic imaging with [1-<sup>13</sup>C]-labeled pyruvate for evaluating real-time *in vivo* metabolism of orthotopic diffuse intrinsic pontine glioma (DIPG) xenografts. **Materials and Methods.** 3D <sup>13</sup>C magnetic resonance spectroscopic imaging (MRSI) data were acquired on a 3T scanner from 8 rats that had been implanted with human-derived DIPG cells in the brainstem and 5 healthy controls, following injection of 2.5 mL (100 mM) hyperpolarized [1-<sup>13</sup>C]-pyruvate. **Results.** Anatomical images from DIPG-bearing rats characteristically exhibited T<sub>2</sub>-hyperintensity throughout the cerebellum and pons that was not accompanied by contrast enhancement. Evaluation of real-time *in vivo* <sup>13</sup>C spectroscopic data revealed ratios of lactate-to-pyruvate ( $p < 0.002$ ), lactate-to-total carbon ( $p < 0.002$ ), and normalized lactate ( $p < 0.002$ ) that were significantly higher in T<sub>2</sub> lesions harboring tumor relative to corresponding values of healthy normal brain. Elevated levels of lactate in lesions demonstrated a distinct metabolic profile that was associated with infiltrative, viable tumor recapitulating the histopathology of pediatric DIPG. **Conclusions.** Results from this study characterized pyruvate and lactate metabolism in orthotopic DIPG xenografts and suggest that hyperpolarized <sup>13</sup>C MRSI may serve as a noninvasive imaging technique for *in vivo* monitoring of biochemical processes in patients with DIPG.

## 1. Introduction

Diffuse intrinsic pontine glioma (DIPG) comprises a heterogeneous class of childhood brainstem cancers that defy molecular stratification and surgical intervention because of their sensitive location. After forming in the pons, this relatively inaccessible disease often undergoes rapid growth that is characterized by diffuse infiltration across the midline through healthy tissue. Despite decades of clinical trials investigating the efficacy of novel treatment regimens, DIPG remains the leading cause of death among pediatric patients with central nervous system cancers and carries an average survival of only 9 months [1].

Magnetic resonance imaging (MRI) serves as the standard modality for diagnosing DIPG and monitoring disease status in response to treatment [2]. While conventional MRI provides information regarding anatomical changes, its prognostic value and ability to assess physiologic or functional alterations associated with therapeutic efficacy are highly limited [3]. Attempts at using positron emission tomography to evaluate DIPG metabolism have also presented challenges owing to the risks of ionizing radiation exposure [4, 5]. Given the heterogeneous presentation of the disease on imaging, which lacks features for stratifying aggressiveness [6], the development of noninvasive metabolic imaging methods may

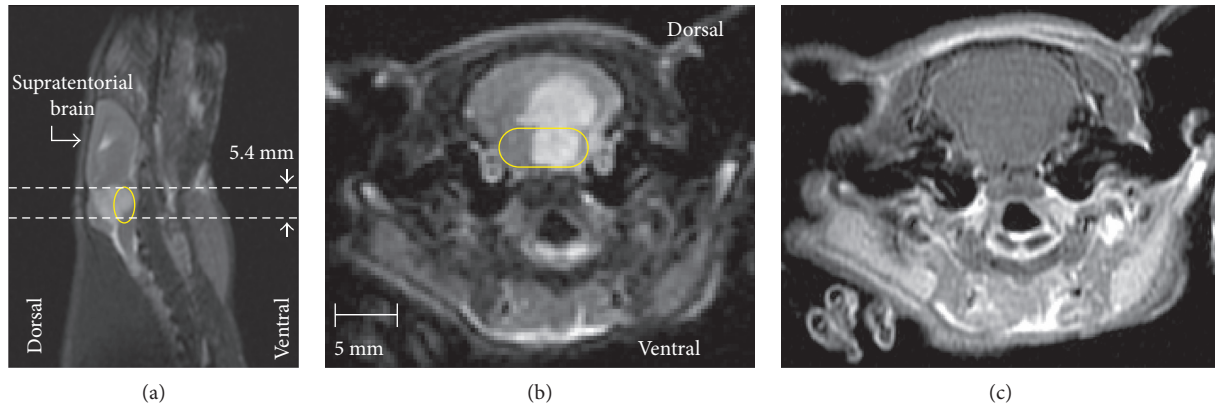


FIGURE 1: Representative anatomical images from a rat ( $n = 8$  total) bearing orthotopic DIPG.  $T_2$ -weighted images in sagittal (a) and axial (b) planes demonstrated a  $T_2$ -hyperintense lesion through the brainstem. The corresponding axial post-Gd  $T_1$ -weighted image (c) exhibited no contrast enhancement. Horizontal dashed lines in (a) delimit the 5.4 mm axial slice of  $^{13}\text{C}$  MRSI data, presented in Figure 2. The yellow boundary in (a) and (b) indicates the location of pons.

enhance the evaluation of molecular characteristics as well as response to therapy.

Representing a novel advance in solid state physics, dissolution dynamic nuclear polarization (d-DNP) enables the acquisition of carbon-13 ( $^{13}\text{C}$ ) magnetic resonance data with an appreciable gain in sensitivity over conventional methods [7]. A phase I first-in-human study using hyperpolarized  $^{13}\text{C}$  magnetic resonance spectroscopic imaging (MRSI) has already demonstrated the safety and feasibility of such technology for probing real-time metabolism in prostate cancer patients [8]. The purpose of this study was to explore the feasibility of using hyperpolarized  $^{13}\text{C}$  metabolic imaging with  $[1-^{13}\text{C}]$ -pyruvate for evaluating real-time *in vivo* metabolism of orthotopic DIPG xenografts.

## 2. Materials and Methods

Eight six-week-old male athymic rats (rnu/rnu, homozygous, and median weight = 290 g) purchased from Harlan (Indianapolis, IN) were implanted with patient-derived human DIPG cells (SF8628) in the brainstem to create an orthotopic DIPG model, while 5 healthy rats served as experimental controls. The details of the cell culture and intracranial implantation procedures have been described elsewhere [9]. Study procedures were approved by the Institutional Animal Care and Use Committee.

All animals were scanned on a 3T clinical MRI system (GE Healthcare, Waukesha, WI, USA) equipped with a custom-designed  $^1\text{H}/^{13}\text{C}$  rat coil on approximately the 58th day after tumor implantation. The body temperature was maintained using a heated pad positioned inside the RF coil. Anesthesia was maintained with a constant delivery of 1.5% isoflurane. For the polarization of pyruvate, a  $35\ \mu\text{L}$  of  $[1-^{13}\text{C}]$ -pyruvate mixed with 15 mM OX063 trityl radical (GE Healthcare, Oslo, Norway), and 1.5 mM gadolinium (Gd)-DOTA was polarized using a HyperSense® (Oxford Instruments, Abingdon, UK) [7, 10]. After 60 minutes of microwave irradiation, the mixture was dissolved in a saline solution with 5.96 g/L Tris (40 mM), 4.00 g/L NaOH (100 mM), and

0.1 mg/L  $\text{Na}_2$  ethylenediaminetetraacetic acid. The final solution had a concentration of 100 mM pyruvate, and  $\text{pH} \sim 7.5$ . 2.7 mL of the dissolved pyruvate solution was injected into the tail vein of the rats over 10 s duration.

The following  $^1\text{H}$  and  $^{13}\text{C}$  data were acquired in sequence for each scan: (1) axial  $T_2$ -weighted images using a fast spin-echo sequence (echo time/repetition time = 60/4000 ms, 8 cm field of view,  $256 \times 256$  matrix, and 2 mm slice thickness), (2) compressed-sensing  $^{13}\text{C}$  3D MRSI data (echo time/repetition time = 140/215 ms, phase encoding in  $x$  and  $y$  axes, flyback echo-planar readout in  $z$ -axis,  $20 \times 16 \times 16$  matrix, and  $2 \times 2 \times 5.4$  mm spatial resolution) [11] acquired at 20 s from the start of the pyruvate injection, and (3) axial  $T_1$ -weighted images using a spin-echo sequence (echo time/repetition time = 10/700 ms, 8 cm field of view,  $320 \times 192$  matrix, and 1.2 mm slice thickness) after the injection of 0.2 mmol/kg Gd-DTPA.

The methods for processing  $^{13}\text{C}$  MRSI data have been described previously [11]. For quantification of  $^{13}\text{C}$  metabolites, the ratio of lactate-to-pyruvate and lactate-to-total carbon (tC: sum of lactate, pyruvate-hydrate, alanine, and pyruvate) was calculated. In addition, the lactate and pyruvate signals in the brainstem were normalized with respect to the relative signals of the normal brain in the supratentorial region (Figure 1(a)). ROIs were manually contoured on  $T_2$ -weighted images for the  $T_2$ -hyperintense lesion, and the percentage of  $T_2$  lesion volume was calculated for each voxel. Comparison of mean  $^{13}\text{C}$  parameters from the  $T_2$ -hyperintense lesion (voxels with  $>75\%$   $T_2$  lesion) and similar region of the infratentorial brain of healthy control animals was performed using the Mann-Whitney rank-sum test. In order to evaluate the spatial variation of  $^{13}\text{C}$  metabolites, the  $T_2$ -hyperintense lesion was also compared with the contralateral brain (voxels with nonhyperintense tissue on the opposite side of the  $T_2$  lesion).

Immediately following the scan, tumor-bearing animals were sacrificed and harvested for their brains, which were fixed in phosphate-buffered 4% formalin. Samples were then dehydrated by graded ethanol and embedded in Paraplast

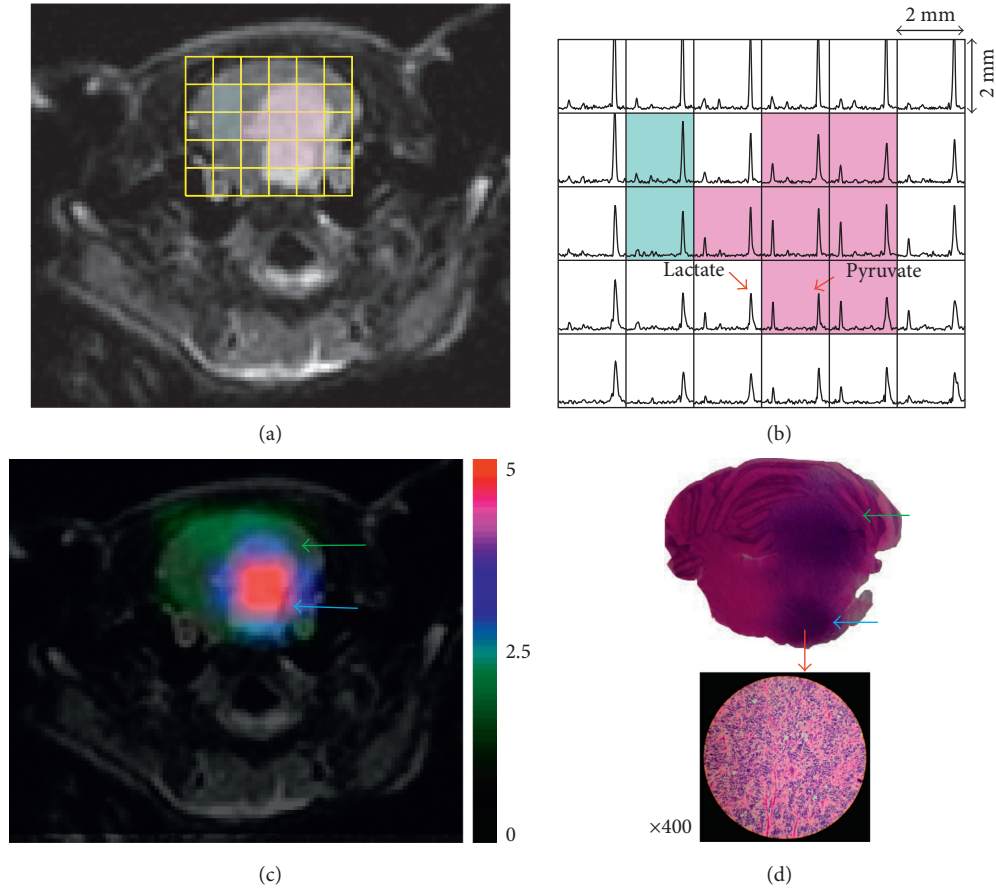


FIGURE 2: Representative hyperpolarized  $^{13}\text{C}$  data from a rat ( $n = 8$  total) bearing DIPG. (a) Axial  $T_2$ -weighted image of the brainstem with a spectral grid overlay for 3D  $^{13}\text{C}$  MRSI data. Pink and light blue boxes represent voxels encompassing the  $T_2$ -hyperintense lesion and contralateral brain tissue, respectively. (b) The corresponding hyperpolarized  $^{13}\text{C}$  spectra with an in-plane spatial resolution of  $2 \times 2 \times 5.4 \text{ mm}^3$ . Voxels encompassing the  $T_2$ -hyperintense lesion (pink boxes) exhibited elevated lactate levels compared to those of the contralateral brain tissue (light blue boxes). (c) The map of normalized lactate shows elevated lactate signal in DIPG. (d) The corresponding slice from H&E staining (top) and the zoomed-in H&E image (bottom) demonstrate infiltrative, viable DIPG. The blue and green arrows in (c) and (d) indicate pons and cerebellum of the rat brain, respectively.

Plus wax (McCormick Scientific).  $5 \mu\text{m}$  sections were examined following haematoxylin and eosin (H&E) staining.

### 3. Results and Discussion

Representative anatomical data from a rat injected with DIPG cells are shown in Figure 1, with panel (a) providing an overview of an orthotopic lesion around the brainstem on a sagittal  $T_2$ -weighted image. The corresponding axial  $T_2$ -weighted image exhibited hyperintensity throughout the cerebellum and pons (Figure 1(b)), while no contrast enhancement was visible from the post-Gd  $T_1$ -weighted image acquired at the same location (Figure 1(c)).

The axial  $T_2$ -weighted image in Figure 2(a) depicts a  $^{13}\text{C}$  MRSI grid superimposed over the brainstem. The corresponding hyperpolarized  $^{13}\text{C}$  spectra from the same animal (Figure 2(b)) demonstrated the spatial distribution of high  $^{13}\text{C}$ -labeled lactate and pyruvate signals over the entire brainstem region. Illustrative of the full cohort, these hyperpolarized  $^{13}\text{C}$  MRSI data demonstrated levels of lactate in the  $T_2$  lesions (pink voxels; Figures 2(a) and 2(b)) that

were elevated relative to the contralateral normal brain (blue voxels; Figures 2(a) and 2(b)).

Metabolite parameters derived from hyperpolarized data are compared between DIPG xenografts and healthy control brains in Table 1. The  $T_2$ -hyperintense tumors exhibited highly elevated metabolism compared to both healthy controls and the contralateral hemisphere, which may contain infiltrating tumor. The ratios of lactate-to-pyruvate, lactate-to-total carbon, and normalized lactate in  $T_2$  lesions ( $0.70 \pm 0.24$ ,  $0.36 \pm 0.08$ , and  $2.9 \pm 1.1$ , resp.) were significantly higher than the corresponding values in the healthy normal brain ( $0.20 \pm 0.06$ ,  $0.14 \pm 0.03$ , and  $1.1 \pm 0.25$ , resp.). The normalized lactate map in Figure 2(c) shows the differential production of lactate between the DIPG xenograft and tissue in the contralateral hemisphere. From the corresponding H&E-stained slice, there was observed infiltrative, viable tumor that recapitulated the histopathology of pediatric DIPG (Figure 2(d)). In contrast, the normalized pyruvate was found to be similar across both regions and comparable to the healthy brain (Table 1).

TABLE 1: Summary of  $^{13}\text{C}$  metabolite quantification. Metabolite values are mean  $\pm$  SD.

|   | Lactate/pyruvate <sup>a,b</sup> | Lactate/total carbon <sup>a,b</sup> | Normalized lactate <sup>a,b</sup> | Normalized pyruvate |
|---|---------------------------------|-------------------------------------|-----------------------------------|---------------------|
| T <sub>2</sub> -hyperintense lesion ( $n = 8$ ) | $0.70 \pm 0.24$                 | $0.36 \pm 0.08$                     | $2.9 \pm 1.1$                     | $1.0 \pm 0.29$      |
| Contralateral brain ( $n = 8$ )                 | $0.28 \pm 0.11$                 | $0.18 \pm 0.07$                     | $1.1 \pm 0.33$                    | $1.1 \pm 0.35$      |
| Healthy rat brain ( $n = 5$ )                   | $0.20 \pm 0.06$                 | $0.14 \pm 0.03$                     | $1.2 \pm 0.25$                    | $1.1 \pm 0.25$      |

<sup>a</sup>Significant difference between T<sub>2</sub>-hyperintense lesion and contralateral brain ( $p < 0.001$ ). <sup>b</sup>Significant difference between T<sub>2</sub>-hyperintense lesion and healthy rat brain ( $p < 0.002$ ).

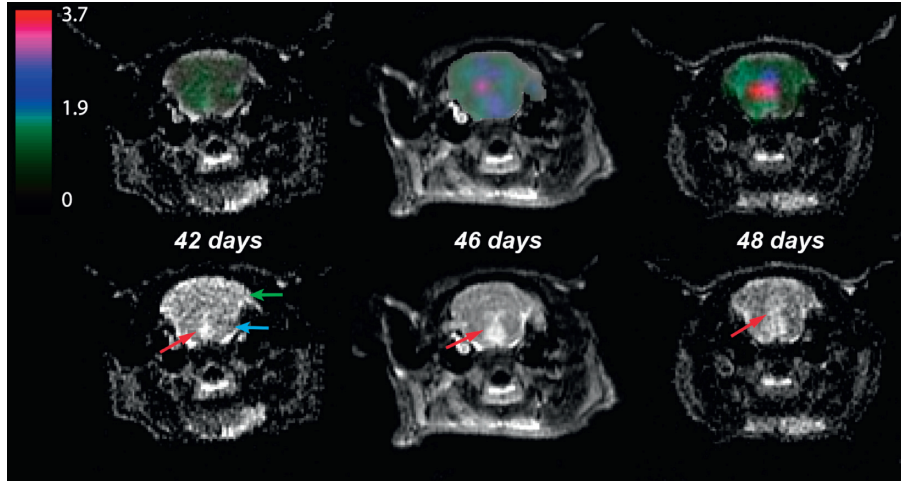


FIGURE 3: Longitudinal  $^{13}\text{C}$  spectral data showing normalized lactate from a rat imaged at 42, 46, and 48 days from implantation (left to right). The top row displays the map of normalized lactate overlaid on the same T<sub>2</sub>-weighted images of the bottom row. These data show a several-fold increase in the metabolic abnormality associated with the evolution of the anatomic lesion. The red arrows indicate T<sub>2</sub> lesion in the brainstem, while blue and green arrows indicate pons and cerebellum of the rat brain, respectively. The tumor initially developed in the pons and diffused across the cerebellum.

In order to assess the ability to observe longitudinal changes in metabolism, hyperpolarized  $^{13}\text{C}$  MRSI data were obtained from an additional single animal imaged over a period of 7 days in the course of tumor development (Figure 3). The longitudinal change in normalized lactate signal and T<sub>2</sub>-hyperintensity are shown in Figure 3. Normalized lactate from the  $^{13}\text{C}$  spectral data imaged at 42, 46, and 48 days from implantation were  $1.2 \pm 0.2$ ,  $2.5 \pm 0.1$ , and  $3.5 \pm 1.0$ , respectively. These data show a severalfold increase in the metabolic abnormality associated with the evolution of the anatomic lesion.

This study has demonstrated the feasibility of using hyperpolarized  $^{13}\text{C}$  metabolic imaging to assess *in vivo* metabolism in orthotopic brainstem xenografts that contain patient-derived primary DIPG cells. By using hyperpolarized  $[1-^{13}\text{C}]$ -pyruvate in conjunction with rapid 3D MRSI acquisition techniques, it was shown that nonenhancing brainstem glioma can be evaluated on the basis of real-time molecular data, as an initial step towards noninvasive disease characterization. To the best of our knowledge, this is the first study to apply hyperpolarized  $^{13}\text{C}$  techniques in brainstem tumor as well as in nonenhancing brain tumor.

An important feature of the orthotopic murine tumor model adopted here was its ability to recapitulate aspects of disease observed in patients. With regard to imaging, the longitudinal data revealed a similar pattern of disease progression, wherein cells implanted in the pons spread from a localized lesion to the cerebellum after a period of rapid

growth, and without visible enhancement [12, 13]. Analysis of the resected brain by histopathology confirmed viable DIPG in the pons, along with the associated cerebellar infiltration, which supported findings from metabolic imaging indicating temporal changes.

Because DIPG is radiographically characterized by poorly perfused and faintly enhancing heterogeneous lesions, its diagnostic assessment remains challenging. In this context, the relative elevation of lactate in nonenhancing lesions compared to healthy control tissue was a defining feature that may hold diagnostic value for patients as an *in vivo* marker of disease. As these tumors frequently display high levels of LDHA [14, 15] that preferentially convert pyruvate to lactate, imaging of hyperpolarized  $[1-^{13}\text{C}]$ -pyruvate might offer a targeted means of monitoring tumor growth and disease status. The nuclear polarization techniques implemented here provided sufficient signal enhancement to detect real-time pyruvate-to-lactate conversion in the brainstem with high sensitivity, as well as distinguish longitudinal variation in metabolism from growing tumor over relatively brief intervals. Based on the quality and spatial resolution of the  $^{13}\text{C}$  spectra achieved via hardware and sequence performance, it was possible to evaluate metabolic differences between T<sub>2</sub>-hyperintense lesions and contralateral brain tissue.

Although our focus was on demonstrating feasibility, we believe that a promising application of this technique may be monitoring response to treatment in patients with DIPG,

given the inadequacy of conventional MR imaging. By administering  $[1-^{13}\text{C}]$ -pyruvate as a hyperpolarized substrate with measurable conversion to  $[1-^{13}\text{C}]$ -lactate, studies have already managed to provide evidence for both localization of malignant tissue and treatment-induced reduction of metabolic activity arising from growth arrest or apoptosis [16, 17]. A recent study has demonstrated the first application of hyperpolarized  $^{13}\text{C}$  MR metabolic imaging in patients with supratentorial glioma and presented the safety and feasibility of using hyperpolarized  $[1-^{13}\text{C}]$ -pyruvate to evaluate *in vivo* brain metabolism [18]. Perhaps the greatest technical challenge to translating hyperpolarized imaging to the clinic for diffusing intrinsic pontine glioma is ensuring adequate SNR in the brainstem, where the surrounding tissue is less perfused and far removed from coil elements.

While several single- and multivoxel  $^1\text{H}$  spectroscopy studies have indicated that  $^1\text{H}$  magnetic resonance spectroscopy (MRS) may be useful for assessing disease progression and monitoring response to treatment [19–22], the acquisition of proton spectra in the infratentorial region is generally challenging due to susceptibility effects around the brainstem region and confounded by overlapping lipid peaks that reflect contamination from the surrounding skull. The susceptibility effects encountered in  $^{13}\text{C}$  MR are considerably smaller relative to  $^1\text{H}$  MR by virtue of the  $^{13}\text{C}$  gyromagnetic ratio, which is one-fourth that of  $^1\text{H}$ . The proposed method of assessing real-time metabolism using hyperpolarized  $^{13}\text{C}$  MRSI, combined with anatomical MRI and  $^1\text{H}$  MRS, may provide complementary information that is of value in assessing disease status and response to treatment in DIPG.

Interestingly, the ratio of lactate-to-pyruvate in the non-enhancing  $T_2$  lesion from this study ( $0.70 \pm 0.24$ ) was significantly smaller than that of enhancing tumor from supratentorial orthotopic glioblastoma xenografts in a previous study ( $1.0 \pm 0.36$ ) ( $p < 0.02$ , unpaired *t*-test), while it remained similar between contralateral brainstem tissue ( $0.28 \pm 0.11$ ) and contralateral supratentorial brain tissue ( $0.29 \pm 0.17$ ) [11]. Future studies will attempt to elucidate the molecular and pathologic mechanisms that produce different characteristics in pyruvate metabolism depending on the type of glioma.

#### 4. Conclusions

The results from this study characterized pyruvate and lactate metabolism in orthotopic DIPG xenografts and suggest that hyperpolarized  $^{13}\text{C}$  pyruvate MRSI is a promising noninvasive imaging tool for the *in vivo* monitoring of biochemical processes in DIPG.

#### Data Availability

The data used to support the findings of this study are available from the corresponding author upon request.

#### Disclosure

An earlier version of this work was presented as a conference abstract at the Joint Annual Meeting ISMRM-ESMRMB on 10–16 May 2014 in Milan, Italy.

#### Conflicts of Interest

There are no conflicts of interest to report in this study.

#### Acknowledgments

Ilwoo Park was supported by an NCI training grant in translational brain tumor research (T32 CA151022), a discovery grant from the American Brain Tumor Association, and Jacobsen Fund from Research Evaluation and Allocation Committee (REAC). Support for the research studies came from National Institutes of Health (NIH) (Grant nos. R01EB013427 and P41EB013598), National Research Foundation (NRF) of Korea grant, funded by Ministry of Science and ICT (Grant no. 2017R1C1B5018396) and grants from Chonnam National University Hospital Biomedical Research Institute (CRI18019-1 and CRI18094-2). The authors gratefully acknowledge the guidance of Dr. Sarah J. Nelson in accomplishing this study.

#### References

- [1] K. J. Cohen, R. L. Heideman, T. Zhou et al., “Temozolomide in the treatment of children with newly diagnosed diffuse intrinsic pontine gliomas: a report from the Children’s Oncology Group,” *Neuro-Oncology*, vol. 13, no. 4, pp. 410–416, 2011.
- [2] P. Rao, “Role of MRI in paediatric neurooncology,” *European Journal of Radiology*, vol. 68, no. 2, pp. 259–270, 2008.
- [3] D. Hargrave, N. Chuang, and E. Bouffet, “Conventional MRI cannot predict survival in childhood diffuse intrinsic pontine glioma,” *Journal of Neuro-Oncology*, vol. 86, no. 3, pp. 313–319, 2008.
- [4] D. Brenner, C. Elliston, E. Hall, and W. Berdon, “Estimated risks of radiation-induced fatal cancer from pediatric CT,” *American Journal of Roentgenology*, vol. 176, no. 2, pp. 289–296, 2001.
- [5] R. A. Kleinerman, “Cancer risks following diagnostic and therapeutic radiation exposure in children,” *Pediatric Radiology*, vol. 36, no. 2, pp. 121–125, 2006.
- [6] M. S. Aboian, D. A. Solomon, E. Felton et al., “Imaging characteristics of pediatric diffuse midline gliomas with histone H3 K27M mutation,” *American Journal of Neuroradiology*, vol. 38, no. 4, pp. 795–800, 2017.
- [7] J. H. Ardenkjaer-Larsen, B. Fridlund, A. Gram et al., “Increase in signal-to-noise ratio of  $>10,000$  times in liquid-state NMR,” *Proceedings of the National Academy of Sciences of the United States of America*, vol. 100, no. 18, pp. 10158–10163, 2003.
- [8] S. J. Nelson, J. Kurhanewicz, D. B. Vigneron et al., “Metabolic imaging of patients with prostate cancer using hyperpolarized  $[1-(1)^3\text{C}]$ pyruvate,” *Science Translational Medicine*, vol. 5, no. 198, p. 198, 2013.
- [9] R. Hashizume, I. Smirnov, S. Liu et al., “Characterization of a diffuse intrinsic pontine glioma cell line: implications for future investigations and treatment,” *Journal of Neuro-Oncology*, vol. 110, no. 3, pp. 305–313, 2012.
- [10] I. Park, P. E. Larson, M. L. Zierhut et al., “Hyperpolarized  $^{13}\text{C}$  magnetic resonance metabolic imaging: application to brain tumors,” *Neuro-Oncology*, vol. 12, no. 2, pp. 133–144, 2010.
- [11] I. Park, S. Hu, R. Bok et al., “Evaluation of heterogeneous metabolic profile in an orthotopic human glioblastoma xenograft model using compressed sensing hyperpolarized  $^3\text{D}$   $^{13}\text{C}$  magnetic resonance spectroscopic imaging,” *Magnetic Resonance in Medicine*, vol. 70, no. 1, pp. 33–39, 2013.

- [12] V. Caretti, M. Bugiani, M. Freret et al., "Subventricular spread of diffuse intrinsic pontine glioma," *Acta Neuropathologica*, vol. 128, no. 4, pp. 605–607, 2014.
- [13] J. Yoshimura, K. Onda, R. Tanaka, and H. Takahashi, "Clinicopathological study of diffuse type brainstem gliomas: analysis of 40 autopsy cases," *Neurologia Medico-Chirurgica*, vol. 43, no. 8, pp. 375–382, 2003.
- [14] A. M. Saratsis, M. Kambhampati, K. Snyder et al., "Comparative multidimensional molecular analyses of pediatric diffuse intrinsic pontine glioma reveals distinct molecular subtypes," *Acta Neuropathologica*, vol. 127, no. 6, pp. 881–895, 2014.
- [15] O. Warburg, "On the origin of cancer cells," *Science*, vol. 123, no. 3191, pp. 309–314, 1956.
- [16] K. Brindle, "New approaches for imaging tumour responses to treatment," *Nature Reviews Cancer*, vol. 8, no. 2, pp. 94–107, 2008.
- [17] C. S. Ward, H. S. Venkatesh, M. M. Chaumeil et al., "Non-invasive detection of target modulation following phosphatidylinositol 3-kinase inhibition using hyperpolarized  $^{13}\text{C}$  magnetic resonance spectroscopy," *Cancer Research*, vol. 70, no. 4, pp. 1296–1305, 2010.
- [18] I. Park, P. E. Z. Larson, J. W. Gordon et al., "Development of methods and feasibility of using hyperpolarized carbon-13 imaging data for evaluating brain metabolism in patient studies," *Magnetic Resonance in Medicine*, vol. 80, no. 3, pp. 864–873, 2018.
- [19] A. Laprie, A. Pirzkall, D. A. Haas-Kogan et al., "Longitudinal multivoxel MR spectroscopy study of pediatric diffuse brainstem gliomas treated with radiotherapy," *International Journal of Radiation Oncology, Biology, Physics*, vol. 62, no. 1, pp. 20–31, 2005.
- [20] A. Panigrahy, M. D. Nelson, J. L. Finlay et al., "Metabolism of diffuse intrinsic brainstem gliomas in children," *Neuro-Oncology*, vol. 10, no. 1, pp. 32–44, 2008.
- [21] E. A. Steffen-Smith, D. J. Venzon, R. S. Bent et al., "Single and multi-voxel proton spectroscopy in pediatric patients with diffuse intrinsic pontine glioma," *International Journal of Radiation Oncology, Biology, Physics*, vol. 84, no. 3, pp. 774–779, 2012.
- [22] F. Yamasaki, K. Kurisu, Y. Kajiwara et al., "Magnetic resonance spectroscopic detection of lactate is predictive of a poor prognosis in patients with diffuse intrinsic pontine glioma," *Neuro-Oncology*, vol. 13, no. 7, pp. 791–801, 2011.

## Research Article

# Comparative Evaluation of Radioiodine and Technetium-Labeled DARPIn 9\_29 for Radionuclide Molecular Imaging of HER2 Expression in Malignant Tumors

Anzhelika Vorobyeva <sup>1</sup>, Olga Bragina,<sup>2</sup> Mohamed Altai,<sup>1</sup> Bogdan Mitran <sup>3</sup>,  
Anna Orlova <sup>3</sup>, Alexey Shulga,<sup>4</sup> Galina Proshkina,<sup>4</sup> Vladimir Chernov,<sup>2,5</sup>  
Vladimir Tolmachev <sup>1</sup> and Sergey Deyev<sup>4,5,6</sup>

<sup>1</sup>Department of Immunology, Genetics and Pathology, Uppsala University, Uppsala, Sweden

<sup>2</sup>Nuclear Medicine Department, Cancer Research Institute,  
Tomsk National Research Medical Center Russian Academy of Sciences, Tomsk, Russia

<sup>3</sup>Department of Medicinal Chemistry, Uppsala University, Uppsala, Sweden

<sup>4</sup>Molecular Immunology Laboratory, Shemyakin & Ovchinnikov Institute of Bioorganic Chemistry,  
Russian Academy of Sciences, Moscow, Russia

<sup>5</sup>National Research Tomsk Polytechnic University, Tomsk, Russia

<sup>6</sup>Bio-Nanophotonic Lab., Institute of Engineering Physics for Biomedicine (PhysBio),  
National Research Nuclear University "MEPhI", Moscow, Russia

Correspondence should be addressed to Vladimir Tolmachev; [vladimir.tolmachev@igp.uu.se](mailto:vladimir.tolmachev@igp.uu.se)

Received 27 February 2018; Revised 14 April 2018; Accepted 22 April 2018; Published 6 June 2018

Academic Editor: Ya-Yao Huang

Copyright © 2018 Anzhelika Vorobyeva et al. This is an open access article distributed under the Creative Commons Attribution License, which permits unrestricted use, distribution, and reproduction in any medium, provided the original work is properly cited.

High expression of human epidermal growth factor receptor 2 (HER2) in breast and gastroesophageal carcinomas is a predictive biomarker for treatment using HER2-targeted therapeutics (antibodies trastuzumab and pertuzumab, antibody-drug conjugate trastuzumab DM1, and tyrosine kinase inhibitor lapatinib). Radionuclide molecular imaging of HER2 expression might permit stratification of patients for HER2-targeting therapies. In this study, we evaluated a new HER2-imaging probe based on the designed ankyrin repeat protein (DARPIn) 9\_29. DARPIn 9\_29 was labeled with iodine-125 by direct radioiodination and with [<sup>99m</sup>Tc]Tc(CO)<sub>3</sub> using the C-terminal hexahistidine tag. DARPIn 9\_29 preserved high specificity and affinity of binding to HER2-expressing cells after labeling. Uptake of [<sup>125</sup>I]-DARPIn 9\_29 and [<sup>99m</sup>Tc]Tc(CO)<sub>3</sub>-DARPIn 9\_29 in HER2-positive SKOV-3 xenografts in mice at 6 h after injection was 3.4 ± 0.7 %ID/g and 2.9 ± 0.7 %ID/g, respectively. This was significantly ( $p < 0.00005$ ) higher than the uptake of the same probes in HER2-negative Ramos lymphoma xenografts, 0.22 ± 0.09 %ID/g and 0.30 ± 0.05 %ID/g, respectively. Retention of [<sup>125</sup>I]-DARPIn 9\_29 in the lung, liver, spleen, and kidneys was appreciably lower compared with [<sup>99m</sup>Tc]Tc(CO)<sub>3</sub>-DARPIn 9\_29, which resulted in significantly ( $p < 0.05$ ) higher tumor-to-organ ratios. The biodistribution data were confirmed by SPECT/CT imaging. In conclusion, radioiodine is a preferable label for DARPIn 9\_29.

## 1. Introduction

Human epidermal growth factor 2 (HER2) is a tyrosine kinase receptor, which is overexpressed in about 15–20% of breast cancer [1] and 7–38% gastroesophageal cancers [2]. American Society of Clinical Oncology recommends HER2-targeted therapy for patients with HER2-positive

metastatic breast cancer [3]. The use of anti-HER2 antibodies in combination with docetaxel in neoadjuvant setting also improves pathological response rate [4]. Since the overexpression of HER2 is a precondition for response to such therapies, College of American Pathologists (CAP), American Society for Clinical Pathology (ASCP), and the American Society of Clinical Oncology (ASCO)

recommend assessment of HER2 status in all patients with breast and gastroesophageal carcinomas [3, 5]. Immunohistochemistry (IHC) and fluorescence in situ hybridization (FISH) assays are the recommended methods for HER2 molecular characterization of primary, recurrent, and metastatic tumors [5]. However, heterogeneity of HER2 expression remains a challenge. Discordances in HER2 expression between primary tumor and metastases are observed in up to 40% of the cases [6–8]. Additionally, the expression of HER2 might change over time leading to failure of HER2-targeted therapy.

Molecular imaging of HER2 expression is a noninvasive method that allows repeated whole-body monitoring of HER2 status [9]. Several types of targeting probes, such as monoclonal antibodies, their proteolytic and engineered fragments, and scaffold proteins, were evaluated for imaging of HER2 [9]. Comparison of data suggests that smaller targeting probes offer an advantage of providing good contrast and enabling imaging of HER2 at the day of injection. In addition, probes with a molecular weight of less than 45 kDa do not accumulate in tumors due to an enhanced permeability and retention (EPR) effect [10]. Thus, smaller targeting probes have a potential to improve both sensitivity and specificity of imaging.

One promising way of creating proteinaceous targeting probes for imaging is the use of engineered scaffold proteins (ESPs) [11–14]. ESPs are developed using a robust polypeptide framework (scaffold) found in natural proteins or designed de novo. Some amino acids in a scaffold are substituted by a random or directed mutagenesis, which generates big libraries and enables selection of specific high-affinity binders to designated molecular targets [12]. Several scaffolds, such as affibody molecules, knottins, designed ankyrin repeat proteins (DARPin), adnectins, and ADAPTs, have been preclinically evaluated for radionuclide molecular imaging and demonstrated capacity of imaging molecular targets in vivo at the day of injection [14]. Affibody molecules, which are based on the scaffold of protein A, have demonstrated that they can be used for in vivo quantification of HER2 expression in breast cancer metastases using PET and SPECT in the clinic [15, 16].

DARPins are built using a scaffold consisting of tightly packed repeats. Every repeat is a sequence of 33 amino acids formed as a  $\beta$ -turn followed by two antiparallel  $\alpha$ -helices [17]. In a DARPin, two or three such repeats are flanked by C- and N-terminal capping repeats forming a protein with a molecular weight of 14–18 kDa. The use of ribosomal or phage display enables selection of binders with low nanomolar or subnanomolar affinity to predetermined targets. DARPins can be cost efficiently produced in prokaryotic hosts. Currently, DARPins are actively evaluated for different therapeutic applications [17].

Earlier, an anti-HER2 DARPin G3 was conjugated with a macrocyclic chelator DOTA, labeled with the radionuclide indium-111, and evaluated for imaging of HER2-expressing xenografts [18]. That study demonstrated the feasibility of using DARPins for radionuclide molecular imaging of HER2. Still, our experience with affibody-based imaging probes suggests that the composition of the binding site of

a scaffold protein may influence off-target interaction of an imaging probe affecting its accumulation in normal tissues and blood clearance rate [19–21]. This may appreciably influence the imaging contrast and, therefore, sensitivity of diagnostics. We concluded that “clones of scaffold proteins should be evaluated to select the best variant for development of an imaging probe with optimal sensitivity for the intended application” [21]. This is in agreement with the findings of Zahnd et al. [22], who found appreciable difference in the blood clearance rate between variants of DARPin G3 with different mutations in the binding site. Therefore, we have selected another variant of the anti-HER2 DARPins, DARPin 9\_29, to evaluate it as targeting agent for imaging of HER2 [23, 24].

Selection of an optimal radionuclide is essential for development of a sensitive probe. Currently, SPECT/CT scanners are the most available imaging devices. Therefore, the use of a single photon emitter as a label might facilitate clinical translation of an imaging probe in hospitals where PET is not available due to logistic or economic reasons. Radionuclides technetium-99m ( $T_{1/2} = 6$  h,  $E_{\gamma} = 140$  keV) and iodine-123 ( $T_{1/2} = 13.3$  h,  $E_{\gamma} = 159$  keV) would offer several advantages for SPECT applications, such as optimal gamma-energies for imaging, short half-life, and low absorbed doses to patients. They permit the use of low energy collimators, providing higher resolution, minimizing the partial volume effect and increasing the registration efficiency. Direct radioiodination is a straightforward and robust method of radioiodination of targeting proteins. The use of tricarbonyl chemistry enables site-specific  $^{99m}\text{Tc}$ -labeling of histidine-tag-containing proteins using a kit technology [25]. Besides, a radioiodine label on a tyrosine (Figure 1(a)) is nonresidualizing while [ $^{99m}\text{Tc}$ ]Tc(CO)<sub>3</sub> label on a histidine tag (Figure 1(b)) possesses strong residualizing properties. Evaluation of several labels might enable selection of a probe with optimal imaging properties due to differences in residualizing properties of radiocatabolites.

The goal of this study was to evaluate DARPin 9\_29 labeled with radioisotopes of iodine and technetium as a targeting agent. The radioisotope [ $^{125}\text{I}$ ]I was used in this study as a surrogate label due to convenience. Labeling of DARPin 9\_29 with iodine-125 and technetium-99m was established, the labeled proteins were evaluated in cell assays *in vitro*, and their biodistribution was compared directly *in vivo*. Specificity of HER2 targeting was evaluated in HER2-positive and HER2-negative breast cancer xenografts in mice.

## 2. Materials and Methods

**2.1. General Materials and Instruments.** Sodium iodide [ $^{125}\text{I}$ ]NaI was purchased from PerkinElmer Sverige AB (Sweden). Technetium-99m was obtained as pertechnetate by elution of Ultra-TechneKow generator (Mallinckrodt) with sterile 0.9% sodium chloride (Mallinckrodt, The Netherlands). The Center for Radiopharmaceutical Sciences (CRS) kits for production of tricarbonyl technetium were purchased from the CRS (PSI, Villigen, Switzerland). HPLC analysis was performed using Hitachi Chromaster HPLC

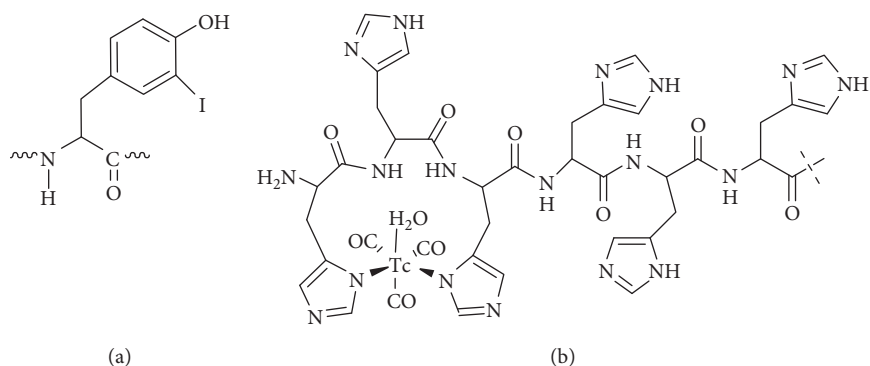


FIGURE 1: Structures of the radiolabeled moiety on the protein: iodine-125 label attached to tyrosine (a) and [ $^{99m}\text{Tc}$ ]Tc(CO) $_3$  chelated by hexahistidine tag (b).

systems with a radioactivity detector. The Vydac RP C18 protein column (300 Å, 3 × 150 mm, 5 μm particle size) was used for the analysis. Solvent A was 0.1% trifluoroacetic acid in H<sub>2</sub>O, and solvent B was 0.1% trifluoroacetic acid in acetonitrile. The flow rate was 1 ml/min with a gradient of 5% B to 80% B over 20 minutes. Instant thin-layer chromatography (iTLC) analysis was performed using iTLC silica gel strips (Varian, Lake Forest, CA, USA). The distribution of activity was measured by a Cyclone storage phosphor system (Packard) and analyzed by OptiQuant image analysis software. Size-exclusion chromatography was performed with disposable NAP-5 columns (GE Healthcare). Activity was measured using an automated gamma-spectrometer with a NaI(Tl) detector (1480 Wizard, Wallac, Finland). SKOV-3, BT474, DU145, and Ramos cells were purchased from the American Type Culture Collection (ATCC) and were cultured in complete RPMI medium supplemented with 10% fetal bovine serum (FBS), 2 mM L-glutamine, 100 IU/ml penicillin, and 100 μg/ml streptomycin in a humidified incubator with 5% CO<sub>2</sub> at 37°C, unless stated otherwise.

**2.2. Production of DARPin 9\_29.** The gene for DARPin 9\_29 was deduced from a DARPin 9\_29 amino acid sequence deposited in PDB (Accession number PDB: 4HRL\_A) taking into account the codon usage in highly expressed *E. coli* genes [26]. The gene was assembled from chemically synthesized overlapped oligonucleotides of 50 bp length by PCR and placed into pET22 plasmid vector between restriction sites NdeI and HindIII. The resultant amino acid sequence encoded by the gene was as follows: MDLGKKLLEAAR AGQDDEVIRLMANGADVNAHDFYGITPLHLAANFGH LEIVEVLLKHGADVNAFDYDNTPLHLAADAGHLEIVE VLLKYGADVNASDRDGHTPLHLAAREGHLEIVEVLLK NGADVNAQDKFGKTAFDISIDNGNEDLAEILQKLAAL EHHHHHHH.

The DARPin 9\_29 gene was expressed in *E. coli* strain BL21(DE3). Cells were grown overnight in the auto-induction ZYM-5052 medium [27] containing 100 μg/ml ampicillin at 25°C. The cells were harvested by centrifugation at 10,000 g for 15 min at 4°C and resuspended in 1/6th of volume of lysis buffer (200 mM Tris-HCl, 500 mM

sucrose, 1 mM EDTA, pH 8.0, 1 mM PMSE, and 60 μg/ml lysozyme). The suspension was diluted two-fold with distilled water and incubated at room temperature for 30 min. Cells were broken on ice by a Vibra Cell ultrasonic liquid processor VCX130 (Sonics, USA) in a cycle mode of 10 s sonication, 10 s cooling, for a total of 30 cycles. The cellular debris was pelleted at 70,000 g for 60 min at 4°C. After addition of imidazole (30 mM final concentration) and NaCl (500 mM final concentration), the supernatant was filtered through a 0.22 μm membrane and applied onto a HisTrap HP, 1 ml column (GE Healthcare) equilibrated with 20 mM sodium phosphate buffer, pH 7.5, 500 mM NaCl and 30 mM imidazole. Column was washed with ten volumes of the same buffer. The bound protein was eluted with a linear 30–500 μM imidazole gradient. The fractions containing DARPin 9\_29 were pooled and desalted on the PD10 column (GE Healthcare). The protein solution was loaded onto a MonoQ 5/50 GL column (GE Healthcare, USA) equilibrated with 20 mM Tris-HCl, pH 8.0. After washing the column with the same buffer, the bound protein was eluted with a linear 0–1 M NaCl gradient. The fractions were analyzed by 15% reducing SDS-PAGE. The fractions containing DARPin 9\_29 were pooled and concentrated with a Amicon Ultra-15 centrifugal filter and then sterilized by filtration through 0.22 μm membrane. Protein concentration was determined by UV spectroscopy using  $\epsilon_{280} = 4470 \text{ cm}^{-1} \cdot \text{M}^{-1}$  [28]. No proteinaceous impurities were found using HPLC analysis.

**2.3. Labeling and Stability.** Direct radioiodination was performed as described previously [29]. To a solution of DARPin 9\_29 (40 μg, 2.20 nmol) in PBS (47 μL), [ $^{125}\text{I}$ ]NaI (3 μL, 10 MBq) and chloramine T (20 μL of 1 mg/mL in PBS, 20 μg, 71 nmol) were added. After incubation at room temperature for 60 sec, sodium metabisulfite (20 μL of 2 mg/mL in water, 40 μg, 211 nmol) was added. The reaction yield was analyzed by iTLC, and the radiolabeled compound was purified using NAP-5 size-exclusion column (pre-equilibrated with 1% BSA in PBS) and eluted with PBS. The *in vitro* stability test was performed by incubating the radioiodinated protein with 1 M KI in PBS at room

temperature for 3 h. Control samples (without KI) were incubated in PBS. Both sample groups were analyzed by iTLC.

Site-specific radiolabeling of DARPIn 9\_29 with [ $^{99m}\text{Tc}$ ][ $\text{Tc}(\text{CO})_3(\text{H}_2\text{O})_3$ ] $^+$  was performed as described earlier [30]. The [ $^{99m}\text{Tc}$ ] $\text{NaTcO}_4$  eluate (400–500  $\mu\text{L}$ ) containing ca. 4 GBq of  $^{99m}\text{Tc}$  was added to a sealed vial containing CRS kit and incubated at 100°C for 20 min. After incubation, 40  $\mu\text{L}$  of technetium-99m tricarbonyl solution was added to a tube containing 168  $\mu\text{g}$  of DARPIn 9\_29 in 100  $\mu\text{L}$  of PBS. The reaction was incubated for 60 min at 40°C, and then, the radiolabeled DARPIn 9\_29 was purified using NAP-5 columns preequilibrated and eluted with PBS. The *in vitro* stability test was performed by incubating the radiolabeled protein with 500- and 5000-fold molar excess of histidine in PBS for 3 h. Control samples were incubated in PBS, and both sample groups were analyzed by iTLC.

The radiochemical yield and radiochemical purity after NAP-5 purification were determined by iTLC. Radio-iTLC analysis was performed in 4:1 acetone: water system and in PBS for DARPIn 9\_29 labeled with [ $^{125}\text{I}$ ]I and [ $^{99m}\text{Tc}$ ]Tc( $\text{CO}$ ) $_3$ , respectively. In both systems, the radiolabeled DARPins remain at the application point, and all forms of free radionuclides (including [ $^{99m}\text{Tc}$ ]TcO $_4^-$  and [ $^{99m}\text{Tc}$ ][ $\text{Tc}(\text{CO})_3(\text{H}_2\text{O})_3$ ] $^+$ ) migrate with the solvent front.

**2.4. In Vitro Binding Specificity and Cellular Processing.** *In vitro* studies were performed using HER2-expressing cell lines SKOV-3 ( $1.6 \times 10^6$  receptors/cell) [19], BT474 ( $1.2 \times 10^6$  receptors/cell) [31], and DU145 ( $5 \times 10^4$  receptors/cell) [32]. Cells were seeded in 3 cm Petri dishes ( $10^6$  cells per dish), and a set of three dishes was used for each group.

HER2 binding specificity assay was performed as described previously [33]. Two sets of dishes were used per each cell line. A 100-fold excess of unlabeled DARPIn 9\_29, cetuximab, trastuzumab, bevacizumab, or anti-HER2 antibody molecule  $Z_{\text{HER2:342}}$  (1000 nM) was added to the control group of cells to saturate HER2 receptors 30 min before addition of the labeled compound. Radiolabeled conjugates [ $^{125}\text{I}$ ]I-DARPIn 9\_29 or [ $^{99m}\text{Tc}$ ]Tc( $\text{CO}$ ) $_3$ -DARPIn 9\_29 were added at 10 nM concentrations. The cells were incubated for 1 h in a humidified incubator at 37°C. The medium was collected, the cells were washed with 1 mL of fresh medium, and 1 mL 1 M NaOH was added to lyse the cells. After 20–30 min of incubation, the cell lysate was collected. The activity in each fraction was measured to calculate the percent of cell-bound activity. The average number of cells per dish at the time of assay was calculated, and the value of cell-bound activity was calculated per  $10^6$  cells.

Cellular retention and processing of radiolabeled conjugates by SKOV-3 and BT474 cells was studied during continuous incubation by an acid-wash method [33]. The cells ( $1 \times 10^6$  cells/dish) were seeded two days before the experiment (three dishes for each time point). Radiolabeled [ $^{125}\text{I}$ ]I-DARPIn 9\_29 or [ $^{99m}\text{Tc}$ ]Tc( $\text{CO}$ ) $_3$ -DARPIn 9\_29 (10 nM) was added to all cells and incubated at 37°C in a humidified incubator. At 1, 2, 4, 6, and 24 h postaddition, the medium was collected from one set of 3 dishes and cells

were washed once with serum-free media (1 mL). To collect the membrane-bound tracer, the cells were treated with 0.2 M glycine buffer containing 4 M urea, pH 2.0 (1 mL) on ice for 5 min, the buffer was collected, and the cells were washed once with 1 mL of buffer. To lyse the cells containing internalized conjugate, the cells were treated with 1 M NaOH (1 mL) for 30 min, and the cells were collected and additionally washed with 1 mL. The activity in the acid fractions was considered as membrane bound, in the alkaline fractions, as internalized.

**2.5. Affinity Measurement Using LigandTracer.** The binding kinetics of radiolabeled DARPins to living SKOV-3 cells was measured using LigandTracer (Ridgeview Instruments, Väinge, Sweden) as described previously [29]. Kinetics of binding to and dissociation from living cells was recorded at room temperature in real time. The TraceDrawer Software (Ridgeview Instruments, Väinge, Sweden) was used to calculate the affinity based on the association and dissociation rates. Increasing concentrations of each radioconjugate (1, 4, and 8 nM) were added to the cells followed by the change of media and measurements of retention in the dissociation phase.

**2.6. Animal Studies.** For tumor implantation,  $10^7$  HER2-positive SKOV-3 cells or  $5 \times 10^6$  HER2-negative Ramos cells in 100  $\mu\text{L}$  of media were subcutaneously injected on the right hind leg of female BALB/c nu/nu mice. The biodistribution experiments were performed two and a half weeks after cell implantation. The average animal weight was  $16 \pm 1$  g in the SKOV-3 group and  $17 \pm 1$  g in the Ramos group. The average tumor weight was  $0.26 \pm 0.16$  g for SKOV-3 xenografts and  $0.22 \pm 0.14$  g for Ramos xenografts. Twenty-four hours before the experiments drinking water was replaced with 1% KI solution in water. For comparative biodistribution of [ $^{125}\text{I}$ ]I-DARPIn 9\_29 and [ $^{99m}\text{Tc}$ ]Tc( $\text{CO}$ ) $_3$ -DARPIn 9\_29, a dual-isotope approach was used. The mice were intravenously (i.v.) injected with a mixture of [ $^{125}\text{I}$ ]I-DARPIn 9\_29 and [ $^{99m}\text{Tc}$ ]Tc( $\text{CO}$ ) $_3$ -DARPIn 9\_29 (4  $\mu\text{g}$  in 100  $\mu\text{L}$  of 1% BSA in PBS/mouse, 15 kBq for [ $^{125}\text{I}$ ]I-DARPIn 9\_29, and 25 kBq for [ $^{99m}\text{Tc}$ ]Tc( $\text{CO}$ ) $_3$ -DARPIn 9\_29). At 6 h post-injection (p.i.), mice were anesthetized by an intraperitoneal injection of Ketalar and Rompun solution and sacrificed by heart puncture. Blood was collected with a heparinized syringe, and organs were collected and weighed, and activity was measured on a gamma-spectrometer using a dual-isotope protocol. The measurements were corrected for dead time, spillover, and background. The percent of injected dose per gram of sample (%ID/g) was calculated. Statistical analysis was performed using GraphPad Prism (GraphPad Software Inc.).

Whole-body SPECT/CT scans of the mice bearing SKOV3 xenografts injected with [ $^{99m}\text{Tc}$ ]Tc-DARPIn 9\_29 (4  $\mu\text{g}$ , 4.3 MBq) or [ $^{125}\text{I}$ ]I-DARPIn 9\_29 (4  $\mu\text{g}$ , 4.4 MBq) were performed using nanoScan SPECT/CT (Mediso Medical Imaging Systems, Hungary) at 6 h p.i. Imaging was performed under sevoflurane anesthesia. CT scans were acquired at the following parameters: 50 keV, 670  $\mu\text{A}$ , 480

TABLE 1: Stability of [ $^{125}\text{I}$ ]I-DARPin 9\_29.

| Test solution | DARPin-associated activity (%) |                |
|---------------|--------------------------------|----------------|
|               | 1 h                            | 3 h            |
| PBS           | 99.7 $\pm$ 0.4                 | 97.9 $\pm$ 1.0 |
| 1 M KI        | 99.0 $\pm$ 0.3                 | 98.5 $\pm$ 0.4 |

TABLE 2: Stability of [ $^{99\text{m}}\text{Tc}$ ]Tc(CO) $_3$ -DARPin 9\_29.

| Test solution                | DARPin-associated activity (%) |                |
|------------------------------|--------------------------------|----------------|
|                              | 1 h                            | 3 h            |
| PBS                          | 99.8 $\pm$ 0.2                 | 98.2 $\pm$ 0.1 |
| Histidine (500-fold excess)  | 99.7 $\pm$ 0.4                 | 98.7 $\pm$ 0.4 |
| Histidine (5000-fold excess) | 99.0 $\pm$ 0.3                 | 97.7 $\pm$ 0.6 |

projections, 5 min acquisition time; SPECT scans were carried out using technetium-99m energy window (126.45 keV–154.56 keV) or iodine-125 energy window (25.56 keV–31.24 keV), 256  $\times$  256 matrix, 30 min acquisition time. The CT raw data were reconstructed using Nucline 2.03 Software (Mediso Medical Imaging Systems, Hungary). SPECT raw data were reconstructed using Tera-Tomo<sup>TM</sup> 3D SPECT.

### 3. Results

**3.1. Radiolabeling.** Direct radioiodination of DARPin 9\_29 provided a radiochemical yield of 96.2  $\pm$  0.7%. Size-exclusion chromatography using disposable NAP-5 column provided radiochemical purity of 99.7  $\pm$  0.5%. The isolated yield was 87  $\pm$  1%. Specific activity of 1.1 MBq/ $\mu\text{g}$  (20 GBq/ $\mu\text{mol}$ ) was achieved. Incubation of [ $^{125}\text{I}$ ]I-DARPin 9\_29 in PBS or challenge with 1 M potassium iodide up to 3 h did not reveal any measurable release of the radionuclide from DARPin 9\_29 (Table 1).

Labeling of DARPin 9\_29 with [ $^{99\text{m}}\text{Tc}$ ]Tc(CO) $_3$  resulted in a radiochemical yield of 80  $\pm$  4%. The radiochemical purity after size-exclusion chromatography was 98  $\pm$  1%. The isolated yield was 72  $\pm$  8%. The maximum specific activity was 1.3 MBq/ $\mu\text{g}$  (23.6 GBq/ $\mu\text{mol}$ ). The labeled protein was stable to a significant degree of up to 3 h in PBS and in both 500-fold and 5000-fold molar excess of histidine (Table 2).

**3.2. In Vitro Evaluation of Radiolabeled DARPins.** Binding of both [ $^{99\text{m}}\text{Tc}$ ]Tc(CO) $_3$ -DARPin and [ $^{125}\text{I}$ ]I-DARPin 9\_29 to HER2-expressing cells in vitro was dependent on the HER2 expression level in these cell lines (SKOV-3 > BT474 >> DU-145) (Figure 2). Blocking the receptors with a large molar excess of unlabeled DARPin 9\_29 resulted in significant ( $p < 0.05$ ) reduction of binding. This demonstrates binding saturability and suggests the specific binding character for both conjugates.

To elucidate the binding specificity further, binding of [ $^{125}\text{I}$ ]I-DARPin 9\_29 was determined after treatment of SKOV-3 cells with anti-HER2 affibody molecules Z<sub>HER2:342</sub>, anti-HER2 antibody trastuzumab, as well as control

antibodies anti-EGFR cetuximab and anti-VEGF bevacizumab. As shown in Figure 3, while reduction in binding after treatment with unlabeled DARPin 9\_29 was highly significant ( $p < 0.000001$ ), there was neither significant reduction in binding after receptor saturation using trastuzumab ( $p > 0.05$ ) nor any reduction in binding after treatment of SKOV-3 cells with cetuximab or bevacizumab. Interestingly, treatment of the SKOV-3 cells with Z<sub>HER2:342</sub> affibody molecule resulted in small (12%) but significant ( $p < 0.05$ ) reduction of [ $^{125}\text{I}$ ]I-DARPin 9\_29 binding.

Representative LigandTracer sensorgrams of [ $^{99\text{m}}\text{Tc}$ ]Tc(CO) $_3$ -DARPin 9\_29 and [ $^{125}\text{I}$ ]I-DARPin 9\_29 binding to HER2-expressing SKOV-3 cells are presented in Figure 4. Sensorgrams show rapid binding and slow dissociation of the conjugates. The best curve fitting for both variants was obtained when 1 : 2 binding model was applied. The analysis suggested the presence of one interaction with high affinity and one with lower. The equilibrium dissociation constant ( $K_D$ ) of the strongest interaction was 362  $\pm$  130 pM for [ $^{125}\text{I}$ ]I-DARPin 9\_29 and 439  $\pm$  156 pM for [ $^{99\text{m}}\text{Tc}$ ]Tc(CO) $_3$ -DARPin. In the case of weaker interactions, the dissociation constants were 7.7  $\pm$  2.8 nM and 9.1  $\pm$  2.7 nM for [ $^{125}\text{I}$ ]I-DARPin 9\_29 and [ $^{99\text{m}}\text{Tc}$ ]Tc(CO) $_3$ -DARPin, respectively. The weaker interaction was approximately 3-fold more abundant.

Processing of [ $^{99\text{m}}\text{Tc}$ ]Tc(CO) $_3$ -DARPin and [ $^{125}\text{I}$ ]I-DARPin 9\_29 by HER2-expressing SKOV-3 and BT474 cells during continuous incubation is presented in Figure 5. Pattern of the cellular processing was concordant in both cell lines. The internalized activity was lower for DARPin 9\_29 labeled using nonresidualizing iodine-125. Total cell-associated activity was also lower in the case of [ $^{125}\text{I}$ ]I-DARPin 9\_29. However, the internalized fraction was not very high (approximately 20–25% at 4 h) even for the residualizing [ $^{99\text{m}}\text{Tc}$ ]Tc(CO) $_3$  label.

**3.3. Animal Studies.** The results of the in vivo specificity test are presented in Figure 6. Accumulation of both [ $^{125}\text{I}$ ]I-DARPin 9\_29 and [ $^{99\text{m}}\text{Tc}$ ]Tc(CO) $_3$ -DARPin 9\_29 in HER2-negative Ramos lymphoma xenografts were on the same level as in muscles (0.2–0.3 %ID/g). Uptake in HER2-positive SKOV-3 xenografts was significantly ( $p < 0.00005$ ) higher, 3.4  $\pm$  0.7 %ID/g and 2.9  $\pm$  0.7 %ID/g for [ $^{125}\text{I}$ ]I-DARPin 9\_29 and [ $^{99\text{m}}\text{Tc}$ ]Tc(CO) $_3$ -DARPin 9\_29, respectively. This demonstrates that the tumor uptake of both variants was HER2 specific.

Data concerning biodistribution of [ $^{125}\text{I}$ ]I-DARPin 9\_29 and [ $^{99\text{m}}\text{Tc}$ ]Tc(CO) $_3$ -DARPin 9\_29 in BALB/C nu/nu mice bearing HER2-positive xenografts at 6 h after injection are presented in Table 3. The common feature of both constructs was relatively rapid clearance from blood. However, there were appreciable differences in biodistribution of these variants. For example, [ $^{125}\text{I}$ ]I-DARPin 9\_29 had significantly lower uptake in the lung, liver, spleen, kidneys, and bone. Besides, accumulation of radioiodine in the content of gastrointestinal tract was also lower, indicating that hepatobiliary excretion plays smaller role for this probe and/or

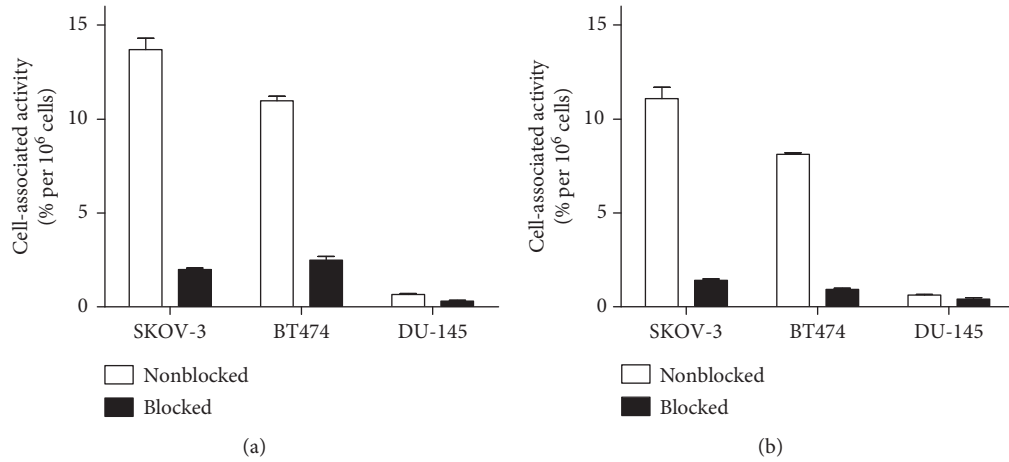


FIGURE 2: In vitro binding specificity of [<sup>99m</sup>Tc]Tc(CO)<sub>3</sub>-DARPin (a) and [<sup>125</sup>I]I-DARPin 9\_29 (b) to HER2-expressing cells. In the blocked group, receptors were presaturated with a 100-fold excess of unlabeled DARPin. Data are presented as the mean of three samples ± SD.

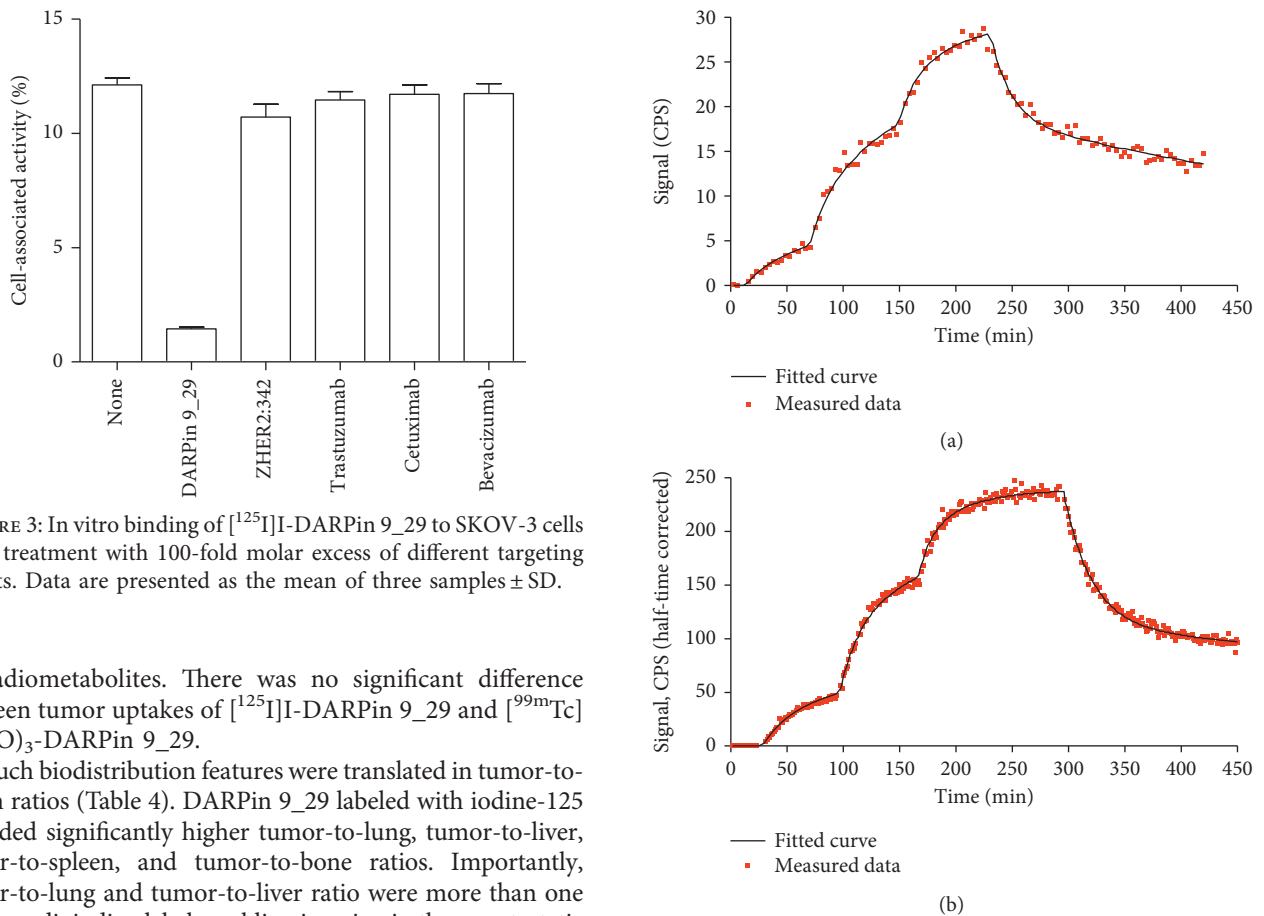


FIGURE 3: In vitro binding of [<sup>125</sup>I]I-DARPin 9\_29 to SKOV-3 cells after treatment with 100-fold molar excess of different targeting agents. Data are presented as the mean of three samples ± SD.

its radiometabolites. There was no significant difference between tumor uptakes of [<sup>125</sup>I]I-DARPin 9\_29 and [<sup>99m</sup>Tc]Tc(CO)<sub>3</sub>-DARPin 9\_29.

Such biodistribution features were translated in tumor-to-organ ratios (Table 4). DARPin 9\_29 labeled with iodine-125 provided significantly higher tumor-to-lung, tumor-to-liver, tumor-to-spleen, and tumor-to-bone ratios. Importantly, tumor-to-lung and tumor-to-liver ratio were more than one for the radioiodine label, enabling imaging in these metastatic sites for many malignancies.

The results of the small-animal SPECT/CT imaging (Figure 7) confirmed the results of the ex vivo biodistribution measurements. The HER2-expressing xenografts were well visualized using both [<sup>125</sup>I]I-DARPin 9\_29 and [<sup>99m</sup>Tc]Tc(CO)<sub>3</sub>-DARPin 9\_29. Due to renal excretion, an appreciable amount of activity was detected in the urinary bladder. In the case of [<sup>99m</sup>Tc]Tc(CO)<sub>3</sub>-DARPin 9\_29, a noticeable amount of activity was detected in the gastrointestinal tract, liver, and

FIGURE 4: Representative LigandTracer sensorgrams of [<sup>125</sup>I]I-DARPin 9\_29 (a) and [<sup>99m</sup>Tc]Tc(CO)<sub>3</sub>-DARPin 9\_29 (b) binding to HER2-expressing SKOV-3 cells. The association was measured at concentrations of 1, 4, and 8 nM.

kidneys. Activity concentration in these organs exceeded concentration in tumors. In the case of [<sup>125</sup>I]I-DARPin 9\_29, the opposite was observed as the tumor had the highest activity accumulation (after the urinary bladder).

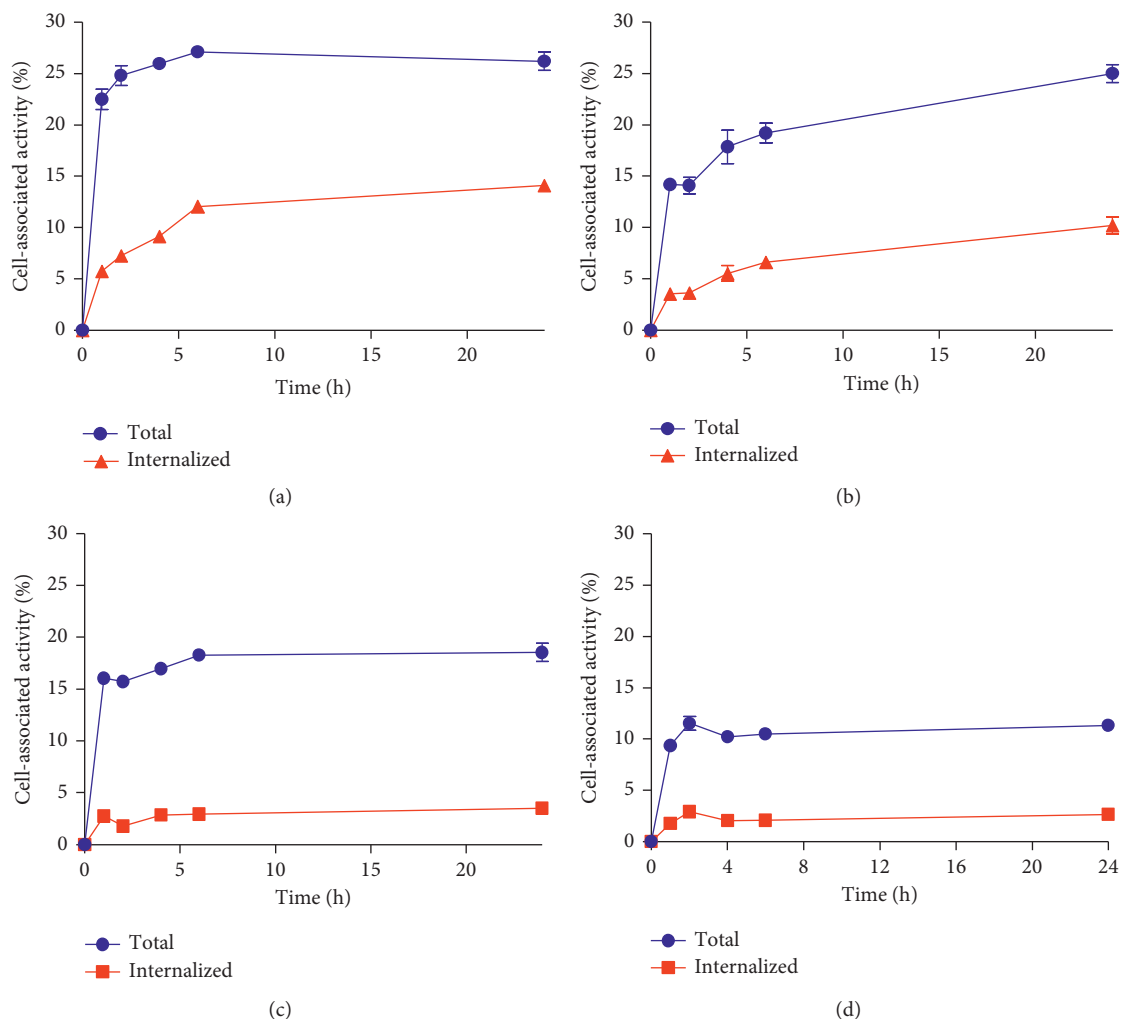


FIGURE 5: Cellular processing of  $[^{99m}\text{Tc}]\text{Tc}(\text{CO})_3$ -DARPin 9\_29 (a, b) and  $[^{125}\text{I}]\text{I}$ -DARPin 9\_29 (c, d) by HER2-expressing SKOV-3 (a, c) and BT474 (b, d) cells. Cells were incubated with the conjugates (10 nM) at 37°C. Data are presented as the mean of three samples  $\pm$  SD.

#### 4. Discussion

We have demonstrated that DARPin 9\_29 can be labeled with  $[^{125}\text{I}]\text{I}$  and  $[^{99m}\text{Tc}]\text{Tc}(\text{CO})_3$  with reasonably good yields and high stability (Tables 1 and 2). Both labeled proteins retained specific binding to HER2-expressing cells, and the level of binding was proportional to HER2 expression in these cell lines (Figures 2 and 3). The binding of  $[^{125}\text{I}]\text{I}$ -DARPin 9\_29 could be saturated by nonlabeled DARPin 9\_29 but not with monoclonal antibody trastuzumab (Figure 3). This is in agreement with the literature data suggesting that DARPin 9\_29 and trastuzumab bind to different epitopes on HER2 [23]. This opens an opportunity to use radiolabeled DARPin 9\_29 for monitoring of HER2 during trastuzumab therapy without interference from antibodies bound to the receptors on malignant cells. It was surprising that small but significant reduction of  $[^{125}\text{I}]\text{I}$ -DARPin 9\_29 binding to SKOV-3 cells was found after treatment of cells with a large excess of anti-HER2 affibody molecules  $Z_{\text{HER2}:342}$ , although this affibody molecules bind to a different epitope [23]. A possible explanation is that the

binding of affibody molecules causes some conformational change of the receptor, which is not favorable for DARPin 9\_29 binding.

The LigandTracer measurements demonstrated that both labeled variants bind with similar affinity to SKOV-3 cells, with  $K_{D1}$  of approximately 0.4 nM and  $K_{D2}$  of 8-9 nM. Two affinities are often found during LigandTracer measurement of binding to living cells for tracers targeting receptors belonging to HER family [34–37]. Björkelund et al. [35] demonstrated that this can be explained by homo- and heterodimerization of receptors. The dissociation constant values are in a good agreement with that obtained earlier for binding of DARPin 9\_29 to the extracellular domain of HER2 (3.8 nM) using surface plasmon resonance (SPR) [38]. The affinity measurements suggest that both methods provide labeled DARPin 9\_29 with preservation of binding affinity to HER2.

The data concerning cellular processing of radiolabeled conjugates after binding to HER2-expressing cells (Figure 5) demonstrated a potential advantage of the residualizing  $^{99m}\text{Tc}(\text{CO})_3$  label. The intracellular fraction was higher for

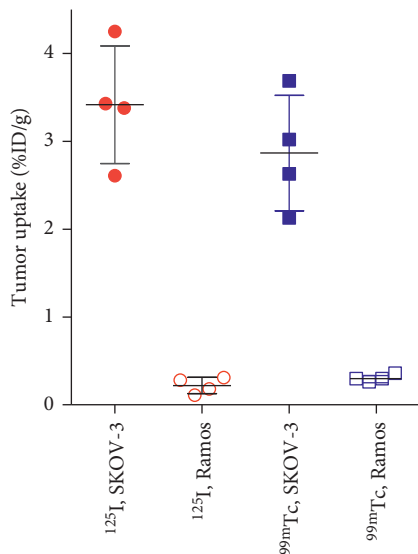


FIGURE 6: In vivo specificity of HER2 targeting using [ $^{125}\text{I}$ ]I-DARPin 9\_29 and [ $^{99\text{m}}\text{Tc}$ ]Tc(CO) $_3$ -DARPin 9\_29. Uptake of both imaging probes was significantly ( $p < 0.00005$ ) higher in HER2-positive SKOV-3 than in HER2-negative Ramos xenografts. Data are presented as mean  $\pm$  SD for four mice.

TABLE 3: Comparison of biodistribution of [ $^{125}\text{I}$ ]I-DARPin 9\_29 and [ $^{99\text{m}}\text{Tc}$ ]Tc(CO) $_3$ -DARPin 9\_29 in BALB/C nu/nu mice bearing SKOV-3 xenografts at 6 h after injection.

|                                     | Uptake (%ID/g)                |  |
|-------------------------------------|-------------------------------|--|
|                                     | $^{125}\text{I}$ -DARPin 9_29 | $^{99\text{m}}\text{Tc}(\text{CO})_3$ -DARPin 9_29 |
| Blood                               | 1.2 $\pm$ 0.4                 | 0.8 $\pm$ 0.1                                      |
| Salivary glands                     | 1.3 $\pm$ 0.3                 | 1.7 $\pm$ 0.4                                      |
| Lung                                | 0.9 $\pm$ 0.3*                | 1.7 $\pm$ 0.2                                      |
| Liver                               | 1.2 $\pm$ 0.2*                | 27 $\pm$ 4   |
| Spleen                              | 0.9 $\pm$ 0.2*                | 8.4 $\pm$ 3.0                                      |
| Stomach                             | 4.3 $\pm$ 3.0                 | 1.3 $\pm$ 0.1                                      |
| Kidney                              | 3.4 $\pm$ 0.4*                | 80 $\pm$ 11  |
| Tumor                               | 3.4 $\pm$ 0.7                 | 2.9 $\pm$ 0.7                                      |
| Muscle                              | 0.3 $\pm$ 0.1                 | 0.5 $\pm$ 0.1                                      |
| Bone                                | 0.77 $\pm$ 0.04*              | 2.0 $\pm$ 0.8                                      |
| Gastrointestinal tract <sup>a</sup> | 1.4 $\pm$ 0.3*                | 5.3 $\pm$ 0.9                                      |

<sup>a</sup>Data for the gastrointestinal tract are presented as %ID per whole sample. \*Significant difference ( $p < 0.05$ ) between uptake of [ $^{125}\text{I}$ ]I-DARPin 9\_29 and [ $^{99\text{m}}\text{Tc}$ ]Tc(CO) $_3$ -DARPin 9\_29. Data are presented as mean  $\pm$  SD for four mice.

technetium-99m compared to radioiodine, which translated into higher total cell-associated activity. However, the internalization was relatively slow, and the difference between total cellular uptake of [ $^{99\text{m}}\text{Tc}$ ]Tc(CO) $_3$ -DARPin 9\_29 and [ $^{125}\text{I}$ ]I-DARPin 9\_29 was moderate (1.5–1.7 fold) at 4 and 6 h, that is, time points relevant for imaging.

The uptake of both [ $^{125}\text{I}$ ]I-DARPin 9\_29 and [ $^{99\text{m}}\text{Tc}$ ]Tc(CO) $_3$ -DARPin 9\_29 in HER2-expressing SKOV-3 xenografts was significantly higher than in HER2-negative Ramos lymphoma xenografts, which is a strong evidence of HER2-specific tumor accumulation. For comparison, an EPR-mediated nonspecific uptake of anti-HER2 monoclonal antibodies might amount to 25–30% of specific one

TABLE 4: Comparison of [ $^{125}\text{I}$ ]I-DARPin 9\_29 and [ $^{99\text{m}}\text{Tc}$ ]Tc(CO) $_3$ -DARPin 9\_29 tumor-to-organ ratios in nude mice bearing SKOV-3 xenografts.

|                 | Tumor-to-organ ratio              |  |
|-----------------|-----------------------------------|--|
|                 | [ $^{125}\text{I}$ ]I-DARPin 9_29 | [ $^{99\text{m}}\text{Tc}$ ]Tc(CO) $_3$ -DARPin 9_29 |
| Blood           | 3.4 $\pm$ 1.8                     | 3.4 $\pm$ 0.5  |
| Salivary glands | 2.0 $\pm$ 0.7                     | 2.0 $\pm$ 0.4  |
| Lung            | 4 $\pm$ 2                         | 1.7 $\pm$ 0.4*                                       |
| Liver           | 3 $\pm$ 1                         | 0.11 $\pm$ 0.02*                                     |
| Spleen          | 4 $\pm$ 1                         | 0.35 $\pm$ 0.04*                                     |
| Stomach         | 1.2 $\pm$ 1.0                     | 2.1 $\pm$ 0.5*                                       |
| Kidney          | 1.00 $\pm$ 0.16                   | 0.035 $\pm$ 0.003*                                   |
| Muscle          | 11.3 $\pm$ 5.5                    | 6.6 $\pm$ 2.6  |
| Bone            | 4.4 $\pm$ 0.9                     | 1.6 $\pm$ 0.4*                                       |

\*Significant difference ( $p < 0.05$ ) between values for [ $^{125}\text{I}$ ]I-DARPin 9\_29 and [ $^{99\text{m}}\text{Tc}$ ]Tc(CO) $_3$ -DARPin 9\_29. Data are presented as mean  $\pm$  SD for four mice.

up to 3 days after injection [31, 39], which might be associated with an elevated risk of false-positive diagnosis.

There was a striking difference between the biodistribution profiles of [ $^{125}\text{I}$ ]I-DARPin 9\_29 and [ $^{99\text{m}}\text{Tc}$ ]Tc(CO) $_3$ -DARPin 9\_29 (Table 3 and Figure 7). Uptake of [ $^{99\text{m}}\text{Tc}$ ]Tc(CO) $_3$ -DARPin 9\_29 in the lung, liver, spleen, and kidneys was several-fold higher than the uptake of [ $^{125}\text{I}$ ]I-DARPin 9\_29. The high renal uptake is characteristic for radiometal-labeled DARPins [18, 22] and is, most likely, associated with the high reabsorption of proteins in proximal tubuli, rapid internalization, and efficient retention of radiometabolites of residualizing radiometal labels. The high hepatic uptake might be due to high lipophilicity of [ $^{99\text{m}}\text{Tc}$ ]Tc(CO) $_3$ -histidine label [40–42]. This effect depends on properties of a targeting protein. For example, elevated hepatic uptake in the case of [ $^{99\text{m}}\text{Tc}$ ]Tc(CO) $_3$ -histidine label was observed for DARPin G3 [22] and affibody molecule Z<sub>HER2:342</sub> [43] but not observed for scFv [25], nanobodies [44], or ADAPTs [45]. The low accumulation of [ $^{125}\text{I}$ ]I in these organs is due to nonresidualizing properties of direct radioiodine label. Due to rapid internalization after renal and hepatic uptake, [ $^{125}\text{I}$ ]I-DARPin 9\_29 undergoes lysosomal degradation, and the main radiometabolite, iodo-tyrosine, “leaks” from cells. Such effect has been described for affibody molecules [30] and ADAPTs [36]. The tumor uptake in vivo of [ $^{125}\text{I}$ ]I-DARPin 9\_29 and [ $^{99\text{m}}\text{Tc}$ ]Tc(CO) $_3$ -DARPin 9\_29 was not different because the internalization of DARPin 9\_29 after binding to the HER2 receptor in cancer cells was slow, and leakage of radiometabolites had no strong effect on tumor-associated activity. In addition, the delivery of [ $^{99\text{m}}\text{Tc}$ ]Tc(CO) $_3$ -DARPin 9\_29 to tumors might be reduced due to sequestering of this conjugate in the liver. The level of the tumor uptake, 3.4  $\pm$  0.7 %ID/g and 2.9  $\pm$  0.7 %ID/g for [ $^{125}\text{I}$ ]I-DARPin 9\_29 and [ $^{99\text{m}}\text{Tc}$ ]Tc(CO) $_3$ -DARPin 9\_29, respectively, was similar to the uptake of [ $^{99\text{m}}\text{Tc}$ ]Tc(CO) $_3$ -labeled DARPin G3-D (4.45  $\pm$  1.18 %ID/g) with the similar affinity to HER2 D (1.48  $\pm$  0.01 nM according to SPR measurements) [22]. The [ $^{99\text{m}}\text{Tc}$ ]Tc(CO) $_3$ -labeled anti-HER2 nanobody 2Rs15d having similar size and affinity (3.9 nM) had also comparable tumor uptake

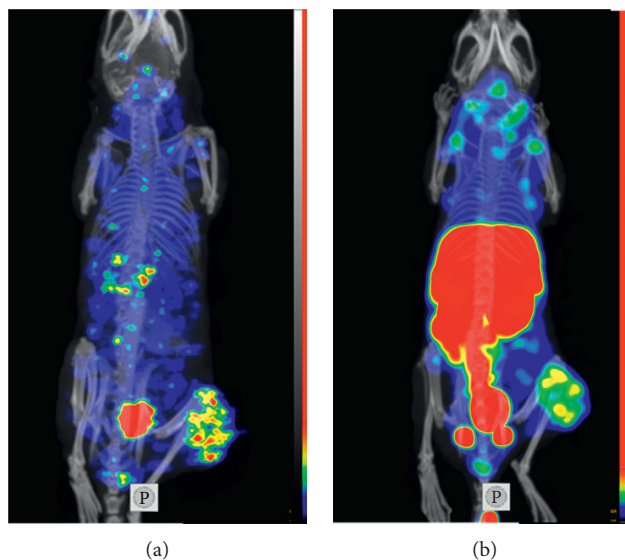


FIGURE 7: Imaging of HER2 expression in SKOV-3 xenografts (maximum intensity projection) using  $[^{125}\text{I}]\text{I-DARPin 9}_{29}$  (a) and  $[^{99\text{m}}\text{Tc}]\text{Tc}(\text{CO})_3\text{-DARPin 9}_{29}$  (b). Small-animal SPECT/CT imaging was performed at 6 h after injection.

( $4.19 \pm 0.47$  %ID/g) [44]. It has to be noted that both the nanobody and DARPin G3-D cleared more rapidly from blood and normal tissues, which resulted in higher tumor-to-organ ratios compared to DARPin 9\_29 [22, 44]. Overall, the iodine-125 label provided better imaging contrast compared to the technetium-99m label. The use of technetium-99m might be limited to special applications, like determination of HER2 status in primary tumor and local lymph node metastases before neoadjuvant therapy of breast carcinomas.

This study utilized iodine-125 ( $T_{1/2} = 59.4$  d) because this radionuclide is convenient for preclinical development due to long half-life and low energy of emitted photons. Our experience suggests that the labeling protocol might be applied with a minimal reoptimization for labeling with iodine-123 ( $T_{1/2} = 13.3$  h) and iodine-124 ( $T_{1/2} = 4.18$  d) for clinical SPECT or PET applications, respectively [46, 47].

## 5. Conclusion

DARPin 9\_29 can be labeled with iodine-125 and  $[^{99\text{m}}\text{Tc}]\text{Tc}(\text{CO})_3$  with high stability and preserved binding specificity and affinity to HER2. Both labeled proteins were internalized slowly by HER2-expressing cells. Both  $[^{125}\text{I}]\text{I-DARPin 9}_{29}$  and  $[^{99\text{m}}\text{Tc}]\text{Tc}(\text{CO})_3\text{-DARPin 9}_{29}$  demonstrated specific uptake in HER2-positive xenografts when compared to HER2-negative xenografts. Radioiodine provided better tumor-to-organ ratios compared to  $[^{99\text{m}}\text{Tc}]\text{Tc}(\text{CO})_3$  label. Radioiodinated DARPin 9\_29 is a promising agent for same-day imaging of HER2 expression in cancer using SPECT.

## Data Availability

Data supporting conclusions of this study are included in the article. Raw data are available from the corresponding author upon request.

## Ethical Approval

Animal studies were performed in agreement with Swedish national legislation concerning protection of laboratory animals and were approved by the Ethics Committee for Animal Research in Uppsala.

## Conflicts of Interest

The authors declare that there are no conflicts of interest regarding the publication of this article.

## Acknowledgments

This research was financially supported by grants from the Swedish Cancer Society (Grant CAN 2015/350 and 2017/425), Swedish Research Council (Grant nos. 2015-02353 and 2015-02509), Swedish Agency for Innovation VINNOVA (Grant 2016-04060), RSF (Grant no. 14-24-00106) as the part of Protein Engineering and Purification, and State Contract of Russian Federation no. 14.N08.11.0163. Research activities of Mohamed Altai were kindly supported by the Swedish Society of Medical Research (SSMF).

## References

- [1] D. J. Slamon, G. M. Clark, S. G. Wong et al., "Human breast cancer: correlation of relapse and survival with amplification of the HER-2/neu oncogene," *Science*, vol. 235, no. 4785, pp. 177–182, 1987.
- [2] E. Van Cutsem, Y. J. Bang, F. Feng-Yi et al., "HER2 screening data from ToGA: targeting HER2 in gastric and gastroesophageal junction cancer," *Gastric Cancer*, vol. 18, no. 3, pp. 476–484, 2015.
- [3] S. H. Giordano, S. Temin, J. J. Kirshner et al., "American Society of Clinical Oncology. Systemic therapy for patients with advanced human epidermal growth factor receptor 2-positive breast cancer: American Society of Clinical Oncology

- clinical practice guideline," *Journal of Clinical Oncology*, vol. 32, no. 19, pp. 2078–2099, 2014.
- [4] L. Gianni, T. Pienkowski, Y. H. Im et al., "Efficacy and safety of neoadjuvant pertuzumab and trastuzumab in women with locally advanced, inflammatory, or early HER2-positive breast cancer (NeoSphere): a randomised multicentre, open-label, phase 2 trial," *The Lancet Oncology*, vol. 13, no. 1, pp. 25–32, 2012.
- [5] A. C. Wolff, M. E. Hammond, D. G. Hicks et al., "American Society of Clinical Oncology; College of American Pathologists. Recommendations for human epidermal growth factor receptor 2 testing in breast cancer: American Society of Clinical Oncology/College of American Pathologists clinical practice guideline update," *Journal of Clinical Oncology*, vol. 31, no. 31, pp. 3997–4013, 2013.
- [6] T. Foukakis, G. Åström, L. Lindström, T. Hatschek, and J. Bergh, "When to order a biopsy to characterise a metastatic relapse in breast cancer," *Annals of Oncology*, vol. 23, no. 10, pp. x349–x353, 2012.
- [7] N. Houssami, P. Macaskill, R. L. Balleine, M. Bilous, and M. D. Pegram, "HER2 discordance between primary breast cancer and its paired metastasis: tumor biology or test artefact? Insights through meta-analysis," *Breast Cancer Research and Treatment*, vol. 129, no. 3, pp. 659–674, 2011.
- [8] U. Wilking, E. Karlsson, L. Skoog et al., "HER2 status in a population-derived breast cancer cohort: discordances during tumor progression," *Breast Cancer Research and Treatment*, vol. 125, no. 2, pp. 553–561, 2011.
- [9] V. Tolmachev, "Imaging of HER-2 overexpression in tumors for guiding therapy," *Current Pharmaceutical Design*, vol. 14, no. 28, pp. 2999–3019, 2008.
- [10] H. J. Wester and H. Kessler, "Molecular targeting with peptides or peptide-polymer conjugates: just a question of size?," *Journal of Nuclear Medicine*, vol. 46, no. 12, pp. 1940–1945, 2005.
- [11] R. Vazquez-Lombardi, T. G. Phan, C. Zimmermann, D. Lowe, L. Jermutus, and D. Christ, "Challenges and opportunities for non-antibody scaffold drugs," *Drug Discovery Today*, vol. 20, no. 10, pp. 1271–1283, 2015.
- [12] R. Simeon and Z. Chen, "In vitro-engineered non-antibody protein therapeutics," *Protein Cell*, vol. 9, no. 1, pp. 3–14, 2017.
- [13] S. M. Deyev, E. N. Lebedenko, L. E. Petrovskaya, D. A. Dolgikh, A. G. Gabibov, and M. P. Kirpichnikov, "Man-made antibodies and immunoconjugates with desired properties: function optimization using structural engineering," *Russian Chemical Reviews*, vol. 84, no. 1, pp. 1–26, 2015.
- [14] A. Krasniqi, M. D'Huyvetter, N. Devoogdt et al., "Same-day imaging using small proteins: clinical experience and translational prospects in oncology," *Journal of Nuclear Medicine* vol. 59, no. 6, pp. 885–891, 2018.
- [15] J. Sörensen, I. Velikyan, D. Sandberg et al., "Measuring HER2-receptor expression in metastatic breast cancer using [68Ga] ABY-025 affibody PET/CT," *Theranostics*, vol. 6, no. 2, pp. 262–271, 2016.
- [16] D. Sandberg, V. Tolmachev, I. Velikyan et al., "Intra-image referencing for simplified assessment of HER2-expression in breast cancer metastases using the affibody molecule ABY-025 with PET and SPECT," *European Journal of Nuclear Medicine and Molecular Imaging*, vol. 44, no. 8, pp. 1337–1346, 2017.
- [17] A. Plückthun, "Designed ankyrin repeat proteins (DARPs): binding proteins for research, diagnostics, and therapy," *Annual Review of Pharmacology and Toxicology*, vol. 55, no. 1, pp. 489–511, 2015.
- [18] R. Goldstein, J. Sosabowski, M. Livanos et al., "Development of the designed ankyrin repeat protein (DARPin) G3 for HER2 molecular imaging," *European Journal of Nuclear Medicine and Molecular Imaging*, vol. 42, no. 2, pp. 288–301, 2015.
- [19] V. Tolmachev, T. A. Tran, D. Rosik, A. Sjöberg, L. Abrahmsén, and A. Orlova, "Tumor targeting using affibody molecules: interplay of affinity, target expression level, and binding site composition," *Journal of Nuclear Medicine*, vol. 53, no. 6, pp. 953–960, 2012.
- [20] K. G. Andersson, M. Rosestedt, Z. Varasteh et al., "Comparative evaluation of 111In-labeled NOTA-conjugated affibody molecules for visualization of HER3 expression in malignant tumors," *Oncology Reports*, vol. 34, no. 2, pp. 1042–1048, 2015.
- [21] J. Garousi, H. Honarvar, K. G. Andersson et al., "Comparative evaluation of affibody molecules for radionuclide imaging of in vivo expression of carbonic anhydrase IX," *Molecular Pharmaceutics*, vol. 13, no. 11, pp. 3676–3687, 2016.
- [22] C. Zahnd, M. Kawe, M. T. Stumpp et al., "Efficient tumor targeting with high-affinity designed ankyrin repeat proteins: effects of affinity and molecular size," *Cancer Research*, vol. 70, no. 4, pp. 1595–1605, 2010.
- [23] C. Jost, J. Schilling, R. Tamaskovic, M. Schwill, A. Honegger, and A. Plückthun, "Structural basis for eliciting a cytotoxic effect in HER2-overexpressing cancer cells via binding to the extracellular domain of HER2," *Structure*, vol. 21, no. 11, pp. 1979–1991, 2013.
- [24] E. Sokolova, G. Proshkina, O. Kutova et al., "Recombinant targeted toxin based on HER2-specific DARPin possesses a strong selective cytotoxic effect in vitro and a potent antitumor activity in vivo," *Journal of Controlled Release*, vol. 233, pp. 48–56, 2016.
- [25] R. Waibel, R. Alberto, J. Willuda et al., "Stable one-step technetium-99m labeling of His-tagged recombinant proteins with a novel Tc(I)-carbonyl complex," *Nature Biotechnology*, vol. 17, no. 9, pp. 897–901, 1999.
- [26] A. Henaut and A. Danchin, *Escherichia coli* and *Salmonella typhimurium* Cellular and Molecular Biology, Vol. 2, F. Neidhardt, R. Curtiss III, J. Ingraham et al., Eds., pp. 2047–2066, American Society for Microbiology, Washington, DC, USA, 1996.
- [27] F. W. Studier, "Stable expression clones and auto-induction for protein production in *E. coli*," *Methods in Molecular Biology*, vol. 1091, pp. 17–32, 2014.
- [28] C. N. Pace, "How to measure and predict the molar absorption coefficient of a protein," *Protein Science*, vol. 4, no. 11, pp. 2411–2423, 1995.
- [29] V. Tolmachev, A. Orlova, and K. Andersson, "Methods for radiolabelling of monoclonal antibodies," *Methods in Molecular Biology*, vol. 1060, pp. 309–330, 2014.
- [30] A. Orlova, F. Y. Nilsson, M. Wikman et al., "Comparative in vivo evaluation of technetium and iodine labels on an anti-HER2 affibody for single-photon imaging of HER2 expression in tumors," *Journal of Nuclear Medicine*, vol. 47, no. 3, pp. 512–519, 2006.
- [31] K. McLarty, B. Cornelissen, D. A. Scollard, S. J. Done, K. Chun, and R. M. Reilly, "Associations between the uptake of 111In-DTPA-trastuzumab, HER2 density and response to trastuzumab (Herceptin) in athymic mice bearing subcutaneous human tumour xenografts," *European Journal of Nuclear Medicine and Molecular Imaging*, vol. 36, no. 1, pp. 81–93, 2009.
- [32] J. Malmberg, V. Tolmachev, and A. Orlova, "Imaging agents for in vivo molecular profiling of disseminated prostate

- cancer: cellular processing of [(111)In]-labeled CHX-A<sup>1</sup>DTPA-trastuzumab and anti-HER2 ABY-025 affibody in prostate cancer cell lines,” *Experimental and Therapeutic Medicine*, vol. 2, no. 3, pp. 523–528, 2011.
- [33] H. Wällberg and A. Orlova, “Slow internalization of anti-HER2 synthetic affibody monomer 111In-DOTA-ZHER2:342-pep2: implications for development of labeled tracers,” *Cancer Biotherapy and Radiopharmaceuticals*, vol. 23, no. 4, pp. 435–442, 2008.
- [34] P. Barta, J. Malmberg, L. Melicharova et al., “Protein interactions with HER-family receptors can have different characteristics depending on the hosting cell line,” *International Journal of Oncology*, vol. 40, no. 5, pp. 1677–1682, 2012.
- [35] H. Björkelund, L. Gedda, M. Malmqvist, and K. Andersson, “Resolving the EGF-EGFR interaction characteristics through a multiple-temperature, multiple-inhibitor, real-time interaction analysis approach,” *Molecular and Clinical Oncology*, vol. 1, no. 2, pp. 343–352, 2013.
- [36] S. Lindbo, J. Garousi, B. Mitran et al., “Radionuclide tumor targeting using ADAPT scaffold proteins: aspects of label positioning and residualizing properties of the label,” *Journal of Nuclear Medicine*, vol. 59, no. 1, pp. 93–99, 2018.
- [37] D. Summer, J. Garousi, M. Oroujeni et al., “Cyclic versus noncyclic chelating scaffold for 89Zr-Labeled ZEGFR:2377 Affibody bioconjugates targeting epidermal growth factor receptor overexpression,” *Molecular Pharmaceutics*, vol. 15, no. 1, pp. 175–185, 2018.
- [38] D. Steiner, P. Forrer, and A. Plückthun, “Efficient selection of DARPs with sub-nanomolar affinities using SRP phage display,” *Journal of Molecular Biology*, vol. 382, no. 5, pp. 1211–1227, 2008.
- [39] M. N. Lub-de Hooge, J. G. Kosterink, P. J. Perik et al., “Preclinical characterisation of 111In-DTPA-trastuzumab,” *British Journal of Pharmacology*, vol. 143, no. 1, pp. 99–106, 2004.
- [40] G. J. Pimentel, J. E. Vazquez, W. Quesada et al., “Hexahistidine tag as a novel alternative for one-step direct labeling of a single-chain Fv antibody fragment with 99mTc,” *Nuclear Medicine Communications*, vol. 22, no. 10, pp. 1089–1094, 2001.
- [41] R. J. Francis, S. J. Mather, K. Chester et al., “Radiolabelling of glycosylated MFE-23::CPG2 fusion protein (MFECp1) with 99mTc for quantitation of tumour antibody-enzyme localisation in antibody-directed enzyme pro-drug therapy (AD-EPT),” *European Journal of Nuclear Medicine and Molecular Imaging*, vol. 31, no. 8, pp. 1090–1096, 2004.
- [42] C. Hofström, M. Altai, H. Honarvar et al., “HEHEHE, HIIHHI, or HKHKHK: influence of position and composition of histidine containing tags on biodistribution of [(99m)Tc(CO)<sub>3</sub>](+)-labeled affibody molecules,” *Journal of Medicinal Chemistry*, vol. 56, no. 12, pp. 4966–4974, 2013.
- [43] V. Tolmachev, C. Hofström, J. Malmberg et al., “HEHEHE-tagged affibody molecule may be purified by IMAC, is conveniently labeled with [<sup>99m</sup>(m)Tc(CO)<sub>3</sub>](+), and shows improved biodistribution with reduced hepatic radioactivity accumulation,” *Bioconjugate Chemistry*, vol. 21, no. 11, pp. 2013–2022, 2010.
- [44] I. Vaneycken, N. Devoogdt, N. Van Gassen et al., “Preclinical screening of anti-HER2 nanobodies for molecular imaging of breast cancer,” *FASEB Journal*, vol. 25, no. 7, pp. 2433–2446, 2011.
- [45] S. Lindbo, J. Garousi, M. Åstrand et al., “Influence of histidine-containing tags on the biodistribution of ADAPT scaffold proteins,” *Bioconjugate Chemistry*, vol. 27, no. 3, pp. 716–726, 2016.
- [46] A. Orlova, H. Wällberg, S. Stone-Elander, and V. Tolmachev, “On the selection of a tracer for PET imaging of HER2-expressing tumors: direct comparison of a 124I-labeled affibody molecule and trastuzumab in a murine xenograft model,” *Journal of Nuclear Medicine*, vol. 50, no. 3, pp. 417–425, 2009.
- [47] V. Tolmachev, J. Malmberg, S. Estrada, O. Eriksson, and A. Orlova, “Development of a 124I-labeled version of the anti-PSMA monoclonal antibody capromab for immunoPET staging of prostate cancer: Aspects of labeling chemistry and biodistribution,” *International Journal of Oncology*, vol. 44, no. 6, pp. 1998–2008, 2014.

## Research Article

# Evaluation of $^{99m}\text{Tc}$ -HYNIC-VCAM-1<sub>scFv</sub> as a Potential Qualitative and Semiquantitative Probe Targeting Various Tumors

Xiao Zhang,<sup>1,2</sup> Fan Hu ,<sup>1,2</sup> Chunbao Liu,<sup>1,2</sup> Lianglan Yin ,<sup>1,2</sup> Yingying Zhang ,<sup>1,2</sup> Yongxue Zhang ,<sup>1,2</sup> and Xiaoli Lan <sup>1,2</sup>

<sup>1</sup>Department of Nuclear Medicine, Union Hospital, Tongji Medical College, Huazhong University of Science and Technology, Wuhan 430022, China

<sup>2</sup>Hubei Key Laboratory of Molecular Imaging, Union Hospital, Tongji Medical College, Huazhong University of Science and Technology, Wuhan 430022, China

Correspondence should be addressed to Xiaoli Lan; [xl730724@hotmail.com](mailto:xl730724@hotmail.com)

Received 15 January 2018; Accepted 25 March 2018; Published 3 May 2018

Academic Editor: Ya-Yao Huang

Copyright © 2018 Xiao Zhang et al. This is an open access article distributed under the Creative Commons Attribution License, which permits unrestricted use, distribution, and reproduction in any medium, provided the original work is properly cited.

Vascular cell adhesion molecule 1 (VCAM-1) is overexpressed in varieties of cancers. This study aimed to evaluate the application of a single chain variable fragment (scFv) of anti-VCAM-1 antibody labeled with  $^{99m}\text{Tc}$  as a possible imaging agent in several tumors. VCAM-1 scFv was labeled with  $^{99m}\text{Tc}$  using succinimidyl 6-hydrazinium nicotinate hydrochloride, and  $^{99m}\text{Tc}$ -HYNIC-VCAM-1<sub>scFv</sub> was successfully synthesized with a high radiolabeling yield. VCAM-1 expression was evaluated in six cell lines by immunofluorescence staining. In vitro binding assays showed different binding affinities of  $^{99m}\text{Tc}$ -HYNIC-VCAM-1<sub>scFv</sub> in different tumor cell lines, with high uptake in B16F10 melanoma and HT1080 fibrosarcoma cells, which was consistent with immunofluorescence staining results. In vivo SPECT planar imaging demonstrated that B16F10 and HT1080 tumors could be clearly visualized. Less intense uptake was observed in human SKOV3.ip ovarian tumor, and weak uptake was observed in human A375m melanoma, MDA-MB-231 breast cancer, and 786-O renal tumors. These findings were confirmed by biodistribution and immunofluorescence studies. High uptake by B16F10 tumors was inhibited by excess unlabeled VCAM-1<sub>scFv</sub>.  $^{99m}\text{Tc}$ -HYNIC-VCAM-1<sub>scFv</sub>, which selectively binds to VCAM-1, can provide a qualitative and semiquantitative method for noninvasive evaluation of VCAM-1 expression by tumors.

## 1. Introduction

Metastasis, one of the hallmarks of malignancy, remains a significant clinical obstacle to a favorable prognosis. Early, accurate diagnosis and targeted therapy are crucial. A prognostic tumor biomarker is very helpful for the diagnosis and targeted therapy of cancers [1]. Vascular cell adhesion molecule 1 (VCAM-1) is an immunoglobulin- (Ig-) like adhesion molecule with seven extracellular Ig domains. VCAM-1 is believed to be responsible for tumor proliferation and metastasis, and its levels correlate with prognosis [2]. It is expressed by multiple types of aggressive neoplasms, including those involving lung, prostate, breast, ovaries, and colon [3]. VCAM-1 has emerged as a target for therapy of these

tumors [4]. Considering the aberrant expression of VCAM-1 in tumor biology, the development of noninvasive molecular imaging for VCAM-1 is crucial for better tumor diagnosis, prognosis, and therapy planning.

Multiple new techniques for targeting VCAM-1 have been developed in the past decades, including monoclonal antibodies, nanobodies, peptides, and single chain variable fragments (scFvs) [5–8]. As we know, intact monoclonal antibodies have strong binding affinity, but their large molecular weight leads to their slow clearance from blood and poor tissue penetration into tumors. [9]. In contrast, small peptides have the advantages of prompt excretion of unbound tracer and allow prompt imaging, but at the cost of low binding affinity [10]. Given all these considerations, small antibody

fragments of moderate size and sufficient targeting ability are becoming attractive candidates for clinical application [11].

We previously prepared the scFv of anti-VCAM-1 (VCAM-1<sub>scFv</sub>) using the phage display method, which is a widely used process to obtain scFvs with high specificity [12, 13]. Due to the small molecular size (~28 kDa), scFv has the advantage of rapid clearance through renal excretion, lower concentration in liver, and stronger penetration into tumor tissues [14].

The aim of this study was to explore the possibility of a noninvasive and semiquantitative method for targeting VCAM-1 in tumors, which may allow early cancer diagnosis, more precise prognosis, and targeted treatment options. In this study, we radiolabeled VCAM-1<sub>scFv</sub> with <sup>99m</sup>Tc using succinimidyl 6-hydrazinium nicotinate hydrochloride (SHNH) to detect levels of VCAM-1 in several tumor models *in vivo*.

## 2. Materials and Methods

**2.1. <sup>99m</sup>Tc-6-Hydrazinonicotinamide- (HYNIC-) VCAM-1<sub>scFv</sub> Labeling Procedure.** SHNH (20 μg, 69.8 nmol, Solulink, Inc., San Diego CA, USA) was added to the scFv (78.4 μg, 28 nmol, Shanghai Raygene Biotech Company) and reacted in darkness overnight at 4°C. Afterwards, 100 μL tricine (100 mg/mL, pH 5.2, Sigma/Aldrich, St. Louis MO, USA), 4 μL SnCl<sub>2</sub>·2H<sub>2</sub>O (7 mg/mL, Sigma-Aldrich), and 500 μL <sup>99m</sup>TcO<sub>4</sub><sup>-</sup> solution (555 MBq, Beijing Atom High Tech, Beijing, China) were added to the reactions and incubated for 30 min at room temperature to prepare <sup>99m</sup>Tc-HYNIC-VCAM-1<sub>scFv</sub>. The product was purified using a PD-10 gel column (General Electric, Fairfield CT, USA). The radiolabeled compound was analyzed by instant thin layer chromatography (ITLC) under identical conditions to calculate its radiolabeling efficiency, radiochemical purity, and *in vitro* stability (1, 3, 6, and 12 h in fetal bovine serum [FBS] and phosphate-buffered saline [PBS], *n* = 5 per group). Fifty percent acetonitrile and 0.01 M PBS were used as the developing solvent system.

**2.2. Cell Culture.** B16F10 and A375m melanoma cells, SKOV3.ip human ovarian cancer cells, and MDA-MB-231 human breast cancer cells were cultured in Dulbecco's modified Eagle's medium (DMEM) (Gibco, Carlsbad CA, USA). 786-O human renal cancer cells and HT-1080 human fibrosarcoma cells were maintained in Roswell Park Memorial Institute (PRMI-1640) and Minimal Essential Medium (MEM), respectively. All of the media were supplemented with 10% FBS (Gibco, Grand Island, NY, USA), 100 U/mL penicillin, and 100 μg/mL streptomycin (Beyotime, Shanghai, China).

**2.3. VCAM-1 Expression Confirmed by Immunofluorescence Staining.** B16F10, HT-1080, SKOV3.ip, A375m, MDA-MB-231, and 786-O cells were digested, resuspended, and seeded in six-well plates at 1 × 10<sup>6</sup> cells/well and incubated overnight. Then the samples were fixed with 4% paraformaldehyde at room temperature for 20 min and blocked in 1% bovine serum albumin (BSA) for 1 h, followed by incubation with VCAM-1 antibody (rabbit anti-VCAM-1, diluted 1:200,

Abcam, Cambridge, MA, USA) at 4°C overnight. The next day, after incubation with fluorescent antibody (fluorescein isothiocyanate- [FITC-] labeled goat anti-rabbit IgG, diluted 1:50, Aspen, Wuhan, China) at 4°C for 30 min, the cells were stained with 4-6-diamidino-2-phenylindole (DAPI) for 5 min. Finally, the samples were observed under a confocal microscope (LSM 710; Zeiss, Oberkochen, Germany).

**2.4. Cell Binding Assay.** The binding affinity of <sup>99m</sup>Tc-HYNIC-VCAM-1<sub>scFv</sub> to B16F10, HT-1080, SKOV3.ip, A375m, MDA-MB-231, and 786-O cells was measured by a cell uptake assay. Briefly, the experiment was carried out in 24-well plates (2 × 10<sup>5</sup> cells/well) and then incubated with 0.5 mL serum-free DMEM, PRMI-1640, or MEM containing <sup>99m</sup>Tc-HYNIC-VCAM-1<sub>scFv</sub> (2 nM) at 37°C for 1, 2, or 4 h, respectively. Thereafter, the cells were rinsed twice with 1 mL PBS and lysed with 1 N NaOH. The radioactivity in the cell lysate was counted using an automatic well-type gamma counter (PerkinElmer WIZARD2 2470, Shelton, CT, USA). For a blocking study, B16F10 cells were incubated with <sup>99m</sup>Tc-HYNIC-VCAM-1<sub>scFv</sub> (2 nM) at 37°C for 4 h in the presence of no other VCAM-1<sub>scFv</sub>, 100 nM unlabeled VCAM-1<sub>scFv</sub>, or 100 nM unlabeled HYNIC-VCAM-1<sub>scFv</sub>, and the radioactivity of the cell suspensions was measured.

**2.5. Preparation of Tumor Models.** All animal studies were performed in accordance with a protocol approved by the Institutional Animal Care and Use Committee (IACUC) of Tongji Medical College, Huazhong University of Science and Technology. Female BALB/c nude mice (3-4 weeks, Beijing HFK Bioscience Company, Beijing, China) were injected subcutaneously in the left shoulder with 5 × 10<sup>6</sup> B16F10, HT-1080, A375m, MDA-MB-231, SKOV3.ip, or 786-O cells (*n* = 5 per group), suspended in 150 μL PBS. The mice were used as models for *in vivo* SPECT planar imaging and biodistribution studies when the xenograft masses reached a size of 5 to 10 mm.

**2.6. SPECT Planar Imaging.** Imaging studies were performed in the tumor-bearing mice using SPECT (Symbia T6, Siemens, Erlangen, Germany) with a 3.0 mm pinhole collimator. Briefly, under isoflurane anesthesia, after intravenous injection of <sup>99m</sup>Tc-HYNIC-VCAM-1<sub>scFv</sub> (7.4–11.1 MBq), images were acquired at 1, 2, and 4 h postinjection. For the blocking study, B16F10 tumor-bearing mice were given a 50-fold excess dose of unlabeled VCAM-1<sub>scFv</sub> 1 h prior to the injection of <sup>99m</sup>Tc-HYNIC-VCAM-1<sub>scFv</sub>. The acquisition time was 10 min for each mouse.

**2.7. Biodistribution Study.** For biodistribution studies, five B16F10 tumor-bearing mice were injected with <sup>99m</sup>Tc-HYNIC-VCAM-1<sub>scFv</sub> (1.85 MBq) via tail vein and sacrificed at 1, 2, and 4 h postinjection. For the blocking study, B16F10 tumor-bearing mice (*n* = 5) were sacrificed at 1 h after the injection. The biological tissues of interest (i.e., blood, brain, myocardium, liver, spleen, lung, kidney, stomach, intestine, muscle, bone, and tumor) were removed, washed, and weighed, and their radioactivity was measured with decay

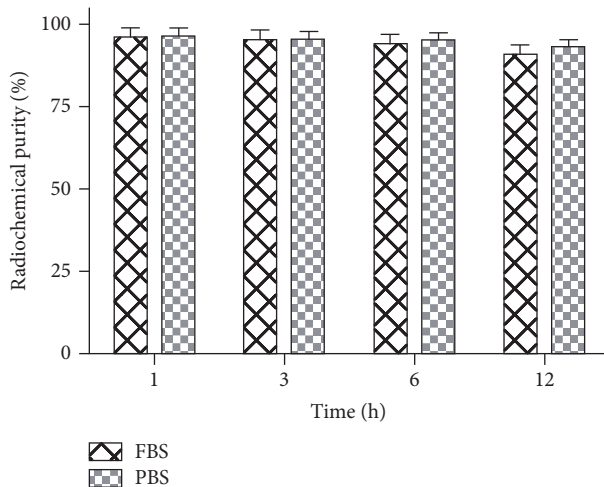


FIGURE 1: Stability of <sup>99m</sup>Tc-HYNIC-VCAM-1<sub>scFv</sub> in FBS and PBS at different time points. All data are expressed as the means  $\pm$  SD ( $n = 5$ ). FBS = fetal bovine serum. PBS = phosphate-buffered saline.

correction using an automatic well-type gamma counter. The uptake in the tissues was expressed as a percentage of the injected dose per gram of tissue (% ID/g). Five groups of five mice, each group grafted with one of the five other tumors, were sacrificed 4 h postinjection of <sup>99m</sup>Tc-HYNIC-VCAM-1<sub>scFv</sub> (1.85 MBq), and the % ID/g was calculated as described above. Portions of the tumors, livers, and kidneys in the 4 h biodistribution groups were removed to check the expression of VCAM-1 with immunofluorescence staining. The results were analyzed using ImageJ software (version 1.46r, Wayne Rasband, National Institutes of Health, Bethesda, MD, USA).

**2.8. Statistical Analysis.** Statistical Package for the Social Sciences (SPSS) software (version 13.0, SPSS Inc., Chicago, IL, USA) and GraphPad Prism (version 5.0, San Diego, CA, USA) were applied in statistical analysis. All data are presented as the mean  $\pm$  standard deviation (SD). Means were compared using Student's *t*-test with  $P < 0.05$  being statistically significant.

### 3. Results

**3.1. Radiolabeling Yield, Radiochemistry, and Stability.** <sup>99m</sup>Tc-HYNIC-VCAM-1<sub>scFv</sub> had a high radiolabeling yield of  $81.5 \pm 3.6\%$  and a specific activity of  $16.2 \pm 1.1$  MBq/nmol ( $n = 5$ ). After purification, the radiochemical purity of <sup>99m</sup>Tc-HYNIC-VCAM-1<sub>scFv</sub> reached  $96.5 \pm 1.7\%$  and was  $>90\%$  at 1, 3, 6, and 12 h in FBS and PBS (Figure 1), indicating good stability *in vitro*.

**3.2. VCAM-1 Expression In Vitro.** The relative VCAM-1 expression levels in the cancer cell lines evaluated by immunofluorescence are shown in Figure 2. The results demonstrated strong intensities in B16F10 and HT1080 cells, a moderate intensity in SKOV3.ip cells, and low intensities in A375m,

MDA-MB-231, and 786-O cells, which correlated with the VCAM-1 expression levels of these cells.

**3.3. Cell Binding Assay.** As shown in Figure 3(a), the uptake of <sup>99m</sup>Tc-HYNIC-VCAM-1<sub>scFv</sub> by B16F10 and HT1080 cells ( $2 \times 10^5$ ) increased with time and reached a plateau ( $6.07 \pm 0.55\%$ ,  $5.73 \pm 0.41\%$ ) at 4 h. The accumulation of radioactivity in SKOV3.ip cells ( $3.40 \pm 0.26\%$ , 4 h) had a moderate increase and the binding of <sup>99m</sup>Tc-HYNIC-VCAM-1<sub>scFv</sub> to A375m, MDA-MB-231, and 786-O cells remained relatively stable over time ( $2.47 \pm 0.09\%$ ,  $2.67 \pm 0.13\%$ , and  $2.53 \pm 0.18\%$ , 4 h). These data reveal that <sup>99m</sup>Tc-HYNIC-VCAM-1<sub>scFv</sub> binds strongly to B16F10 and HT1080 cells, moderately to SKOV3.ip cells, and weakly to A375m, MDA-MB-231, and 786-O cells. The blocking study (Figure 3(b)) showed that the uptake of <sup>99m</sup>Tc-HYNIC-VCAM-1<sub>scFv</sub> in the presence of 100 nM unlabeled HYNIC-VCAM-1<sub>scFv</sub> or 100 nM unlabeled VCAM-1<sub>scFv</sub> in B16F10 cells was much lower than their corresponding nonblocked groups at 4 h ( $6.07 \pm 0.55\%$ ,  $2.67 \pm 0.12\%$ , and  $2.77 \pm 0.15\%$ ,  $P < 0.01$ ). The blocking study demonstrates the specificity of <sup>99m</sup>Tc-HYNIC-VCAM-1<sub>scFv</sub> for VCAM-1-positive cells.

**3.4. SPECT Planar Imaging.** B16F10 and HT1080 tumor images were clearly visualized, with high tumor-to-background contrast at all scan time points ( $3.20 \pm 0.63$ ,  $3.90 \pm 0.85$ , and  $3.21 \pm 1.05$  for B16F10;  $3.39 \pm 0.65$ ,  $3.28 \pm 0.84$ , and  $3.13 \pm 0.63$  for HT1080, Figures 4(a) and 4(b)). We chose contralateral limb of the tumor as background value. Weaker uptake was observed by SKOV3.ip tumor ( $2.75 \pm 0.57$ , 1h, Figure 4(c)), and the probe uptakes in A375m, MDA-MB-231, and 786-O tumors (Figures 4(d), 4(e), and 4(f)) were indistinguishable from background ( $1.85 \pm 0.32$ ,  $1.84 \pm 0.75$ , and  $1.77 \pm 0.47$ , 1h). As shown in Figure 5, the accumulation of radioactivity in B16F10 tumors clearly decreased in the presence of excess unlabeled VCAM-1. These results indicate that <sup>99m</sup>Tc-HYNIC-VCAM-1<sub>scFv</sub> can specifically target VCAM-1-positive tumors. In addition, the images of the kidneys and the livers were visualized clearly, which confirmed that *in vivo* clearance of the probe is mainly through the renal and hepatic routes.

**3.5. Biodistribution Study.** We also assessed tumor targeting and nontumor tissue distribution of <sup>99m</sup>Tc-HYNIC-VCAM-1<sub>scFv</sub> in the six tumor models (Figure 6). In B16F10 tumor models (Figure 6(a)), highest accumulation was noted in the kidneys at all time points, and the radioactivities in kidneys decreased steadily. The results indicated urinary system was the main pathway of <sup>99m</sup>Tc-HYNIC-VCAM-1<sub>scFv</sub> excretion. The B16F10 tumor uptakes were  $5.51 \pm 0.37\%$  ID/g,  $5.04 \pm 0.61\%$  ID/g, and  $4.93 \pm 0.52\%$  ID/g at 1, 2, and 4 h postinjection, respectively, and tumor-to-blood (T/B) and tumor-to-muscle (T/M) ratios increased over time from  $1.25 \pm 0.08$  and  $6.68 \pm 0.79$  at 1 h postinjection to  $1.88 \pm 0.17$  and  $8.47 \pm 1.05$  at 4 h postinjection in B16F10 xenograft mice (Figure 6(c)), which bodes well for the application of <sup>99m</sup>Tc-HYNIC-VCAM-1<sub>scFv</sub> as an *in vivo* molecular imaging agent.

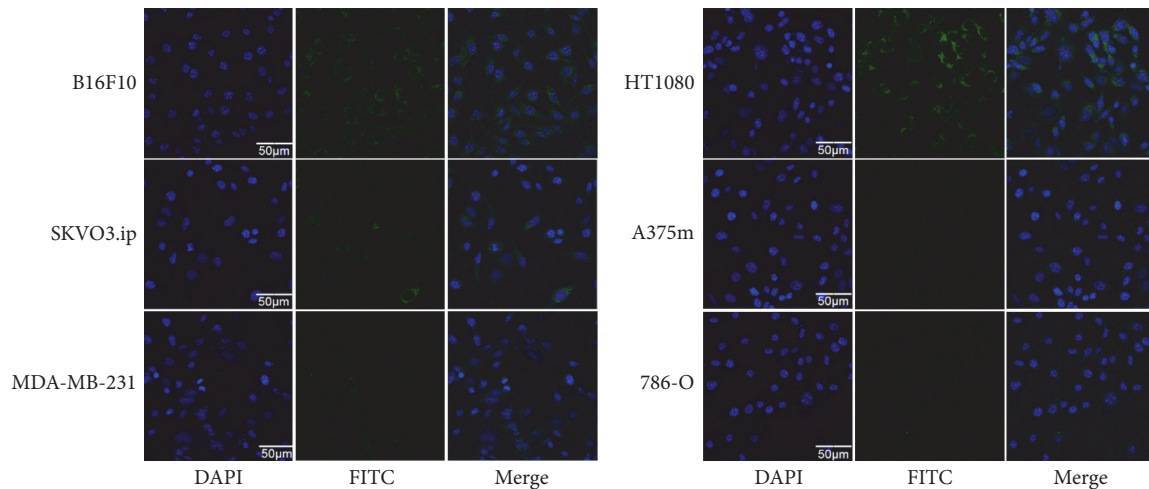


FIGURE 2: Immunofluorescence staining of six cancer cell lines. The cells were incubated with VCAM-1 antibody (green) and nuclei were stained with 4',6-diamidino-2-phenylindole (DAPI). Representative images are displayed at the same scale ( $\times 600$ ) ( $n = 5$ ). DAPI = 4',6-diamidino-2-phenylindole. FITC = fluorescein isothiocyanate.

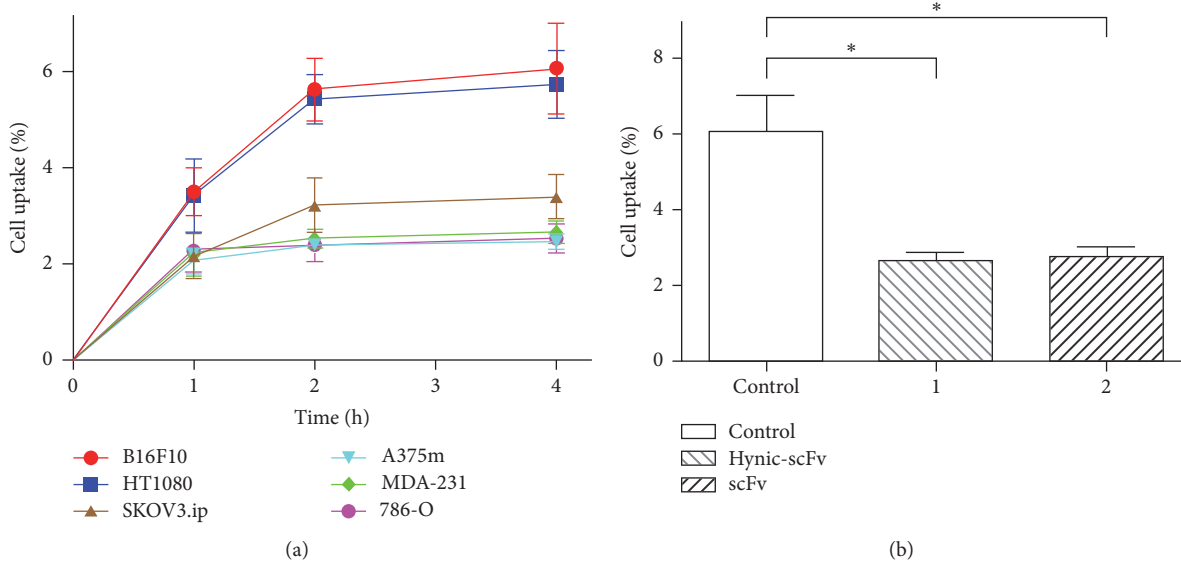


FIGURE 3: Cell uptake and blocking studies of  $^{99m}\text{Tc}$ -HYNIC-VCAM-1<sub>scFv</sub> *in vitro*. The  $^{99m}\text{Tc}$ -HYNIC-VCAM-1<sub>scFv</sub> (2 nM) cell uptake studies (a) were performed on a series of cancer cell lines at serial time points. The comparisons of  $^{99m}\text{Tc}$ -HYNIC-VCAM-1<sub>scFv</sub> uptake in the blocking experiments (b) with no other VCAM-1<sub>scFv</sub>, excess unlabeled VCAM-1<sub>scFv</sub>, and HYNIC-VCAM-1<sub>scFv</sub>. \*  $P < 0.01$ . All data are expressed as mean  $\pm$  SD in triplicate.

As expected, the tumor concentration of  $^{99m}\text{Tc}$ -HYNIC-VCAM-1<sub>scFv</sub> in the blocked mice was significantly lower than that in the unblocked mice ( $2.92 \pm 0.26\%$  ID/g versus  $5.51 \pm 0.37\%$  ID/g,  $P < 0.001$ , Figure 6(b)) at 1 h, while the uptake in nontumor tissues was not significantly reduced by the blocking dose, suggesting that nontumor tissues did not express significant VCAM-1 and took up the tracer nonspecifically. The uptakes of  $^{99m}\text{Tc}$ -HYNIC-VCAM-1<sub>scFv</sub> in HT-1080, SKOV3.ip, A375m, MDA-MB-231, and 786-O tumor models were  $4.65 \pm 0.39\%$  ID/g,  $2.99 \pm 0.44\%$  ID/g,  $1.33 \pm 0.22\%$  ID/g,  $1.49 \pm 0.23\%$  ID/g, and  $1.47 \pm 0.31\%$  ID/g at

4 h postinjection (Figures 6(d) and 6(e)), respectively, which were in agreement with *in vivo* images. The ratios of T/B and T/M (Figures 6(f) and 6(g)) were also similar.

As shown in Figure 7, immunofluorescence staining of the kidneys and liver showed relatively low signals, indicating that these tissues did not express VCAM-1 significantly, again showing that high uptake in the kidneys and liver was unrelated to specific binding to VCAM-1 in these organs and largely attributed to the clearance of the probe. The immunofluorescence intensities of the tumor tissues (Figure 7), which were extracted from different tumor-bearing mice of the 4 h

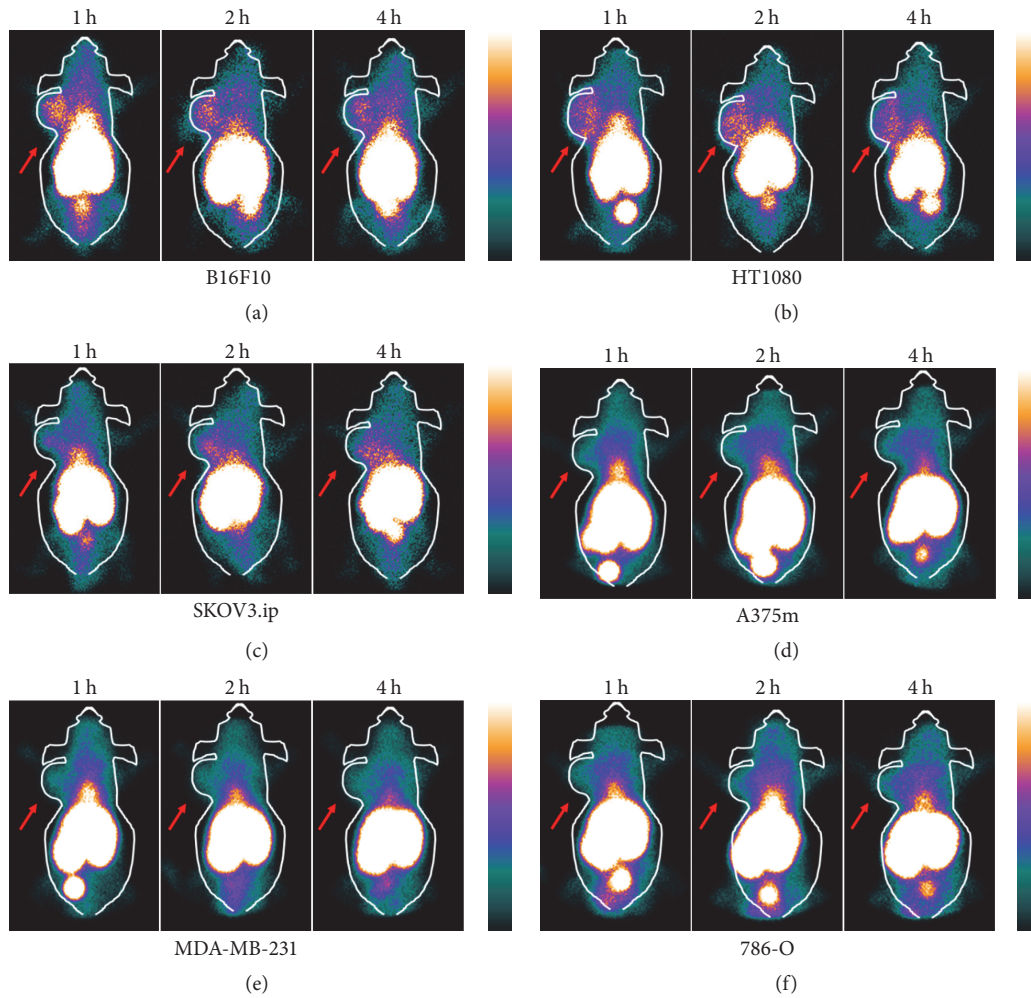


FIGURE 4: Representative SPECT planar imaging of  $^{99m}\text{Tc}$ -HYNIC-VCAM-1- $\text{scFv}$  in six tumor models ( $n = 5$  per group) obtained at 1, 2, and 4 h, respectively. Arrows refer to tumors.

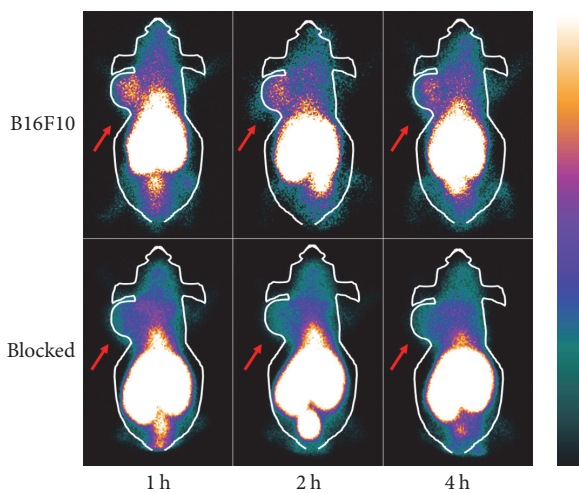


FIGURE 5: SPECT planar imaging of B16F10 tumor-bearing mice at the indicated time points after  $^{99m}\text{Tc}$ -HYNIC-VCAM-1- $\text{scFv}$  injection, with/without preinjection of excess unlabeled VCAM-1- $\text{scFv}$ . Arrows indicate tumors.

biodistribution groups, further validated the different VCAM-1 expression levels of six tumor models.  $^{99m}\text{Tc}$ -HYNIC-VCAM-1- $\text{scFv}$  accumulation in the tumors significantly correlated well with average integral optical density of VCAM-1 expression (Figure 8,  $R^2 = 0.875$ ,  $P < 0.0001$ ), which suggested the possibility of semiquantitative evaluation for VCAM-1 noninvasively *in vivo*.

#### 4. Discussion

Recently, strategies for targeting VCAM-1 [5–8], such as  $^{18}\text{F}$  labeled nanobodies and  $^{111}\text{In}$  labeled peptides, have been investigated. VCAM-1 expressed in atherosclerosis has been the main target of research. For the availability and low costs,  $^{99m}\text{Tc}$  is an ideal radionuclide for radiopharmaceutical synthesis and has been used more widely than  $^{18}\text{F}$  and  $^{111}\text{In}$  in clinical applications. Therefore, we used  $^{99m}\text{Tc}$ -HYNIC-VCAM-1- $\text{scFv}$  to target VCAM-1 in various tumors to assess the binding affinity and characteristics of VCAM-1- $\text{scFv}$ .

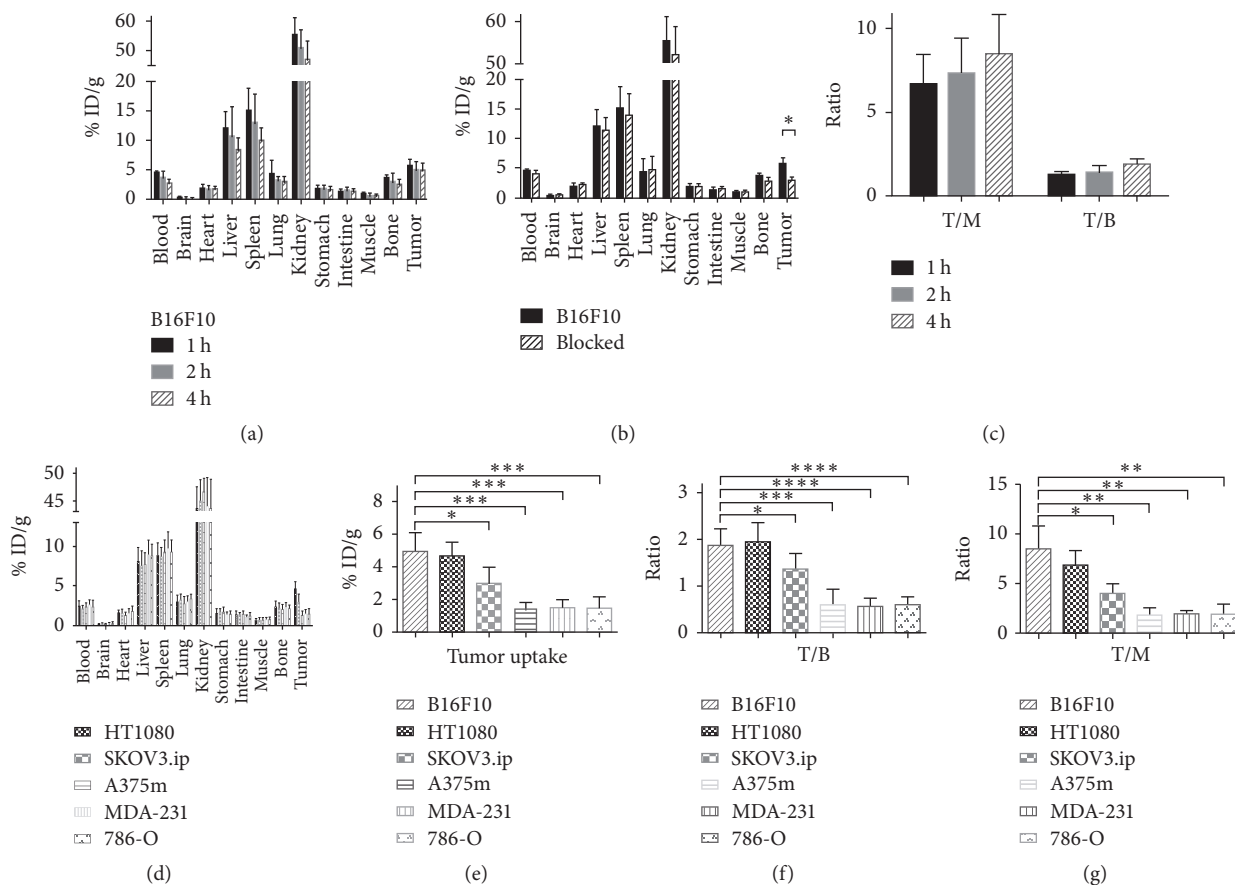


FIGURE 6: Tissue biodistribution of  $^{99m}\text{Tc}$ -HYNIC-VCAM-1-scFv in tumor xenografts. Biodistribution of  $^{99m}\text{Tc}$ -HYNIC-VCAM-1-scFv was assessed in mice bearing B16F10 tumors at 1, 2, and 4 h postinjection ((a),  $n = 5$ ). The blocking study with excess VCAM-1-scFv was performed at 1 h after  $^{99m}\text{Tc}$ -HYNIC-VCAM-1-scFv injection in B16F10 tumor-bearing mice (b). Tumor-to-blood (T/B) and tumor-to-muscle (T/M) ratios in mice bearing B16F10 tumors at the indicated time points (c). Biodistribution was similarly examined in five tumor models at 4 h postinjection (d). The comparison of tumor uptake (e), T/B (f), and T/M (g) in the different tumors. \*  $P < 0.05$ , \*\*  $P < 0.01$ , \*\*\*  $P < 0.001$ , and \*\*\*\*  $P < 0.0001$ .

$^{99m}\text{Tc}$  has a half-life of 6 h, which is well matched with the relatively short physiological blood half-life of VCAM-1-scFv, making the probe's clinical translation feasible in future [15]. In addition, HYNIC-NHS, as a bifunctional chelating agent, participates in the radiolabeling of  $^{99m}\text{Tc}$  with peptides or antibodies, which is easily prepared, with a high radiolabeling yield, radiochemical purity, and stability [16, 17]. As an alternative to PET, we sought to evaluate the feasibility of a  $^{99m}\text{Tc}$ -HYNIC-VCAM-1-scFv as a SPECT tracer to target VCAM-1, which is much cheaper and more easily available. In the uptake studies, six cell lines with different VCAM-1 expression levels confirmed by immunofluorescence staining showed corresponding binding affinities of the radiolabeled VCAM-1-scFv. The uptake value in B16F10 cells (VCAM-1 positive) was effectively blocked by an excess of unlabeled VCAM-1-scFv, further verifying the specificity of  $^{99m}\text{Tc}$ -HYNIC-VCAM-1-scFv to VCAM-1 *in vitro*.

The uptake pattern and blocking studies in the different cell lines closely correlated with the SPECT planar imaging and biodistribution study of xenograft models. In the imaging of B16F10 and HT1080 xenograft mice, tumors were visualized clearly from normal tissues as early as 1 h after

injection of  $^{99m}\text{Tc}$ -HYNIC-VCAM-1-scFv. Based on the high tissue penetrability of small antibody fragments, the probe can reach the tumor site more quickly [18]. It is significantly different from tumor imaging with intact monoclonal antibodies, mainly due to slow clearance of the larger tracers from the blood pool [19]. Moderate uptake was seen in SKOV3.ip tumors, measuring  $2.99 \pm 0.44\%$  ID/g at 4 h. In contrast with VCAM-1- $^{111}\text{In}$  peptide distribution in omentum of SKOV3ip1 cells (about 2% ID/g),  $^{99m}\text{Tc}$ -HYNIC-VCAM-1-scFv has a relatively higher binding affinity with SKOV3.ip tumors [8]. No obvious tracer uptake could be seen in the imaging of A375m, MDA-MB-231, and 786-O tumor models, which are consistent with the lack of VCAM-1 expression in these tumor tissues and also confirmed by immunofluorescence staining of the tissues. High T/M ratios in B16F10 and HT1080 xenografts ( $8.47 \pm 1.05$  and  $6.89 \pm 0.64$ ) were observed at 4 h postinjection, showing ideal contrast for imaging of these tumors. These results suggest the targeting ability and specificity of the probe *in vivo*.

As the main excretory organs, the kidneys showed the highest accumulation in the biodistribution study, which is in agreement with Broisat et al. [20]. This is due to the small

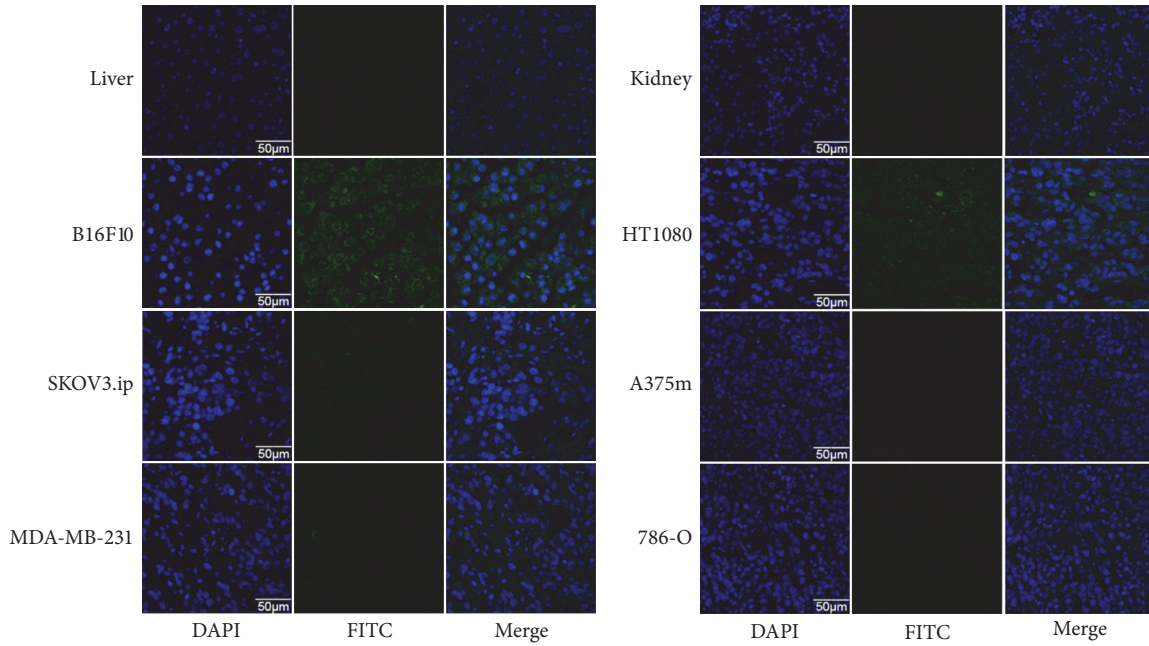


FIGURE 7: Immunofluorescence staining of kidneys, livers, and various tumors. The tissues were incubated with VCAM-1 antibody (green), followed by staining with DAPI. Representative images are displayed at the same scale ( $\times 600$ ,  $n = 5$ ).

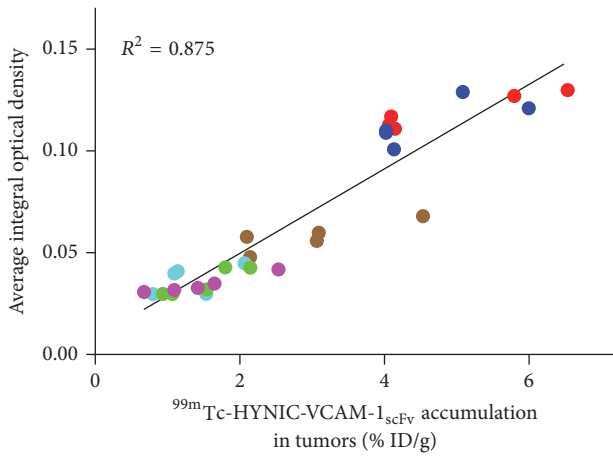


FIGURE 8: Relationship between the tumor uptake and mean integral optical density of VCAM-1 expression ( $n = 5$  per group).

molecular weight ( $\sim 28$  kDa) of scFv, which is below the cut-off for renal clearance. Immunofluorescence staining showed liver and kidneys do not express significant VCAM-1, demonstrating that the accumulations in the kidneys and livers is mainly related to the excretion mode. The immunofluorescence intensity of VCAM-1 has a relationship with the radioactivity accumulated in tumors, which indicates the feasibility of achieving semiquantitative evaluation of VCAM-1 expression *in vivo*.

There are various methods to detect protein expression using molecular biological techniques [21], such as immunohistochemistry, immunofluorescence, western blotting, and ELISA. Among them, ELISA is mainly applied for the

detection of secretory proteins [22]. Although the specificity of western blotting is high, the procedure is complex. This research focuses on the study of immunofluorescence and radioimmunoassay, which are both based on the antigen-antibody reaction. VCAM-1 expression detected by  $^{99m}\text{Tc}$ -HYNIC-VCAM-1<sub>scFv</sub> relies on the binding of the radioactive antibody fragment (VCAM-1<sub>scFv</sub>) with the antigen. After the binding, the radioactivity uptake is measured to quantitate the antigen expression [23]. This technique is easy to perform with high sensitivity. Immunofluorescence, which makes use of labeling antibodies with fluorescent substances, has gained more and more attention due to its high sensitivity and superiority of obtaining anatomic and physiological information. However, it needs to get specimen which is invasive and hard to repeat in the living body, and it also has some shortcomings, such as inadequate penetration depth [24]. In contrast, PET and SPECT imaging with the ability to image the living human body deeply, are more advantageous in clinical applications. The results of immunofluorescence in our study are consistent with radioimmunoassay, indicating that  $^{99m}\text{Tc}$ -HYNIC-VCAM-1<sub>scFv</sub> has the potential to be used to detect VCAM-1 noninvasively and repeatedly *in vitro* and *in vivo*.

There are several issues that need to be pointed out in this study. First, high activity in blood was also observed, which renders T/B ratios ( $1.25 \pm 0.08$ ) not ideal in VCAM-1 positive tumor models at 1 h. Fortunately, the accumulation in blood decreased rapidly (from  $4.54 \pm 0.13\%$  ID/g at 1 h to  $2.67 \pm 0.32\%$  ID/g at 4 h) and the T/B value increased steadily. Second, although lower accumulation was seen in liver than that with intact monoclonal antibodies [25], the liver retained high amounts of activity after  $^{99m}\text{Tc}$ -HYNIC-VCAM-1<sub>scFv</sub> administration. This will interfere with imaging of lesions in

the liver and surrounding tissues. Further studies will focus on modifying and optimizing the probe to minimize its blood and liver accumulation.

## 5. Conclusion

We successfully labeled an scFv-based probe,  $^{99m}\text{Tc}$ -HYNIC-VCAM-1<sub>scFv</sub>, that specifically binds to VCAM-1. We identified different expression levels of VCAM-1 with SPECT planar imaging of corresponding tumor lesions, which potentially provides a qualitative and semiquantitative method for non-invasive evaluation of VCAM-1 expression *in vivo*.

## Conflicts of Interest

The authors declare no potential conflicts of interest.

## Acknowledgments

This work was supported by the National Natural Science Foundation of China (nos. 81630049 and 81771863).

## References

- [1] E. Andreopoulou and M. Cristofanilli, "Circulating tumor cells as prognostic marker in metastatic breast cancer," *Expert Review of Anticancer Therapy*, vol. 10, no. 2, pp. 171–177, 2010.
- [2] F. Tas, S. Karabulut, M. Serilmez, R. Ciftci, and D. Duranyildiz, "Clinical significance of serum epithelial cell adhesion molecule (EPCAM) and vascular cell adhesion molecule-1 (VCAM-1) levels in patients with epithelial ovarian cancer," *Tumor Biology*, vol. 35, no. 4, pp. 3095–3102, 2014.
- [3] M. Schlesinger and G. Bendas, "Vascular cell adhesion molecule-1 (VCAM-1) - An increasing insight into its role in tumorigenicity and metastasis," *International Journal of Cancer*, vol. 136, no. 11, pp. 2504–2514, 2015.
- [4] Q. Chen and J. Massagué, "Molecular pathways: VCAM-1 as a potential therapeutic target in metastasis," *Clinical Cancer Research*, vol. 18, no. 20, pp. 5520–5525, 2012.
- [5] B. A. Kaufmann, C. L. Carr, J. T. Belcik et al., "Molecular imaging of the initial inflammatory response in atherosclerosis: Implications for early detection of disease," *Arteriosclerosis, Thrombosis, and Vascular Biology*, vol. 30, no. 1, pp. 54–59, 2010.
- [6] C. Liu, X. Zhang, Y. Song et al., "SPECT and fluorescence imaging of vulnerable atherosclerotic plaque with a vascular cell adhesion molecule 1 single-chain antibody fragment," *Atherosclerosis*, vol. 254, pp. 263–270, 2016.
- [7] G. Bala, A. Blykers, C. Xavier et al., "Targeting of vascular cell adhesion molecule-1 by 18F-labelled nanobodies for PET/CT imaging of inflamed atherosclerotic plaques," *European Heart Journal—Cardiovascular Imaging*, vol. 17, no. 9, pp. 1001–1008, 2016.
- [8] J. M. Scalici, S. Thomas, C. Harrer et al., "Imaging VCAM-1 as an indicator of treatment efficacy in metastatic ovarian cancer," *Journal of Nuclear Medicine*, vol. 54, no. 11, pp. 1883–1889, 2013.
- [9] Y. Liu, X. Jin, X. Lan, J. Lang, Q. Wen, and R. An, "SPECT imaging of colorectal cancer by targeting CD133 receptor with  $^{99m}\text{Tc}$ -labeled monoclonal antibody," *The Quarterly Journal of Nuclear Medicine and Molecular Imaging*, 2016.
- [10] C. Li, H. Feng, X. Xia et al., " $^{99m}\text{Tc}$ -labeled tetramer and pentamer of single-domain antibody for targeting epidermal growth factor receptor in xenografted tumors," *Journal of Labelled Compounds and Radiopharmaceuticals*, vol. 59, no. 8, pp. 305–312, 2016.
- [11] C. Li, Y. Zhang, L. Wang et al., "A novel multivalent  $^{99m}\text{Tc}$ -labeled EG2-C4bp $\alpha$  antibody for targeting the epidermal growth factor receptor in tumor xenografts," *Nuclear Medicine and Biology*, vol. 42, no. 6, pp. 547–554, 2015.
- [12] C. M. Hammers and J. R. Stanley, "Antibody phage display: technique and applications," *Journal of Investigative Dermatology*, vol. 134, no. 2, p. e17, 2014.
- [13] A. K. Iyer, X. Lan, X. Zhu et al., "Novel human single chain antibody fragments that are rapidly internalizing effectively target epithelioid and sarcomatoid mesotheliomas," *Cancer Research*, vol. 71, no. 7, pp. 2428–2432, 2011.
- [14] S. K. Sharma, M. Wuest, J. D. Way, V. R. Bouvet, M. Wang, and F. R. Wuest, "Synthesis and pre-clinical evaluation of an (18)F-labeled single-chain antibody fragment for PET imaging of epithelial ovarian cancer," *American Journal of Nuclear Medicine and Molecular Imaging*, vol. 6, no. 3, pp. 185–198, 2016.
- [15] F. Li, T. Cheng, Q. Dong et al., "Evaluation of  $^{99m}\text{Tc}$ -HYNIC-TMTP1 as a tumor-homing imaging agent targeting metastasis with SPECT," *Nuclear Medicine and Biology*, vol. 42, no. 3, pp. 256–262, 2015.
- [16] L. K. Meszaros, A. Dose, S. C. G. Biagini, and P. J. Blower, "Synthesis and evaluation of analogues of HYNIC as bifunctional chelators for technetium," *Dalton Transactions*, vol. 40, no. 23, pp. 6260–6267, 2011.
- [17] J. D. G. Correia, A. Paulo, P. D. Raposinho, and I. Santos, "Radiometallated peptides for molecular imaging and targeted therapy," *Dalton Transactions*, vol. 40, no. 23, pp. 6144–6167, 2011.
- [18] P. P. Monnier, R. J. Vigouroux, and N. G. Tassew, "In vivo applications of single chain Fv (variable domain) (scFv) fragments," *Antibodies*, vol. 2, no. 2, pp. 193–208, 2013.
- [19] J. Lang, X. Lan, Y. Liu et al., "Targeting cancer stem cells with an  $^{131}\text{I}$ -labeled anti-AC133 monoclonal antibody in human colorectal cancer xenografts," *Nuclear Medicine and Biology*, vol. 42, no. 5, pp. 505–512, 2015.
- [20] A. Broisat, J. Toczec, L. S. Dumas et al., " $^{99m}\text{Tc}$ -cAbVCAM1-5 imaging is a sensitive and reproducible tool for the detection of inflamed atherosclerotic lesions in mice," *Journal of Nuclear Medicine*, vol. 55, no. 10, pp. 1678–1684, 2014.
- [21] X. Ying and T. M. Monticello, "Modern Imaging Technologies in Toxicologic Pathology: An Overview," *Toxicologic Pathology*, vol. 34, no. 7, pp. 815–826, 2006.
- [22] L. E. Ott and S. Carson, "Immunological tools: Engaging students in the use and analysis of flow cytometry and enzyme-linked immunosorbent assay (ELISA)," *Biochemistry and Molecular Biology Education*, vol. 42, no. 5, pp. 382–397, 2014.
- [23] V. A. Lennon, S. Whittingham, P. R. Carnegie, T. A. McPherson, and I. R. Mackay, "Detection of antibodies to the basic protein of human myelin by radioimmunoassay and immunofluorescence," *The Journal of Immunology*, vol. 107, no. 1, pp. 56–62, 1971.
- [24] G. Hong, J. T. Robinson, Y. Zhang et al., "In Vivo Fluorescence Imaging with Ag," *Angewandte Chemie*, vol. 124, no. 39, pp. 9956–9959, 2012.
- [25] Z. Liu, T. Ma, H. Liu et al., " $^{177}\text{Lu}$ -labeled antibodies for EGFR-targeted SPECT/CT imaging and radioimmunotherapy in a preclinical head and neck carcinoma model," *Molecular Pharmaceutics*, vol. 11, no. 3, pp. 800–807, 2014.

## Research Article

# Thallium Labeled Citrate-Coated Prussian Blue Nanoparticles as Potential Imaging Agent

Krisztián Szigeti <sup>1</sup>, Nikolett Hegedűs <sup>1</sup>, Kitti Rácz, <sup>1</sup> Ildikó Horváth, <sup>1</sup> Dániel S. Veres, <sup>1</sup> Dávid Szöllősi, <sup>1</sup> Ildikó Futó, <sup>1</sup> Károly Módos, <sup>1</sup> Tamás Bozó, <sup>1</sup> Kinga Karlinger, <sup>2</sup> Noémi Kovács, <sup>3</sup> Zoltán Varga <sup>1,4</sup>, Magor Babos, <sup>5</sup> Ferenc Budán, <sup>3,6</sup> Parasuraman Padmanabhan <sup>7</sup>, Balázs Gulyás, <sup>7,8</sup> and Domokos Máthé <sup>1,3</sup>

<sup>1</sup>Department of Biophysics and Radiation Biology, Semmelweis University, Budapest 1094, Hungary

<sup>2</sup>Department of Radiology and Oncotherapy, Semmelweis University, Budapest 1094, Hungary

<sup>3</sup>CROmed Translational Research Centers, Budapest 1047, Hungary

<sup>4</sup>Institute of Materials and Environmental Chemistry, Research Center for Natural Sciences of the Hungarian Academy of Sciences, Budapest, Hungary

<sup>5</sup>Mediso Medical Imaging Systems Ltd., Budapest 1022, Hungary

<sup>6</sup>Department of Public Health Medicine, Medical School, University of Pécs, Pécs 7624, Hungary

<sup>7</sup>Lee Kong Chian School of Medicine, Nanyang Technological University, Singapore

<sup>8</sup>Imperial College London, Kensington, London, UK

Correspondence should be addressed to Krisztián Szigeti; [szigeti.krisztian@med.semmelweis-univ.hu](mailto:szigeti.krisztian@med.semmelweis-univ.hu)

Received 23 November 2017; Accepted 15 March 2018; Published 26 April 2018

Academic Editor: Daniela Haeusler

Copyright © 2018 Krisztián Szigeti et al. This is an open access article distributed under the Creative Commons Attribution License, which permits unrestricted use, distribution, and reproduction in any medium, provided the original work is properly cited.

**Background.** The aim of this study was to develop and characterize a nanoparticle-based image-contrast platform which is biocompatible, chemically stable, and accessible for radiolabeling with <sup>201</sup>Tl. We explored whether this nanoparticle enhanced the T1 signal which might make it an MRI contrast agent as well. **Methods.** The physical properties of citrate-coated Prussian blue nanoparticles (PBNPs) (iron(II);iron(III);octadecacyanide) doped with <sup>201</sup>Tl isotope were characterized with atomic force microscopy, dynamic light scattering, and zeta potential measurement. PBNP biodistribution was determined by using SPECT and MRI following intravenous administration into C57BL6 mice. Activity concentrations (MBq/cm<sup>3</sup>) were calculated from the SPECT scans for each dedicated volume of interest (VOI) of liver, kidneys, salivary glands, heart, lungs, and brain. **Results.** PBNP accumulation peaked at 2 hours after injection predominantly in the kidneys and the liver followed by a gradual decrease in activity in later time points. **Conclusion.** We synthesized, characterized, and radiolabeled a Prussian blue-based nanoparticle platform for contrast material applications. Its in vivo radiochemical stability and biodistribution open up the way for further diagnostic applications.

## 1. Introduction

Two or more imaging techniques applied simultaneously or within a very close timeframe ideally complement each others. Powerful new high-resolution imaging tools such as optical whole body imaging, micro-X-ray-based computed tomography (CT), and magnetic resonance imaging (MRI)

could thus nowadays enable very good anatomical detail fusion to functional image data of living organisms and disease. These functional data have been obtained for decades in nuclear medicine using positron emission tomography (PET) and single photon emission computed tomography (SPECT). PET and SPECT possess unparalleled sensitivity and functionality but their resolution can be enhanced much

further by hybrid imaging. This provides the ability of acquiring (almost) simultaneous *in vivo* images of highly resolved anatomy and accurately measured physiology in a noninvasive manner in animal models, clinical research, or diagnostics. This approach enables the explicit localization as well as the quantification of metabolic activity in target tissues [1, 2]. Nanoparticles embody unique imaging possibilities. A high signal concentration for well-amplified biologic readouts can be combined by their use for both anatomy and (patho)physiology. With the availability of novel multimodal imaging devices, the demand for innovative multimodal contrast materials is higher than ever before [1, 3]. The greatest concern of *in vivo* functional imaging with isotopes is whether the isotope's binding to the nanoparticle is stable enough in the living organism. Magnetic resonance imaging (MRI) is an ideal modality to elucidate morphological qualities in living organisms. In the past two decades, research of MRI contrast agents such as nanoparticles (NP) with paramagnetic properties started to burgeon. These particles were mostly paramagnetic iron oxides such as magnetite ( $\text{Fe}_3\text{O}_4$ ), maghemite ( $\gamma\text{Fe}_2\text{O}_3$ ), and other ferrites. The contrast property of these materials (hypointense signal in T2-weighted images) is not optimal for anatomical mapping [4, 5], where, in turn, an enhancement (positive) in MRI signal is expected from contrast materials. To overcome these difficulties, the development of a proper T1 enhancing iron-containing particulate contrast agent seemed to be a good solution.

Our aim was to create a biocompatible Prussian blue nanoparticle (PBNP) (iron(II);iron(III);octadecacyanide) platform for preclinical imaging which has three important qualities: first, the long-term stability of the NP platform (surface characteristics, i.e., coating to avoid phagocytosis and aggregation, the stability of the NP component's diameter, and homogeneity and colloidal stability); second, T1 signal enhancement suitable for MR imaging; and third, the stability of the bond between the radionuclide and nanoparticle structure in most environments.

Thanks to the special structure of PBNP (Figure 1), it is capable of very stably binding thallium cations and thereby acts as an appropriate SPECT radiotracer [6, 7].

The exact binding mechanism has not been published until this time. In general chemical ion-exchange, physical adsorption (Prussian blue crystals are dubbed "chemical sponges" to absorb metal ions [4, 8]), and ion trapping may all be involved in the PBNP-thallium binding process depending on the pH condition and physical properties of particles (e.g., particle size or moisture content) [6]. The stability of the PBNP-thallium binding is high as quantified by Gupta which makes Prussian blue a suitable antidote for thallium poisoning [9].

The investigation of *in vivo* stability and biodistribution of the radiolabeled PBNPs was our goal as well. Quantitative tomographic imaging using emitted gamma rays was carried out in a dedicated small animal SPECT/CT instrument. Briefly, we wished to explore  $^{201}\text{Tl}$  radiolabeled PBNPs as a form of chemically stable contrast material with applications in MRI and SPECT. This approach has been patented in 2012 by two of the authors [10].

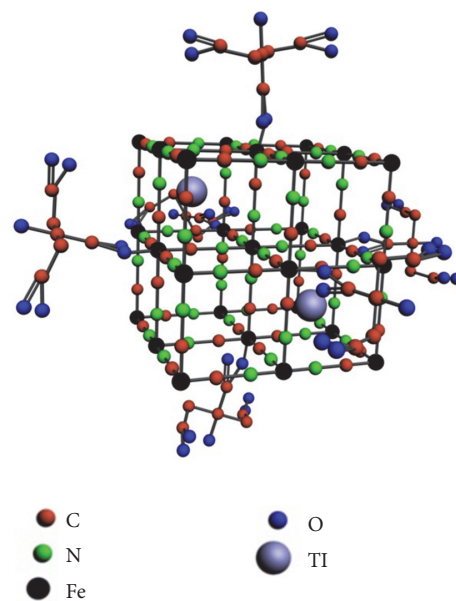


FIGURE 1: The structure of Prussian blue. Citrate bound to Fe(III) forms the coating. The colors represent the following ions or atoms, respectively: red: C; green: N; black: Fe (both of Fe(II) and Fe(III)); blue: O; gray:  $^{201}\text{Tl}$ .

## 2. Materials and Methods

**2.1. Synthesis of PBNPs.** A modified method of Shokouhimehr was used to prepare citrate-coated PBNPs [4]. Briefly, PBNPs were prepared by slowly adding 20 mL of a 1.0 mM Fe(III) chloride (anhydrous) ( $\text{FeCl}_3$ ) (Sigma-Aldrich) solution containing 0.5 mmol of citric acid (Sigma-Aldrich) to a solution containing an equimolar amount of potassium ferrocyanide (anhydrous) ( $\text{K}_4[\text{Fe}(\text{CN})_6]$ ) (Sigma-Aldrich) under rigorous stirring at  $40^\circ\text{C}$ . Three samples ( $n = 3$ ) were synthesized. The products were isolated by centrifugation at 29000 rpm (Beckman Ti 50.2 rotor, 30 min at  $4^\circ\text{C}$ ) and then dialyzed for  $3 \times 1$  hour (14 kDa filter) (Sigma-Aldrich, D9277).

### 2.2. In Vitro Measurements

**2.2.1. Atomic Force Microscopy.** After 15 min incubation the mica surface was dried in  $\text{N}_2$  stream. AFM images were collected in noncontact mode with a Cypher S instrument (Asylum Research, Santa Barbara, CA) at 1 Hz line-scanning rate in air, using a silicon cantilever (OMCL AC-160TS, Olympus, Japan) oscillated at its resonance frequency (300–320 Hz). Temperature during the measurements was  $29 \pm 1^\circ\text{C}$ . AFM amplitude-contrast images are shown in this paper. AFM images were analyzed by using the built-in algorithms of the AFM driver software (IgorPro, WaveMetrics Inc., Lake Oswego, OR). Particle statistics was done by analyzing a  $10 \times 10 \mu\text{m}$  height-contrast image with  $n = 1162$  particles. Maximum height values were taken as height of particles; rectangularity was calculated as the ratio of the particle area to the area of a nonrotated inscribing rectangle. The closer a particle is to a rectangle the closer this value is to unity.

**2.2.2. Transmission Electron Microscopy (TEM).** Morphological investigations of the NPs were carried out on a MORGAGNI 268(D) (FEI, Eindhoven, Netherlands) transmission electron microscope. Diluted sample was dropped and dried on a carbon-coated copper grid. Size distribution was determined by manually measuring the diameter of 700 particles on the images, using a software custom designed for this purpose (tem\_circlefind by András Wacha, MTA TTK, Hungary).

**2.2.3. Zeta Potential and Light Scattering Measurement.** Zeta potential and hydrodynamic diameter measurements were performed using a Zetasizer Nano ZS instrument (from Malvern Instruments Ltd., Worcestershire, UK), fitted with a He-Ne laser ( $\lambda = 633$  nm) and a backscatter detector fixed at  $173^\circ$ . For zeta potential measurements, PBNP samples were diluted thirtyfold with a solution containing 0.9% NaCl in order to mimic physiological ion concentrations. The pH of the sample was adjusted by the addition of a 0.01M NaOH solution. DLS measurement was performed in a W130i DLS instrument (Avid Nano Ltd., High Wycombe, UK) using low volume disposable cuvettes (UVette, Eppendorf Austria GmbH). The sample was diluted tenfold with ultrapure water and filtered through a 0.22  $\mu\text{m}$  membrane filter. Data were processed with iSize 2.0 software utilizing the CONTIN algorithm. DLS measurements were performed weekly for a period of 6 weeks to determine colloidal stability. Samples were stored at  $4^\circ\text{C}$ .

**2.2.4. Magnetic Resonance Imaging (MRI).** MRI measurements were performed in vitro with a nanoScan<sup>®</sup> PET/MR system (Mediso, Hungary) in a permanent magnetic field of 1T in a 450 mT/m gradient system using a volume transmit/receive coil with a diameter of 60 mm. A phantom consisting of six 1.5 ml microcentrifuge tubes was prepared, with each microcentrifuge tube containing a 150  $\mu\text{l}$  aliquot of a PBNP solution. PBNP concentrations were 0.00 mM, 0.125 mM, 0.25 mM, 0.38 mM, 0.76 mM, and 1.25 mM. Particle concentrations were based on the molecular weight calculated using the illustrated crystal structure model (Figure 1). Four different sequences were used for imaging, two of them for relaxivity measurements and two others for basic imaging to exploit different contrast mechanisms. T1-weighted 2D Spin Echo sequence was acquired using the below parameters: field of view (FOV) 74 mm, 0.41 mm in-plane resolution, 1.6 mm slice thickness, and TR/TE 500/9.2 ms. Fast spin T2-weighted echo sequence was acquired with the same geometric parameters but with TR/TE 4000/77.1 ms and 4 averages. T1 relaxation rates and  $r_1$  relaxivity were calculated from inversion prepared snapshot gradient echo (IR GRE-SNAP) images acquired with 50 mm FOV, plane resolution of 0.39 mm, slice thickness of 2 mm, 8 averages, TR/snap TR/TE 12000/8.2/3 ms, flip angle of  $8^\circ$ , and 8 different transmission intervals ranging from 50 to 6400 ms. T2 relaxation rates and  $r_2$  relaxivity were calculated from multiecho spin echo (ME-SE) images scanned with 50 mm FOV, plane resolution of 0.5 mm, slice thickness of 2 mm, TR of 2000 ms, and 32 different TEs ranging from 15 to 480 ms. MRI signal enhancement of PBNPs was measured at six different

concentrations (0.00 mM, 0.125 mM, 0.25 mM, 0.38 mM, 0.76 mM, and 1.25 mM). After scanning the concentration dependent signal changes were calculated and compared to the signal of pure water.

**2.2.5. Viability Assay.** Human cervical carcinoma (HeLa) cells were chosen for cell viability assay tests. They were seeded at a density of  $10^4$  cells/mL to each Petri dish. The cells were exposed to saline (negative control) and three different PBNP containing solutions (4-, 16-, and 32-fold dilutions of PBNP) for 20 min. The medium was then removed and the cells were rinsed in Hanks' Balanced Salt Solutions (HBSS; Sigma-Aldrich) twice. The rinsed cells were harvested by adding 200  $\mu\text{l}$  of 0.1% trypsin (Sigma-Aldrich) for 3 min, then adding 800  $\mu\text{l}$  of modified eagle medium (MEM; Sigma-Aldrich) with 0.1% trypan blue, and counting the number of living cells.

**2.2.6. Radiolabeling with  $^{201}\text{Tl}$ .** Thallium-201labeled PBNPs were prepared as follows: 15  $\mu\text{l}$  (37 MBq) [ $^{201}\text{Tl}$ ]TlCl (Coviden, Netherlands) was added to 20  $\mu\text{l}$  PBNP in 250  $\mu\text{l}$  isotonic 0.9% NaCl solution (Braun, Hungary) and the reaction mixture was incubated at room temperature for 60 minutes. The calculated specific activity of the radiolabeled product was 62 GBq/g, based on the specific activity of [ $^{201}\text{Tl}$ ]TlCl, the size and molar weights of nonhydrated PBNPs, and the molar amount of Fe in the reaction vial.

**2.2.7. Chromatography of Radiolabeled NP Suspension.** Radiochemical purity of the labeled suspension was determined by paper chromatography using 18 cm long Mackerey-Nagel 813 paper strips and double distilled water as mobile phase ( $n = 7$ ). After photographic evaluation the chromatography paper was cut into 0.5 cm pieces and the activity of each piece was measured in a well-type NaI (Tl) scintillation detector (NZ-310 Gamma, Budapest). Retention factors (RF) were calculated as a ratio of the distance the spots and the solvent front had moved from the baseline.

### 2.3. In Vivo Measurements

**2.3.1. Animals.** In vivo imaging was carried out in C57BL/6 male mice ( $n = 5$  for SPECT/CT scans,  $n = 2$  for MRI scans, Charles River, Hungary). Animals had ad libitum access to food and water and were housed under temperature-, humidity-, and light-controlled conditions. All procedures were conducted in accordance with the ARRIVE guidelines and the guidelines set by the European Communities Council Directive (86/609 EEC) and approved by the Animal Care and Use Committee of Semmelweis University (protocol number: XIV-I-001/29-7/2012). Mice were 10–12 weeks old with an average body weight of  $28 \pm 5$  g. During imaging animals were kept under anesthesia using a mixture of 2.5% isoflurane gas and medical oxygen. Their body temperature was maintained at  $37^\circ\text{C}$  throughout imaging.

**2.3.2. SPECT/CT Imaging.** Images were acquired with a NanoSPECT/CTPLUS (Mediso Ltd., Hungary) sequential

animal SPECT/CT imaging system. For SPECT/CT imaging,  $21.07 \pm 2.38$  MBq of  $^{201}\text{Tl}$  labeled PBNP was injected in  $150 \mu\text{l}$  physiological saline (Braun, Hungary) into a lateral tail vein.

During imaging animals were fixed to a MultiCellTM Imaging Chamber (Mediso Ltd., Hungary) to avoid movement and placed in the center of the FOV. Image acquisitions started with CT scanning (without any contrast agent) 60 min after the intravenous injection of  $^{201}\text{Tl}$ -labeled PBNP. Further SPECT/CT scans were acquired at 24, 48, and 72 hours after injection. Both the CT and subsequent SPECT imaging took 30 min each. The reconstructed cubic voxel side size was  $150 \mu\text{m}$  in a  $198 \times 198 \times 546$  voxel matrix in both the SPECT and CT modalities. Fusion (Mediso Ltd., Hungary) and VivoQuant (inviCRO LLC, US) image analysis software were used to further analyze the reconstructed, reoriented, and coregistered images by drawing appropriate volumes of interests (VOIs) over the specified target organs. These VOIs were delineated manually on each CT scan. Activity concentrations ( $\text{MBq}/\text{cm}^3$ ) were determined for each volume of interest and data was corrected for the scatter and isotopic decay during the reconstruction. Organs were initially ranked based on the visually representative uptake of activity. Then a quantitative threshold (0.1% of injected activity) was applied on the images. Organs with a higher uptake of 0.1% were quantified by placing three-dimensionally corresponding activity measuring VOIs on them. With this method the uptake of radioactivity was selected and measured in the following organs: liver, kidneys, salivary glands, heart, lungs, and brain.

**2.3.3. Magnetic Resonance Imaging (MRI).** Images were acquired before (prescan) and after the PBNP injection with a nanoScan® PET/MR system (Mediso, Hungary) in a permanent magnetic field of 1 T in a 450 mT/m gradient system using a volume transmit/receive coil with a diameter of 60 mm. For imaging 1.25 mM PBNP was injected in  $250 \mu\text{l}$  physiological saline (Braun, Hungary) into a lateral tail vein.

Two different sequences were used for imaging. T2-weighted 2D Fast Spin Echo sequence was acquired using the below parameters: field of view (FOV) 70 mm, 0.35 mm in-plane resolution, 0.2 mm slice thickness, and TR/TE 4809/70 ms. T1-weighted Gradients-echo sequence was acquired using the below parameters: field of view (FOV) 70 mm, 0.40 mm in-plane resolution, 0.4 mm slice thickness, and TR/TE 3.4/25 ms.

## 3. Results

### 3.1. In Vitro Measurements

**3.1.1. Atomic Force Microscopy.** AFM images are shown in Figure 2. PBNPs appeared as objects with a flat rectangular surface protruding from a rounded halo (Figure 2(a)). The rectangular surface represents the real geometry of the particles (Figure 2(b)), while their halo is the consequence of tip convolution, that is, the effect of imaging a rectangular prism by a tetrahedral AFM tip. Rectangularity of the particles (together with their halo) was found to be  $0.81 \pm 0.09$  (mean

$\pm$  SD), indicating that PBNPs indeed represent rectangular topography. Height of the particles showed monomodal distribution with a mean  $\pm$  SD of  $23.0 \pm 8.3$  nm (Figure 2(c)).

**3.1.2. Transmission Electron Microscopy.** The nonhydrated shape and size of the NPs were also analyzed with TEM. The shape of the nanoparticles on TEM and AFM images was similar. PBNPs appeared as flat rectangular, dense objects in this case as well. The mean diameter of the nanoparticles was  $17.54 \pm 4.56$  nm (average  $\pm$  SD,  $n = 700$ ) (Figure 3).

**3.1.3. Zeta Potential and Light Scattering Measurement.** The mean zeta potential of PBNPs at the measured pH range did not exceed 15 mV ( $n = 3$ ). At pH 7.4 the zeta potential was  $-25.7 \pm 1.8$  mV ( $n = 3$ ).

The mean hydrodynamic diameter (intensity-based harmonic mean or  $z$ -average) of citrate-coated PBNPs was  $32.10 \pm 0.1801$  (average  $\pm$  SD,  $n = 10$ ), as determined by DLS. This had only changed slightly with time. There was no significant colloidal alteration during the 6-week duration of the study, as the calculated  $0.203 \pm 0.004$  polydispersity index (PDI) shows the PBNPs did not flocculate or aggregate during this time (not illustrated).

**3.1.4. Magnetic Resonance Imaging.** T1-weighted (Figure 4(a)) and T2-weighted spin echo (Figure 4(b)) images of a phantom (containing five different concentrations (0.00 mM, 0.125 mM, 0.25 mM, 0.38 mM, 0.76 mM, and 1.25 mM) of PBNP solutions and a pure solvent) were scanned to visually evaluate the signal enhancement on T1-weighted image instead of decreased signal on T2-weighted image. Based on the inversion prepared gradient echo scan and the multislice multiecho scan T1 and T2 relaxation rates were calculated. Afterward from these values, longitudinal relaxivity ( $r_1 = 0.64 \pm 0.02 \text{ mM}^{-1} \text{ ms}^{-1}$ ) and transversal relaxivity values ( $r_2 = 0.96 \pm 0.03 \text{ mM}^{-1} \text{ ms}^{-1}$ ) were fitted and are presented in Table 1.

**3.1.5. Viability Assay.** The survival rate of HeLa cells exposed to PBNP was above 95%. There was almost no difference between the numbers of intact cells in case of different PBNP concentration. For detailed information, see Table S1.

**3.1.6. Stability of Radiolabeling.** Using paper chromatography, we found that both unlabeled and radiolabeled particles have an Rf value of 0.0–0.1. Nonreacted  $^{201}\text{Tl}$  ions moved together with the solvent front. Only 2% of the whole  $^{201}\text{Tl}$  activity was detected at the solvent front. Therefore, the radiochemical purity was estimated as being >98% in all experiments (Table 2). Comparing the total added activity of  $^{201}\text{Tl}$  to the solution and particle-bound  $^{201}\text{Tl}$  activity the radioactive labeling yield was 99.84% (SD: 1.01%).

### 3.2. In Vivo Biodistribution Studies

**3.2.1. SPECT/CT Imaging.** Activity originating from  $^{201}\text{Tl}$ -radiolabeled (doped) PBNPs was detected 2 hours after injection in the liver ( $7.89 \pm 2.25\%$  ID) and in the intestines

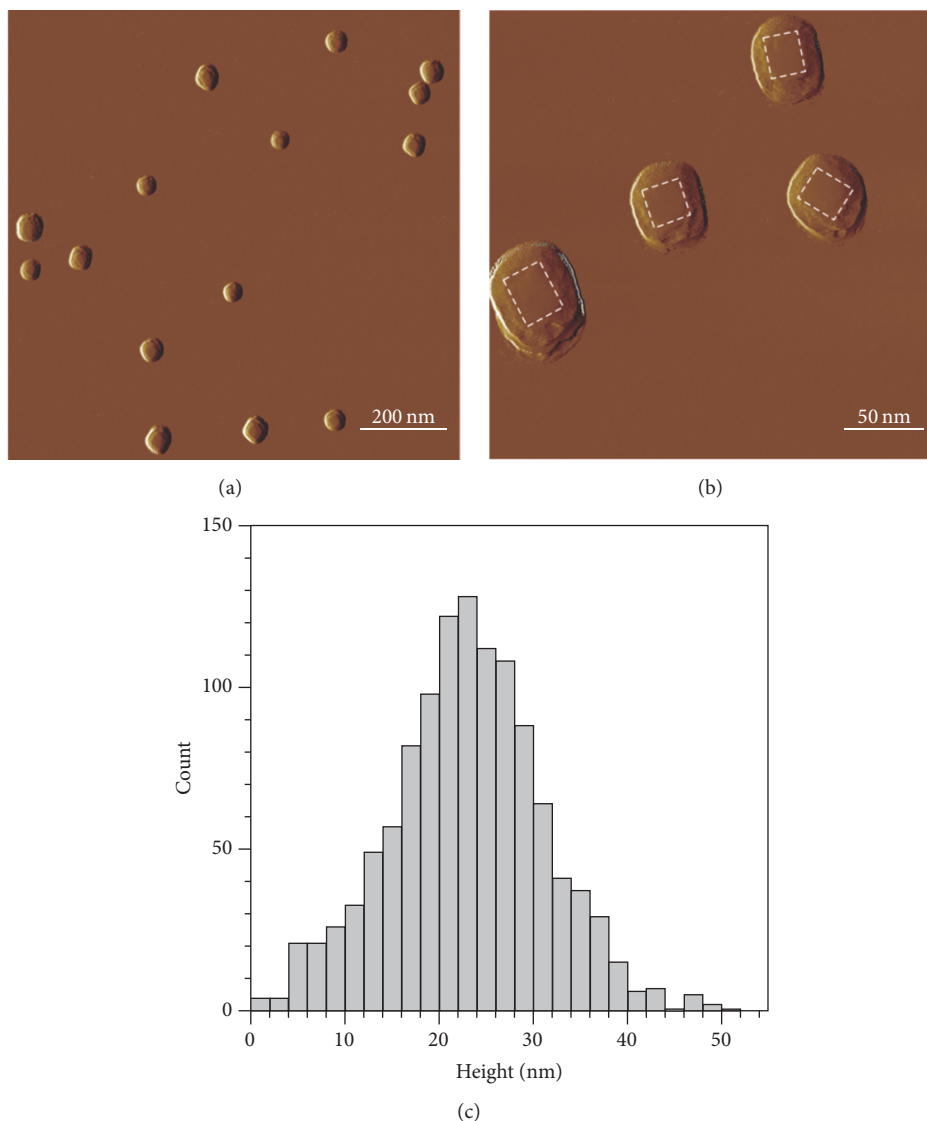


FIGURE 2: ((a) and (b)) AFM amplitude-contrast images of PBNPs on mica surface. Contours of particles are shown by white dashed lines on (b). (c) Height distribution of PBNPs ( $n = 1162$ ).

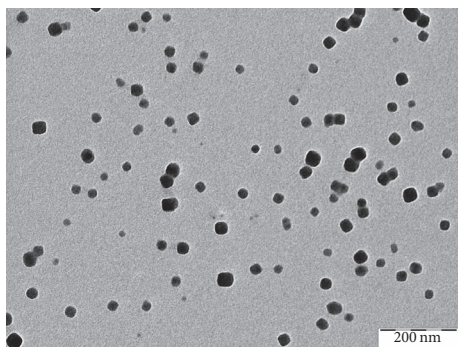


FIGURE 3: TEM image of PBNPs on carbon-coated copper grid.

TABLE 1: Result of relaxivities ( $r_1$  and  $r_2$ ), ordered to examine concentrations of  $^{201}\text{Tl}$  doped PBNPs.

| Relaxivity ( $\text{mM}^{-1}\text{ms}^{-1}$ ) | $R$ ( $\text{mM}^{-1}\text{ms}^{-1}$ ) | Error of $R$ ( $\text{mM}^{-1}\text{ms}^{-1}$ ) |
|---|--|---|
| $r_1 = 0.64 \pm 0.02$                         | 3089                                   | 91  |
| $r_2 = 0.96 \pm 0.03$                         | 2119                                   | 350   |

TABLE 2: Retention factors of  $^{201}\text{Tl(I)}$  ions and  $^{201}\text{Tl}$  doped PBNP examined with paper chromatography.

| Sample   | Retention factor | Activity |
|--|------------------|----------|
| Standard [ $^{201}\text{Tl}$ ]TlCl <sub>aq</sub> | 0.85             | 86.8%    |
| $^{201}\text{Tl}$ doped PBNP                     | 0.02             | 85.2%    |

( $6.88 \pm 1.37\%$  ID). In later time points (24 hours, 48 hours, and 72 hours) activity in the liver gradually decreased to

$5.92 \pm 1.78\%$ ,  $4.17 \pm 0.43\%$ , and  $4.11 \pm 0.64\%$ , respectively. Meanwhile, the activity in the intestines increased to  $12.34 \pm$

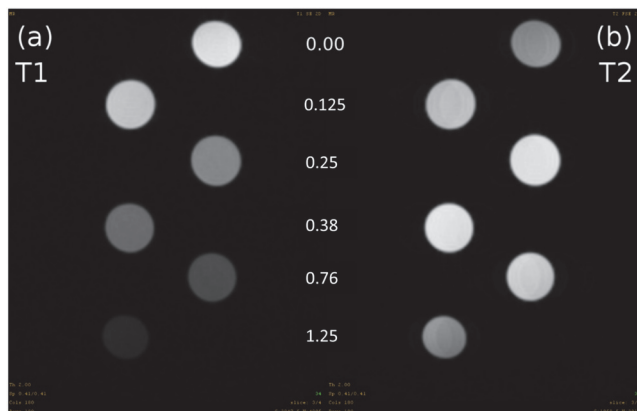


FIGURE 4: T1-weighted inversion prepared snapshot gradient echo (a) and T2-weighted multiecho spin echo (b) images of a phantom containing five different concentrations 0.125 mM, 0.25 mM, 0.38 mM, 0.76 mM, and 1.25 mM of PBNP solutions were scanned and signal changes compared to the bidistilled water signal.

1.67%,  $19.25 \pm 2.32\%$ , and  $19.48 \pm 3.02\%$ , respectively (Figures 5 and 6(a)).

In the *kidneys*  $15.24 \pm 4.06\%$  of the injected activity was recovered 2 hours after the administration of  $^{201}\text{Tl}$  doped PBNPs, gradually decreasing to  $8.45 \pm 0.38\%$  by 72 hours after injection (Figures 5 and 6(b)).

In the *salivary glands* relatively high ( $0.83 \pm 0.08\%$ ) activity of  $^{201}\text{Tl}$  doped PBNPs was observed 2 hours after injection. By 24 hours after injection a statistically significant increase in salivary gland uptake was observed ( $1.27 \pm 0.21\%$ ,  $p < 0.05$ ). By 48 and 72 hours after injection activity measured in the salivary glands decreased to  $0.78 \pm 0.05\%$  and  $0.82 \pm 0.58\%$ , respectively (Figure 6(c)).

In the *heart ventricles* constantly decreasing activity was observed in every time point when compared to the initial value of  $0.59 \pm 0.08\%$  (Figures 5 and 6(c)). This is contrary to the usually observed free  $^{201}\text{Tl}$  ion uptake by heart muscles due to both the very small accumulation and the constant decrease.

In the *lungs* the level of  $^{201}\text{Tl}$  doped PBNPs was  $0.39 \pm 0.29\%$  2 hours after injection, slightly decreasing with time to  $0.29 \pm 0.05\%$  at 24 hours,  $0.27 \pm 0.08\%$  at 48 hours, and  $0.30 \pm 0.06\%$  at 72 hours (Figure 6(d)).

In the *brain* negligible PBNP uptake was recorded 2 hours after injection which did not increase significantly in the next 70 hours (not illustrated).

**3.2.2. MRI Measurements.** T2-weighted Fast Spin Echo and T1-weighted gradient echo images were acquired to visually evaluate the in vivo biodistribution of PBNP. No signal changes were registered under the applied conditions compared to the prescans.

## 4. Discussion

PB has long been used as a treatment agent of radioactive  $^{137}\text{Cs}$  poisoning in human medicine based on its successful

application in the accident of Goiânia, Brazil [11]. It easily adsorbs  $\text{Cs}^+$  and thus facilitating its excretion from the human body. PB has been registered for the above indication by Food and Drug Administration (FDA) and European Medicines Agency (EMA) as well.

AFM is one of the foremost tools for imaging, measuring, and manipulating subnanometer samples [12]. It measures the shape of nonhydrated particles. The exact diameter of NPs was difficult to determine by AFM due to the tip convolution which leads to artificially increased lateral dimensions on AFM images [13]. Only the height of the particles should be taken into account because the measured width is influenced by tip convolution. The measured height by AFM supported the results of TEM measurements which describe the shape of nonhydrated particles. In both cases the particles appeared as flat rectangular objects which represent the real geometry of the particles. Furthermore, the size distribution of PBNP showed monomodal distribution in cases of TEM and AFM measurements, too.

The average diameter of our PBNPs measured by DLS was similar to the size range reported by Shokouhimehr et al. [4]. These measured hydrodynamic diameters of particles with the small PDI values represent a monodisperse and stable nanobased system in the investigated time frame.

According to the homogeneity and colloidal stability results of PBNPs, the measurements of their other properties were constant. The thermodynamic stability of PB ensured that the synthesized PBNPs could fulfill requirements of long stability as well.

Based on the claims found in the present study authors' 2012 US patent [10], Gallium incorporating PBNP (Ga-PBNP) production studies were performed at the University of Ohio [14]. The resulting structurally very similar Ga-PBNPs to the Tl-PBNPs reported in our study have been thoroughly characterized. They were also found to be cubic shaped as shown in our results. The size differences could be attributed to the different surface-capping agent (polyvinylpyrrolidone).

Citric acid as surface-capping agent to control size and biocompatibility and to avoid agglomeration of the synthesized particles is able to chelate  $\text{Ca}^{2+}$  ions [15]. However, physiological  $\text{Ca}^{2+}$  concentration does not affect in vivo colloidal properties [16]. At physiological pH of 7.4, the zeta potential of PBNPs and the steric stabilization effect of citrate coating further enhance the colloidal stability.

MRI T1- and T2-weighted scans showed a more significant T1 shortening effect for PBNPs than T2 shortening.  $\text{Fe}^{2+}$  in the PB structure is carbon-bound and has a low-spin ( $S = 0$ ), while the nitrogen-bound  $\text{Fe}^{3+}$  has high spin ( $S = 5/2$ ). Thus, the compound is able to alter both the longitudinal and transverse relaxation times of protons in water molecules [4]. Based on the longitudinal and transversal relaxivity results, a local concentration in the range of 0.5 mM of the  $^{201}\text{Tl}$  doped PBNPs is needed to achieve proper MRI signal enhancement.

In the case of in vivo MRI scans, we were not able to register any contrast changes between the pre- and postinjection scans. Presumably the iron content of the injected PBNP sample (2.5 mM 250  $\mu\text{L}$  PBNP) was not high enough

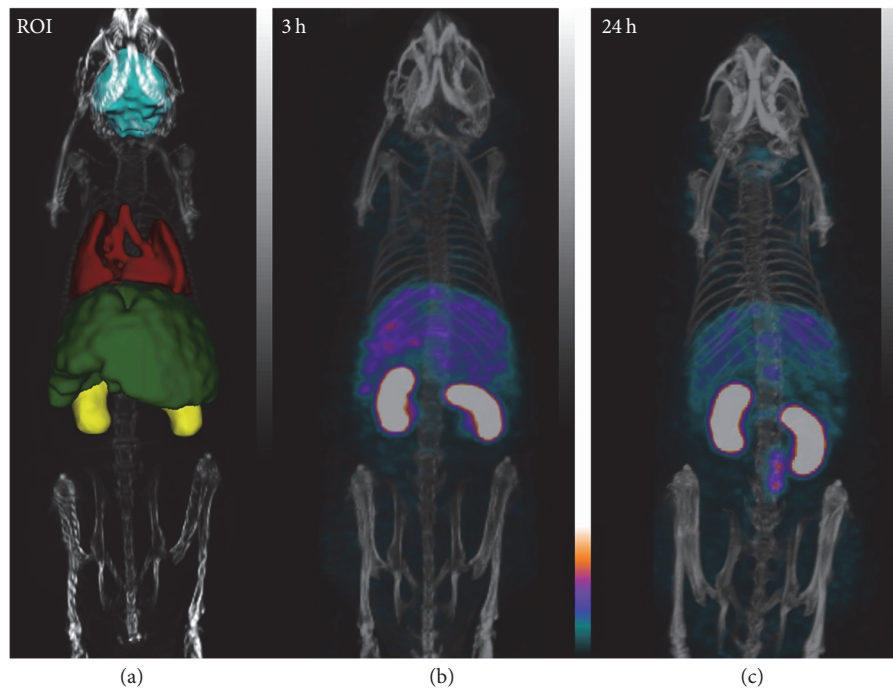


FIGURE 5: VOI of liver, kidneys, heart, and brain (a). Biodistribution of  $^{201}\text{Tl}$  labeled PBNPs after 2 hours (b) and 24 hours (c) injection. The mice were under isoflurane anesthesia during the 30 minutes long SPECT scans. The injected activity was  $21.07 \pm 2.38$  MBq.

after the intravenous administration to alter the microscopic magnetic properties of the living system. Further chemical improvement is needed in the future which can enhance the iron (paramagnetic agent) content of the NP or alter the relaxivity of our contrast material. The newly developed iron-based contrast material should be a reliably applicable multimodal contrast agent for in vivo biodistribution studies.

In vivo SPECT scans (based on heart and blood biodistribution measurements) seem to justify that we have attained our main goal of long-term in vivo stability of the labeled PB particles.

No sign of  $^{201}\text{Tl}$  accumulation in the heart muscles points to any significant in vivo release of free  $^{201}\text{Tl}$  ions from the particles. As a “biological quality control,” no physiological cardiomyocyte uptake of that free  $^{201}\text{Tl}$  (which is a potassium ion analogue) is measured.

According to Kevin et al. the in vivo behavior of NPs is mostly regulated by their characteristics such as size, shape, composition, surface chemistry, and associated physical properties [17]. In accordance with the colloidal stability of PBNPs determined by DLS and zeta potential measurements, they were stable in vivo and they did not aggregate in a biologically relevant manner.

The reported citrate-coated PBNPs accumulate in the liver followed by biliary excretion into the intestines. The measured activity in the liver gradually decreased, while the activity in the intestines increased during the 72-hour time period. Uptake mechanisms by Kupffer cells favor larger, negatively charged particles and are responsible for the retention of most NPs in the liver. Other cell types (liver sinusoidal

endothelial cells (LSEC), hepatic stellate cells (HSC), hepatocytes, cholangiocytes, and resident immune cells) also interact with NPs. Uptake by hepatocytes favors smaller and more positively charged particles and leads to their hepatobiliary clearance [18]. Based on the available literature, the size of our PBNPs suggests they were able to extravasate into the spaces of Disse where they were most likely taken up directly by hepatocytes. Kupffer cells and LSECs uptake could have also taken place based on the measured zeta potential. The assumption of Disse-space extravasation and hepatocyte uptake could be further investigated with ultrastructural methods as it represents a targeting opportunity.

Histological examination of previous studies about the biodistribution of NPs provides important insight into the routes of accumulation of PBNPs inside the kidneys [19–21]. Based on these experiments, filtration of PBNPs is not possible due to their negative charge and large size; larger PBNPs deposit in the mesangium while smaller NPs remain inside the peritubular vessels.

Kaiser et al. published that salivary glands took up some hydrophilic and negatively charged, cubic shaped NPs already one hour after the i.v. administration [22]. With regard to early tissue distribution pattern of NPs (in our study 2 hours after injection), our results were similar to those of other research groups [17]. The accumulation of our  $^{201}\text{Tl}$  doped PBNPs in the salivary glands was continuous in the first 24 hours due to the negative surface charge of PBNPs (negative zeta potential) and the abundance of sodium hydrogen carbonate ( $\text{NaHCO}_3$ ) in the salivary glands which are essential for entrapping the injected PBNPs. 48 hours

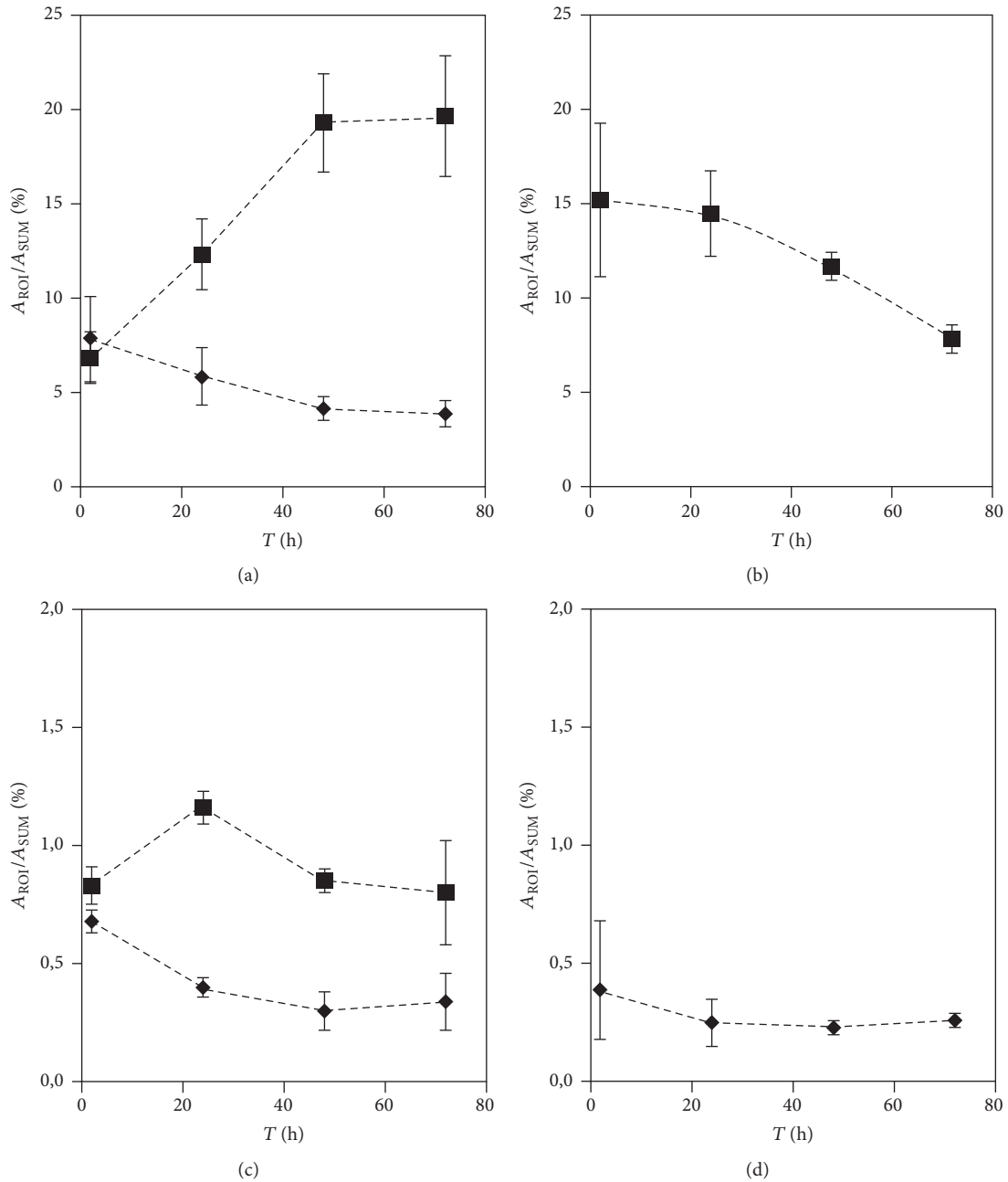


FIGURE 6: The biodistribution of  $^{201}\text{Tl}$  doped PBNPs in (a) intestines (square) and liver (diamond), (b) kidneys (square); (c) salivary glands (square) and heart (diamond); and (d) lungs (diamond) in 2, 24, 48, and 72 hours after injection. Brain uptake constantly remained under the threshold level. The mice were under isoflurane anesthesia during the 30 minutes long SPECT scans. The injected activity was  $21.07 \pm 2.38$  MBq.

after injection the activity detected in the salivary glands decreased most probably due to the excretion of PBNPs into the saliva. Activity levels in the salivary glands decreased and in parallel activity recovered from the intestines continued to increase due to continuous hepatic excretion.

The heart, skeletal muscles, and lungs are not supposed to accumulate PBNPs. The very small radioactivity detected in these organs could be the result of a minuscule proportion of  $^{201}\text{Tl}$  ions probably released by PBNPs in the bloodstream,

where just like in the liver and in the intestines the activity is decreasing.

Because of the radioactive metal binding capability of PBNPs (e.g.,  $^{201}\text{Tl}$ -labeled PBNP), it could be a useful SPECT tracer in preclinical research (in biliary obstructive diseases (e.g., hepatocarcinoma, pancreatic tumors) due to the high and intensive liver uptake and biliary excretion [18]) and could have the potential for translation into clinical practice too.  $^{201}\text{Tl}$  could be substituted with other radiometals that

similarly could be doping the PB structure to  $^{201}\text{Tl}$ , for example, the beta emitters  $^{64}\text{Cu}$ ,  $^{90}\text{Sr}$ ,  $^{90}\text{Y}$ , and  $^{161}\text{Tb}$  and the alpha emitters  $^{149}\text{Tb}$  and  $^{213}\text{Bi}$ .

Altogether further development of our NP platform for dual diagnostic and therapeutic functions (theranostics) is of great interest [1]; appropriately modified PBNPs could fulfill the above-mentioned criteria and be useful for the diagnosis and therapy of various diseases including the local radiotherapy of cancer.

## 5. Conclusions

In this study, we successfully synthesized, characterized, and demonstrated the biodistribution of citrate-coated Prussian blue nanoparticles labeled using  $^{201}\text{Tl}$  isotope. The results show a chemically stable and biocompatible  $^{201}\text{Tl}$ -labeled nanoparticulate SPECT tracer. Important hepatic and salivary glands uptake was seen to be of particular interest upon evaluation of the particle biodistribution. These PB-based particles could be applied as a drug delivery platform or a contrast agent in preclinical research. They could further be tailored towards clinical application, too.

## Conflicts of Interest

The authors declare that they have no conflicts of interest.

## Authors' Contributions

Domokos Máthé conceived the study; Krisztián Szigeti, Domokos Máthé, Kinga Karlinger, and Balázs Gulyás designed research methodology; Nikolett Hegedűs, Kitti Rácz, Krisztián Szigeti, Ildikó Horváth, Dániel S. Veres, Dávid Szöllösi, Noémi Kovács, Zoltán Varga, Magor Babos, Ferenc Budán, and Noémi Kovács performed research; Krisztián Szigeti, Ildikó Horváth, Dániel S. Veres, Noémi Kovács, Károly Módos, Domokos Máthé, and Ildikó Futó analyzed the data; and Domokos Máthé, Krisztián Szigeti, Nikolett Hegedűs, Dávid Szöllösi, and Parasuraman Padmanabhan wrote the paper.

## Acknowledgments

The authors acknowledge the helpful discussions of Miklós Kellermayer (Department of Biophysics and Radiation Biology, Semmelweis University). Dr. Levente Mészáros (King's College, London) is gratefully acknowledged for valuable contributions in editing and proofing the manuscript. The high value technical support in SPECT/MRI image acquisitions from Mediso (Gábor Németh, Sándor Hóbor) is gratefully acknowledged. The research leading to these results has received funding from the European Union's Seventh Framework Programme (FP7/2007-2013) under Grant Agreements HEALTH-F2-2011-278850 (INMiND), FP7 HEALTH-305311 (INSERT), and TÁMOP-4.2.1/B-09/1/KMR-2010-0001. This study was supported by the National Research, Development

and Innovation Office of Hungary (NKFIA; NVKP-16-1-2016-0017 National Heart Program). Krisztián Szigeti was supported by the Janos Bolyai Research Fellowship Program of the Hungarian Academy of Science. Parasuraman Padmanabhan and Balázs Gulyás acknowledge the support from the Lee Kong Chian School of Medicine, Nanyang Technological University Start-Up Grant. This work was supported by the NVKP.0017 Project of the Hungarian National Research Development and Innovation Office.

## Supplementary Materials

Table S1: the result of viability assays in cases of saline and three different PBNP dilutions. After 20-minute incubation period intact and dead HeLa cells were counted by each dilution. Cell morphology of dead cells from viable ones was distinguished by shape, light reflection, and scattering properties and lack of motion. (*Supplementary Materials*)

## References

- [1] N. Singh, *Radioisotopes - Applications in Bio-Medical Science*, InTech, Rijeka, Croatia, 2011.
- [2] J. L. Tremoleda, M. Khalil, L. L. Gompels, M. Wylezinska-Arridge, T. Vincent, and W. Gsell, "Imaging technologies for preclinical models of bone and joint disorders," *European Journal of Nuclear Medicine and Molecular Imaging Research*, vol. 1, no. 1, pp. 1–14, 2011.
- [3] P. Sharma, A. Singh, S. C. Brown et al., "Multimodal nanoparticulate bioimaging contrast agents," *Methods in Molecular Biology (Clifton, N.J.)*, vol. 624, pp. 67–81, 2010.
- [4] M. Shokouhimehr, E. S. Soehnlen, A. Khitrin, S. Basu, and S. D. Huang, "Biocompatible Prussian blue nanoparticles: Preparation, stability, cytotoxicity, and potential use as an MRI contrast agent," *Inorganic Chemistry Communications*, vol. 13, no. 1, pp. 58–61, 2010.
- [5] M. Verdaguier and G. S. Girolami, "Magnetic Prussian Blue Analogs," in *Magnetism: Molecules to Materials*, J. S. Miller and M. Drillon, Eds., vol. 5, pp. 283–346, Wiley-VCH Verlag GmbH & Co. KGaA, 2004.
- [6] Y. Yang, P. J. Faustino, J. J. Progar et al., "Quantitative determination of thallium binding to ferric hexacyanoferrate: Prussian blue," *International Journal of Pharmaceutics*, vol. 353, no. 1-2, pp. 187–194, 2008.
- [7] S. Matsunaga, T. Shuto, H. Takase et al., "Semi-quantitative analysis using thallium-201 SPECT for differential diagnosis between tumor recurrence and radiation necrosis after gamma knife surgery for malignant brain tumors," *International Journal of Radiation Oncology • Biology • Physics*, vol. 85, no. 1, pp. 47–52, 2013.
- [8] W. Hummel, "The influence of cyanide complexation on the speciation and solubility of radionuclides in a geological repository," *Environmental Geology*, vol. 45, no. 5, pp. 633–646, 2004.
- [9] R. C. Gupta, Ed., *Handbook of toxicology of chemical warfare agents*, Academic Press, 2015.
- [10] D. Máthé and K. Szigeti, Prussian blue based nanoparticle as multimodal imaging contrast material, International Patent, PCT/HU2012/000010, 2012.
- [11] M. Oberhofer and J. B. Leao, "The radiological accident at Goiania," in *Proceedings of the ,The radiological accident at Goiania*, vol. 2, pp. 80–136, Vienna, 1988.

- [12] M. Baalousha and J. R. Lead, "Characterization of natural and manufactured nanoparticles by atomic force microscopy: Effect of analysis mode, environment and sample preparation," *Colloids and Surfaces A: Physicochemical and Engineering Aspects*, vol. 419, pp. 238–247, 2013.
- [13] J. Sitterberg, A. Özçetin, C. Ehrhardt, and U. Bakowsky, "Utilising atomic force microscopy for the characterisation of nanoscale drug delivery systems," *European Journal of Pharmaceutics and Biopharmaceutics*, vol. 74, no. 1, pp. 2–13, 2010.
- [14] M. S. Kandanapitiye, M. D. Gott, A. Sharits, S. S. Jurisson, P. M. Woodward, and S. D. Huang, "Incorporation of gallium-68 into the crystal structure of Prussian blue to form K68Ga: XFe<sub>1-x</sub>[Fe(CN)<sub>6</sub>] nanoparticles: Toward a novel bimodal PET/MRI imaging agent," *Dalton Transactions*, vol. 45, no. 22, pp. 9174–9181, 2016.
- [15] H. K. Walker, W. D. Hall, and J. W. Hurst, *Clinical Methods: The History, Physical, and Laboratory Examinations*, LexisNexis Butterworths, Boston, Massachusetts, USA, 3rd edition, 1990.
- [16] E. Keowmaneechai and D. J. McClements, "Influence of EDTA and citrate on physicochemical properties of whey protein-stabilized oil-in-water emulsions containing CaCl<sub>2</sub>," *Journal of Agricultural and Food Chemistry*, vol. 50, no. 24, pp. 7145–7153, 2002.
- [17] W. P. Kevin, C. B. Scott, B. K. Vijay, C. W. Scott, B. M. Moudgil, and S. M. Roberts, "Research strategies for safety evaluation of nanomaterials. Part VI. Characterization of nanoscale particles for toxicological evaluation," *Toxicological Sciences*, vol. 90, no. 2, pp. 296–303, 2006.
- [18] Y.-N. Zhang, W. Poon, A. J. Tavares, I. D. McGilvray, and W. C. W. Chan, "Nanoparticle–liver interactions: Cellular uptake and hepatobiliary elimination," *Journal of Controlled Release*, vol. 240, pp. 332–348, 2016.
- [19] S. Ogawa, Z. Ota, K. Shikata et al., "High-resolution ultrastructural comparison of renal glomerular and tubular basement membranes," *American Journal of Nephrology*, vol. 19, no. 6, pp. 686–693, 1999.
- [20] C. H. Choi, J. E. Zuckerman, P. Webster, and M. E. Davis, "Targeting kidney mesangium by nanoparticles of defined size," *Proceedings of the National Academy of Sciences of the United States of America*, vol. 108, no. 16, pp. 6656–6661, 2011.
- [21] M. Longmire, P. L. Choyke, and H. Kobayashi, "Clearance properties of nano-sized particles and molecules as imaging agents: Considerations and caveats," *Nanomedicine*, vol. 3, no. 5, pp. 703–717, 2008.
- [22] C. R. Kaiser, M. L. Flenniken, E. Gillitzer et al., "Biodistribution studies of protein cage nanoparticles demonstrate broad tissue distribution and rapid clearance in vivo," *International Journal of Nanomedicine*, vol. 2, no. 4, pp. 715–733, 2007.

## Research Article

# Exploiting the Concept of Multivalency with $^{68}\text{Ga}$ - and $^{89}\text{Zr}$ -Labelled Fusarinine C-Minigastrin Bioconjugates for Targeting CCK2R Expression

Dominik Summer,<sup>1</sup> Christine Rangger ,<sup>1</sup> Maximilian Klingler,<sup>1</sup> Peter Laverman,<sup>2</sup> Gerben M. Franssen,<sup>2</sup> Beatrix E. Lechner,<sup>3</sup> Thomas Orasch,<sup>3</sup> Hubertus Haas,<sup>3</sup> Elisabeth von Guggenberg,<sup>1</sup> and Clemens Decristoforo <sup>1</sup>

<sup>1</sup>Department of Nuclear Medicine, Medical University Innsbruck, Anichstrasse 35, 6020 Innsbruck, Austria

<sup>2</sup>Department of Radiology & Nuclear Medicine, Radboud University Medical Center, Geert Grooteplein Zuid 10, 6525 GA Nijmegen, Netherlands

<sup>3</sup>Division of Molecular Biology, Medical University Innsbruck, Innrain 80/82, 6020 Innsbruck, Austria

Correspondence should be addressed to Clemens Decristoforo; [clemens.decristoforo@i-med.ac.at](mailto:clemens.decristoforo@i-med.ac.at)

Received 11 December 2017; Accepted 20 February 2018; Published 10 April 2018

Academic Editor: Anne Roivainen

Copyright © 2018 Dominik Summer et al. This is an open access article distributed under the Creative Commons Attribution License, which permits unrestricted use, distribution, and reproduction in any medium, provided the original work is properly cited.

Cholecystokinin-2 receptors (CCK2R) are overexpressed in a variety of malignant diseases and therefore have gained certain attention for peptide receptor radionuclide imaging. Among extensive approaches to improve pharmacokinetics and metabolic stability of minigastrin (MG) based radioligands, the concept of multivalency for enhanced tumour targeting has not been investigated extensively. We therefore utilized fusarinine C (FSC) as chelating scaffold for novel mono-, di-, and trimeric bioconjugates for targeting CCK2R expression. FSC-based imaging probes were radiolabelled with positron emitting radionuclides (gallium-68 and zirconium-89) and characterized *in vitro* ( $\log D$ ,  $IC_{50}$ , and cell uptake) and *in vivo* (metabolic stability in BALB/c mice, biodistribution profile, and microPET/CT imaging in A431-CCK2R/A431-mock tumour xenografted BALB/c nude mice). Improved targeting did not fully correlate with the grade of multimerization. The divalent probe showed higher receptor affinity and increased CCK2R mediated cell uptake while the trimer remained comparable to the monomer. *In vivo* biodistribution studies 1 h after administration of the  $^{68}\text{Ga}$ -labelled radioligands confirmed this trend, but imaging at late time point (24 h) with  $^{89}\text{Zr}$ -labelled counterparts showed a clearly enhanced imaging contrast of the trimeric probe compared to the mono- and dimer. Furthermore, *in vivo* stability studies showed a higher metabolic stability for multimeric probes compared to the monomeric bioconjugate. In summary, we could show that FSC can be utilized as suitable scaffold for novel mono- and multivalent imaging probes for CCK2R-related malignancies with partly improved targeting properties for multivalent conjugates. The increased tumour accumulation of the trimer 24 h postinjection (p.i.) can be explained by slower clearance and increased metabolic stability of multimeric conjugates.

## 1. Introduction

Receptor targeting with radiolabelled peptides has become an emerging field in nuclear medicine for early diagnosis and therapy of cancerous diseases [1, 2]. The overexpression of cholecystokinin receptor subtype 2 (CCK2R) is involved in various malignancies, such as medullary thyroid carcinoma (MTC), small cell lung cancer (SCLC), and neuroendocrine tumours (NET) [3, 4] and therefore represents an interesting target for peptide receptor radionuclide imaging and

therapy. In a preclinical study, different derivatives based on human minigastrin ( $\text{H}_2\text{N-Leu-(Glu)}_5\text{-Ala-Tyr-Gly-Trp-Met-Asp-Phe-NH}_2$ ) for targeting CCK2R expression were investigated in order to find the ideal targeting sequence [5]. This study reported that four C-terminal amino acids (-Trp-Met-Asp-Phe-NH<sub>2</sub>) are mandatory for selectivity and high affinity towards CCK2R. Different variations are allowed in the N-terminal region to improve *in vivo* targeting properties and pharmacokinetics, especially kidney uptake which is

closely related to the appearance of negatively charged amino acids. Based on this knowledge a variety of MG derivatives have been synthesized by different groups with the aim of reducing kidney but retaining tumour uptake [6]. Further studies have shown that these modifications are unfortunately accompanied by low metabolic stability predominantly for MG11 [7, 8]. *In vivo* stability is a major issue for imaging of receptor expression with small peptide-based molecules. Rapid degradation may lead to decreased tumour uptake and low imaging contrast. Several attempts have been made to overcome this issue, for example, coinjection of the neutral endopeptidase inhibitor phosphoramidon [9] with promising results. Less effort has been spent on a different approach: the design of multivalent constructs. This could increase the probability of receptor target interaction and therefore increase receptor avidity [10, 11] as well as promoting the formation of metabolites able to rebind to the receptor. By this, increased apparent stability tumour uptake and therefore improved imaging contrast would be achieved as has been proposed by Carlucci and coworkers [12]. Sosabowski and coworkers were, to the best of our knowledge, the only group so far reporting on a divalent probe (MGD5) for nuclear imaging of CCK2R expression. This tracer consisting of the bifunctional chelator (1,4,7,10-tetraazacyclododecane-1,4,7,10-tetraacetic acid, DOTA) conjugated to a MG derivative crosslinked via thiol-maleimide to a second sequence of the peptide was radiolabelled with indium-111 for single photon emission tomography (SPECT). It showed increased affinity and tumour uptake compared to its monomeric counterpart <sup>111</sup>In-APH070 [13]. Our group recently reported on fusarinine C (FSC), a cyclic siderophore based bifunctional chelator, providing a scaffold for site-specific conjugation of up to three targeting vectors with excellent complexing properties towards the PET radionuclides gallium-68 and zirconium-89 [14, 15]. As positron emission tomography (PET) provides higher resolution compared to SPECT we initiated this study to compare novel mono-, di-, and trimeric FSC-conjugates for targeting CCK2R expression. Due to low metabolic stability minigastrin analogue (MG11) was chosen as model peptide and was conjugated via thiol-maleimide crosslink as shown in Scheme 1. The resulting mono- and multimeric conjugates were radiolabelled with gallium-68 and zirconium-89 followed by *in vitro* and *in vivo* characterization.

## 2. Experimental Section

**2.1. Analytical [Radio]-RP-HPLC.** Reversed-phase (RP) high-performance liquid chromatography (HPLC) analysis was carried out using the following instrumentation: UltiMate 3000 RS UHPLC pump, UltiMate 3000 autosampler, UltiMate 3000 column compartment (25°C oven temperature), UltiMate 3000 Variable Wavelength Detector (Dionex, Germering, Germany; UV detection at  $\lambda = 220$  nm), radio-detector (Gabi Star, Raytest; Straubenhardt, Germany), Jupiter 5  $\mu\text{m}$  C<sub>18</sub> 300 Å 150 × 4.6 mm (Phenomenex Ltd. Aschaffenburg, Germany) column with acetonitrile (ACN)/H<sub>2</sub>O/0.1% trifluoroacetic acid (TFA) as mobile phase; flow rate of 1 mL/min; gradient: 0.0–3.0 min 0%

ACN, 3.0–5.0 min 0–30% ACN, 5.0–20.0 min 30–60% ACN, 20.0–25.0 min 60–80% ACN.

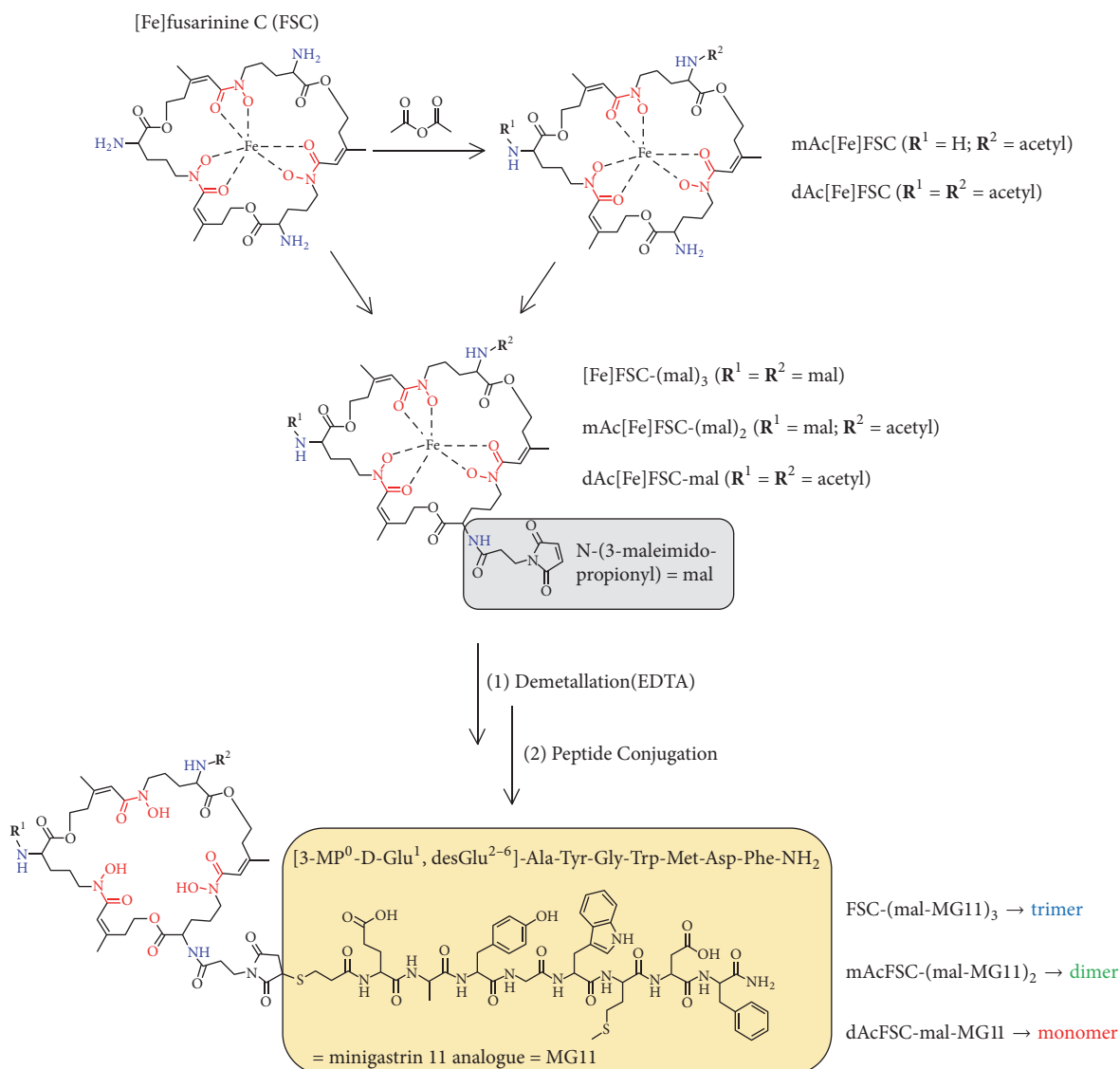
**2.2. Preparative RP-HPLC.** Sample purification via RP-HPLC was performed on a Gilson 322 Pump with a Gilson UV/VIS-155 detector (UV detection at  $\lambda = 220$  nm) using a PrepFC™ automatic fraction collector (Gilson, Middleton, WI, USA). Following ACN/H<sub>2</sub>O/0.1% TFA multistep gradients were used on a Eurosil Bioselect Vertex Plus 30 × 8 mm 5  $\mu\text{m}$  C<sub>18</sub>A 300 Å precolumn and Eurosil Bioselect Vertex Plus 300 × 8 mm 5  $\mu\text{m}$  C<sub>18</sub>A 300 Å column (Knauer, Berlin, Germany) and a flow rate of 2 mL/min: *gradient A*: 0.0–1.0 min 10% ACN, 1.0–25.0 min 10–50% ACN, 25.0–28.0 min 50% ACN, 28.0–30.0 min 10% ACN; *gradient B*: 0.0–1.0 min 20% ACN, 1.0–26.0 min 20–60% ACN, 26.0–28.0 min 60% ACN, 28.0–30.0 min 60–20% ACN; *gradient C*: 0.0–1.0 min 20% ACN, 1.0–26.0 min 20–80% ACN, 26.0–28.0 min 80% ACN, 28.0–30.0 min 20% CAN.

**2.3. MALDI-TOF MS.** Matrix-assisted laser desorption/ionization time-of-flight mass spectrometry was performed on a Bruker microflex™ bench-top MALDI-TOF MS (Bruker Daltonics, Bremen, Germany). Samples were prepared on a microscout target (MSP96 target ground steel BC, Bruker Daltonics) using dried-droplet method and  $\alpha$ -cyano-4-hydroxycinnamic acid (HCCA, Sigma-Aldrich, Handels GmbH, Vienna, Austria) as matrix. All spectra were recorded by summarizing 800 laser shots per spot and Flex Analysis 2.4 software was used for data processing.

**2.4. Radio-ITLC.** Instant thin layer chromatography (ITLC) analysis was performed using TLC-SG strips (Varian, Lake Forest, CA, USA) and 0.1 M sodium citrate solution (pH 5) for <sup>68</sup>Ga-conjugates and 0.05 M EDTA solution (pH 7) for <sup>89</sup>Zr-conjugates as mobile phase. The strips were analyzed using a TLC scanner (Scan-RAM™, LabLogistic, Sheffield, UK). Radiolabelled bioconjugates remained at the start ( $R_f = < 0.1$ ) while free radionuclides migrated with the solvent front ( $R_f = > 0.9$ ).

**2.5. Gamma Counter.** A 2480 Automatic Gamma Counter Wizard2 3<sup>rd</sup> (Perkin Elmer, Waltham, MA, USA) was used to measure the radioactivity of samples retrieved from *in vitro* and *in vivo* experiments.

**2.6. Cell Culture.** The human epidermoid carcinoma cell line (A431) stably transfected with the plasmid pCR3.1 containing the full coding sequence for the human CCK2R (A431-CCK2R) and with the empty vector alone (A431-mock) was a kind gift from Aloj [16]. Both cell lines were maintained at 37°C in a humidified atmosphere of 95% air/5% carbon dioxide in tissue culture flasks (Cellstar; Greiner Bio-One, Kremmunster, Austria) using Dulbecco's Modified Eagle's Medium (DMEM) supplemented with 10% v/v fetal bovine serum (FBS) and 1% v/v penicillin-streptomycin-glutamine (PSG) solution media (Gibco, Invitrogen Corporation, Paisley, UK).



SCHEME 1: Route of synthesis for novel mono- and multimeric MG conjugates (stereochemistry omitted).

**2.7. Precursor Preparation.** The synthesis of mono- and multivalent FSC-based minigastrin derivatives is presented in detail in the supplementary materials sections.

## 2.8. Radiochemistry

**2.8.1. Radiolabelling with Gallium-68.** Fractionated elution of a commercially available <sup>68</sup>Ga/<sup>68</sup>Ge-generator (IGG100, Eckert & Ziegler Isotope Products, Berlin, Germany; nominal activity of 1850 MBq) with 0.1 M hydrochloric acid (HCl, Rotem Industries, Israel) was used to obtain <sup>68</sup>GaCl<sub>3</sub> (gallium chloride, ~310 MBq) in 1 mL eluate. For labelling 20 μg (5–10 nmol) of conjugate (mono-, di-, or trimer) was mixed with 100–500 μL eluate (~30–160 MBq) and the pH was adjusted to 4.5 by adding 20 μL of sodium acetate solution (1.14 M) per 100 μL eluate. The mixture was incubated for 5–15 min at RT and then analyzed by *radio*-ITLC and

*radio*-RP-HPLC. Following this procedure but using a 100-fold molar excess of GaBr<sub>3</sub> (gallium bromide) dissolved in 0.1 N HCl instead of generator eluate gave the <sup>nat</sup>Ga-chelated peptides which were used for binding affinity measurements.

**2.8.2. Radiolabelling with Zirconium-89.** The cyclotron produced radionuclide was purchased from PerkinElmer (Waltham, US) and delivered as <sup>89</sup>Zr-oxalic acid solution (1 M and ~1 MBq/μL). Approximately 10 MBq (10 μL) was neutralized with 9.6 μL sodium carbonate solution (1 M) at RT. After 3 min 100 μL of 4-(2-hydroxyethyl)-1-piperazineethanesulfonic acid (HEPES) buffer (0.5 M, pH 6.98) was mixed with the radionuclide solution followed by addition of the corresponding peptide (20 μg) and the mixture was incubated for 30–60 min at ambient temperature. The reaction was monitored by *radio*-ITLC. In case of

animal experiments 20  $\mu\text{L}$  of  $\text{CaCl}_2$  (calcium chloride) was added to precipitate  $\text{CaC}_2\text{O}_4$  (calcium oxalate). The resulting suspension was centrifuged for 5 min at  $14 \times 10^3$  rpm (Eppendorf Centrifuge 5424, Hamburg, Germany) and an aliquot from the supernatant was further diluted in PBS for *in vivo* evaluation. Representative chromatograms are shown in the Supplementary Materials (Figure S1).

## 2.9. In Vitro Characterization

**2.9.1. Stability Study.** To assess the stability of the radionuclide complex the radiolabelled peptides were diluted with PBS to a concentration of 5  $\mu\text{M}$ . Aliquots of 50  $\mu\text{L}$  were mixed with PBS (as control), human serum, and a 1.000-fold molar excess over radioligand of either EDTA (pH 7), DTPA (pH 7), or  $\text{FeCl}_3$  (pH 5). Then samples were incubated in duplicate at 37°C up to 4 h for gallium-68 and up to 7 days for zirconium-89 labelled peptides. Samples were analyzed at selected time points via radio-RP-HPLC for  $^{68}\text{Ga}$ -labelled probes and radio-ITLC for  $^{89}\text{Zr}$ -labelled peptides. The ITLC strips were cut into half and measured in the gamma counter to determine the percentage of labelled peptide (origin) to free radionuclide (solvent front).

**2.9.2. Distribution Coefficient (log *D*).** Aliquots (50  $\mu\text{L}$ ) of  $^{68}\text{Ga}$ - and  $^{89}\text{Zr}$ -labelled mono-, di-, and trimer (10  $\mu\text{M}$ ) were diluted in 450  $\mu\text{L}$  PBS. After adding 500  $\mu\text{L}$  octanol the mixture was vortexed with 1400 rpm (MS 3 basic vortexer, IKA, Staufen, Germany) for 15 min at RT followed by centrifugation for 2 min at 4500 rpm. Subsequently, 100  $\mu\text{L}$  aliquots of the organic and the aqueous layer were collected and log *D* values were calculated using Excel ( $n = 3$ , six replicates) after gamma counter measurement.

**2.9.3. Protein Binding.** For protein binding measurement  $^{68}\text{Ga}$ - and  $^{89}\text{Zr}$ -labelled peptides were incubated in PBS as control and fresh human serum and samples were maintained at 37°C. After 1, 2, and 4 h aliquots (25  $\mu\text{L}$ ) were analyzed by size exclusion chromatography using MicroSpin G-50 columns (Sephadex G-50, GE Healthcare, Vienna, Austria) according to manufacturer's protocol. The samples were measured in the gamma counter and the percentage between protein-bound (eluate) and free conjugate (column) was calculated.

**2.9.4. Whole Cell Receptor Binding Affinity Studies ( $IC_{50}$ ).** A431-CCK2R cells were diluted to a density of  $5 \times 10^6$  cells/mL in 50 mM HEPES buffer (pH 7.3) containing 5 mM  $\text{MgCl}_2$  (magnesium chloride) and 0.3% bovine serum albumin (BSA). MultiScreen Filter Plates HTS (96-wells, 1  $\mu\text{m}$  glass fiber filter, Merck Millipore, Darmstadt, Germany) were washed twice with 200  $\mu\text{L}$  of 10 mM TRIS-buffered saline (pH 7.3) and 100  $\mu\text{L}$  of cell suspension was added to each well. Hereafter cells were incubated in triplicate with increasing concentrations [0.001–1.000 nM] of competitor solution (50  $\mu\text{L}$  of metal-bound ( $^{nat}\text{Ga}$ ) mono-, di-, and trimer as well as DOTA-MG11 as reference diluted in 20 mM HEPES, 10 mM  $\text{MgCl}_2$  and 0.1% BSA). After 10 min incubation at RT

50  $\mu\text{L}$  of radioligand (human  $^{125}\text{I}$ -[Leu $^{15}$ ]-Gastrin I,  $4.5 \times 10^4$  cpm, prepared as previously published [17]) was added and the plate was maintained under shaking conditions (Compact Shaker KS-15 control, 200/min) for 1 h. Thereafter each well was washed twice with 200  $\mu\text{L}$  TRIS-buffered saline. Then the filters were measured in the gamma counter and  $IC_{50}$  values were calculated by using nonlinear curve fitting with Origin 6.1 software (Northampton, MA, USA) according to the following formula:  $[\text{NS} + \text{SB}/(1 + x/\text{IC}_{50})]$ .

**2.9.5. CCK-2 Receptor Internalization Assay.** Determination of the receptor-mediated radioligand uptake in A431-CCK2R cells was conducted as previously published [17]. Briefly,  $2 \times 10^6$  cells were seeded per well (12-well plates, Nunc, Thermo Scientific) and left to grow over night. After washing twice and adjusting the volume to 1.2 mL with DMEM containing 1% FBS, 150  $\mu\text{L}$  blocking solution (100-fold molar excess of pentagastrin in PBS/0.5% BSA solution) was added to one-half while 150  $\mu\text{L}$  PBS/0.5% BSA was added to the other half of wells for volume compensation. Hereafter, 150  $\mu\text{L}$  of the radiolabelled conjugate (diluted in PBS/0.5% BSA, approximately 30.000 cpm) was added to have a final concentration of approximately 1 nM in the assay and the plates were incubated at 37°C. After 1 h, 2 h, and 4 h (in case of zirconium-89) the cells were washed with ice-cold medium (=wash fraction), with ice-cold 0.05 M glycine buffer (pH 2.8) (membrane bound fraction) and finally lysed with 2 M sodium hydroxide (internalized fraction). All fractions were measured in the gamma counter to determine the percentage of cell associated radioactivity in relation to total activity added.

**2.10. In Vivo Characterization.** All animal experiments were conducted in compliance with the Austrian and Dutch animal protection laws and with approval of the Austrian Ministry of Science (BMWF-66.011/000604-II/3b/2012 and BMWFW-66.011/0049-WF/II/3b/2014). *In vivo* stability studies were conducted in 5-week-old female BALB/c mice (in-house breed, ZVTA Innsbruck, Dr. Hermann Dietrich). The biodistribution studies were performed using female 8–10-week-old athymic BALB/c nude mice (Charles River Laboratories, Sulzfeld, Germany). Tumour xenografts were induced by subcutaneous injection of  $2 \times 10^6$  A431-CCK2R cells (receptor positive) in the right and the same amount of A431-mock (receptor negative) in the left flank. Tumours were allowed to grow until they had reached a volume of 0.3–0.6  $\text{cm}^3$ .

**2.10.1. In Vivo Stability.**  $^{68}\text{Ga}$ -labelled conjugates were injected via a lateral tail vein using an amount of 1.5 nmol and a radioactivity of 15 MBq. After 5 min mice were euthanized by cervical dislocation and blood samples were taken by heart puncture. Aliquots of the blood were immediately precipitated by adding 0.1% TFA/ACN (1:1 v/v) and the supernatant was diluted with  $\text{H}_2\text{O}$  and analyzed by radio-RP-HPLC.

**2.10.2. Ex Vivo Biodistribution.** To evaluate the biodistribution profile nude mice ( $n = 4$ ) were intravenously injected

with either 1–2 MBq  $^{68}\text{Ga}$ - or 0.3 MBq  $^{89}\text{Zr}$ -labelled mono-, di-, and trimer (0.1–0.2 nmol). The animals were sacrificed by cervical dislocation after 1 h as well as 2 h and 4 h in case of  $^{68}\text{Ga}$ - and  $^{89}\text{Zr}$ -labelled trimer, followed by the collection of organs and tissue. The collected samples were measured in the gamma counter and the results were calculated as percentage of injected dose per gram tissue (% ID/g).

**2.10.3. MicroPET/CT Imaging.** Small animal imaging experiments were carried out with an Inveon microPET/CT scanner (Siemens Preclinical Solutions, Knoxville, USA). A group of eight double tumour xenografted mice were injected intravenously with either 8–13 MBq of  $^{68}\text{Ga}$ -labelled tracers (0.2–0.5 nmol) or 3–5 MBq of  $^{89}\text{Zr}$ -labelled peptides (0.4–1.0 nmol). MicroPET images were acquired under general anaesthesia (isoflurane/ $\text{O}_2$ ) for 15–60 min with static PET/CT scans after 1 h and additionally after 4 and 24 h for  $^{89}\text{Zr}$ -labelled conjugates. The microPET/CT scans were reconstructed with OSEM3D-SPMAP (PET, matrix size 256 × 256) and Feldkamp (CT, Shepp Logan filter).

**2.11. Statistical Analysis.** Statistical analysis was performed using the Student's *t*-test with *P* value < 0.05 indicating significance.

### 3. Results

**3.1. Precursor Synthesis.** MG11-SH could be obtained in good yield following SPPS protocol. [Fe]FSC could be extracted from fungal culture in sufficient purity to be used for further modification without additional purification. Acetylation reaction resulted in a mixture of mono- and multiple acetylated derivatives of [Fe]FSC due to three identical primary amines but the desired products were easily accessible via preparative RP-HPLC purification. Functionalization with maleimide linker was straightforward utilizing a NHS-ester strategy and conjugation of up to three targeting vectors was conducted site-specifically via maleimide-thiol crosslink reaction. All intermediates as well as final conjugates were obtained in good yield, with excellent chemical purity (>95%; analytical RP-HPLC, UV absorption at  $\lambda = 220$  nm), and corresponding mass analysis was in good agreement with the calculated values.

**3.2. Radiolabelling.** Mono- and multimeric conjugates were quantitatively labelled with gallium-68 after 5–15 min and after 30–60 min with zirconium-89 at high molar activities and used without further purification.

**3.3. In Vitro Characterization.** The complex stability was evaluated by incubating the radiolabelled conjugates in 1000-fold molar excess of EDTA, DTPA,  $\text{FeCl}_3$  (iron chloride), fresh human serum, and PBS over a period of 4 h for gallium-68 and 7 days for zirconium-89, respectively. The radiolabelled peptides showed no significant release of radionuclide in all media except EDTA after 7 d where 20 to 30% release of radionuclide was observed indicating excellent stability of  $^{68}\text{Ga}$  and  $^{89}\text{Zr}$ -FSC. The data from this transchelation study

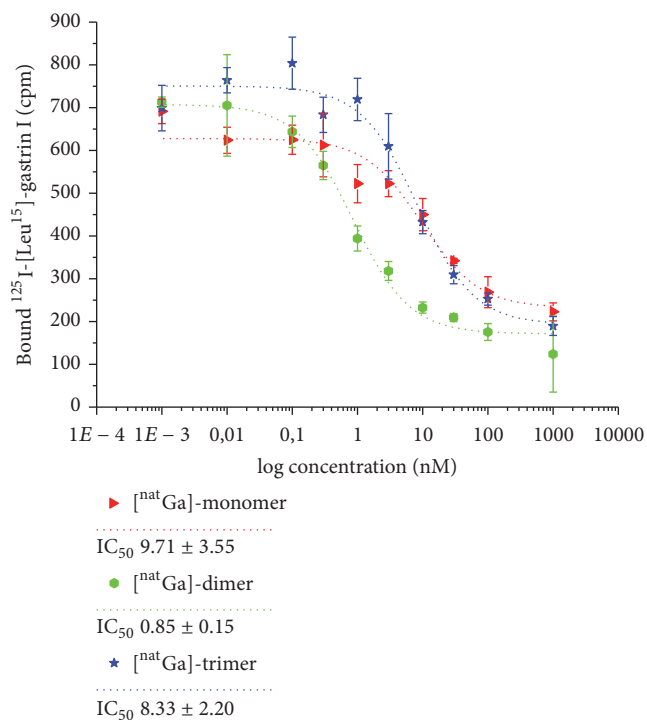


FIGURE 1: Binding affinity ( $\text{IC}_{50}$  values) of metal-bound ( $^{nat}\text{Ga}$ ) mono-, di-, and trimer on whole A431-CCK2R cells.

are presented in detail in the Supplementary Materials (Table S1).

Distribution coefficient ( $\log D$ ) values and protein binding data are summarized in Table 1. The results indicate a hydrophilic character of all conjugates but, as expected, clearly showed that the grade of multimerization is accompanied by increased lipophilicity. Binding to serum proteins was low (<10%) for monomeric, moderate (10–25%) for dimeric, and high for (30–50%) trimeric conjugates. Furthermore, protein binding was consistent over time for  $^{68}\text{Ga}$ -labelled mono- and dimer but increased for  $^{68}\text{Ga}$ -trimer whereas all  $^{89}\text{Zr}$ -labelled counterparts showed a slight increase over a period of 4 h.

Competition assays on whole A431-CCK2R (Figure 1) revealed high binding affinity as the  $\text{IC}_{50}$  values were in the low nanomolar range for all bioconjugates. The affinity of the dimer ( $0.85 \pm 0.15$  nM) was approximately 10-fold higher while the monomer ( $9.7 \pm 3.5$  nM) and the trimer ( $8.3 \pm 2.2$  nM) remained comparable to the reference peptide DOTA-MG11 ( $9.5 \pm 0.5$  nM) [17].

Cellular processing of A431-CCK2R cells incubated with  $^{68}\text{Ga}$ - and  $^{89}\text{Zr}$ -labelled mono- and multimeric tracers is summarized in Figure 2. In general, all conjugates showed increasing uptake over time while the unspecific cell bound fraction of corresponding blocking studies remained <1%, thus indicating highly specific receptor-mediated cell uptake. Furthermore the  $^{68}\text{Ga}$ -dimer showed significantly increased uptake after 1 h-incubation compared to the monomer ( $P = 9.01 \times 10^{-6}$ ) and the trimer ( $P = 0.009$ ) while after 2 h-incubation only the uptake of the monomer remained lower

TABLE 1: Distribution coefficient and protein binding of mono- and multimeric conjugates radiolabelled with gallium-68 and zirconium-89.

| Distribution coefficient | log $D$ (pH 7.4) | $^{68}\text{Ga}$ -labelled |                  |                  | $^{89}\text{Zr}$ -labelled |                  |                  |
|--------------------------|------------------|----------------------------|------------------|------------------|----------------------------|------------------|------------------|
|                          |                  | Monomer                    | Dimer            | Trimer           | Monomer                    | Dimer            | Trimer           |
|                          |                  | $-2.99 \pm 0.02$           | $-2.38 \pm 0.04$ | $-2.20 \pm 0.07$ | $-3.17 \pm 0.06$           | $-2.83 \pm 0.02$ | $-2.41 \pm 0.04$ |
| Protein binding (%)      | 1 h              | $3.71 \pm 0.86$            | $15.94 \pm 1.25$ | $40.69 \pm 0.93$ | $5.51 \pm 0.41$            | $15.86 \pm 0.31$ | $31.52 \pm 0.19$ |
|                          | 2 h              | $4.16 \pm 0.22$            | $18.77 \pm 2.93$ | $44.33 \pm 1.41$ | $6.48 \pm 0.45$            | $20.83 \pm 0.15$ | $35.73 \pm 0.92$ |
|                          | 4 h              | $3.16 \pm 0.49$            | $17.86 \pm 0.32$ | $48.32 \pm 1.71$ | $7.28 \pm 0.40$            | $26.75 \pm 0.49$ | $41.39 \pm 2.81$ |

Data are presented as mean  $\pm$  SD ( $n = 3$ ).

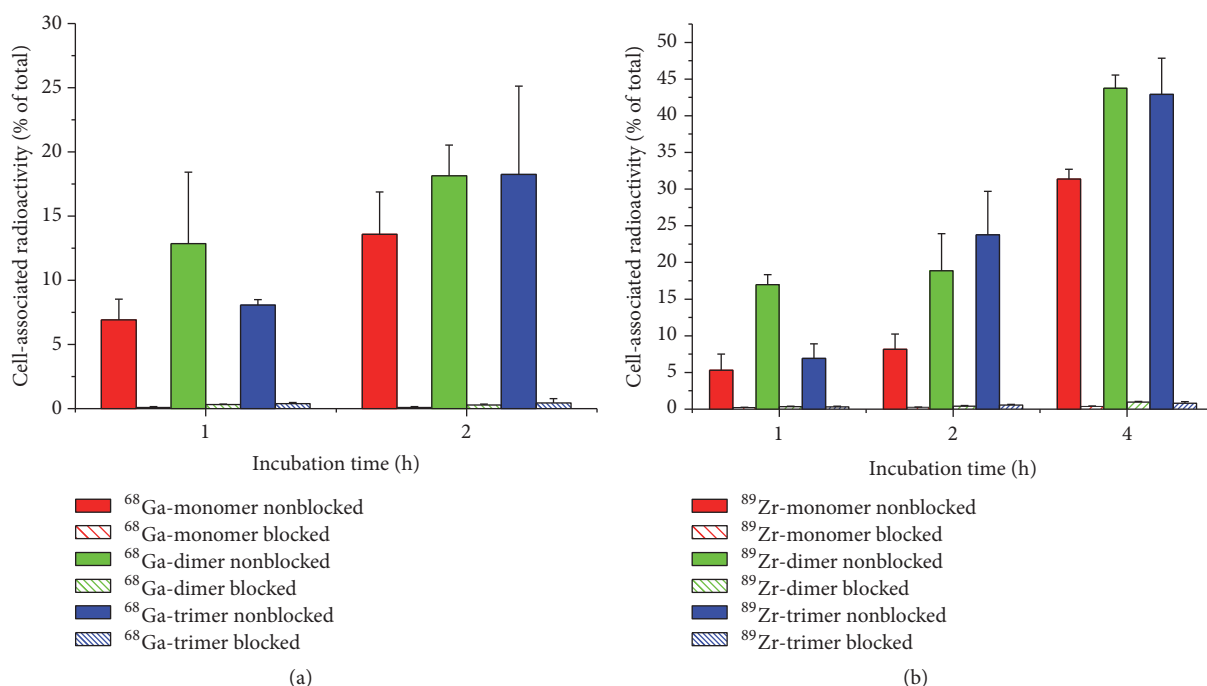


FIGURE 2: Cell-uptake studies of A431-CCK2R cells incubated with  $^{68}\text{Ga}$ -labelled mono- and multimers (a) and  $^{89}\text{Zr}$ -labelled counterparts (b). Blocking was performed with pentagastrin in 100-fold molar excess over the conjugate.

( $P = 0.001$ ). This trend was observed in the same manner for the  $^{89}\text{Zr}$ -labelled counterparts and was substantiated by the results after 4 h of incubation.

**3.4. In Vivo Characterization.** Investigations on the *in vivo* stability are shown in Figure 3. RP-HPLC analysis of the corresponding blood samples showed increasing amount of intact radioligand to be found in following order trimer > dimer > monomer, indicating that multimerization is accompanied with increased metabolic stability. The results of the *ex vivo* biodistribution studies in double tumour xenografted nude mice are summarized in Table 2 and corresponding tumour-to-organ ratios are presented in Table 3. Mono- and dimeric bioconjugates radiolabelled with gallium-68 were rapidly cleared from the bloodstream and showed highly specific tumour targeting properties as the uptake in nontargeted tissue was very low, except kidneys, 1 h after administration of the radiotracers. Furthermore, the dimer

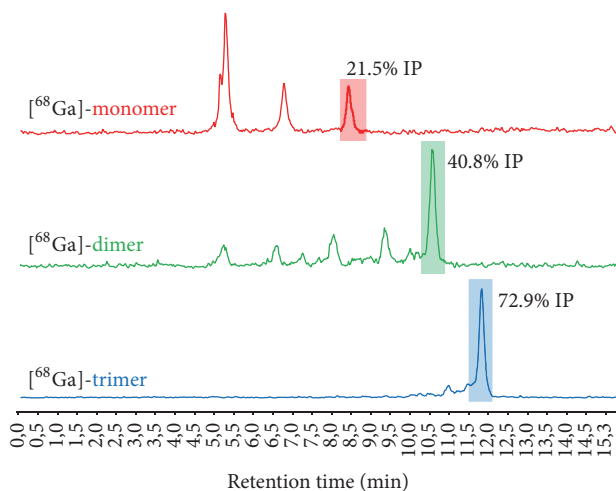


FIGURE 3: Representative *radio*-RP-HPLC chromatograms of *in vivo* stability studies in BALB/c mice 5 min p.i. (IP: intact peptide).

TABLE 2: *Ex vivo* biodistribution studies of <sup>68</sup>Ga-labelled mono- and multimers as well as <sup>89</sup>Zr-labelled counterparts in double tumour (±) xenografted BALB/C nude mice; data are presented as percentage of injected dose per gram tissue (% ID/g); mean (n = 4) ± SD.

|            | <sup>68</sup> Ga-labelled  |                           |                          | <sup>89</sup> Zr-labelled  |                           |                          |
|------------|----------------------------|---------------------------|--------------------------|----------------------------|---------------------------|--------------------------|
|            | Monomer<br>1h              | Dimer<br>1h               | Trimer<br>2h             | Monomer<br>1h              | Dimer<br>1h               | Trimer<br>2h             |
| Blood      | 0.35 ± 0.06 <sup>ab</sup>  | 0.53 ± 0.06 <sup>cd</sup> | 2.53 ± 0.67              | 0.30 ± 0.19 <sup>ab</sup>  | 1.17 ± 0.28               | 1.19 ± 0.32 <sup>d</sup> |
| Spleen     | 0.18 ± 0.04 <sup>ab</sup>  | 0.37 ± 0.04 <sup>cd</sup> | 2.89 ± 0.53              | 0.12 ± 0.04 <sup>ab</sup>  | 0.99 ± 0.40               | 0.90 ± 0.25 <sup>d</sup> |
| Pancreas   | 0.29 ± 0.02 <sup>ab</sup>  | 0.48 ± 0.06 <sup>cd</sup> | 1.80 ± 0.31              | 0.15 ± 0.04 <sup>abd</sup> | 0.95 ± 0.23 <sup>c</sup>  | 1.51 ± 0.40              |
| Stomach    | 1.07 ± 0.14 <sup>ab</sup>  | 2.13 ± 0.23 <sup>c</sup>  | 3.86 ± 1.36 <sup>f</sup> | 0.42 ± 0.14 <sup>abd</sup> | 2.99 ± 1.13               | 3.15 ± 0.75              |
| Intestine  | 0.58 ± 0.17 <sup>b</sup>   | 0.44 ± 0.06 <sup>c</sup>  | 1.86 ± 0.33              | 0.27 ± 0.10 <sup>abd</sup> | 0.73 ± 0.25               | 0.44 ± 0.30 <sup>d</sup> |
| Kidneys    | 5.57 ± 0.57 <sup>abd</sup> | 28.9 ± 3.4 <sup>cd</sup>  | 59.6 ± 4.3 <sup>f</sup>  | 11.3 ± 2.10 <sup>ab</sup>  | 55.5 ± 10.3               | 96.5 ± 23.6 <sup>f</sup> |
| Liver      | 0.23 ± 0.02 <sup>ab</sup>  | 0.78 ± 0.09 <sup>c</sup>  | 4.09 ± 0.85              | 0.16 ± 0.04 <sup>abd</sup> | 0.83 ± 0.20               | 1.28 ± 0.35 <sup>d</sup> |
| Heart      | 0.17 ± 0.02 <sup>ab</sup>  | 0.31 ± 0.04 <sup>cd</sup> | 2.18 ± 0.31              | 0.14 ± 0.05 <sup>ab</sup>  | 1.01 ± 0.37               | 0.91 ± 0.25 <sup>d</sup> |
| Lung       | 0.42 ± 0.06 <sup>ab</sup>  | 0.59 ± 0.08 <sup>cd</sup> | 5.78 ± 0.92              | 0.31 ± 0.09 <sup>ab</sup>  | 1.16 ± 0.28               | 1.21 ± 0.23 <sup>d</sup> |
| Muscle     | 0.20 ± 0.05 <sup>b</sup>   | 0.30 ± 0.08 <sup>cd</sup> | 0.65 ± 0.14              | 0.13 ± 0.04 <sup>ab</sup>  | 1.51 ± 0.70               | 0.42 ± 0.07 <sup>d</sup> |
| Bone       | 0.31 ± 0.08 <sup>b</sup>   | 0.60 ± 0.21 <sup>cd</sup> | 2.52 ± 0.79              | 0.42 ± 0.10 <sup>ab</sup>  | 1.36 ± 0.42               | 2.07 ± 0.68              |
| A431-CCK2R | 4.86 ± 1.00 <sup>d</sup>   | 8.36 ± 0.90 <sup>ac</sup> | 8.73 ± 2.65 <sup>e</sup> | 1.91 ± 0.40                | 7.69 ± 1.34 <sup>ac</sup> | 8.90 ± 3.10 <sup>e</sup> |
| A431-mock  | 0.30 ± 0.04 <sup>b</sup>   | 0.36 ± 0.22 <sup>cd</sup> | 3.18 ± 0.51              | 0.26 ± 0.05 <sup>ab</sup>  | 0.86 ± 0.22               | 0.93 ± 0.29 <sup>d</sup> |
|            |                            |                           |                          |                            |                           | 0.75 ± 0.26 <sup>d</sup> |
|            |                            |                           |                          |                            |                           | 0.95 ± 0.13 <sup>d</sup> |
|            |                            |                           |                          |                            |                           | 2.34 ± 0.59              |
|            |                            |                           |                          |                            |                           | 3.50 ± 0.86 <sup>d</sup> |
|            |                            |                           |                          |                            |                           | 0.65 ± 0.07 <sup>d</sup> |
|            |                            |                           |                          |                            |                           | 150.5 ± 18.3             |
|            |                            |                           |                          |                            |                           | 1.71 ± 0.32 <sup>d</sup> |
|            |                            |                           |                          |                            |                           | 0.91 ± 0.09 <sup>d</sup> |
|            |                            |                           |                          |                            |                           | 0.84 ± 0.20 <sup>d</sup> |
|            |                            |                           |                          |                            |                           | 0.62 ± 0.23              |
|            |                            |                           |                          |                            |                           | 4.41 ± 1.31              |
|            |                            |                           |                          |                            |                           | 14.39 ± 3.92             |
|            |                            |                           |                          |                            |                           | 0.66 ± 0.06 <sup>d</sup> |

Statistical analysis was performed using the Student's *t*-test with *P* values indicating significant (*P* < 0.05) difference (a) between mono- and dimer, (b) between mono- and trimer, (c) between di- and trimer, (d) between <sup>68</sup>Ga-labelled tracers and corresponding <sup>89</sup>Zr-labelled counterparts, (e) between 1h and 2h, and (f) between 2h and 4h of radiolabelled trimer.

TABLE 3: Corresponding tumour-to-organ ratios of  $^{68}\text{Ga}$ - and  $^{89}\text{Zr}$ -labelled bioconjugates; data are presented as mean  $\pm$  SD.

| Ratio T/O | $^{68}\text{Ga}$ -labelled |                      |                 |                   |                  |                   | $^{89}\text{Zr}$ -labelled |                 |                     |                     |        |    |    |
|-----------|----------------------------|----------------------|-----------------|-------------------|------------------|-------------------|----------------------------|-----------------|---------------------|---------------------|--------|----|----|
|           | Monomer                    |                      | Dimer           |                   | Trimer           |                   | Monomer                    |                 | Dimer               |                     | Trimer |    |    |
|           | 1h                         |                      | 1h              |                   | 2h               | 4h                | 1h                         |                 | 1h                  |                     | 1h     | 2h | 4h |
| Blood     | $14.4 \pm 3.6^b$           | $16.0 \pm 3.1^{cd}$  | $1.8 \pm 0.5$   | $3.6 \pm 1.0^e$   | $8.5 \pm 2.1^f$  | $9.0 \pm 4.7^b$   | $7.4 \pm 2.3^c$            | $3.2 \pm 0.8^d$ | $7.3 \pm 0.8^{de}$  | $20.1 \pm 4.8^{df}$ |        |    |    |
| Spleen    | $27.3 \pm 6.3^b$           | $23.1 \pm 4.2^{cd}$  | $2.8 \pm 0.4$   | $3.1 \pm 0.7$     | $5.5 \pm 1.4^f$  | $18.7 \pm 6.1^b$  | $10.5 \pm 4.5$             | $6.1 \pm 1.8^d$ | $9.7 \pm 1.5^{de}$  | $14.9 \pm 2.5^{fe}$ |        |    |    |
| Pancreas  | $16.7 \pm 3.0^{bd}$        | $17.9 \pm 3.2^{cd}$  | $4.5 \pm 1.0^d$ | $4.9 \pm 1.1$     | $4.7 \pm 1.5$    | $13.3 \pm 2.9^b$  | $9.2 \pm 3.1^c$            | $2.7 \pm 0.2$   | $6.0 \pm 2.0^e$     | $6.3 \pm 1.7$       |        |    |    |
| Stomach   | $4.6 \pm 1.1^b$            | $4.0 \pm 0.5^c$      | $2.0 \pm 0.8$   | $2.3 \pm 0.3^f$   | $1.1 \pm 0.3$    | $4.9 \pm 1.3^b$   | $3.4 \pm 1.1$              | $1.6 \pm 0.3$   | $2.8 \pm 0.7^e$     | $4.5 \pm 1.9^d$     |        |    |    |
| Intestine | $9.4 \pm 3.7^b$            | $19.9 \pm 4.9^{acd}$ | $5.4 \pm 1.1$   | $4.8 \pm 1.3$     | $6.0 \pm 1.3$    | $7.9 \pm 2.3$     | $12.5 \pm 3.1$             | $8.4 \pm 2.0^d$ | $15.7 \pm 1.5^{de}$ | $22.2 \pm 5.5^d$    |        |    |    |
| Kidneys   | $0.86 \pm 0.13^{abd}$      | $0.30 \pm 0.06^{cd}$ | $0.13 \pm 0.05$ | $0.13 \pm 0.02^f$ | $0.07 \pm 0.01$  | $0.17 \pm 0.03^b$ | $0.15 \pm 0.06$            | $0.08 \pm 0.02$ | $0.09 \pm 0.02$     | $0.10 \pm 0.03$     |        |    |    |
| Liver     | $21.1 \pm 3.1^{abd}$       | $11.1 \pm 2.4^c$     | $1.7 \pm 0.6$   | $2.1 \pm 0.4$     | $2.8 \pm 1.0$    | $12.4 \pm 2.8^b$  | $10.3 \pm 3.2^c$           | $5.7 \pm 1.1^d$ | $6.9 \pm 0.8^d$     | $8.8 \pm 3.1^d$     |        |    |    |
| Heart     | $29.5 \pm 9.3^{bd}$        | $27.2 \pm 4.8^{cd}$  | $3.8 \pm 1.0$   | $4.0 \pm 0.8$     | $10.1 \pm 3.2^f$ | $14.8 \pm 4.7^b$  | $9.8 \pm 4.8$              | $5.0 \pm 1.0$   | $9.7 \pm 1.2^{de}$  | $15.6 \pm 2.7^{df}$ |        |    |    |
| Lung      | $11.7 \pm 2.1^{bd}$        | $14.4 \pm 2.3^{cd}$  | $1.5 \pm 0.4$   | $1.5 \pm 0.5$     | $3.9 \pm 0.8^f$  | $6.5 \pm 1.6^b$   | $7.6 \pm 2.9^c$            | $3.3 \pm 0.7^d$ | $7.1 \pm 1.5^{de}$  | $17.3 \pm 2.9^{df}$ |        |    |    |
| Muscle    | $20.4 \pm 1.8^b$           | $31.4 \pm 13.2^{cd}$ | $8.4 \pm 2.6$   | $14.5 \pm 5.9^e$  | $13.5 \pm 5.4$   | $15.9 \pm 4.2^b$  | $7.9 \pm 5.3$              | $8.4 \pm 0.9$   | $20.7 \pm 6.1^e$    | $25.4 \pm 6.8$      |        |    |    |
| Bone      | $17.1 \pm 7.4^{bd}$        | $11.6 \pm 1.9^c$     | $2.6 \pm 1.0$   | $3.8 \pm 1.3$     | $7.2 \pm 2.6$    | $4.7 \pm 1.3^b$   | $7.4 \pm 1.2^c$            | $2.2 \pm 0.1$   | $4.4 \pm 1.9$       | $3.4 \pm 0.8$       |        |    |    |
| A431-mock | $16.3 \pm 3.3^{bd}$        | $17.9 \pm 6.1^c$     | $2.9 \pm 0.4$   | $2.9 \pm 0.5$     | $7.0 \pm 1.9^f$  | $7.5 \pm 1.8$     | $11.2 \pm 2.3$             | $6.3 \pm 2.6^d$ | $10.7 \pm 4.3^d$    | $21.6 \pm 5.0^{df}$ |        |    |    |

Statistical analysis was performed using the Student's *t*-test with *P* values indicating significant ( $P < 0.05$ ) difference (a) between mono- and dimer, (b) between mono- and trimer, (c) between di- and trimer, (d) between  $^{68}\text{Ga}$ -labelled tracers and corresponding  $^{89}\text{Zr}$ -labelled counterparts, (e) between 1h and 2h, and (f) between 2h and 4h of radiolabelled trimer.

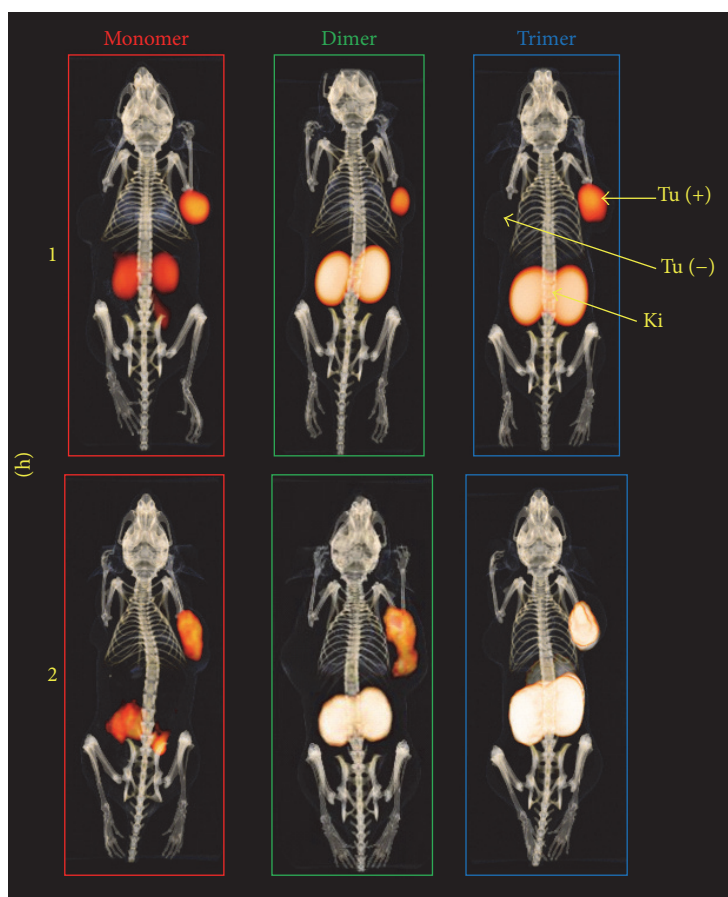


FIGURE 4: Three-dimensional volume projections of fused microPET/CT static images in A431-CCK2R [Tu (+)] and A431-mock [Tu (-)] tumour xenograft-bearing BALB/c nude mice 1 and 2 h p.i. of the  $^{68}\text{Ga}$ -labelled conjugates. [Ki: kidneys]

showed significantly ( $P < 0.005$ ) increased tumour uptake compared to the monomer but also higher accumulation in renal tissue. However, the corresponding tumour-to-organ ratios revealed no significant difference in most of the organs. In contrast, the  $^{68}\text{Ga}$ -trimer cleared slowly from the body and showed higher blood level 1 h p.i. This was substantiated as the uptake in malignant tissue was comparable to the monomer 1 h p.i. but increased consistently over time accompanied by very high accumulation renal tissue. In addition, also an elevated accumulation in nontargeted tissue was observed for the  $^{68}\text{Ga}$ -trimer, resulting in significantly lower tumour-to-organ ratios compared to mono- and dimer. In comparison, the respective  $^{89}\text{Zr}$ -labelled counterparts showed a similar behaviour *in vivo* with somewhat lower tumour uptake 1 h p.i. but consistently higher accumulation in renal tissue.  $^{89}\text{Zr}$  mono- and dimers revealed a trend towards reduced tumour-to-organ ratios as compared to the  $^{68}\text{Ga}$ -counterparts. In contrast, over time the  $^{89}\text{Zr}$ -trimer showed a faster elimination from blood and lower unspecific tissue uptake. This resulted in higher tumour-to-organ ratios compared to the  $^{68}\text{Ga}$ -labelled counterpart especially 4 h p.i. and may be attributed to the increased hydrophilic character of this radiotracer. Small animal PET/CT imaging studies confirmed these findings and the results for  $^{68}\text{Ga}$ -labelled conjugates

are presented in Figure 4 whereas imaging of the  $^{89}\text{Zr}$ -labelled counterparts is shown in Figure 5. The predominant accumulation of radioactivity found in the kidneys, related to elimination via renal pathway accompanied by tubular reabsorption, was in good agreement with the results of our biodistribution studies and clearly showed that kidney uptake is increased with the grade of multimerization. Furthermore, imaging showed highly specific targeting properties for all conjugates as CCK2 related malignancies were clearly visualized already 1 h after injection without major differences between the bioconjugates. However, imaging at 2 h p.i. for  $^{68}\text{Ga}$ -labelled and that at 24 h p.i. for  $^{89}\text{Zr}$ -labelled probe pronounce the increased uptake in CCK2R expressing tissue.

#### 4. Discussion

The cyclic siderophore based chelator FSC enables a straightforward multistep synthesis of multivalent imaging probes. Three amines attached to the chelating scaffold of FSC can be utilized for further modifications whereas DOTA, for example, offers only one binding site for conjugation of targeting probes. This results in a different but more symmetrical architecture of FSC-related multivalent bioconjugates.

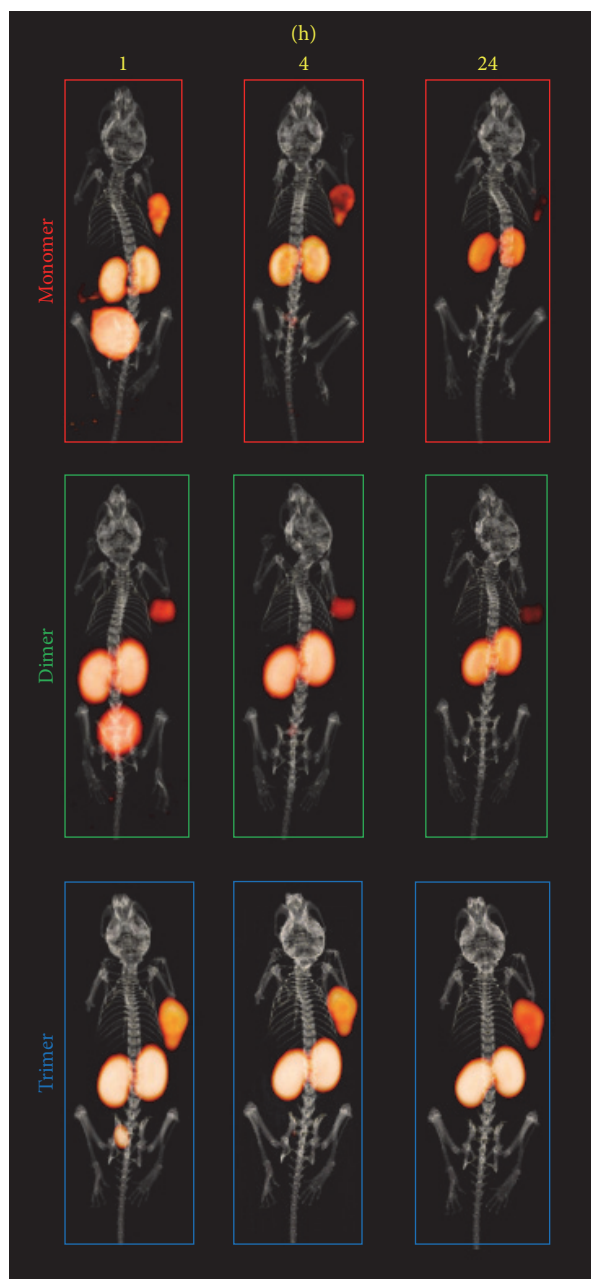


FIGURE 5: Animal imaging studies of  $^{89}\text{Zr}$ -labelled conjugates in A431-CCK2R/A431-mock tumour xenografted BALB/C nude mice; 3D volume rendered projections of fused static microPET/CT images.

Asymmetric tracer design might not be critical in case of small peptides for targeted imaging but can become an issue in case of multimerization of larger biomolecules (e.g., engineered scaffold proteins, ESP) as the asymmetry can result in less flexibility or increased sterical hindrance at the target interaction site. The suitability for FSC as chelating scaffold for ESP has recently been shown although acetylation of two amines was conducted to design a monovalent affibody construct [18]. Furthermore, FSC can be labelled with gallium-68 and zirconium-89 at RT with sufficient

complex stability (Table S1), which is beneficial in case of heat-sensitive molecules. This is also of particular interest for CCK2R targeting peptide derivatives containing methionine as previous studies have shown that heating related oxidation is accompanied by reduced receptor affinity [19]. In contrast, DOTA-conjugates have to be heated for efficient radiolabelling with gallium-68 and in case of oxidation sensitivity of the targeting probe additives (e.g., ascorbic acid) are needed to improve radiochemical purity. Both  $^{68}\text{Ga}$  and  $^{89}\text{Zr}$  FSC-conjugates showed *high in vivo* stability; there was also no significant difference in bone uptake between  $^{68}\text{Ga}$  and  $^{89}\text{Zr}$  counterparts, indicating insignificant *in vivo* release of  $^{89}\text{Zr}$ , confirming recent findings [15].

Overall FSC-based imaging probes showed high CCK2R binding affinity (Figure 1) with values in the low nanomolar range. The divalent probe showing higher affinity is quite consistent with previous reports on  $^{111}\text{In}$ -MGD5 [11]. Interestingly, increasing the valency from mono- to trimeric constructs, no increase in binding affinity was achieved.

All FSC-based conjugates showed highly specific receptor targeting as demonstrated *in vitro* (Figure 2) and also *in vivo* imaging (Figures 4 and 5) confirmed these findings. Multimerization is accompanied by decreased hydrophilicity and increased binding to serum proteins (Table 2) leading to slower pharmacokinetics *in vivo*, especially for the trimer. Furthermore, kidney retention was considerably increased by the grade of multimerization (Table 3). This is substantiated by the faster blood clearance of  $^{89}\text{Zr}$ -labelled counterparts due to higher hydrophilicity but increased kidney uptake which may be related to the additional charge introduced as the hexadentate chelator FSC only compensates three of four positive charges of  $\text{Zr}^{4+}$ . Overall, high kidney retention might be critical in case of therapeutic use but is tolerable for diagnostic applications of radiopharmaceuticals [20].

Interestingly, improvement due to multimerization was more pronounced at later time points. While internalization data revealed higher cell uptake at 1 h for the dimer over the trimer, at later time points the trimer showed higher internalization rates. This phenomenon was also seen *in vivo* where the dimer revealed a higher tumour uptake at 1 h p.i., whereas the uptake increased substantially after 2 and 4 h p.i. for the trimer exceeding the values of the dimer at 1 h p.i. This *in vivo* effects may be explained by a slower target accumulation of the trimer but also by the higher protein binding and slow blood clearance that may act as depot to prolong the tracer concentration at the tumour site, improving imaging contrast over time (Table 3). Furthermore, the improved metabolic stability (Figure 3) of multimeric radioligands targeting CCK2R expression, which has been shown in this study for the first time, also may result in the formation of rebinding metabolites enhancing the imaging contrast over time. This hypothesis is substantiated by the slow tumour washout particularly observed for  $^{89}\text{Zr}$ -trimer at 24 h p.i. (Figure 5) making imaging at late timepoints with multivalent peptides tracers radiolabelled with zirconium-89 not per se uninteresting. Additionally, improving metabolic stability by this multivalency-approach might also be highly interesting for non-radiopharmaceutical-based applications

such as therapeutic peptides but definitely warrants further investigations regarding formation of metabolites and their target interaction ability.

## 5. Conclusion

In this study, novel mono- and multimeric bioconjugates utilizing FSC for radiolabelling with gallium-68 and zirconium-89 for PET applications targeting CCK2R expression were synthesized and evaluated for the first time. The resulting imaging probes showed highly specific receptor targeting characteristics which were only partly improved in terms of binding affinity and *in vivo* targeting by the grade of multimerization. However, the higher metabolic stability and improved target retention *in vivo* of multivalent conjugates warrant further investigations on the formation of metabolites with the retained receptor binding ability. Overall this study established FSC as a promising scaffold for the development of mono- and multimeric targeted bioconjugates for molecular imaging with PET.

## Abbreviations

|          |   |
|----------|---|
| FSC:     | Fusarinine C  |
| MG:      | Minigastrin   |
| CCK2:    | Cholecystokinin receptor subtype 2                        |
| PET/CT:  | Positron emission computed tomography                     |
| RT:      | Room temperature  |
| DOTA:    | 1,4,7,10-Tetraazacyclododecane-1,4,7,10-tetraacetic acid  |
| DTPA:    | Diethylene triamine pentaacetic acid                      |
| PBS:     | Phosphate buffered saline                                 |
| BSA:     | Bovine serum albumin                                      |
| HEPES:   | 4-(2-Hydroxyethyl)-1-piperazineethanesulfonic acid buffer |
| TRIS:    | Tris-(hydroxymethyl)aminomethane                          |
| EDTA:    | Ethylenediaminetetra acetic acid                          |
| RP-HPLC: | Reversed-phase high-performance liquid chromatography     |
| TLC:     | Thin layer chromatography                                 |
| p.i.:    | Postinjection.  |

## Disclosure

Dominik Summer's contributions to this study are part of his Ph.D. thesis within the IGDT programme of the Medical University Innsbruck, Austria.

## Conflicts of Interest

The authors declare no conflicts of interest.

## Acknowledgments

This study was financially supported by the Austrian Science Foundation (FWF) Grant P 25899-B23 (Dominik Summer, Christine Rangger, Maximilian Klingler, Elisabeth

von Guggenberg, Clemens Decristoforo) and Grant I 1346 (Thomas Orasch, Beatrix E. Lechner, Hubertus Haas).

## Supplementary Materials

This section contains a detailed description regarding the synthesis of the conjugates. Furthermore representative RP-HPLC chromatograms of <sup>68</sup>Ga-labelled as well as radio-ITLC analysis of <sup>89</sup>Zr-labelled probes are shown in Figure S1. The results of transchelation studies for <sup>68</sup>Ga- and <sup>89</sup>Zr-labelled conjugates are presented in Table S1. Figure S1: (A) radio-RP-HPLC chromatograms of <sup>68</sup>Ga- and (B) radio-ITLC analysis of <sup>89</sup>Zr-labelled mono- and multimeric conjugates. Table S1: transchelation studies of <sup>68</sup>Ga and <sup>89</sup>Zr mono- and multimers; data is expressed as percentage of peptide-associated radioactivity. (*Supplementary Materials*)

## References

- [1] J. C. Reubi, "Peptide receptors as molecular targets for cancer diagnosis and therapy," *Endocrine Reviews*, vol. 24, no. 4, pp. 389–427, 2003.
- [2] M. Fani and H. R. Maecke, "Radiopharmaceutical development of radiolabelled peptides," *European Journal of Nuclear Medicine and Molecular Imaging*, vol. 39, no. 1, pp. S11–S30, 2012.
- [3] M. Dufresne, C. Seva, and D. Fourmy, "Cholecystokinin and gastrin receptors," *Physiological Reviews*, vol. 86, no. 3, pp. 805–847, 2006.
- [4] A. Dash, S. Chakraborty, M. R. A. Pillai, and F. F. R. Knapp, "Peptide receptor radionuclide therapy: An overview," *Cancer Biotherapy and Radiopharmaceuticals*, vol. 30, no. 2, pp. 47–71, 2015.
- [5] T. M. Behr, N. Jenner, M. Béhé et al., "Radiolabeled Peptides for Targeting Cholecystokinin-B/Gastrin Receptor-Expressing Tumors," *Journal of Nuclear Medicine*, no. 40, pp. 1029–1044, 1999.
- [6] P. Laverman, L. Joosten, A. Eek et al., "Comparative biodistribution of 12 <sup>111</sup>In-labelled gastrin/CCK2 receptor-targeting peptides," *European Journal of Nuclear Medicine and Molecular Imaging*, vol. 38, no. 8, pp. 1410–1416, 2011.
- [7] M. Ocak, A. Helbok, C. Rangger et al., "Comparison of biological stability and metabolism of CCK2 receptor targeting peptides, a collaborative project under COST BM0607," *European Journal of Nuclear Medicine and Molecular Imaging*, vol. 38, no. 8, pp. 1426–1435, 2011.
- [8] S. Roosenburg, P. Laverman, F. L. Van Delft, and O. C. Boerman, "Radiolabeled CCK/gastrin peptides for imaging and therapy of CCK2 receptor-expressing tumors," *Amino Acids*, vol. 41, no. 5, pp. 1049–1058, 2011.
- [9] A. Kaloudi, B. A. Nock, E. Lymperis, E. P. Krenning, M. De Jong, and T. Maina, "Improving the *in Vivo* Profile of Minigastrin Radiotracers: A Comparative Study Involving the Neutral Endopeptidase Inhibitor Phosphoramidon," *Cancer Biotherapy and Radiopharmaceuticals*, vol. 31, no. 1, pp. 20–28, 2016.
- [10] S. Lindner, C. Michler, B. Wängler et al., "PESIN multimerization improves receptor avidities and *in vivo* tumor targeting properties to GRPR-overexpressing tumors," *Bioconjugate Chemistry*, vol. 25, no. 3, pp. 489–500, 2014.
- [11] C. Wängler, S. Maschauer, O. Prante et al., "Multimerization of cRGD peptides by click chemistry: Synthetic strategies,

- chemical limitations, and influence on biological properties,” *ChemBioChem*, vol. 11, no. 15, pp. 2168–2181, 2010.
- [12] G. Carlucci, H. J. K. Ananias, Z. Yu et al., “Multimerization improves targeting of peptide Radio-Pharmaceuticals,” *Current Pharmaceutical Design*, vol. 18, no. 17, pp. 2501–2516, 2012.
- [13] J. K. Sosabowski, T. Matzow, J. M. Foster et al., “Targeting of CCK-2 receptor-expressing tumors using a radiolabeled divalent gastrin peptide,” *Journal of Nuclear Medicine*, vol. 50, no. 12, pp. 2082–2089, 2009.
- [14] P. A. Knetsch, C. Zhai, C. Rangger et al., “[68Ga]FSC-(RGD)<sub>3</sub> a trimeric RGD peptide for imaging  $\alpha v\beta 3$  integrin expression based on a novel siderophore derived chelating scaffold-synthesis and evaluation,” *Nuclear Medicine and Biology*, vol. 42, no. 2, pp. 115–122, 2015.
- [15] C. Zhai, D. Summer, C. Rangger et al., “Novel bifunctional cyclic chelator for <sup>89</sup>Zr labeling-radiolabeling and targeting properties of RGD conjugates,” *Molecular Pharmaceutics*, vol. 12, no. 6, pp. 2142–2150, 2015.
- [16] L. Aloj, C. Caracò, M. Panico et al., “In vitro and in vivo evaluation of <sup>111</sup>In-DTPAGlu-G-CCK8 for cholecystokinin-b receptor imaging,” *Journal of Nuclear Medicine*, vol. 45, no. 3, pp. 485–494, 2004.
- [17] D. Summer, L. Grossrubatscher, M. Petrik et al., “Developing Targeted Hybrid Imaging Probes by Chelator Scaffolding,” *Bioconjugate Chemistry*, vol. 28, no. 6, pp. 1722–1733, 2017.
- [18] D. Summer, J. Garousi, M. Oroujeni et al., “Cyclic versus Noncyclic Chelating Scaffold for ,” *Molecular Pharmaceutics*, vol. 15, no. 1, pp. 175–185, 2017.
- [19] W. A. P. Breeman, A. C. Fröberg, E. de Blois et al., “Optimised labeling, preclinical and initial clinical aspects of CCK-2 receptor-targeting with 3 radiolabeled peptides,” *Nuclear Medicine and Biology*, vol. 35, no. 8, pp. 839–849, 2008.
- [20] J. Sörensen, I. Velikyan, D. Sandberg et al., “Measuring HER2-receptor expression in metastatic breast cancer using [68Ga]ABY-025 Affibody PET/CT,” *Theranostics*, vol. 6, no. 2, pp. 262–271, 2016.

## Research Article

# Tumor-Shed Antigen Affects Antibody Tumor Targeting: Comparison of Two $^{89}\text{Zr}$ -Labeled Antibodies Directed against Shed or Nonshed Antigens

Jae-Ho Lee <sup>1</sup>, Heejung Kim <sup>1</sup>, Zhengsheng Yao,<sup>1</sup> Lawrence P. Szajek,<sup>2</sup> Luigi Grasso,<sup>3</sup> Insook Kim,<sup>4</sup> and Chang H. Paik <sup>1</sup>

<sup>1</sup>Radiopharmaceutical Laboratory, Nuclear Medicine, Radiology and Imaging Sciences, Clinical Center, NIH, Bethesda, MD, USA

<sup>2</sup>Positron Emission Tomography Department, Clinical Center, NIH, Bethesda, MD, USA

<sup>3</sup>Morphotek, Inc., Exton, PA, USA

<sup>4</sup>Applied/Developmental Research Directorate, Leidos Biomedical Research, Inc., Frederick National Laboratory for Cancer Research, Frederick, MD, USA

Correspondence should be addressed to Jae-Ho Lee; [jaeho.jhlee@gmail.com](mailto:jaeho.jhlee@gmail.com) and Chang H. Paik; [cpaik@mail.nih.gov](mailto:cpaik@mail.nih.gov)

Received 20 November 2017; Accepted 11 January 2018; Published 12 March 2018

Academic Editor: Clemens Decristoforo

Copyright © 2018 Jae-Ho Lee et al. This is an open access article distributed under the Creative Commons Attribution License, which permits unrestricted use, distribution, and reproduction in any medium, provided the original work is properly cited.

We investigated the effect of shed antigen mesothelin on the tumor uptake of amatuximab, a therapeutic anti-mesothelin mAb clinically tested in mesothelioma patients. The B3 mAb targeting a nonshed antigen was also analyzed for comparison. The mouse model implanted with A431/H9 tumor, which expresses both shed mesothelin and nonshed Lewis-Y antigen, provided an ideal system to compare the biodistribution and PET imaging profiles of the two mAbs. Our study demonstrated that the tumor and organ uptakes of  $^{89}\text{Zr}$ -B3 were dose-independent when 3 doses, 2, 15, and 60  $\mu\text{g}$  B3, were compared at 24 h after injection. In contrast, tumor and organ uptakes of  $^{89}\text{Zr}$ -amatuximab were dose-dependent, whereby a high dose (60  $\mu\text{g}$ ) was needed to achieve tumor targeting comparable to the low dose (2  $\mu\text{g}$ ) of  $^{89}\text{Zr}$ -B3, suggesting that shed mesothelin may affect amatuximab tumor targeting as well as serum half-life. The autoradiography analysis showed that the distribution of  $^{89}\text{Zr}$ -B3 was nonuniform with the radioactivity primarily localized at the tumor periphery independent of the B3 dose. However, the autoradiography analysis for  $^{89}\text{Zr}$ -amatuximab showed dose-dependent distribution profiles of the radiolabel; at 10  $\mu\text{g}$  dose, the radiolabel penetrated toward the tumor core with its activity comparable to that at the tumor periphery, whereas at 60  $\mu\text{g}$  dose, the distribution profile became similar to those of  $^{89}\text{Zr}$ -B3. These results suggest that shed antigen in blood may act as a decoy requiring higher doses of mAb to improve serum half-life as well as tumor targeting. Systemic mAb concentration should be at a severalfold molar excess to the shed Ag in blood to overcome the hepatic processing of mAb-Ag complexes. On the other hand, mAb concentration should remain lower than the shed Ag concentration in the tumor ECS to maximize tumor penetration by passing binding site barriers.

## 1. Introduction

Monoclonal antibody- (mAb-) based solid tumor therapy is challenging due to various parameters that can impede the tumor delivery and penetration of mAb. Some parameters are related to tumor environment factors, including vascular and stroma density, interstitial pressure, and tumor binding site barriers [1–3]. In addition, the antigen- (Ag-) mediated tumor targeting of mAb may be hampered by the presence of high levels of shed Ag in blood which could act as a

decoy preventing mAbs from binding to antigens expressed on tumor cells [4–7]. We previously reported that shed mesothelin (MSLN) in blood circulation negatively affected the tumor targeting of amatuximab labeled with  $^{111}\text{In}$  or  $^{64}\text{Cu}$  by increasing its liver and spleen uptakes while decreasing its blood retention and tumor uptake when the injection dose of amatuximab was not sufficient to saturate the shed MSLN in blood circulation [5, 6]. In contrast to the negative effect of shed MSLN in blood circulation, a mathematical simulation suggested that the shed MSLN in the extracellular

space (ECS) could positively affect the tumor uptake by improving the penetration of the antibody toward tumor core [8].

In this study, we investigated the effects of shed Ag on the tumor targeting and penetration of mAb. To achieve this goal, we used a nude mouse model implanted with A431/H9 tumor that overexpresses both shed MSLN (5 million Ag molecules/cell) and nonshed Lewis-Y (4 million Ag molecules/cell). MSLN is a membrane glycoprotein of 40 kDa that is actively internalized into the cell's cytosol as well as shed from the tumor cell surface, generating soluble MSLN in the tumor's interstitial space and blood circulation with its concentrations proportional to the size of tumor [5, 7, 9]. Lewis-Y is a carbohydrate antigen that is not actively internalized nor shed from the tumor surface [9–13]. As model antibodies, we used two mAbs: anti-MSLN mAb amatuximab (mouse/human chimeric antibody with 82.6% amino acid sequence identity to a human IgG1 $\kappa$  and  $10^{-9}$  M  $K_D$  binding affinity), a therapeutic mAb currently investigated in mesothelioma patients, and control anti-Lewis-Y mAb B3 (murine IgG1 $\kappa$  with  $10^{-8}$  M  $K_D$  binding affinity). Comparative studies using this system enabled us to define the effects of shed Ag on the tumor uptake and penetration of mAb apart from the effects of other factors such as vascular density, high interstitial fluid pressure (IFP), and extracellular protein contents.

The two mAbs were labeled with  $^{89}\text{Zr}$  (decay half-life, 78.4 h), which decays with a low positron emission energy of 395.5 keV, allowing for PET imaging with higher resolution [14–16].  $^{89}\text{Zr}$  can enhance PET radioimmune detection of labeled mAbs and extend autoradiography preparation time due to the longer half-life and higher imaging resolution compared with  $^{111}\text{In}$  and  $^{64}\text{Cu}$ . In addition to the biodistribution (BD), PET imaging, and autoradiography studies for the two  $^{89}\text{Zr}$ -labeled mAbs, here we also report a new autoradiography analysis method to define the tumor uptake profile of the two  $^{89}\text{Zr}$  mAbs irrespective of tumor size and shape.

## 2. Materials and Methods

Amatuximab was obtained from Morphotek, Inc. (Exton, PA), and B3 was provided by Dr. Ira Pastan (LMB, NCI, NIH). p-Isothiocyanatobenzyl-desferrioxamine (p-SCN-Df) was purchased from Macrocyclics, Inc. (Dallas, TX). Zirconium-89 ( $^{89}\text{Zr}$ ) was produced at the National Institute of Health (Bethesda, MD) cyclotron facility using a 16.5 MeV proton cyclotron (PET trace, General Electric, Fairfield, CT) by proton irradiation (beam energy; 14 MeV, current; 20  $\mu\text{A}$ ) ( $p, n$ ) reaction (2–5 h) on  $^{89}\text{Y}$ -metal mesh (200 mg, 4N purity, American Elements).  $^{89}\text{Zr}$  was separated as  $^{89}\text{Zr}$ -oxalate from irradiated  $^{89}\text{Y}$ -metal mesh using 0.1 M oxalic acid solution [16].

**2.1. Conjugation of p-SCN-Df to Amatuximab or B3 Antibody.** The mAbs were radiolabeled with  $^{89}\text{Zr}$  using desferrioxamine (Df) with an isothiocyanate linker as a chelating agent following a method of Vosjan et al. [17]. Briefly, amatuximab

or B3 was reacted with p-SCN-Df at a molar ratio of 1:3 in 0.1 M sodium bicarbonate, at pH 9.5 at 37°C. The Df-amatuximab or Df-B3 conjugate was purified with a size exclusion PD-10 column (GE Healthcare Bio-Sciences AB, Uppsala, Sweden) and concentrated with a Microcon® filter with a 30 kDa cutoff (Millipore, Bedford, MA). The column or the filter was pretreated with 25 mg BSA containing 1  $\mu\text{mol}$  DTPA to block nonspecific protein binding sites and remove potential metal contaminants and then washed with metal-free sodium acetate (0.25 M, pH 5.5). The mAb concentrations were measured according to the method of Bradford [18]. The level of p-SCN-Df conjugated per mAb was determined by the percent  $^{89}\text{Zr}$  distribution between the peaks corresponding to Df-mAb and free DF on the size exclusion HPLC when the product mixture was radiolabeled as described below.

**2.2. Radiolabeling.** Purified Df-amatuximab or Df-B3 (1.0 mg/ml, 6.9  $\mu\text{M}$ ) was labeled with  $^{89}\text{Zr}$  (344 MBq/0.15 M oxalic acid for Df-amatuximab and 148 MBq/0.15 M oxalic acid for Df-B3), which was neutralized with a solution containing sodium carbonate (0.135 M)/HEPES buffer (pH = 7, 0.25 M) and d-mannitol (5.5 mg/mL) at 25°C for 1 h. One mL of 0.25 M sodium acetate containing 5 mg/mL gentisic acid (pH 5.5) was then added to the reaction solution. The labeled product was purified with PD 10 columns eluted with metal-free elution buffer (0.25 M sodium acetate containing 5 mg/mL gentisic acid, pH 5.5). Each PD 10 column was pretreated with 25 mg BSA containing 1  $\mu\text{mol}$  DTPA to block nonspecific protein binding sites and remove potential metal contaminants and then washed with metal-free elution buffer. The radiolabeling yield and the radiochemical purity were assessed by analytical size exclusion HPLC (Gilson, Middleton, WI) before and after the purification (please see the Materials and Methods section in the previous paper for detailed information [5]). The radiolabeling yield was determined based on the distribution of  $^{89}\text{Zr}$  between  $^{89}\text{Zr}$ -labeled amatuximab (retention time: 8.53 min) and unbound  $^{89}\text{Zr}$  (retention time: 9.45 min) on the HPLC profiles.

**2.3. Immunoreactivity Determination.** The immunoreactivity of  $^{89}\text{Zr}$ -amatuximab or B3 was determined by a modified cell-binding assay of Lindmo and Bunn [19], as previously reported [5]. Aliquots (5 ng/50  $\mu\text{L}$ ) of the conjugate samples were incubated side-by-side with an increasing number of A431/H9 cells (positive for both mesothelin and Lewis-Y;  $2 \times 10^4$ – $1 \times 10^6$  cells) in 100  $\mu\text{L}$  of PBS with 1% BSA at 4°C for 3 hours. Nonspecific binding to the cells was determined by performing the cell-binding assays under a condition of excess amount of antibodies (50  $\mu\text{g}$  amatuximab and 50  $\mu\text{g}$  B3).

**2.4. Tumor Model.** A431/H9 is a derivative of the A431 epidermoid carcinoma cell line that has been stably transfected with vectors for human mesothelin and grown in media supplemented with 750 mg/mL G-418 (Geneticin) for selection [20]. This cell line was grown at 37°C with 5%  $\text{CO}_2$  in media supplemented with 10% FBS, 2 mmol/L L-glutamine,

100 U penicillin, and 100 mg streptomycin (Invitrogen Corporation). The cell line was authenticated at the source and grown from frozen stocks prepared from an early passage of the original line [21].

**2.5. Biodistribution Studies.** For the BD studies with  $^{89}\text{Zr}$ -labeled amatuximab or B3 conjugate with Df molecules, groups ( $n = 4\text{--}5$  mice/group) of mice were injected (i.v.) with  $^{89}\text{Zr}$ -labeled mAb conjugates (111 kBq for  $^{89}\text{Zr}$ -amatuximab; 74 kBq for  $^{89}\text{Zr}$ -B3) mixed with corresponding unlabeled intact antibodies (2, 10, or 60  $\mu\text{g}$  amatuximab; 2, 15, or 60  $\mu\text{g}$  B3) in 0.2 mL PBS containing 1% BSA. The tumor sizes at the time of the BD studies were as follows:  $245.5 \pm 6.5$ ,  $190.8 \pm 5.0$ , and  $226.4 \pm 7.1 \text{ mm}^3$  for 2, 10, and 60  $\mu\text{g}$  amatuximab, respectively, and  $205.9 \pm 3.4$ ,  $321.2 \pm 9.0$ , and  $372.5 \pm 8.2 \text{ mm}^3$  for 2, 15, and 60  $\mu\text{g}$  B3, respectively. The animals were euthanized at 24 hours by  $\text{CO}_2$  inhalation and exsanguination by cardiac puncture. We performed the BD studies as described previously (please see the Materials and Methods section in the previous paper for detailed information [5]). All animal experiments were performed under a protocol approved by the NIH Animal Care and Use Committee.

**2.6. PET Imaging.** PET imaging studies were performed as described in the previous study of  $^{64}\text{Cu}$ -NOTA-amatuximab (please see PET Imaging section in the previous paper [5]). The mice ( $n = 5$ ) with A431/H9 tumor were injected (i.v.) with  $^{89}\text{Zr}$ -amatuximab (2.96 MBq/10 or 60  $\mu\text{g}$  total amatuximab) or  $^{89}\text{Zr}$ -B3 (2.22 MBq/15 or 60  $\mu\text{g}$  total B3) in 0.2 ml of normal saline through the tail vein and then 15 min static PET scans were performed at 3, 24, and 48 h p.i. The tumor sizes at the time of the PET imaging were as follows:  $429 \pm 141 \text{ mm}^3$  (range: 253–599  $\text{mm}^3$ ) for 10  $\mu\text{g}$  amatuximab and  $406 \pm 23 \text{ mm}^3$  (range: 385–440  $\text{mm}^3$ ) for 60  $\mu\text{g}$  amatuximab;  $700 \pm 220 \text{ mm}^3$  (range: 436–1042  $\text{mm}^3$ ) for 15  $\mu\text{g}$  B3 and  $441 \pm 126 \text{ mm}^3$  (range: 304–630  $\text{mm}^3$ ) for 60  $\mu\text{g}$  B3.

**2.7. Autoradiography and Its Analysis.** For Ex vivo autoradiography, the mice were selected according to tumor volume by PET and euthanized immediately after 48 h PET imaging session and the tumors were excised. The tumors with the following sizes were used for autoradiography studies:  $285 \pm 46 \text{ mm}^3$  (range: 252–318  $\text{mm}^3$ ;  $n = 2$ ) and  $388 \pm 5 \text{ mm}^3$  (range: 385–392  $\text{mm}^3$ ;  $n = 2$ ) for 10 and 60  $\mu\text{g}$  amatuximab, respectively, and  $574 \pm 121 \text{ mm}^3$  (range: 437–666  $\text{mm}^3$ ;  $n = 3$ ) and  $364 \pm 60 \text{ mm}^3$  (range: 304–424  $\text{mm}^3$ ;  $n = 3$ ) for 15 and 60  $\mu\text{g}$  B3, respectively. The tumors were embedded and frozen in Tissue-Tek® CRYO-OCT compound (Sakura® Finetek USA Inc., Torrance, CA, USA) at  $-20^\circ\text{C}$  for 3 h. Serial 20  $\mu\text{m}$  thick short axis sections were cut in 400  $\mu\text{m}$  intervals covering the entire tumor. Two or three consecutive tumor slices were selected at 3 tumor regions (25%, 50%, and 75% long axis regions from the tumor surface) as representative sections throughout the tumor and exposed on the phosphor screen for 16 h. Signals were obtained by the use of the Typhoon FLA 7000 (GE Healthcare Life

Sciences, Pittsburgh, PA, USA) with 25  $\mu\text{m}$  pixel resolution and analyzed with Image Quant TL8.1 software. Values were grouped together from the 3 tumor regions to represent a tumor. Each tumor was treated as an independent sample. To analyze the microdistribution of the radioactivity in the tumor sections, we introduced a normalized length analysis method as described below. The first line was drawn along the longest axis, and the second line was drawn along a short axis perpendicularly at the center of the first longest line (see Figure 1). The center was selected as the point where the two lines meet. Additional lines were drawn evenly and continuously between the two original lines passing through the same center point (total of 8 lines). Radioactivity profile of each line was analyzed with ImageJ (NIH, Bethesda, MD) and exported into Excel files to redefine values with Matlab's interpolation function `interp1`. The maximum length of each line in  $x$ -axis was normalized to 1 to correct for the differences in the length of each line for reconstruction of the radioactivity versus tumor penetration distance profiles of each tumor section. The maximum signal intensity within each tumor section in  $y$ -axis was also normalized to 100 to correct for the differences in the signal intensity between each tumor section. Mean radioactivity versus distance profiles with standard deviation were then reconstructed for tumor sections obtained at 25%, 50%, and 75% regions.

**2.8. Statistical Analysis.** Statistical analysis was performed using ANOVA for comparing multiple groups, and Student's  $t$ -test was performed for unpaired data between two groups. All tests were two-sided, and a probability value ( $p$ ) of less than 0.05 was considered significant.

### 3. Results

**3.1. Characterization of  $^{89}\text{Zr}$  mAbs.** The level of Df conjugation was  $1.6 \pm 0.3$  ( $n = 3$ ) for B3 and  $0.9 \pm 0.2$  ( $n = 3$ ) for amatuximab. The  $^{89}\text{Zr}$ -labeled mAbs were purified on PD-10 columns eluted with acetate buffer (pH 5.5) containing gentisic acid at 5 mg/ml. The purified products were >95% radiochemically pure based on the size exclusion HPLC profiles. The specific activities of the purified product were 296 kBq/ $\mu\text{g}$  for  $^{89}\text{Zr}$ -amatuximab and 148 kBq/ $\mu\text{g}$  for  $^{89}\text{Zr}$ -B3. The immunoreactivities of  $^{89}\text{Zr}$ -amatuximab and  $^{89}\text{Zr}$ -B3 were  $84.0 \pm 2.2\%$  ( $n = 2$ ) and  $70.0 \pm 1.0\%$  ( $n = 2$ ), respectively.

**3.2. Biodistribution Studies.** The results of comparative BD studies at 24 h indicated that the uptake of  $^{89}\text{Zr}$ -amatuximab in tumor, liver, spleen, and blood directly correlated with dose levels whereas the uptake of anti-Lewis-Y antibody  $^{89}\text{Zr}$ -B3 in these organs was dose-independent. In fact,  $^{89}\text{Zr}$ -amatuximab tumor uptake and blood retention increased as the injection dose increased (Figure 2(a) and Table 1). However, the liver and spleen uptake decreased as the injection dose increased. The tumor-to-organ ratios increased and conversely the tumor-to-blood ratio decreased as the dose increased, as previously reported for  $^{64}\text{Cu}$ -NOTA-amatuximab [5]. In contrast, a dose effect on tumor uptake,

TABLE 1: Effect of mAb dose on tumor-to-blood and tumor-to-organ uptake ratios of  $^{89}\text{Zr}$ -amatuximab (111 kBq/2, 10 or 60  $\mu\text{g}$ ) or  $^{89}\text{Zr}$ -B3 (74 kBq/2, 15 or 60  $\mu\text{g}$ ) in nude mice with A431/H9 tumor. All values are reported as mean  $\pm$  standard deviation ( $n = 5$ ).

| mAb        | Time | Injection dose   | Tumor/blood     | Tumor/liver     | Tumor/kidney    | Tumor/spleen    | Tumor/muscle    |
|------------|------|------------------|-----------------|-----------------|-----------------|-----------------|-----------------|
| Amatuximab | 24 h | 2 $\mu\text{g}$  | 2.66 $\pm$ 0.43 | 0.11 $\pm$ 0.06 | 0.73 $\pm$ 0.32 | 0.23 $\pm$ 0.10 | 3.67 $\pm$ 0.86 |
| Amatuximab | 24 h | 10 $\mu\text{g}$ | 2.30 $\pm$ 1.35 | 0.24 $\pm$ 0.07 | 1.32 $\pm$ 0.49 | 0.38 $\pm$ 0.25 | 5.54 $\pm$ 2.00 |
| Amatuximab | 24 h | 60 $\mu\text{g}$ | 1.37 $\pm$ 0.54 | 0.66 $\pm$ 0.22 | 2.05 $\pm$ 0.54 | 1.01 $\pm$ 0.28 | 8.97 $\pm$ 2.44 |
| B3         | 24 h | 2 $\mu\text{g}$  | 0.98 $\pm$ 0.34 | 1.00 $\pm$ 0.27 | 1.59 $\pm$ 0.39 | 2.71 $\pm$ 0.88 | 4.58 $\pm$ 1.23 |
| B3         | 24 h | 15 $\mu\text{g}$ | 0.80 $\pm$ 0.17 | 0.89 $\pm$ 0.19 | 1.57 $\pm$ 0.22 | 1.95 $\pm$ 0.44 | 4.23 $\pm$ 0.81 |
| B3         | 24 h | 60 $\mu\text{g}$ | 0.74 $\pm$ 0.10 | 0.90 $\pm$ 0.13 | 1.48 $\pm$ 0.18 | 2.15 $\pm$ 0.26 | 4.01 $\pm$ 0.57 |

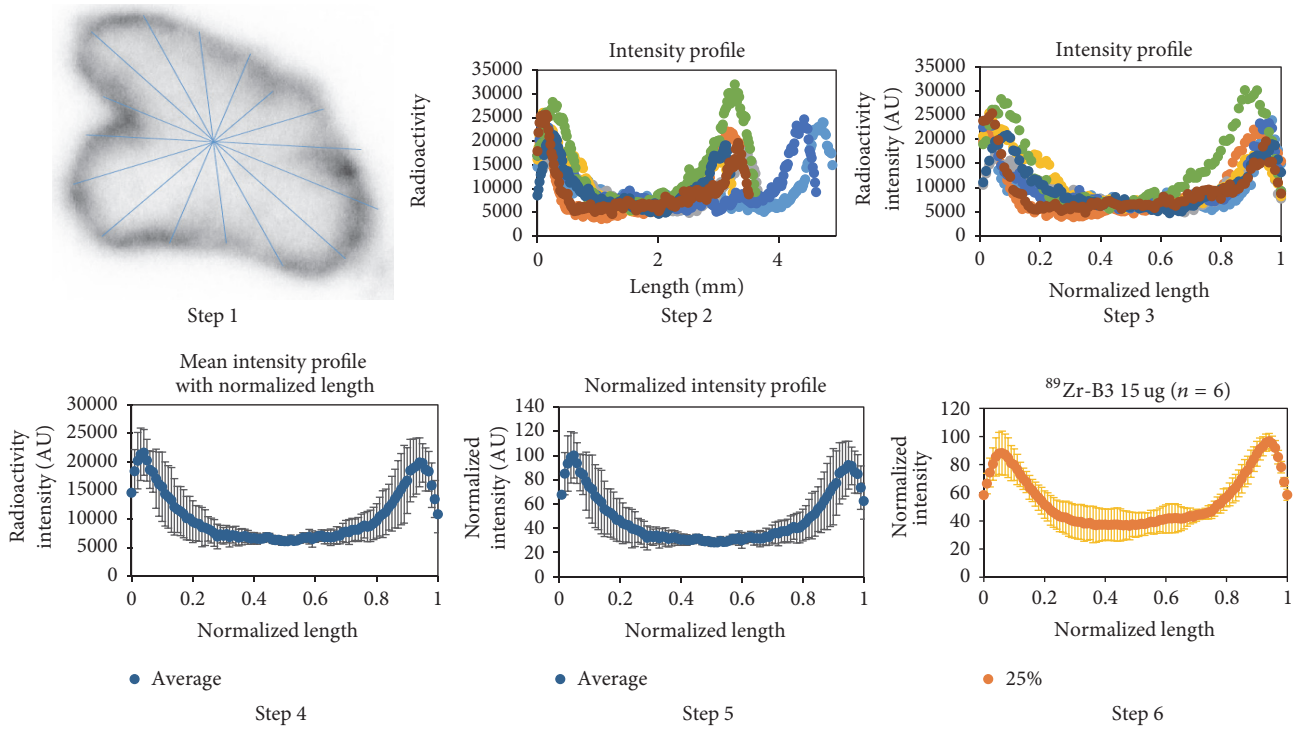


FIGURE 1: Procedure of a new normalized length analysis method for autoradiography. Step 1: draw lines on autoradiography image imported into ImageJ. Step 2: export each line plot data file and plot the original intensity versus line length profile. Step 3: normalize each length and replot with the interpolation function, interp1, in Matlab. Step 4: plot mean and standard deviation intensity profile with normalized length. Step 5: plot normalized intensity profile with normalized length. Step 6: repeat steps 1–5 for each tumor section and get mean normalized intensity profile to represent tumor sections cut at 25%, 50%, and 75% regions of the long tumor axis.

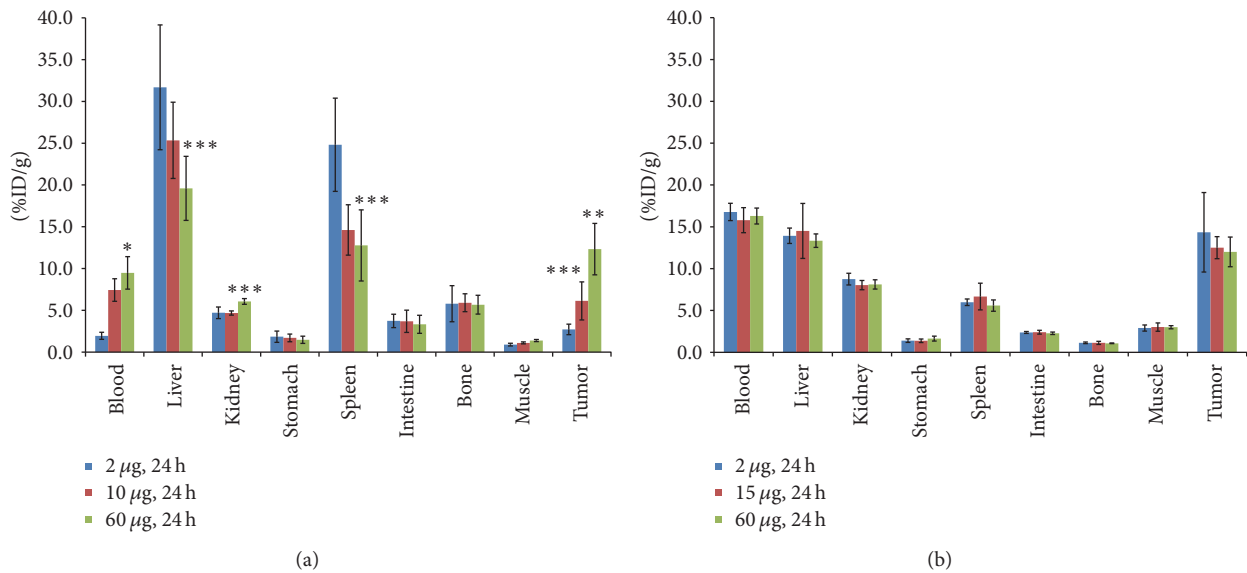


FIGURE 2: Effects of total injection dose of mAb on the BD of  $^{89}\text{Zr}$ -mAb in nude mice ( $n = 4\text{--}5$  per group) with A431/H9 tumor: (a) the BD data from  $^{89}\text{Zr}$ -amatuximab (111 kBq) with different injection doses of amatuximab ( $2\ \mu\text{g}$ ,  $10\ \mu\text{g}$ , and  $60\ \mu\text{g}$ ) are compared at 24 h p.i. in nude mice with tumor sizes  $245.5 \pm 6.5$ ,  $190.8 \pm 5.0$ , and  $226.4 \pm 7.1\ \text{mm}^3$  for 2, 10, and  $60\ \mu\text{g}$  amatuximab. The results demonstrate that tumor uptake and blood retention significantly increased whereas liver uptake decreased as the antibody dose was increased; (b) the BD data from  $^{89}\text{Zr}$ -B3 (74 kBq) with different injection doses of B3 ( $2\ \mu\text{g}$ ,  $15\ \mu\text{g}$ , and  $60\ \mu\text{g}$ ) are compared at 24 h p.i. in nude mice with tumor sizes  $205.9 \pm 3.4$ ,  $321.2 \pm 9.0$ , and  $372.5 \pm 8.2\ \text{mm}^3$  for 2, 15, and  $60\ \mu\text{g}$ . The results demonstrate that tumor uptake, blood retention, and liver uptake were not affected by the antibody dose. The data are mean  $\pm$  SD. Analysis of statistical significance in each organ uptake data compared to the data from  $2\ \mu\text{g}$  injection: \*  $p < 0.001$ ,  $0.001 < **p < 0.01$ , and  $0.01 < ***p < 0.05$ ; column: mean; bar: SD.

blood retention, and liver uptake, as well as the tumor-to-organ and the tumor-to-blood ratios for  $^{89}\text{Zr}$ -B3, was not appreciable (Figure 2(b) and Table 1).

**3.3. PET Imaging Studies.** The findings from the BD studies were supported by the PET imaging results.  $^{89}\text{Zr}$ -amatuximab tumor uptake was visualized as early as 3 h postinjection (p.i.) at both dose levels, while the majority of radioactivity was still localized in heart (blood pool) and liver (Figure 3(a)). During the 3–48 h period,  $^{89}\text{Zr}$ -amatuximab was cleared rapidly from blood at the 10  $\mu\text{g}$  dose while tumor uptake remained unchanged (Figures 3(a) and 4(a)). In contrast, at the 60  $\mu\text{g}$  dose  $^{89}\text{Zr}$ -amatuximab cleared more gradually from blood and produced a drastic increase in tumor uptake (%ID/g) at 24 h and 48 h (Figure 4). The tumor uptake (%ID/g) was  $7.46 \pm 1.26$ ,  $9.88 \pm 1.25$ , and  $7.74 \pm 1.22$  at 3, 24, and 48 h, respectively, for 10  $\mu\text{g}$  and  $9.85 \pm 21.3$ ,  $22.37 \pm 4.18$ , and  $22.90 \pm 6.18$  at 3, 24, and 48 h, respectively, for 60  $\mu\text{g}$ . Blood retention (%ID/g) was  $20.43 \pm 2.49$ ,  $5.09 \pm 1.78$ , and  $2.52 \pm 0.78$  at 3, 24, and 48 h, respectively, for 10  $\mu\text{g}$  and  $27.37 \pm 4.03$ ,  $12.44 \pm 3.66$ , and  $6.80 \pm 2.04$  at 3, 24, and 48 h, respectively, for 60  $\mu\text{g}$ . Liver uptake (%ID/g) was  $24.17 \pm 3.11$ ,  $25.64 \pm 2.43$ , and  $23.03 \pm 3.51$  at 3, 24, and 48 h, respectively, for 10  $\mu\text{g}$  and  $22.33 \pm 3.89$ ,  $21.14 \pm 2.21$ , and  $20.78 \pm 3.67$  at 3, 24, and 48 h, respectively, for 60  $\mu\text{g}$ . Thus, these data indicate that a higher injection dose of amatuximab is advantageous for the tumor visualization by PET. The tumor-to-organ and the tumor-to-blood ratios from PET imaging had similar values observed in  $^{64}\text{Cu}$ -NOTA-amatuximab study [5]. The tumor-to-liver ratio showed a value  $>1$  at 24 and 48 h p.i. for 60  $\mu\text{g}$  but a value  $<1$  for 10  $\mu\text{g}$  (Table 2), suggesting that it is feasible to visualize tumors in the upper abdomen with the higher dose.

The PET images of  $^{89}\text{Zr}$ -B3 showed tumor uptake as early as 3 h p.i. at both 15 and 60  $\mu\text{g}$  doses. Compared to  $^{89}\text{Zr}$ -amatuximab, the PET images from  $^{89}\text{Zr}$ -B3 did not show any significant dose effects on its uptake and the clearance pharmacokinetics from tumor, blood, and liver (Figure 3(b)). The tumor uptake of the  $^{89}\text{Zr}$ -B3 increased steadily over a 48 h period while clearing gradually from the blood and the liver as follows (Figure 4): tumor uptake (%ID/g) of  $7.36 \pm 0.54$ ,  $14.43 \pm 1.94$ , and  $20.99 \pm 4.33$  at 3, 24, and 48 h, respectively, for 15  $\mu\text{g}$  and  $6.71 \pm 0.78$ ,  $15.36 \pm 3.98$ , and  $20.78 \pm 2.21$  at 3, 24, and 48 h, respectively, for 60  $\mu\text{g}$ ; blood retention (%ID/g) of  $21.28 \pm 1.54$ ,  $12.99 \pm 2.83$ , and  $10.21 \pm 1.92$  at 3, 24, and 48 h, respectively, for 15  $\mu\text{g}$  and  $21.05 \pm 1.85$ ,  $12.40 \pm 0.56$ , and  $9.92 \pm 1.33$  at 3, 24, and 48 h, respectively, for 60  $\mu\text{g}$ ; liver uptake (%ID/g) of  $25.04 \pm 1.03$ ,  $20.37 \pm 3.4$ , and  $16.55 \pm 3.98$  at 3, 24, and 48 h, respectively, for 15  $\mu\text{g}$  and  $25.21 \pm 1.90$  %ID/g,  $18.90 \pm 1.06$ , and  $16.72 \pm 1.83$  at 3, 24, and 48 h, respectively, for 60  $\mu\text{g}$ . The tumor-to-organ and the tumor-to-blood ratios from PET imaging did not change as the dose increased (Table 2).

These results suggest a significant difference in biodistribution characteristics between  $^{89}\text{Zr}$ -amatuximab and  $^{89}\text{Zr}$ -B3, which may be due to the presence of shed mesothelin in blood and tumor tissue that may affect the serum half-life as well as Ag-specific tumor uptake of radiolabeled amatuximab as previously reported [5].

**3.4. Autoradiography Studies.** To investigate if the shed mesothelin in the ECS of tumor could affect the penetration of  $^{89}\text{Zr}$ -amatuximab, we performed the autoradiography of tumor segments at 48 h p.i. immediately after the completion of the PET imaging studies. The data of autoradiography images analysis (see Figure 1 for image analysis method) demonstrated that  $^{89}\text{Zr}$ -amatuximab had similar radioactivity intensity at the tumor core and the periphery when the injection dose was 10  $\mu\text{g}$  (Figures 5(a) and 6(a)). However, increasing the dose to 60  $\mu\text{g}$  increased the uptake to the periphery but not to the center of the tumor (Figures 5(b) and 6(b)). In contrast, the radioactivity data and the normalized radioactivity versus distance profiles for  $^{89}\text{Zr}$ -B3 showed that the uptake peaked at the tumor periphery while it decreased rapidly toward the tumor core at either dose levels (Figures 5(c), 5(d), 6(c), and 6(d)).

## 4. Discussion

The studies reported here highlight an important property of anti-mesothelin mAb amatuximab as compared to anti-Lewis-Y mAb B3 for the Ag-mediated targeting of A431/H9 tumor overexpressing both a shed Ag, mesothelin, and a nonshed Ag, Lewis-Y, in a mouse model. The comparative BD, PET imaging, and autoradiography studies between these two mAbs allowed us to define the effect of shed Ag on the tumor targeting and penetration, apart from the effects of other factors related to the tumor microenvironment. While the biodistribution and tumor uptake of  $^{89}\text{Zr}$ -B3 were not significantly affected by the injected dose, the tumor uptake of  $^{89}\text{Zr}$ -amatuximab increased whereas the uptake in liver and spleen decreased as the injected dose increased. This finding is consistent with the previously reported dose-dependent effect on the biodistribution and tumor uptake of  $^{64}\text{Cu}$ -NOTA-amatuximab [5]. The BD and tumor uptake of  $^{89}\text{Zr}$ -B3 were not appreciably affected by the injection dose levels because its target, Lewis-Y Ag, is not shed by tumor cells. The ROI analysis of PET images corresponded to the BD results and is consistent with the hypothesis of a decoy effect caused by soluble shed Ag in blood and tumor.

These findings could be explained by a threshold effect whereby  $^{89}\text{Zr}$ -amatuximab is mostly bound to shed MSLN in blood at the lower dose (10  $\mu\text{g}$ ) and sequestered into the reticular endothelial system of liver and spleen, thereby lowering both blood retention and tumor uptake. Based on this knowledge, we hypothesized that a dose of 60  $\mu\text{g}$  could be sufficiently high to saturate shed MSLN as well as create an excess of  $^{89}\text{Zr}$ -amatuximab available for a more effective tumor targeting. This effect could be explained by correlating the concentration of shed MSLN in the blood and in the ECS of A431/H9 tumor, as estimated in previous studies [8, 22, 23], similarly to that of  $^{64}\text{Cu}$ -NOTA-amatuximab.  $^{89}\text{Zr}$ -amatuximab injected at 10  $\mu\text{g}$  dose results in an estimated blood concentration of 43.3 nM (assuming blood volume of 1.6 mL for a 20 g mouse) immediately after injection and 1.75 nM at 48 h (based on 2.52%ID/g blood in Figure 3). Because the average concentration of shed MSLN in the blood is  $\sim 6$  nM in a tumor of  $\sim 300$  mm<sup>3</sup>,  $^{89}\text{Zr}$ -amatuximab

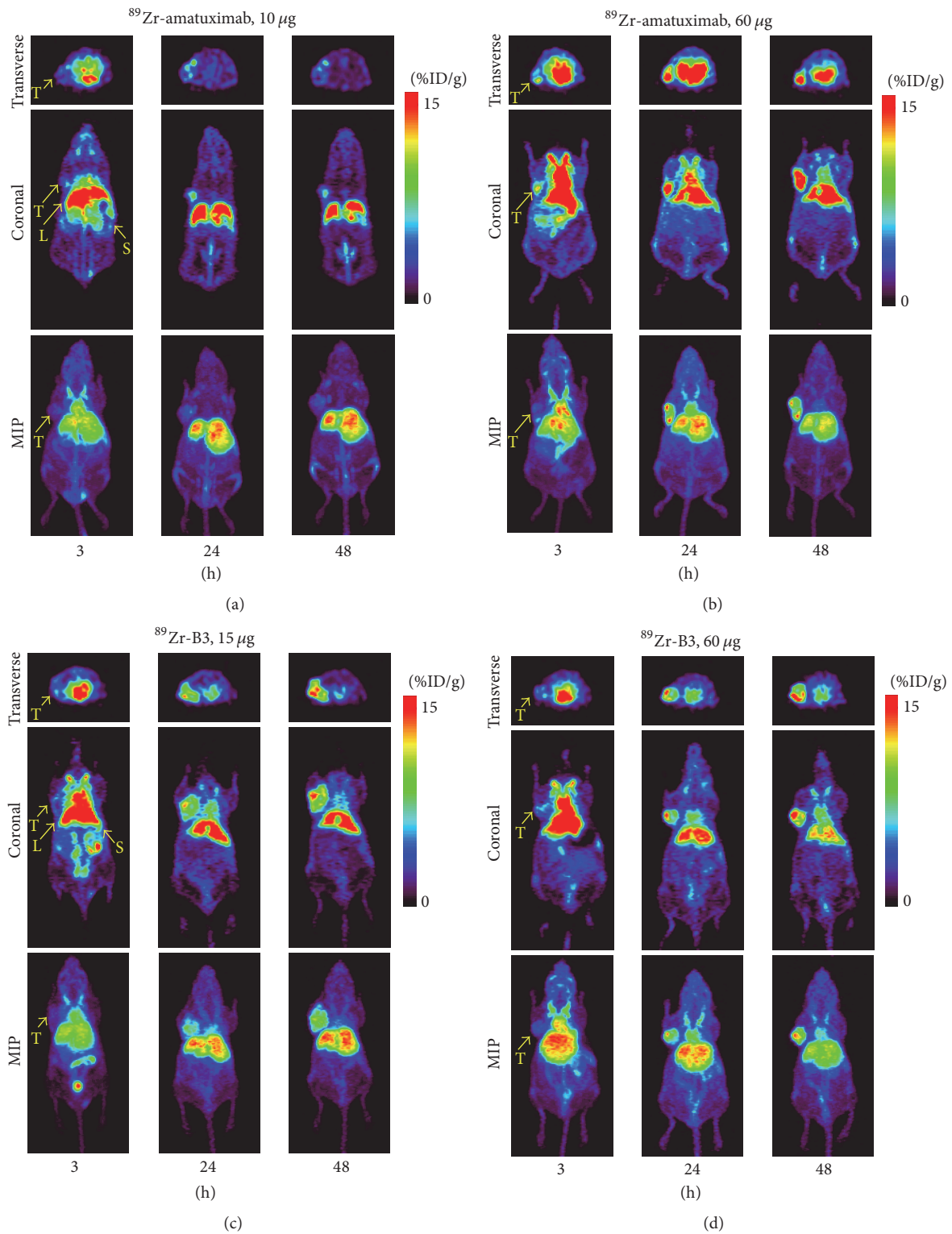


FIGURE 3: Representative PET images of  $^{89}\text{Zr}$ -mAb in nude mice with A431/H9 tumor: (a)  $^{89}\text{Zr}$ -amatuximab (2.96 MBq) coinjected with 10  $\mu\text{g}$  and 60  $\mu\text{g}$  amatuximab; (b)  $^{89}\text{Zr}$ -B3 (2.22 MBq) coinjected with 15  $\mu\text{g}$  and 60  $\mu\text{g}$  B3. Fifteen-minute static PET scans were performed at 3, 24, and 48 h p.i. PET images demonstrate that (a) the tumor uptake significantly increased when the injection dose of  $^{89}\text{Zr}$ -amatuximab was 60  $\mu\text{g}$  compared with 10  $\mu\text{g}$  dose and (b) there was no significant dose effect on the tumor uptake of  $^{89}\text{Zr}$ -B3 and the tumor uptake gradually increased over time.

TABLE 2: Effect of mAb dose on tumor-to-blood and tumor-to-organ uptake ratios of  $^{89}\text{Zr}$ -amatuximab (2.96 MBq/10 or 60  $\mu\text{g}$ ) or  $^{89}\text{Zr}$ -B3 (2.22 MBq/15 or 60  $\mu\text{g}$ ) in nude mice with A431/H9 tumor. The ratios were calculated by maximum uptake values from ROI analysis of PET images. Blood-H represents the blood activity in the heart. All values are reported as mean  $\pm$  standard deviation ( $n = 5$ ).

| mAb        | Time | Injection dose   | Tumor/liver     | Tumor/spleen    | Tumor/muscle     | Tumor/blood-H   |
|------------|------|------------------|-----------------|-----------------|------------------|-----------------|
| Amatuximab | 3 h  | 10 $\mu\text{g}$ | 0.31 $\pm$ 0.06 | 0.65 $\pm$ 0.14 | 5.03 $\pm$ 1.53  | 0.38 $\pm$ 0.10 |
| Amatuximab | 24 h | 10 $\mu\text{g}$ | 0.40 $\pm$ 0.03 | 0.69 $\pm$ 0.21 | 10.20 $\pm$ 1.05 | 2.10 $\pm$ 0.64 |
| Amatuximab | 48 h | 10 $\mu\text{g}$ | 0.35 $\pm$ 0.02 | 0.54 $\pm$ 0.21 | 13.31 $\pm$ 1.68 | 3.21 $\pm$ 0.77 |
| Amatuximab | 3 h  | 60 $\mu\text{g}$ | 0.36 $\pm$ 0.03 | 0.84 $\pm$ 0.18 | 9.57 $\pm$ 3.52  | 0.36 $\pm$ 0.03 |
| Amatuximab | 24 h | 60 $\mu\text{g}$ | 1.04 $\pm$ 0.07 | 1.98 $\pm$ 0.63 | 18.90 $\pm$ 1.57 | 1.68 $\pm$ 0.17 |
| Amatuximab | 48 h | 60 $\mu\text{g}$ | 1.02 $\pm$ 0.20 | 2.68 $\pm$ 0.86 | 31.16 $\pm$ 5.58 | 3.46 $\pm$ 0.69 |
| B3         | 3 h  | 15 $\mu\text{g}$ | 0.30 $\pm$ 0.03 | 0.89 $\pm$ 0.14 | 6.11 $\pm$ 0.45  | 0.35 $\pm$ 0.03 |
| B3         | 24 h | 15 $\mu\text{g}$ | 0.72 $\pm$ 0.10 | 2.15 $\pm$ 0.29 | 14.26 $\pm$ 3.60 | 1.09 $\pm$ 0.15 |
| B3         | 48 h | 15 $\mu\text{g}$ | 1.30 $\pm$ 0.01 | 3.67 $\pm$ 1.34 | 20.00 $\pm$ 4.08 | 2.15 $\pm$ 0.74 |
| B3         | 3 h  | 60 $\mu\text{g}$ | 0.28 $\pm$ 0.03 | 0.86 $\pm$ 0.19 | 5.51 $\pm$ 1.84  | 0.32 $\pm$ 0.02 |
| B3         | 24 h | 60 $\mu\text{g}$ | 0.82 $\pm$ 0.21 | 2.40 $\pm$ 0.68 | 14.53 $\pm$ 5.49 | 1.24 $\pm$ 0.34 |
| B3         | 48 h | 60 $\mu\text{g}$ | 1.21 $\pm$ 0.05 | 3.12 $\pm$ 0.35 | 19.03 $\pm$ 1.59 | 1.98 $\pm$ 0.15 |

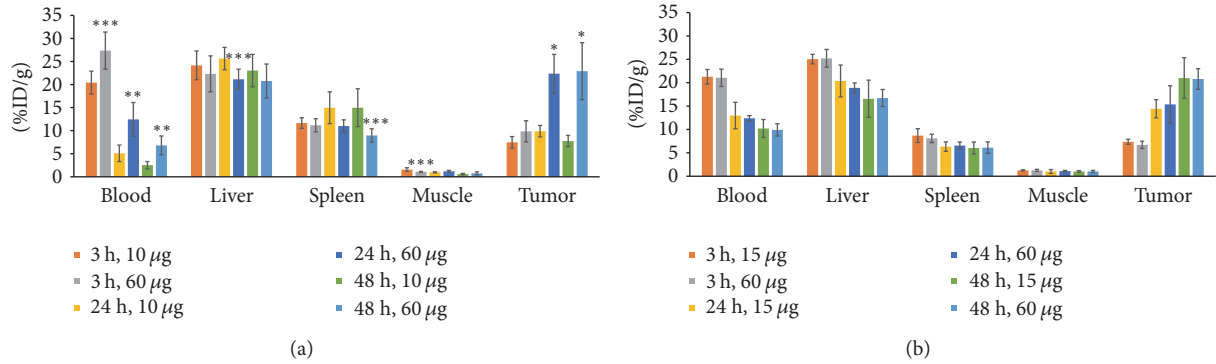


FIGURE 4: Effect of mAb dose on accumulation of <sup>89</sup>Zr-mAb in nude mice ( $n = 5$  per group) with A431/H9 tumor by PET analysis: (a) effect of amatuximab dose ( $10 \mu\text{g}$  and  $60 \mu\text{g}$ ) on accumulation of <sup>89</sup>Zr-amatuximab ( $2.96 \text{ MBq}$ ) in nude mice with tumor ( $429 \pm 141 \text{ mm}^3$ ; range:  $253\text{--}599 \text{ mm}^3$ ) for  $10 \mu\text{g}$  amatuximab and ( $406 \pm 23 \text{ mm}^3$ ; range:  $385\text{--}440 \text{ mm}^3$ ) for  $60 \mu\text{g}$  amatuximab. (b) Effect of B3 antibody dose ( $15 \mu\text{g}$  and  $60 \mu\text{g}$ ) on accumulation of <sup>89</sup>Zr-B3 ( $2.22 \text{ MBq}$ ) in nude mice with tumor ( $700 \pm 220 \text{ mm}^3$ ; range:  $436\text{--}1042 \text{ mm}^3$ ) for  $15 \mu\text{g}$  B3 and ( $441 \pm 126 \text{ mm}^3$ ; range:  $304\text{--}630 \text{ mm}^3$ ) for  $60 \mu\text{g}$  B3. The uptake value (%ID/g) was calculated by ROI analysis of PET images. Analysis of statistical significance in each organ uptake data (a) compared to the data from  $10 \mu\text{g}$  for amatuximab or (b)  $15 \mu\text{g}$  for B3. \* $p < 0.001$ ,  $0.001 < **p < 0.01$ , and  $0.01 < ***p < 0.05$ .

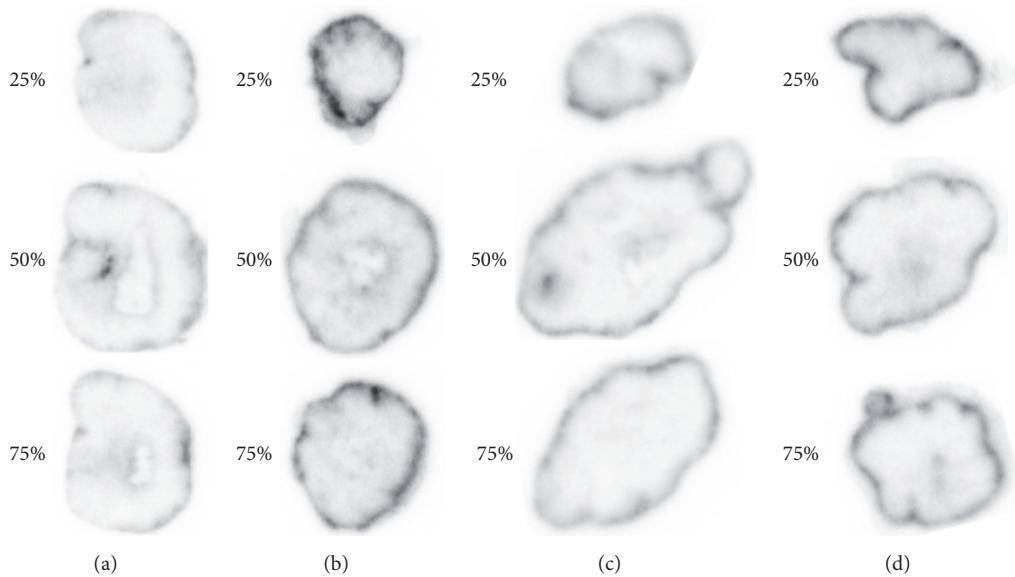


FIGURE 5: Representative autoradiography images of <sup>89</sup>Zr-labeled antibody. <sup>89</sup>Zr-amatuximab ( $2.96 \text{ MBq}$ ) coinjected with (a)  $10 \mu\text{g}$  and (b)  $60 \mu\text{g}$  amatuximab; <sup>89</sup>Zr-B3 ( $2.22 \text{ MBq}$ ) coinjected with (c)  $15 \mu\text{g}$  and (d)  $60 \mu\text{g}$  B3 mAb.

( $1.75 \text{ nM}$ ) would be mostly bound to shed MSLN in blood during a 48 h period and this complex sequestered into liver and spleen. At 48 h, unbound <sup>89</sup>Zr-amatuximab would have crossed the tumor vasculature and diffused into tumor ECS ( $5.36 \text{ nM}$  based on  $7.74\% \text{ ID/g}$  tumor at 48 h and  $53.6 \text{ nM}$  in the ECS, assuming that ECS constitutes 10% of total tumor volume). Because the concentration of shed MSLN is  $\sim 300 \text{ nM}$  in the ECS of a tumor of  $300 \text{ mm}^3$ , <sup>89</sup>Zr-amatuximab ( $53.6 \text{ nM}$ ) in the ECS would mostly exist as an antibody-Ag complex distributed throughout the entire tumor, presumably bypassing the binding sites on the surface of tumor cells nearest to the vasculature. On the other hand, <sup>89</sup>Zr-amatuximab injected at  $60 \mu\text{g}$  dose results in an

estimated blood concentration of  $260 \text{ nM}$  immediately after injection and  $28.3 \text{ nM}$  at 48 h ( $6.8\% \text{ ID/g}$  blood), that is, at a molar excess compared to the average concentration of shed MSLN in the blood ( $\sim 6 \text{ nM}$ ). Consequently, <sup>89</sup>Zr-amatuximab would remain mostly unbound, overcoming the sequestration into the hepatic reticuloendothelial system during a 48 h period. Therefore, a larger portion of the injected dose ( $95.2 \text{ nM}$  based on  $22.90\% \text{ ID/g}$  tumor at 48 h and  $952 \text{ nM}$  in the ECS) would have crossed the tumor vasculature and diffused into the tumor ECS. This concentration ( $952 \text{ nM}$ ) is larger than the shed MSLN concentration in the tumor ECS. The excess of <sup>89</sup>Zr-amatuximab not bound to shed MSLN would bind to MSLN on tumor cells in

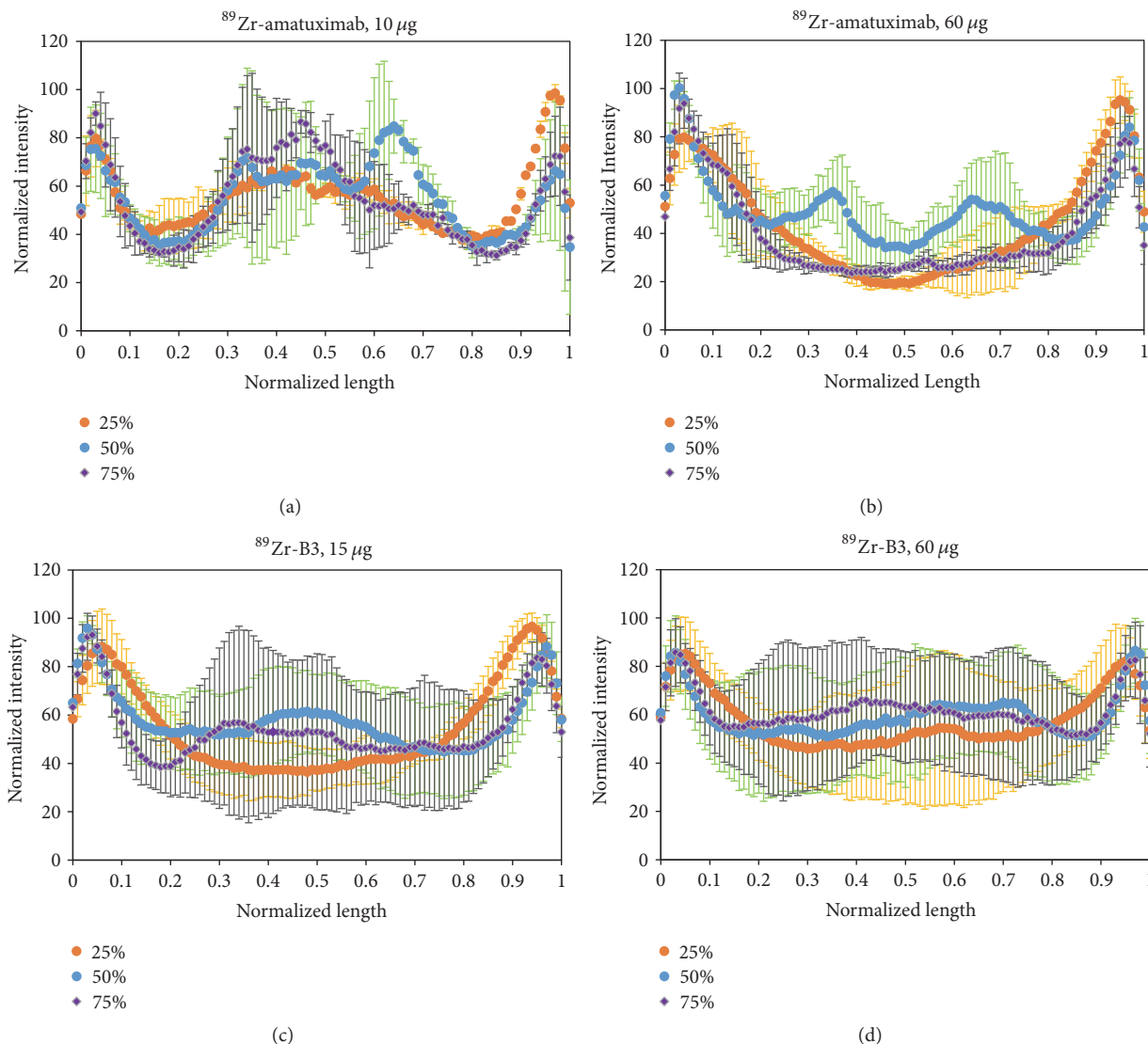


FIGURE 6: Autoradiography analysis of  $^{89}\text{Zr}$ -mAbs depicted as normalized intensity versus normalized length profiles:  $^{89}\text{Zr}$ -amatuximab (2.96 MBq) was coinjected with (a) 10  $\mu\text{g}$  and (b) 60  $\mu\text{g}$  amatuximab.  $^{89}\text{Zr}$ -B3 (2.22 MBq) was coinjected with (c) 15  $\mu\text{g}$  and (d) 60  $\mu\text{g}$  B3. The results demonstrate that the normalized radioactivity of  $^{89}\text{Zr}$ -amatuximab at the tumor core and the periphery was similar with the low dose of amatuximab but the relative  $^{89}\text{Zr}$  intensity at the tumor periphery was higher as the injection dose was increased to 60  $\mu\text{g}$ . In contrast, the radioactivity profile of  $^{89}\text{Zr}$ -B3 was not affected by the B3 dose between 15 and 60  $\mu\text{g}$  B3 and the radioactivity preferentially accumulated in the tumor periphery.

the periphery rather than in the tumor core, as observed for  $^{89}\text{Zr}$ -B3 as well as Alexa-labeled B3 [24]. According to Boucher et al. the interstitial fluid pressure is often elevated in solid tumors but declines in the tumor periphery in the outer 0.2–1.1 mm [25]. Therefore, the accumulation in the tumor periphery might be favored by the lower interstitial fluid pressure in this region allowing for more antibody extravasation than in tumor core.

It is noteworthy that our PET study demonstrated that the tumor localized outside of the abdomen could be visualized even with the lower dose (10  $\mu\text{g}$ ) at 24 h and thereafter because the tumor-to-blood and tumor-to-muscle ratios of  $^{89}\text{Zr}$ -amatuximab were higher than 2. However, it would

be necessary to inject the higher dose (60  $\mu\text{g}$ ) to visualize the tumor in the abdominal area. The PET study also suggests that  $^{89}\text{Zr}$ -amatuximab could be useful in a clinical setting because  $^{89}\text{Zr}$  with a long half-life (78.4 h) would be more suitable for the detection of tumor and the tumor-to-background ratio increased over time with the injection of the higher dose (60  $\mu\text{g}$ ).

In this study, we demonstrated the effect of shed mesothelin on the tumor targeting and tumor microdistribution of anti-mesothelin mAb amatuximab in A431/H9 tumor using anti-Lewis-Y B3 as a negative control. However, it is possible that other shed antigens with a different binding epitope or a different affinity for the targeting mAb might show a different

degree of shed antigen effects. Thus, careful investigation of other shed antigen systems would be needed to determine whether our findings could be generalized.

## 5. Conclusion

The use of A431/H9 tumor which overexpresses both the shed Ag mesothelin and the nonshed Ag Lewis-Y as a tumor model and the use of anti-mesothelin mAb amatuximab and anti-Lewis-Y mAb B3 as model mAbs for the BD, PET, and autoradiography studies allowed us to make a direct assessment on the effect of the shed Ag on the tumor and organ uptakes and tumor penetration, apart from the effects of other factors related to the tumor microenvironment. In addition, the use of  $^{89}\text{Zr}$  with a 3.4-day half-life to label the mAbs for PET imaging and autoradiography studies provided the advantages of high image sensitivity and resolution which enabled us to quantify the tumor and organ uptakes as well as tumor penetration of the mAbs.

The findings of this study imply that the systemic mAb concentration should be at a severalfold molar excess to the shed Ag concentration in the blood to increase the concentration of free mAb available for the tumor uptake and reduce the fraction of the mAb bound to the shed Ag in the blood and the subsequent hepatic processing of the mAb-Ag complexes. However, the mAb concentration in the tumor ECS should remain lower than the shed Ag concentration in the tumor ECS to maximize the tumor penetration of the mAb-Ag complexes by bypassing the binding site barrier. It will be the future challenge for both antibody engineers and clinical investigators to find this balance.

## Disclosure

The authors disclose that the preliminary work of this research was presented as an abstract at the annual meeting of the Society of Nuclear Medicine and Molecular Imaging, 2017.

## Conflicts of Interest

The authors have declared that no conflicts of interest exist.

## Authors' Contributions

Conceptualization was the responsibility of Jae-Ho Lee and Chang H. Paik. Data curation was the responsibility of Heejung Kim, Zhengsheng Yao, Insook Kim, Jae-Ho Lee, and Chang H. Paik. Formal analysis was the responsibility of Heejung Kim and Jae-Ho Lee. Funding acquisition was the responsibility of Chang H. Paik. Investigation was the responsibility of Heejung Kim, Zhengsheng Yao, Insook Kim, and Jae-Ho Lee. Methodology was the responsibility of Heejung Kim, Zhengsheng Yao, Jae-Ho Lee, and Chang H. Paik. Project administration was the responsibility of Chang H. Paik. Resource was the responsibility of Lawrence P. Szajek and Luigi Grasso. Supervision was the responsibility of Chang H. Paik. Validation was the responsibility of Jae-Ho Lee and Chang H. Paik. Visualization was the responsibility of

Heejung Kim and Jae-Ho Lee. Writing the original draft was the responsibility of Jae-Ho Lee and Chang H. Paik. Writing, reviewing, and editing the manuscript were the responsibility of Heejung Kim, Zhengsheng Yao, Insook Kim, Lawrence P. Szajek, Jae-Ho Lee, Luigi Grasso, and Chang H. Paik.

## Acknowledgments

This research was supported by the Intramural Research Program of the NIH Clinical Center and funded in part with federal funds from the National Cancer Institute, NIH (under Contract no. HHSN261200800001E) (Dr. Insook Kim). The authors would like to acknowledge Dr. Ira Pastan for his support.

## References

- [1] A. M. Scott, J. D. Wolchok, and L. J. Old, "Antibody therapy of cancer," *Nature Reviews Cancer*, vol. 12, no. 4, pp. 278–287, 2012.
- [2] M. R. Junttila and F. J. de Sauvage, "Influence of tumour micro-environment heterogeneity on therapeutic response," *Nature*, vol. 501, no. 7467, pp. 346–354, 2013.
- [3] P. A. Jones, J. J. Issa, and S. Baylin, "Targeting the cancer epigenome for therapy," *Nature Reviews Genetics*, vol. 17, no. 10, pp. 630–641, 2016.
- [4] J. L. Houghton, B. M. Zeglis, D. Abdel-Atti, R. Sawada, W. W. Scholz, and J. S. Lewis, "Pretargeted immuno-PET of pancreatic cancer: Overcoming circulating antigen and internalized antibody to reduce radiation doses," *Journal of Nuclear Medicine*, vol. 57, no. 3, pp. 453–459, 2016.
- [5] J.-H. Lee, H. Kim, Z. Yao et al., "Tumor and organ uptake of  $^{64}\text{Cu}$ -labeled MORAb-009 (amatuximab), an anti-mesothelin antibody, by PET imaging and biodistribution studies," *Nuclear Medicine and Biology*, vol. 42, no. 11, pp. 880–886, 2015.
- [6] I. S. Shin, S.-M. Lee, H. S. Kim et al., "Effect of chelator conjugation level and injection dose on tumor and organ uptake of  $^{111}\text{In}$ -labeled MORAb-009, an anti-mesothelin antibody," *Nuclear Medicine and Biology*, vol. 38, no. 8, pp. 1119–1127, 2011.
- [7] M. V. Pimm, "Circulating antigen: Bad or good for immunoscintigraphy?" *Nuclear Medicine and Biology*, vol. 22, no. 2, pp. 137–145, 1995.
- [8] Y. Pak, I. Pastan, R. J. Kreitman, and B. Lee, "Effect of antigen shedding on targeted delivery of immunotoxins in solid tumors from a mathematical model," *PLoS ONE*, vol. 9, no. 10, Article ID e110716, 2014.
- [9] J. A. Westwood, W. K. Murray, M. Trivett et al., "The Lewis-Y carbohydrate antigen is expressed by many human tumors and can serve as a target for genetically redirected T cells despite the presence of soluble antigen in serum," *Journal of Immunotherapy*, vol. 32, no. 3, pp. 292–301, 2009.
- [10] L. Camera, S. Kinuya, C. H. Paik, and J. A. Carrasquillo, "Pre-clinical Evaluation of  $^{111}\text{In}$ -labeled B3 Monoclonal Antibody: Biodistribution and Imaging Studies in Nude Mice Bearing Human Epidermoid Carcinoma Xenografts," *Cancer Research*, vol. 53, no. 12, pp. 2834–2839, 1993.
- [11] I. Pastan, E. T. Lovelace, M. G. Gallo, A. V. Rutherford, J. L. Mag-nani, and M. C. Willingham, "Characterization of monoclonal antibodies B1 and B3 that react with mucinous adenocarcinomas," *Cancer Research*, vol. 51, no. 14, pp. 3781–3787, 1991.
- [12] L. H. Pai-Scherf, J. A. Carrasquillo, C. Paik et al., "Imaging and phase I study of  $^{111}\text{In}$ - and  $^{90\text{Y}}$ -labeled anti-LewisY monoclonal

- antibody B3,” *Clinical Cancer Research*, vol. 6, no. 5, pp. 1720–1730, 2000.
- [13] Z. Yao, M. Zhang, D. B. Axworthy et al., “Radioimmunotherapy of A431 xenografted mice with pretargeted B3 antibody-streptavidin and<sup>90</sup>Y-labeled 1, 4, 7, 10-tetraazacyclododecane-N, N′, N′′, N′′′-tetraacetic acid (DOTA)-biotin,” *Cancer Research*, vol. 62, no. 20, pp. 5755–5760, 2002.
- [14] J. P. Holland, E. Caldas-Lopes, V. Divilov et al., “Measuring the pharmacodynamic effects of a novel Hsp90 inhibitor on HER2/neu expression in mice using <sup>89</sup>Zr-DFO-trastuzumab,” *PLoS ONE*, vol. 5, no. 1, Article ID e8859, 2010.
- [15] I. Verel, G. W. Visser, R. Boellaard, M. Stigter-van Walsum, G. B. Snow, and G. A. van Dongen, “<sup>89</sup>Zr immuno-PET: comprehensive procedures for the production of <sup>89</sup>Zr-labeled monoclonal antibodies,” *Journal of Nuclear Medicine*, vol. 44, no. 8, pp. 1271–1281, 2003.
- [16] J. P. Holland, Y. Sheh, and J. S. Lewis, “Standardized methods for the production of high specific-activity zirconium-89,” *Nuclear Medicine and Biology*, vol. 36, no. 7, pp. 729–739, 2009.
- [17] M. J. W. D. Vosjan, L. R. Perk, G. W. M. Visser et al., “Conjugation and radiolabeling of monoclonal antibodies with zirconium-89 for PET imaging using the bifunctional chelate p-isothiocyanatobenzyl-desferrioxamine,” *Nature Protocols*, vol. 5, no. 4, pp. 739–743, 2010.
- [18] M. M. Bradford, “A rapid and sensitive method for the quantitation of microgram quantities of protein utilizing the principle of protein dye binding,” *Analytical Biochemistry*, vol. 72, no. 1-2, pp. 248–254, 1976.
- [19] T. Lindmo and P. A. Bunn, “[<sup>65</sup>] Determination of the True Immunoreactive Fraction of Monoclonal Antibodies after Radiolabeling,” *Methods in Enzymology*, vol. 121, no. C, pp. 678–691, 1986.
- [20] M. Ho, R. Hassan, J. Zhang et al., “Humoral immune response to mesothelin in mesothelioma and ovarian cancer patients,” *Clinical Cancer Research*, vol. 11, no. 10, pp. 3814–3820, 2005.
- [21] J. E. Weldon, L. Xiang, J. Zhang et al., “A recombinant immunotoxin against the tumor-associated antigen mesothelin reengineered for high activity, low off-target toxicity, and reduced antigenicity,” *Molecular Cancer Therapeutics*, vol. 12, no. 1, pp. 48–57, 2013.
- [22] Y. Zhang, J. K. Hansen, L. Xiang et al., “A flow cytometry method to quantitate internalized immunotoxins shows that taxol synergistically increases cellular immunotoxins uptake,” *Cancer Research*, vol. 70, no. 3, pp. 1082–1089, 2010.
- [23] Y. Zhang, L. Xiang, R. Hassan, and I. Pastan, “Immunotoxin and Taxol synergy results from a decrease in shed mesothelin levels in the extracellular space of tumors,” *Proceedings of the National Academy of Sciences of the United States of America*, vol. 104, no. 43, pp. 17099–17104, 2007.
- [24] S. Wang, I. S. Shin, H. Hancock et al., “Pulsed high intensity focused ultrasound increases penetration and therapeutic efficacy of monoclonal antibodies in murine xenograft tumors,” *Journal of Controlled Release*, vol. 162, no. 1, pp. 218–224, 2012.
- [25] Y. Boucher, L. T. Baxter, and R. K. Jain, “Interstitial Pressure Gradients in Tissue-isolated and Subcutaneous Tumors: Implications for Therapy,” *Cancer Research*, vol. 50, no. 15, pp. 4478–4484, 1990.

## Research Article

# Construction and Evaluation of the Tumor-Targeting, Cell-Penetrating Multifunctional Molecular Probe iCREKA

Li-juan Wang, Hong-sheng Li, Quan-shi Wang , Hu-bing Wu, Yan-jiang Han, Wen-lan Zhou, Meng Wang, and Shun Huang

PET Center, Nanfang Hospital, Southern Medical University, Guangzhou, Guangdong 510515, China

Correspondence should be addressed to Quan-shi Wang; [wqslph@163.net](mailto:wqslph@163.net)

Received 11 August 2017; Revised 24 December 2017; Accepted 5 February 2018; Published 4 March 2018

Academic Editor: James Frost

Copyright © 2018 Li-juan Wang et al. This is an open access article distributed under the Creative Commons Attribution License, which permits unrestricted use, distribution, and reproduction in any medium, provided the original work is properly cited.

A novel tumor stroma targeting and membrane-penetrating cyclic peptide, named iCREKA, was designed and labeled by fluorescein isothiocyanate (FITC) and positron emitter  $^{18}\text{F}$  to build the tumor-targeting tracers. The FITC-iCREKA was proved to have significantly higher cellular uptake in the glioma U87 cells in the presence of activated MMP-2 than that in absence of activated MMP-2 by cells fluorescence test *in vitro*. The tumor tissue fluorescence microscope imaging demonstrated that FITC-iCREKA accumulated in the walls of the blood vessels and the surrounding stroma in the glioma tumor at 1 h after intravenous injection. While at 3 h after injection, FITC-iCREKA was found to be uptaken in the tumor cells. However, the control FITC-CREKA can only be found in the tumor stroma, not in the tumor cells, no matter at 1 h or 3 h after injection. The whole-animal fluorescence imaging showed that the glioma tumor could be visualized clearly with high fluorescence signal. The microPET/CT imaging further demonstrated that  $^{18}\text{F}$ -iCREKA could target U87MG tumor *in vivo* from 30 min to 2 h after injection. The present study indicated the iCREKA had the capacity of tumor stroma targeting and the membrane-penetrating. It was potential to be developed as the fluorescent and PET tracers for tumor imaging.

## 1. Introduction

Currently, the diagnosis and treatment of malignant tumors remain extremely difficult. Molecular imaging and high-precision targeted therapy represent important directions for the future development of cancer therapy. Molecular recognition is the cornerstone of molecular imaging and targeted therapy. The construction of molecular probes that not only are capable of recognizing specific molecular targets in tumor tissues but also possess the ability to penetrate into tumor cells is of great significance for the specific diagnosis of tumors. Constructing such molecular probes is even more important for specific targeted therapies that need to overcome the biological barrier effect of the cell membrane.

Cell-penetrating peptides (CPPs), also known as protein transduction domains (PTDs), are a special class of polypeptides that have the ability to overcome the physiological barrier imposed by the cell membrane. These peptides can freely penetrate the cell membrane and enter the cytoplasm through endocytosis or specific channels. In addition, CPPs

may serve as carriers, carrying exogenous macromolecules up to 100 times their molecular weight (such as drugs or imaging agents) into cells. Therefore, CPPs have been used as important vectors to deliver imaging agents or therapeutic drugs into cells. However, conventional CPPs have no tumor-targeting activity, entering tumor cells and normal cells with equal ease [1–13]. Numerous studies have been carried out to develop CPPs that possess both tumor-targeting and cell-penetrating properties. In particular, conventional CPPs have been chemically modified and screened to identify CPPs capable of binding to specific targets (such as tLyP-1 and RGD) [14–20]. However, in general, broad-spectrum tumor-specific targeting is extremely difficult to achieve.

To this end, a novel multifunctional polypeptide molecular probe that possesses both tumor-targeting and cell-penetrating properties, iCREKA, was designed in the present study. The probe was constructed by connecting the following 3 main parts (Figure 1): the homing peptide CREKA, which is capable of targeting the tumor stroma, the cell-penetrating peptide Tat, and a linker (PLGLAG) that can be cleaved by

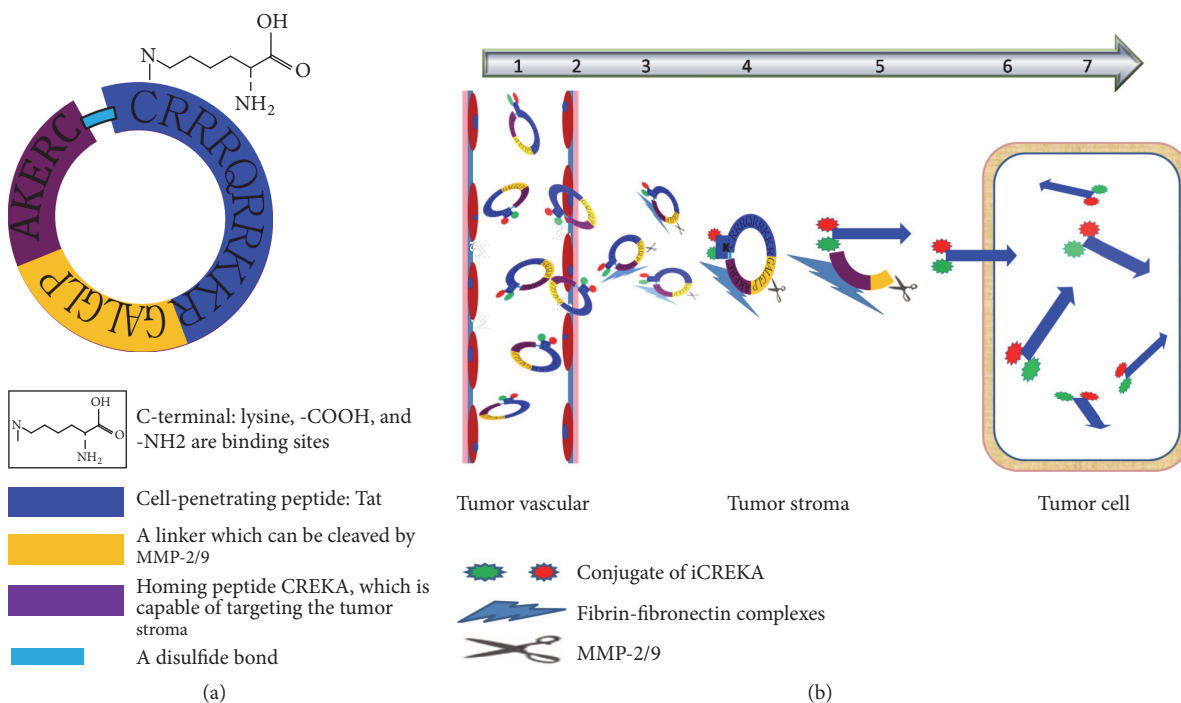


FIGURE 1: The structure (a) and the mechanism of action (b) of iCREKA.

matrix metalloproteinase-2 and -9 (MMP-2/9). To improve the stability of iCREKA in the blood, the 2 terminal cysteine (Cys) residues in the homing peptide and the membrane-penetrating peptide were covalently linked via a disulfide bond, forming a cyclic peptide. In addition, a lysine residue was added to the C-terminus of the cyclic peptide, which was used for fluorescein or radionuclide labeling.

The cyclic peptide iCREKA reaches tumor tissues via blood circulation. CREKA is expected to bind specifically to the fibrin-fibronectin complexes that are widely and abundantly distributed in tumor stroma but rarely present in normal tissues. Tumor tissues also overexpress MMP-2/9 and hydrolytic enzymes. MMP-2/9 recognize and cleave iCREKA between CREKA and the membrane-penetrating peptide, while hydrolytic enzymes hydrolyze the disulfide bond. As a result, the fluorescent or radionuclide-labeled membrane-penetrating peptide is released, which penetrates the plasma membrane and enters tumor cells. Since normal tissues express no or low levels of fibrin-fibronectin complexes and MMP-2/9, the cyclic peptide probe iCREKA should not be accumulated and be cleaved in normal tissues. Consequently, iCREKA is unable to enter normal cells. Thus, tumor-specific targeting and cell penetration are achieved (Figure 1).

In order to verify whether the cyclic peptide iCREKA specifically targets tumor tissues and possesses cell-penetrating function, the present study used CREKA as a control peptide and employed a fluorescent labeling approach to investigate the differences between iCREKA and CREKA at the cell, tissue, and whole-animal levels. In addition, the present study attempted to label iCREKA using the positron-emitting nuclide fluorine-18 (<sup>18</sup>F) and examine the *in vivo* tumor-targeting activity of labeled

iCREKA using live-animal positron emission tomography (PET)/computerized tomography (CT) imaging. The results are reported below.

## 2. Materials and Methods

**2.1. Materials.** <sup>18</sup>F was produced in our center using the PET-trace accelerator (GE Healthcare, USA). iCREKA, fluorescein isothiocyanate-conjugated iCREKA (FITC-iCREKA), and the control peptides CREKA and FITC-CREKA were custom-synthesized at Shanghai Qiangyao Biological Technology Co., Ltd. The anti-fibrinogen antibody was purchased from Abcam, UK (number: ab34269). The anti-MMP-2 antibody was purchased from ABclonal, America (number: A1558). Cyanine 3- (Cy3-) labeled goat anti-rabbit IgG and 4',6-diamidino-2-phenylindole dihydrochloride (DAPI) were purchased from Beyotime Biotechnology Co., Ltd.

**2.2. Tumor Cell Lines.** A human glioma cell line U87 was used in this study, and it was purchased from the Institute of Biochemistry and Cell Biology, Shanghai Institutes for Biological Sciences, Chinese Academy of Sciences (Shanghai, China). Cells were cultured at 37°C in a humidified 5% carbon dioxide-containing atmosphere, using Dulbecco's modified Eagle's medium (DMEM) (Hyclone, America) supplemented with 10% fetal calf serum (Hyclone, America).

**2.3. Animal Model.** Animal experiments were conducted under a protocol approved by the Nanfang hospital animal ethics committee at the Southern Medical University (Application number NFYY-2011-126). All surgery was performed under isoflurane anesthesia, and all efforts were made to minimize suffering.

The Laboratory Animal Center at the Southern Medical University provided female BALB/C athymic nude mice (nude mice) 4–6 wk of age. Glioma xenografts (U87 cells) were transplanted into subcutaneous of nude mice by injecting  $1 \times 10^6$  cells intramuscularly into the right flank. Tumor xenografts were monitored until the largest tumor diameter was approximately 0.5–1 cm, which took 2–3 weeks. Forty mice were inoculated, and models of human glioma in nude mice were made successful in 32 mice. The success rate was 80%.

**2.4. Chemical Synthesis of the Cyclic Peptide iCREKA and the Fluorescent Probes FITC-iCREKA and FITC-CREKA.** The linear polypeptide CREKAPLGLAGRKKRRQRRC was synthesized using solid-phase peptide synthesis (SPPS) [21]. Subsequently, cyclization was performed between the two Cys residues located at the N- and C-termini of the peptide. A lysine residue was then added to the C-terminus of the cyclized peptide, generating the cyclic peptide iCREKA. To prepare the fluorescent probe FITC-iCREKA, FITC was coupled to the amine group of the lysine side chain.

The control peptides CREKA and FITC-CREKA were synthesized using the same approach.

**2.5. Cytotoxicity.** The cytotoxicity of iCREKA was examined in U87 glioma cells using the Cell Counting Kit-8 (KeyGen Biotech) according to the instruction of the manufacturer. Cells were seeded at a density of  $1 \times 10^4$  cells/well in 96-well plates, allowed to grow for 24 h, and exposed to various concentrations of iCREKA for 24 h. The absorbance of each well at 450 nm was measured with an absorbance microplate reader (BIOTEK ELX800, USA). The cell viability was calculated by

$$\text{Viability \%} = \frac{\text{Absorbance}_{\text{test}} - \text{Absorbance}_{\text{blank}}}{\text{Absorbance}_{\text{control}} - \text{Absorbance}_{\text{blank}}} \times 100\% \quad (1)$$

**2.6. The Membrane Penetration Effect of FITC-iCREKA after Cleavage by MMP-2.** (1) Examination of the binding of FITC-iCREKA to U87 glioma cells after MMP-2 addition.

(a) MMP-2 activation: to obtain active MMP-2, 80  $\mu\text{l}$  of 0.7 mg/ml mouse MMP2/Tris-HCl solution was mixed with 0.1 ml of 2.5 mmol/14-aminophenylmercuric acetate (APMA) and incubated for 2 h in a 37°C water bath.

(b) Fluorescence examination: one hundred microliters of active MMP-2/1640 solution (0.7 mg/ml) was mixed with 0.9 ml of freshly prepared serum-free cell culture medium containing FITC-iCREKA (10  $\mu\text{M}$ ). Following filter sterilization, 1 ml of the mixture was added to cell culture dishes containing exponentially growing U87 glioma cells. After incubation at 4°C for 60 min, U87 cells were washed with phosphate-buffered saline (PBS, 5 min  $\times$  3 times), fixed with 75% ethanol, and stained with DAPI. Fluorescence distribution in live cells was examined on a confocal microscope.

U87 cells were seeded into 96-well plates at a density of  $1 \times 10^4$  per well and grew to confluence over 24 h. The cells were incubated with 10  $\mu\text{M}$  of FITC-iCREKA with

activated MMP-2 as test group and 10  $\mu\text{M}$  of FITC-iCREKA without activated MMP-2 as control one for 1 h at 37°C. After the incubation, the culture media were removed and the cells were washed twice using the PBS. The cells were then trypsinized, centrifuged (4°C, 5 min, 1000 rpm), and diluted to  $1 \times 10^6$  cells/mL. The test and control samples were analyzed on a flow cytometer (Becton Dickinson, Oxford, UK) to measure the cellular fluorescence.

(2) Examination of the binding of FITC-iCREKA to U87 glioma cells without MMP-2 addition.

FITC-iCREKA (the same amount as above) was sterilized by filtration. Subsequently, 1 ml of the FITC-iCREKA solution was added to U87 glioma cells. After incubation at 4°C for 60 min, U87 cells were washed 3 times with PBS (5 min each). The fluorescence distribution in live cells was examined on a confocal microscope. The intracellular fluorescence intensity, which reflected the level of FITC-iCREKA uptake, was analyzed using flow cytometry.

(3) Examination of the binding of the control peptide FITC-CREKA to U87 glioma cells.

The binding between U87 cells and the control peptide FITC-CREKA was assayed using the same approach. The fluorescence distribution was examined using confocal microscopy. The intracellular fluorescence intensity, which reflected the level of FITC-CREKA uptake, was analyzed using flow cytometry.

**2.7. Expression of Fibrin and MMP-2 in Tumor Tissues.** Tumor samples from U87 tumor xenografts were examined for fibrin and MMP-2 expression using an immunofluorescent and an immunohistochemical staining. Tumor sliders were firstly handled using rabbit anti-fibrinogen antibody or anti-MMP-2 antibody as the primary antibody. Then Cy3-labeled or horseradish peroxidase enzyme-labeled polymers conjugated to anti-rabbit immunoglobulins as the secondary antibody were added to react with the primary antibody. The dilution factors for primary antibody were 1:1000 for antifibrin and 1:100 for anti-MMP-2. The images of fibrinogen and MMP-2 expression in tumor tissues were acquired via a fluorescent microscope and immunohistochemical staining.

**2.8. The Targeting and Cell-Penetrating Activities of FITC-iCREKA in Tumor Tissues.** Tumor-bearing mice were randomly divided into the experimental group ( $n = 6$ ) and the control group ( $n = 6$ ). The experimental group and the control group received FITC-iCREKA and FITC-CREKA, respectively (1 mM, 150  $\mu\text{l}$ ), via tail-vein injection. Subsequently, tumor tissues were collected from each group at multiple time points. The collected tumor tissues were frozen, sectioned, and stained with DAPI. The distribution of FITC-iCREKA and FITC-CREKA in tumor tissues was observed and compared at each time point using confocal microscopy.

**2.9. The Tumor-Targeting Activity of FITC-iCREKA in Tumor-Bearing Mice.** Tumor-bearing mice were randomly divided into the experimental group ( $n = 6$ ) and the control group ( $n = 6$ ), which received FITC-iCREKA and FITC-CREKA, respectively (1 mM, 150  $\mu\text{l}$ ), via tail-vein injection.

At 1 h after injection, tumors and various organs were isolated, washed, and imaged using the Kodak *in vivo* imaging system F. Fluorescence distribution was examined in tumors and in various organs and tissues. Images were analyzed using the built-in Kodak Molecular Imaging (MI) software. Regions of interest (ROIs) were outlined on the fluorescence images along the edges of the tumors and various tissues. Fluorescence counts in each ROI were determined, and the tumor/nontumor uptake ratios of FITC-iCREKA and FITC-CREKA were calculated by comparing the corresponding fluorescence counts in tumor and normal tissues.

**2.10. The Tumor-Targeting Activity of  $^{18}\text{F}$ -iCREKA in Tumor-Bearing Mice.**  $^{18}\text{F}$ -FP-iCREKA was synthesized using the method developed by Chin et al. [22], which involved multiple reactions. The chemical and radiochemical purities of  $^{18}\text{F}$ -FP-iCREKA were determined by high-performance liquid chromatography (HPLC) and thin layer chromatography (TLC) combined with radioactivity detection.

Tumor-bearing mice received 5.50–7.40 MBq (150–200  $\mu\text{Ci}$ ) of the imaging agent  $^{18}\text{F}$ -iCREKA via tail-vein injection and were anesthetized using isoflurane. The mice were then subjected to microPET/CT imaging at 30, 60, and 120 min after  $^{18}\text{F}$ -iCREKA injection. The uptake of  $^{18}\text{F}$ -iCREKA by tumors and various tissues was examined.

ROIs were outlined on the PET images using the Syngo image analysis software installed on the microPET/CT system. The radioactivity counts were determined, and the tumor/brain ratio was calculated.

**2.11. Statistical Analysis.** The results were analyzed using the SPSS 20.0 statistical software. Measurement data were presented as the mean  $\pm$  standard deviation. The Kolmogorov-Smirnov (K-S) test was employed to examine the normality of the data. The independent two-sample *t*-test was conducted to compare the fluorescent intensity and tumor/nontumor ratios between the experimental group and the control group. *P* values less than 0.05 were considered statistically significant.

### 3. Results

**3.1. Chemical Synthesis of the Cyclic Peptide iCREKA and the Fluorescent Probes FITC-iCREKA and FITC-CREKA.** The peptides iCREKA and CREKA were chemically synthesized using the SPPS approach. The fluorescent probes FITC-iCREKA and FITC-CREKA were prepared using FITC, a derivative of fluorescein. The calculated molecular weights are 2665.26 for iCREKA, 3169.81 for FITC-iCREKA, and 995.09 for FITC-CREKA, respectively. The measured molecular weights of the peptides are  $[\text{M} + \text{H}]^+$ . The ESI-HRMS  $m/z$   $[\text{M} + \text{H}]^+$  were found to be 2665.6 for iCREKA, 3170.4 for FITC-iCREKA and 994.6 for FITC-CREKA, respectively. HPLC analysis demonstrated that the purity of iCREKA, FITC-iCREKA, and FITC-CREKA was 98.27%, 98.23%, and 98.66%, respectively, after purification.

**3.2. Cytotoxicity.** The cell viability was only slightly damaged by the iCREKA. The cell viability was approximately

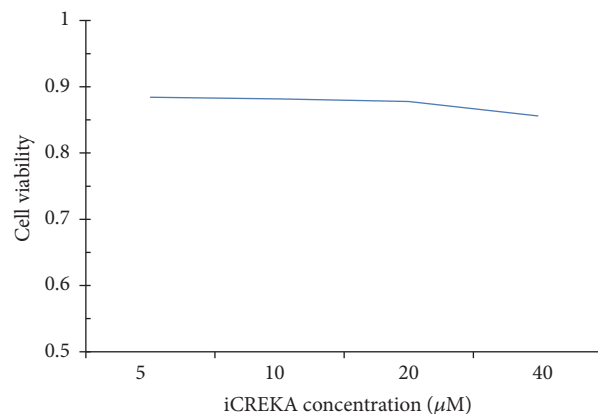


FIGURE 2: Cytotoxicity of iCREKA at various concentrations.

88.0% when the concentration of added iCREKA was 10  $\mu\text{M}$ , which was the added concentration of iCREKA in the cell-penetrating experiments (Figure 2).

**3.3. FITC-iCREKA Penetrates the Cell Membrane and Enters Tumor Cells after Cleavage by MMP-2.** The cell-penetrating activity of FITC-iCREKA was examined in the presence and absence of activated MMP-2. In the presence of activated MMP-2, we found that accumulation of green fluorescence within the tumor cells was intense, and the green fluorescence accumulated not only into the cytoplasm, but also into the nucleoli of U87 cells. However, in the absence of activated MMP-2, the uptake of green fluorescence within the tumor cells was minimal (Figure 3). Flow cytometry indicated that the addition of activated MMP-2 to the culture medium resulted in significantly increased FITC-iCREKA uptake into U87 cells (the fluorescence intensities in the presence and absence of activated MMP-2 were  $14110.0 \pm 3205.65$  and  $3921.33 \pm 821.27$ , resp.,  $t = 7.542$ ,  $P = 0.000$ ) (Figure 4(a)).

The cell-penetrating activity of the control peptide FITC-CREKA was examined in the presence and absence of activated MMP-2. Only extremely low levels of green fluorescence were detected in the plasma membrane of U87 cells and inside U87 cells, regardless of the presence of activated MMP-2 in the culture medium (Figure 3).

Flow cytometry analysis revealed that FITC-iCREKA uptake was significantly higher than FITC-CREKA uptake in U87 cells ( $14110.0 \pm 3205.65$  versus  $2569.50 \pm 975.84$ ,  $t = 8.436$ ,  $P = 0.000$ ) (Figure 4(b)).

**3.4. Fibrin and MMP-2 Are Highly Expressed in Tumor Tissues.** Immunofluorescent and an immunohistochemical staining demonstrated that fibrin and MMP-2 were highly expressed in tumor tissue (Figures 5–7).

**3.5. The Targeting and Cell-Penetrating Activities of FITC-iCREKA in Tumor Tissues.** Tumor-bearing mice received FITC-iCREKA or the control fluorescent probe FITC-CREKA via tail-vein injection. Fluorescence imaging revealed that FITC-iCREKA accumulated mainly within the stroma of tumor tissues at 1 h after tail-vein injection. In addition, FITC-iCREKA showed the same distribution

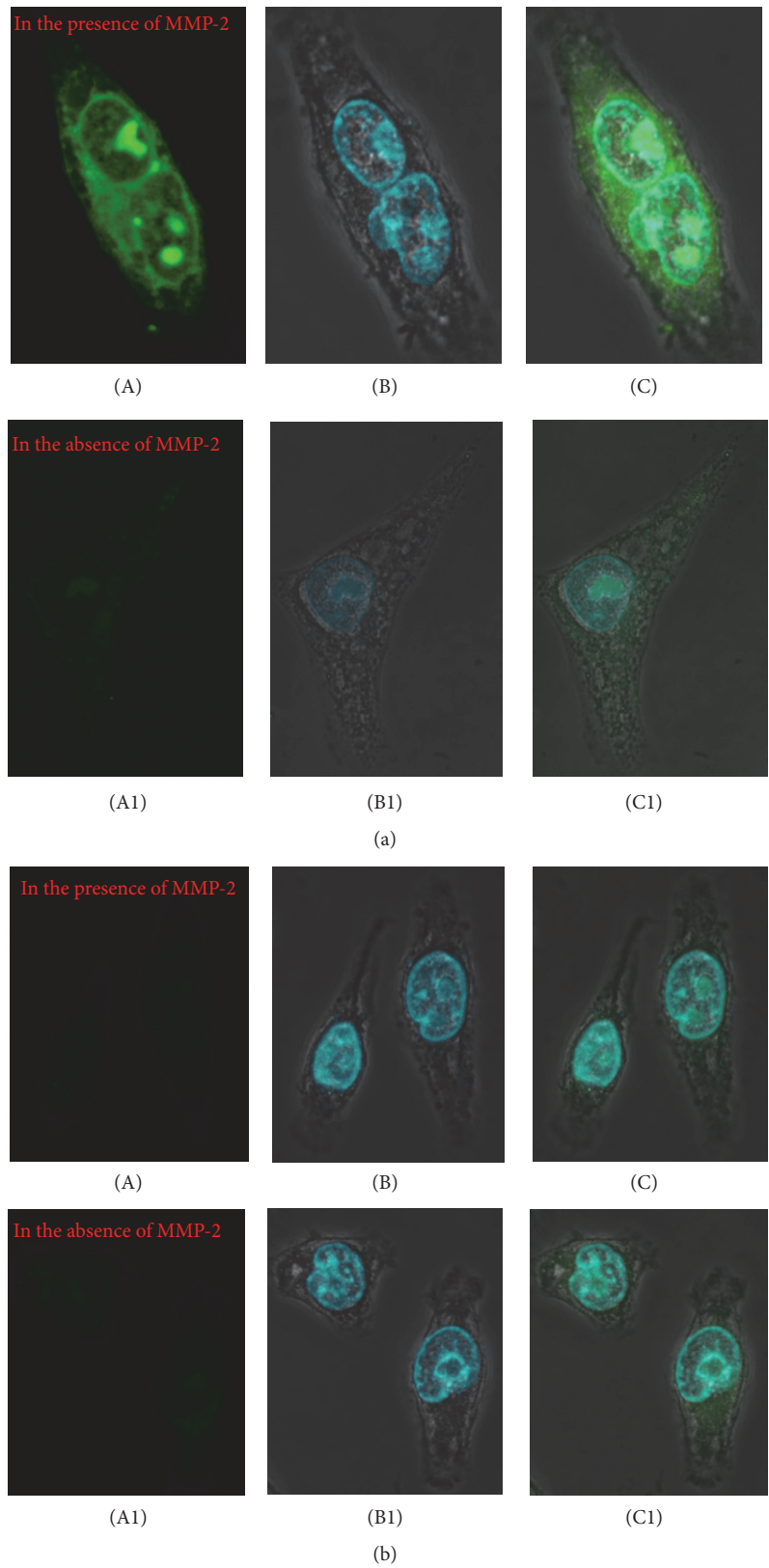


FIGURE 3: Fluorescent confocal imaging of cell internalization of FITC-iCREKA and FITC-CREKA in the fixed U87 glioma cells ((a) and (b)). (a) Cell internalization of FITC-iCREKA in the presence and in the absence of MMP-2 (green, (A), (A1)), staining of nucleus (blue, (B), (B1)), and merged image of FITC-iCREKA uptake and nucleus ((C), (C1)). (b) Cell internalization of FITC-CREKA in the presence and in the absence of MMP-2 (green, (A), (A1)), staining of nucleus (blue, (B), (B1)), and merged image of FITC-CREKA uptake and nucleus ((C), (C1)). Magnification:  $\times 60$ .

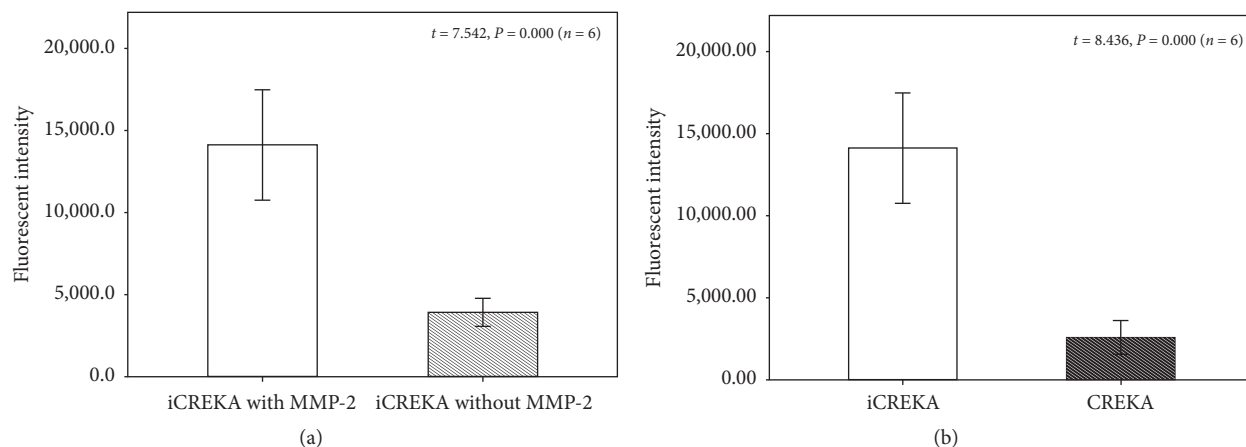


FIGURE 4: (a) Fluorescent intensity of FITC-iCREKA with and without activated MMP-2 in U87 cells using the flow cytometry analysis. (b) Fluorescent intensity of FITC-iCREKA and FITC-CREKA in U87 cells using the flow cytometry analysis.

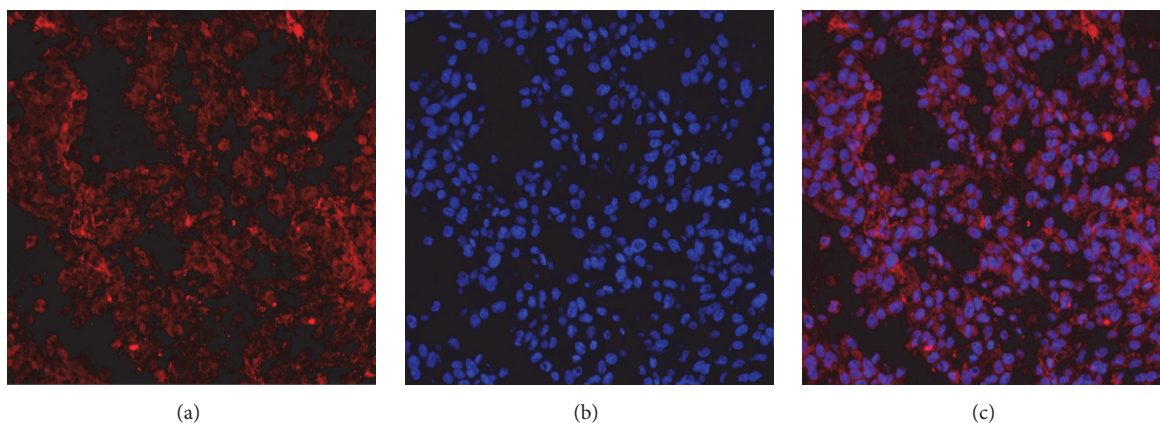


FIGURE 5: Immunofluorescent staining of the fibrin expression in the tumor tissues. (a) The immunofluorescent staining of the fibrin expression in the tumor tissues (red). (b) DAPI staining of cell nuclei (blue). (c) Fusion of (a) and (b). Positive expression of fibrin was detected in U87 tumor tissues. (magnification:  $\times 200$ ; scale bars,  $3 \mu\text{m}$ ).

as that of fibrinogen. At 1 h after tail-vein injection, FITC-CREKA also accumulated in the tumor stroma and exhibited essentially the same distribution as FITC-iCREKA (Figure 8).

Three hours after tail-vein injection of FITC-iCREKA or the control fluorescent probe FITC-CREKA into the tumor-bearing mice, fluorescence imaging analysis revealed that FITC-iCREKA accumulated in tumor cells. In contrast, the control fluorescent probe FITC-CREKA remained in the tumor stroma. No significant uptake of FITC-CREKA fluorescence was detected in tumor cells (Figure 8).

**3.6. The Tumor-Targeting Activity of FITC-iCREKA in Tumor-Bearing Mice.** At 1 h after tail-vein injection of tumor-bearing mice with FITC-iCREKA or the control fluorescent probe FITC-CREKA, tumor lesions and various organs and tissues were isolated and subjected to fluorescence imaging. Significant uptake of FITC-iCREKA was observed in tumors, whereas only a low level of fluorescence uptake was detected in normal brain tissues, yielding a tumor/brain ratio of  $3.27 \pm 0.78$ . The fluorescent probe FITC-iCREKA was eliminated via biliary, intestinal, and urinary excretion. Consistently,

fluorescence largely accumulated in the gallbladder, intestinal tract, and both kidneys. Only low levels of fluorescence were distributed in other organs and tissues. Compared with the control fluorescent probe FITC-CREKA, tumor lesions took up considerably higher amounts of FITC-iCREKA. In addition, significant differences were observed in the tumor/brain ratio between FITC-iCREKA and FITC-CREKA ( $3.27 \pm 0.78$  versus  $1.63 \pm 0.68$ ,  $t = 5.067$ ,  $P \leq 0.001$ ) (Figure 9).

**3.7. The Tumor-Targeting Activity of  $^{18}\text{F}$ -iCREKA in Tumor-Bearing Mice.**  $^{18}\text{F}$ -iCREKA was successfully prepared by acylation. 4-Nitrophenyl-2- $^{18}\text{F}$ -fluoropropionate ( $^{18}\text{F}$ -NFP) is a reaction precursor. Its nitrophenyl group can react with amino group of peptide, which can then form an amide bond between 2- $^{18}\text{F}$ -fluoropropionate and peptide. As a result,  $^{18}\text{F}$  was coupled to the peptides. The synthetic procedure was shown in Figure 10. The overall reaction time was 180 min. After HPLC purification, the radiochemical purity of  $^{18}\text{F}$ -iCREKA reached 97.0%. From the PET images in Figure 11, the tumor could be clearly visualized because the radioactivity uptake was significantly higher than that of

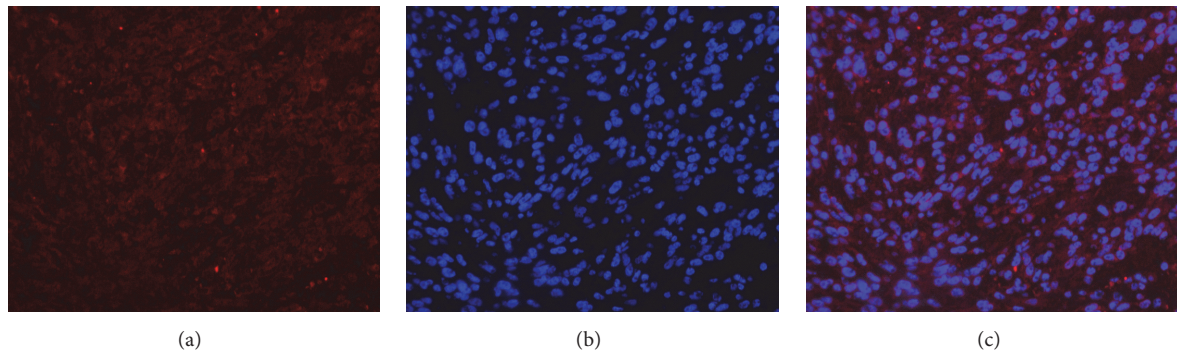


FIGURE 6: Immunofluorescent staining of the MMP-2 expression in the tumor tissues. (a) The immunofluorescent staining of the MMP-2 expression in the tumor tissues (red). (b) DAPI staining of cell nuclei (blue). (c) Fusion of (a) and (b). Positive expression of MMP-2 was detected in U87 tumor tissues. (magnification:  $\times 200$ ; scale bars,  $3 \mu\text{m}$ ).

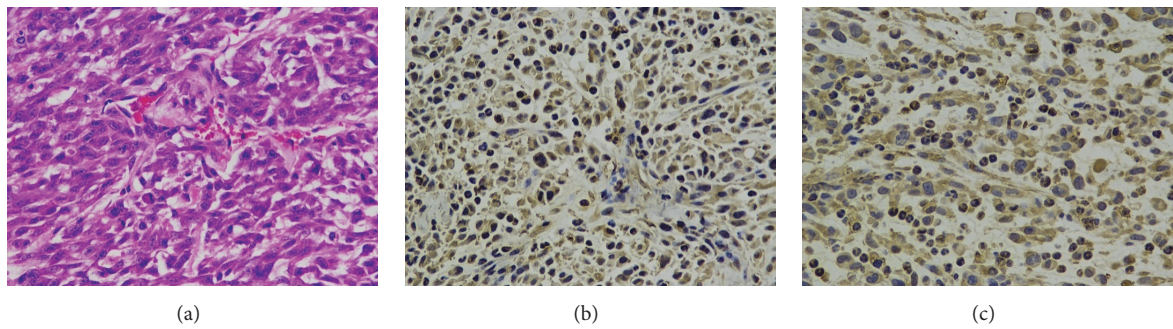


FIGURE 7: Immunohistochemical staining of the fibrin and MMP-2 expression in the tumor tissues. (a) The HE staining of tumor tissue. (b, c) Immunohistochemical staining of fibrin and MMP-2 expressions in tumor tissue (brown). Positive expressions of fibrin and MMP-2 were detected in U87 tumor tissues. (magnification:  $\times 200$ ; scale bars,  $3 \mu\text{m}$ ).

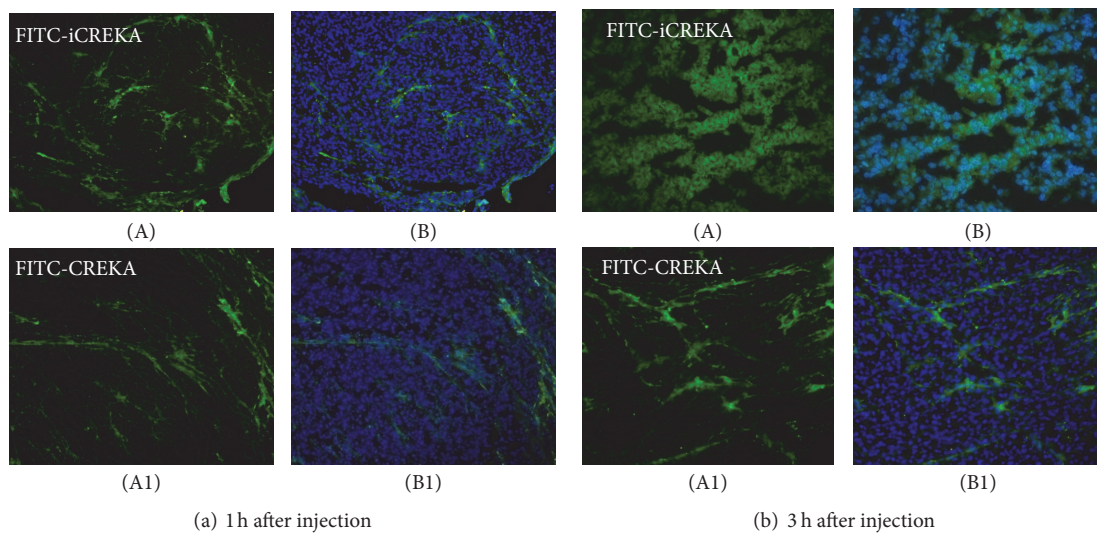


FIGURE 8: Fluorescence distribution in tumor tissues at 1 h (a) and 3 h (b) after tail-vein injection of FITC-iCREKA (A) and FITC-CREKA (A1) into model mice bearing U87 gliomas. (A) FITC-iCREKA; (A1) FITC-CREKA; (B) and (B1) merged images showing FITC-iCREKA/FITC-CREKA and the nucleus. Magnification:  $\times 200$ .

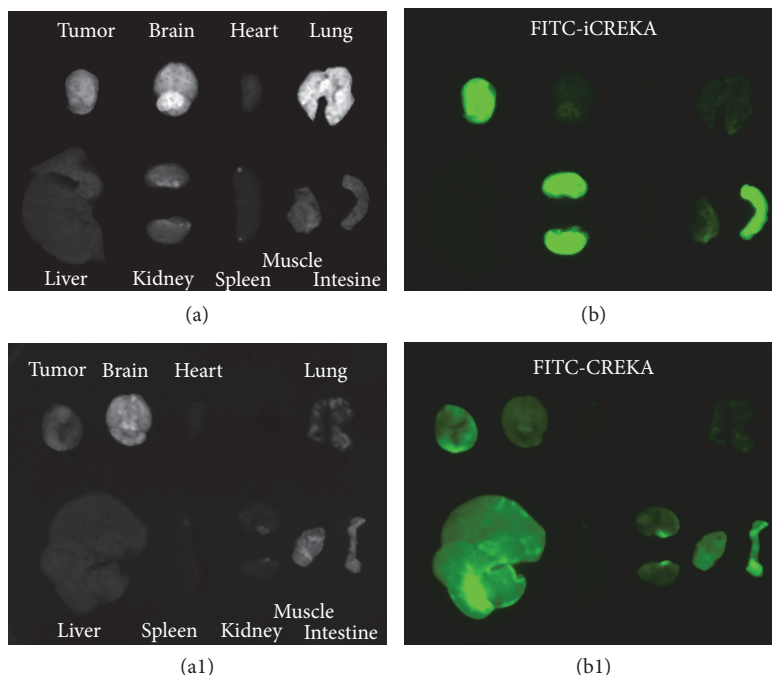


FIGURE 9: *In vivo* fluorescence imaging of tumors and normal organs at 1 h after tail-vein injection of nude mice bearing U87 gliomas with FITC-iCREKA (a and b) and FITC-CREKA (a1 and b1). Gallbladder was excluded from the figure. ((a) and (a1)) White light images; ((b) and (b1)) fluorescence images.

the neighboring normal tissues. During the imaging process, although the uptake in tumor decreased slightly over time, the visualization of tumor was not obviously affected. High radioactivity distribution was also noted in both kidneys, which indicated  $^{18}\text{F}$ -iCREKA was eliminated mainly via the urinary system. The radioactivity distribution in the liver, gallbladder, and intestine was not very high, which implied that the hepatobiliary system was not the main elimination route of  $^{18}\text{F}$ -iCREKA. The radioactivity in the brain, head and neck, lungs, heart, and muscle was also minimal. Low radioactivity uptake in the brain contributed to a high tumor/brain ratio of  $2.11 \pm 0.24$  at 30 min,  $3.53 \pm 0.31$  at 60 min, and  $3.04 \pm 0.37$  at 120 min, respectively. However, low tumor/kidney ( $0.88 \pm 0.11$  at 60 min) was observed.

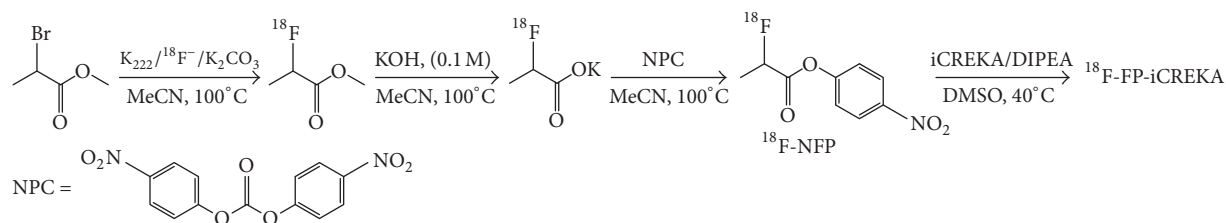
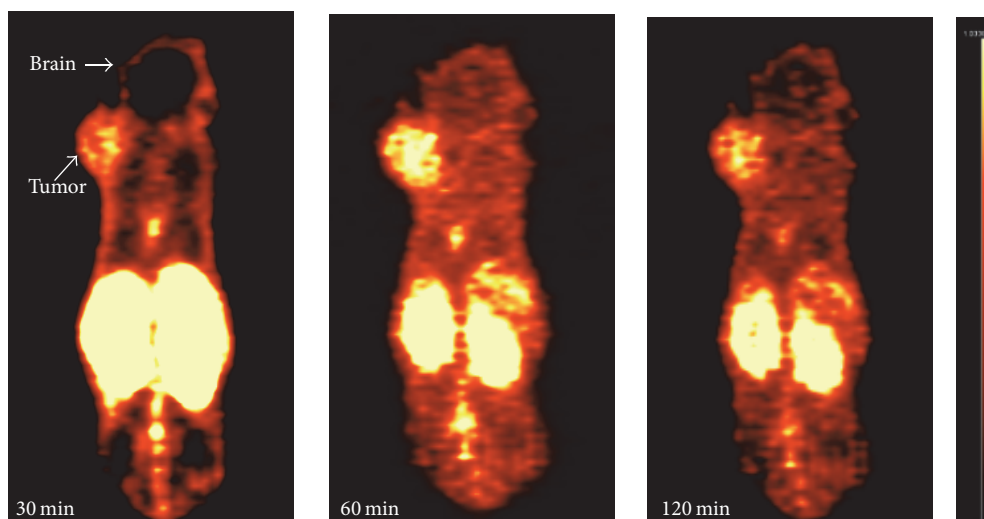
#### 4. Discussion

In the present study, the cyclic peptide iCREKA was successfully synthesized and prepared as a fluorescent and PET probe. Cytological examination, histological examination, and tumor imaging demonstrated that iCREKA-based molecular probes specifically targeted the fibrin-fibronectin complexes abundantly present in the tumor stroma. In addition, these molecular probes were able to achieve a tumor cell-penetrating effect after cleavage by MMP-2. Fluorescence and PET imaging showed that iCREKA-based molecular probes have the potential to be developed into molecular probes for tumor imaging.

The development of molecular probes capable of specifically targeting tumors holds great significance for tumor diagnosis, tumor staging, and the evaluation of therapeutic

efficacy. Currently,  $^{18}\text{F}$ -fluorodeoxyglucose ( $^{18}\text{F}$ -FDG) is the most commonly used molecular probe in the diagnosis and staging of malignant tumors and the evaluation of therapeutic efficacy. The application of  $^{18}\text{F}$ -FDG PET/CT imaging has a significant impact on the diagnosis and treatment of tumors [23–27]. However,  $^{18}\text{F}$ -FDG is a glucose analog and is therefore not a tumor-specific imaging agent. Some benign lesions such as inflammation, tuberculosis, and granulomatous lesions show increased metabolism, which may cause false positive results in  $^{18}\text{F}$ -FDG PET/CT imaging. Therefore, certain limitations exist in the application of  $^{18}\text{F}$ -FDG to diagnose tumors. A number of other imaging agents have been gradually developed. However, these imaging agents have been unable to surpass  $^{18}\text{F}$ -FDG and achieve wide recognition in clinical practice [28–30].

Studies have shown that fibrin-fibronectin complexes are abundantly present in the tumor stroma. The levels of fibrin-fibronectin complexes are significantly higher in the tumor stroma than in normal tissues. The above findings lay a foundation for studies that focus on targeting the tumor stroma. Fibrin-fibronectin complexes are expected to become targets for tumor stroma imaging. Work by Simberg et al. has shown that the small polypeptide CREKA is capable of specifically targeting fibrin-fibronectin complexes and thus possesses tumor-homing functions [8, 31, 32]. However, it is theoretically impossible to achieve tumor-specific targeting by simply targeting the fibrin-fibronectin complexes in the tumor stroma. In cases of inflammatory healing and trauma, large amounts of fibrin-fibronectin complexes often accumulate in the lesioned tissues. Thus, distinguishing tumors from inflammation is an important obstacle commonly facing

FIGURE 10: Schematic synthetic procedure of  $^{18}\text{F}$ -FP-iCREKA.FIGURE 11: MicroPET/CT images at 30, 60, and 120 min after tail-vein injection of nude mice bearing U87 gliomas with  $^{18}\text{F}$ -iCREKA.

tumor-imaging agents. In addition, as a linear polypeptide, CREKA is readily degraded by soluble peptidases present in the blood. The *in vivo* stability of CREKA is therefore much lower than that of the cyclic peptides.

Dual-target recognition is expected to achieve better tumor-specific targeting and be more conducive to distinguishing tumors from inflammation. Numerous studies have shown that MMP-2/9 are highly expressed in tumor tissues, which promotes the formation, repair, and maturation of tumor neovasculature and stimulates tumor growth [33–37]. MMP-2/9 is expressed at lower levels in normal tissues. Targeting MMP-2/9 in tumor tissues has been attempted in targeted cancer therapies [36–38]. In the present study, the polypeptide iCREKA was designed to incorporate an MMP2/9-cleavable linker. Consequently, specific penetration of iCREKA into tumor cells can be achieved only after iCREKA is cleaved by MMP-2/9. Therefore, iCREKA possesses dual-targeting properties, which is conducive to the enhancement of targeting specificity. In the presence of activated MMP-2, the accumulation of green fluorescence within the tumor cells was intense; however, in the absence of activated MMP-2, the uptake of green fluorescence within the tumor cells was minimal, which indicated that Tat mediated cellular internalization occurred in the presence of activated MMP-2, but not in the absence of activated MMP-2. The very slightly green fluorescence within the tumor cells in the absence of activated MMP-2 might be due to

the self-luminescence of the substance within the cells, but not the cellular internalization. Dual targeting of fibrin-fibronectin complexes and MMP-2/9 in tumor tissues lays the foundation for achieving tumor-targeting and tumor-specific cell penetration.

The development of molecular probes that are taken up only by tumor cells and not by normal cells or cells with benign pathological changes is the basis for achieving tumor-specific imaging and targeted cancer therapy. Tumor-specific cell penetration is particularly important for targeted cancer therapies, especially for therapies designed to damage specific organelles in tumor cells. The tumor cell membrane often represents an insurmountable physiological barrier to a large number of drugs, and only after crossing this physiological barrier may tumor-cell-organelle-targeting drugs exert their effects. Therefore, tumor cell penetration has been a hot topic in cancer research. The present study showed that the addition of MMP-2 to the medium during incubation of tumor cells with FITC-iCREKA allowed FITC-iCREKA to penetrate into tumor cells. FITC-iCREKA not only accumulated in the cytoplasm of tumor cells but also reached the nucleus. At 3 h after intravenous injection of FITC-iCREKA into tumor-bearing mice, a large amount of fluorescence accumulated in the tumor cells but not in the tumor stroma. The above results indicated that the combination of dual targeting of fibrin-fibronectin complexes and MMP-2/9 and MMP-2/9-mediated cleavage allowed iCREKA to achieve

tumor cell-specific targeting and membrane penetration. Fluorescence and PET imaging of tumor-bearing mice revealed significant uptake of the imaging probe by tumors and the accumulation of the imaging probe in normal pathways of excretion. In contrast, no apparent accumulation of the imaging probe was detected in other normal tissues in tumor-bearing mice. The results of the present study indicate that iCREKA has the potential to serve as a tumor-specific imaging agent as well as a tumor-targeting cell-penetrating carrier. It is expected that iCREKA can overcome the cell membrane barrier and enter cells freely while carrying therapeutic drugs, thereby playing a role in targeted cancer therapy.

Although the present study has demonstrated to a certain extent that iCREKA has the potential to serve as a tumor-targeting imaging agent or a carrier for targeted drugs, the following aspects of the PET imaging study need to be further addressed in detail: (1) iCREKA-based PET imaging should be conducted on a large number of tumor models to demonstrate repeatability. (2) iCREKA-based PET imaging should be conducted on other types of tumors besides glioma to determine the feasibility of broad-spectrum application of iCREKA. (3) In this study,  $^{18}\text{F}$ -iCREKA was synthesized by acylation. The labeling process was time consuming, and the yields were fairly low. The development of other labels to enhance synthetic yields and reduce the reaction time is a difficult issue that needs to be solved in future studies. Previous reports used a backbone-modified version of CREKA in order to increase the activity *in vivo*, such as David [39] that transformed CREKA into pocket-like shape to increase its accumulation in tumors. However, in the present study, we have not studied the differences on tumor PET imaging between these two different versions. Although we have confirmed the feasibility of tumor imaging of  $^{18}\text{F}$ -iCREKA on PET in the present study, further research is warranted to determine the superiority of the two versions of CREKA.

## 5. Conclusions

*In vivo* and *in vitro* experiments showed that iCREKA was able to target fibrin in the tumor stroma and subsequently penetrate into glioma cells, allowing successful tumor imaging. MicroPET/CT imaging demonstrated that  $^{18}\text{F}$ -iCREKA specifically targeted glioma lesions, which enables the visualization of the tumors.

## Disclosure

Li-juan Wang, M.D., and Hong-sheng Li are co-first authors.

## Conflicts of Interest

The authors declare no conflicts of interest.

## Acknowledgments

This work was supported by the National Natural Science Foundation Project of China (nos. 81271641, 81501511, and 81301215).

## References

- [1] S. E. Blondelle and R. A. Houghten, "Hemolytic and antimicrobial activities of the twenty-four individual omission analogues of melittin," *Biochemistry*, vol. 30, no. 19, pp. 4671–4678, 1991.
- [2] T. Higashijima, K. Wakamatsu, M. Takemitsu, M. Fujino, T. Nakajima, and T. Miyazawa, "Conformational change of mastoparan from wasp venom on binding with phospholipid membrane," *FEBS Letters*, vol. 152, no. 2, pp. 227–230, 1983.
- [3] G. P. H. Dietz and M. Bähr, "Delivery of bioactive molecules into the cell: The Trojan horse approach," *Molecular and Cellular Neuroscience*, vol. 27, no. 2, pp. 85–131, 2004.
- [4] B. E. Vogel, S. J. Lee, A. Hildebrand et al., "A novel integrin specificity exemplified by binding of the alpha v beta 5 integrin to the basic domain of the HIV Tat protein and vitronectin," *Journal of Cell Biology*, vol. 121, no. 2, pp. 461–468, 1993.
- [5] S. Fawell, J. Seery, Y. Daikh et al., "Tat-mediated delivery of heterologous proteins into cells," *Proceedings of the National Academy of Sciences of the United States of America*, vol. 91, no. 2, pp. 664–668, 1994.
- [6] H. Brooks, B. Lebleu, and E. Vivès, "Tat peptide-mediated cellular delivery: back to basics," *Advanced Drug Delivery Reviews*, vol. 57, no. 4, pp. 559–577, 2005.
- [7] F. Said Hassane, A. F. Saleh, R. Abes, M. J. Gait, and B. Lebleu, "Cell penetrating peptides: overview and applications to the delivery of oligonucleotides," *Cellular and Molecular Life Sciences*, vol. 67, no. 5, pp. 715–726, 2010.
- [8] J. P. Richard, K. Melikov, E. Vives et al., "Cell-penetrating peptides: A reevaluation of the mechanism of cellular uptake," *The Journal of Biological Chemistry*, vol. 278, no. 1, pp. 585–590, 2003.
- [9] C. Palm-Apergi, A. Lorents, K. Padari, M. Pooga, and M. Hällbrink, "The membrane repair response masks membrane disturbances caused by cell-penetrating peptide uptake," *The FASEB Journal*, vol. 23, no. 1, pp. 214–223, 2009.
- [10] I. Mäger, E. Eiríksdóttir, K. Langel, S. EL Andaloussi, and Ü. Langel, "Assessing the uptake kinetics and internalization mechanisms of cell-penetrating peptides using a quenched fluorescence assay," *Biochimica et Biophysica Acta*, vol. 1798, no. 3, pp. 338–343, 2010.
- [11] A. D. Frankel and C. O. Pabo, "Cellular uptake of the tat protein from human immunodeficiency virus," *Cell*, vol. 55, no. 6, pp. 1189–1193, 1988.
- [12] M. Rusnati, D. Coltrini, P. Oreste et al., "Interaction of HIV-1 Tat protein with heparin. Role of the backbone structure, sulfation, and size," *The Journal of Biological Chemistry*, vol. 272, no. 17, pp. 11313–11320, 1997.
- [13] A. Prochiantz, "Messenger proteins: homeoproteins, TAT and others," *Current Opinion in Cell Biology*, vol. 12, no. 4, pp. 400–406, 2000.
- [14] L. Roth, L. Agemy, V. R. Kotamraju et al., "Transtumoral targeting enabled by a novel neuropilin-binding peptide," *Oncogene*, vol. 31, no. 33, pp. 3754–3763, 2012.
- [15] P. Laakkonen, K. Porkka, J. A. Hoffman, and E. Ruoslahti, "A tumor-homing peptide with a targeting specificity related to lymphatic vessels," *Nature Medicine*, vol. 8, no. 7, pp. 751–755, 2002.
- [16] P. Laakkonen, M. E. Åkerman, H. Biliran et al., "Antitumor activity of a homing peptide that targets tumor lymphatics and tumor cells," *Proceedings of the National Academy of Sciences of the United States of America*, vol. 101, no. 25, pp. 9381–9386, 2004.

- [17] V. Fogal, L. Zhang, S. Krajewski, and E. Ruoslahti, "Mitochondrial/cell-surface protein p32/gC1qR as a molecular target in tumor cells and tumor stroma," *Cancer Research*, vol. 68, no. 17, pp. 7210–7218, 2008.
- [18] J. Park, G. von Maltzahn, M. J. Xu et al., "Cooperative nanomaterial system to sensitize, target, and treat tumors," *Proceedings of the National Academy of Sciences of the United States of America*, vol. 107, no. 3, pp. 981–986, 2010.
- [19] T. P. Herrington and J. G. Altin, "Effective tumor targeting and enhanced anti-tumor effect of liposomes engrafted with peptides specific for tumor lymphatics and vasculature," *International Journal of Pharmaceutics*, vol. 411, no. 1-2, pp. 206–214, 2011.
- [20] F. Zhang, G. Niu, X. Lin et al., "Imaging tumor-induced sentinel lymph node lymphangiogenesis with LyP-1 peptide," *Amino Acids*, vol. 42, no. 6, pp. 2343–2351, 2012.
- [21] R. B. Merrifield, "Solid-phase peptide synthesis. III. An improved synthesis of bradykinin," *Biochemistry*, vol. 3, no. 9, pp. 1385–1390, 1964.
- [22] F. T. Chin, B. Shen, S. Liu et al., "First experience with clinical-grade [18F]FPP (RGD) 2: An automated multi-step radiosynthesis for clinical PET studies," *Molecular Imaging and Biology*, vol. 14, no. 1, pp. 88–95, 2012.
- [23] T. Wehner, "The role of functional imaging in the tumor patient," *Epilepsia*, vol. 54, no. 9, pp. 44–49, 2013.
- [24] C. Viswanathan, P. R. Bhosale, S. N. Shah, and R. Vikram, "Positron Emission Tomography-Computed Tomography Imaging for Malignancies in Women," *Radiologic Clinics of North America*, vol. 51, no. 6, pp. 1111–1125, 2013.
- [25] H. Jadvar, "Molecular imaging of prostate cancer with PET," *Journal of Nuclear Medicine*, vol. 54, no. 10, pp. 1685–1688, 2013.
- [26] S. Mirpour, J. C. Mhlanga, P. Logeswaran, G. Russo, G. Mercier, and R. M. Subramaniam, "The role of PET/CT in the management of cervical cancer," *American Journal of Roentgenology*, vol. 201, no. 2, pp. W192–W205, 2013.
- [27] B. Bai, J. Bading, and P. S. Conti, "Tumor quantification in clinical positron emission tomography," *Theranostics*, vol. 3, no. 10, pp. 787–801, 2013.
- [28] H. Hoshikawa, T. Mori, Y. Yamamoto et al., "Prognostic value comparison between 18F-FLT PET/CT and 18F-FDG PET/CT volume-based metabolic parameters in patients with head and neck cancer," *Clinical Nuclear Medicine*, vol. 40, no. 6, pp. 464–468, 2015.
- [29] S. Kwee, L. Wong, B. Hernandez, O. Chan, M. Sato, and N. Tsai, "Chronic liver disease and the detection of hepatocellular carcinoma by [18F]fluorocholine PET/CT," *Diagnostics*, vol. 5, no. 4, pp. 189–199, 2015.
- [30] M. Bieze, H.-J. Klumpen, J. Verheij et al., "Diagnostic accuracy of 18F-methylcholine positron emission tomography/computed tomography for intra- and extrahepatic hepatocellular carcinoma," *Hepatology*, vol. 59, no. 3, pp. 996–1006, 2014.
- [31] D. Simberg, T. Duza, J. H. Park et al., "Biomimetic amplification of nanoparticle homing to tumors," *Proceedings of the National Academy of Sciences of the United States of America*, vol. 104, no. 3, pp. 932–936, 2007.
- [32] J. Pilch, D. M. Brown, M. Komatsu et al., "Peptides selected for binding to clotted plasma accumulate in tumor stroma and wounds," *Proceedings of the National Academy of Sciences of the United States of America*, vol. 103, no. 8, pp. 2800–2804, 2006.
- [33] M. Libra, A. Scalisi, N. Vella et al., "Uterine cervical carcinoma: role of matrix metalloproteinases (review)," *International Journal of Oncology*, vol. 34, no. 4, pp. 897–903, 2009.
- [34] A. Ghosh, A. Moirangthem, R. Dalui et al., "Expression of matrix metalloproteinase-2 and 9 in cervical intraepithelial neoplasia and cervical carcinoma among different age groups of premenopausal and postmenopausal women," *Journal of Cancer Research and Clinical Oncology*, vol. 140, no. 9, pp. 1585–1593, 2014.
- [35] B. Davies, J. Waxman, H. Wasan et al., "Levels of Matrix Metalloproteases in Bladder Cancer Correlate with Tumor Grade and Invasion," *Cancer Research*, vol. 53, no. 22, pp. 5365–5369, 1993.
- [36] M. H. Tayebjee, G. Y. H. Lip, and R. J. MacFadyen, "Matrix metalloproteinases in coronary artery disease: Clinical and therapeutic implications and pathological significance," *Current Medicinal Chemistry*, vol. 12, no. 8, pp. 917–925, 2005.
- [37] A. G. Arroyo, L. Genís, P. Gonzalo, S. Matías-Román, A. Pollán, and B. G. Gálvez, "Matrix metalloproteinases: New routes to the use of MT1-MMP as a therapeutic target in angiogenesis-related disease," *Current Pharmaceutical Design*, vol. 13, no. 17, pp. 1787–1802, 2007.
- [38] H. J. Breyholz, S. Wagner, B. Levkau et al., "A 18F-radiolabeled analogue of CGS 27023A as a potential agent for assessment of matrix-metalloproteinase activity in vivo," *The Quarterly Journal of Nuclear Medicine and Molecular Imaging*, vol. 51, no. 1, pp. 24–32, 2007.
- [39] D. Zanuy, F. J. Sayago, G. Revilla-López et al., "Engineering strategy to improve peptide analogs: From structure-based computational design to tumor homing," *Journal of Computer-Aided Molecular Design*, vol. 27, no. 1, pp. 31–43, 2013.

## Research Article

# Preclinical *In Vitro* and *In Vivo* Evaluation of [<sup>18</sup>F]FE@SUPPY for Cancer PET Imaging: Limitations of a Xenograft Model for Colorectal Cancer

**T. Balber,<sup>1,2</sup> J. Singer,<sup>1,3,4</sup> N. Berroterán-Infante,<sup>1</sup> M. Dumanic,<sup>1</sup>  
L. Fetty,<sup>1,5</sup> J. Fazekas-Singer ,<sup>3,6</sup> C. Vraha,<sup>1</sup> L. Nics,<sup>1,7</sup> M. Bergmann,<sup>8</sup> K. Pallitsch,<sup>9</sup>  
H. Spreitzer,<sup>10</sup> W. Wadsak ,<sup>1,11</sup> M. Hacker,<sup>1</sup> E. Jensen-Jarolim,<sup>3,6</sup>  
H. Viernstein,<sup>2</sup> and M. Mitterhauser <sup>1,12</sup>**

<sup>1</sup> Biomedical Imaging and Image-Guided Therapy, Division of Nuclear Medicine, Medical University of Vienna, Vienna, Austria

<sup>2</sup> Department of Pharmaceutical Technology and Biopharmaceutics, Faculty of Life Sciences, University of Vienna, Vienna, Austria

<sup>3</sup> Institute of Pathophysiology and Allergy Research, Center of Pathophysiology, Infectiology and Immunology, Medical University of Vienna, Vienna, Austria

<sup>4</sup> Department of Internal Medicine II, University Hospital Krems, Karl Landsteiner University of Health Sciences, Krems an der Donau, Austria

<sup>5</sup> Department of Radiation Oncology, Division of Medical Physics, Medical University of Vienna, Vienna, Austria

<sup>6</sup> Comparative Medicine, The Interuniversity Messerli Research Institute, The University of Veterinary Medicine Vienna, Medical University of Vienna, and University of Vienna, Vienna, Austria

<sup>7</sup> Department of Nutritional Sciences, Faculty of Life Sciences, University of Vienna, Vienna, Austria

<sup>8</sup> Department of Surgery, Surgical Research Laboratories, Medical University of Vienna, Vienna, Austria

<sup>9</sup> Institute of Organic Chemistry, University of Vienna, Vienna, Austria

<sup>10</sup> Department of Pharmaceutical Chemistry, Faculty of Life Sciences, University of Vienna, Vienna, Austria

<sup>11</sup> CBmed GmbH, Graz, Austria

<sup>12</sup> Ludwig Boltzmann Institute Applied Diagnostics, Vienna, Austria

Correspondence should be addressed to M. Mitterhauser; [markus.mitterhauser@meduniwien.ac.at](mailto:markus.mitterhauser@meduniwien.ac.at)

Received 23 November 2017; Accepted 27 December 2017; Published 13 February 2018

Academic Editor: Giorgio Biasiotto

Copyright © 2018 T. Balber et al. This is an open access article distributed under the Creative Commons Attribution License, which permits unrestricted use, distribution, and reproduction in any medium, provided the original work is properly cited.

Molecular imaging probes such as PET-tracers have the potential to improve the accuracy of tumor characterization by directly visualizing the biochemical situation. Thus, molecular changes can be detected early before morphological manifestation. The A<sub>3</sub> adenosine receptor (A<sub>3</sub>AR) is described to be highly expressed in colon cancer cell lines and human colorectal cancer (CRC), suggesting this receptor as a tumor marker. The aim of this preclinical study was the evaluation of [<sup>18</sup>F]FE@SUPPY as a PET-tracer for CRC using *in vitro* imaging and *in vivo* PET imaging. First, affinity and selectivity of FE@SUPPY and its metabolites were determined, proving the favorable binding profile of FE@SUPPY. The human adenocarcinoma cell line HT-29 was characterized regarding its hA<sub>3</sub>AR expression and was subsequently chosen as tumor graft. Promising results regarding the potential of [<sup>18</sup>F]FE@SUPPY as a PET-tracer for CRC imaging were obtained by autoradiography as ≥2.3-fold higher accumulation of [<sup>18</sup>F]FE@SUPPY was found in CRC tissue compared to adjacent healthy colon tissue from the same patient. Nevertheless, first *in vivo* studies using HT-29 xenografts showed insufficient tumor uptake due to (1) poor conservation of target expression in xenografts and (2) unfavorable pharmacokinetics of [<sup>18</sup>F]FE@SUPPY in mice. We therefore conclude that HT-29 xenografts are not adequate to visualize hA<sub>3</sub>ARs using [<sup>18</sup>F]FE@SUPPY.

## 1. Introduction

Colorectal cancer (CRC) is the fourth leading cause of cancer-related deaths in men and women worldwide [1]. The primary diagnosis is usually made by colonoscopy and biopsy, which often does not reflect the full extent of the disease due to tumor heterogeneity and disregard of potential metastases. Positron Emission Tomography (PET) provides a noninvasive imaging technique, which is valuable for tumor staging and clinical decision making and to estimate the patient's prognosis [2]. Besides the routinely used PET-tracer [ $^{18}\text{F}$ ]FDG, the availability of specific tumor tracers would enhance the characterization of colorectal tumors and help in CRC staging and with the choice of treatment.

An essential characteristic of most solid tumors is hypoxia, which inevitably leads to accumulation of adenosine within the tumor microenvironment as a result of the breakdown of adenine nucleotides, which has been recognized in the 1990s [3, 4]. Since then, many efforts have been made to clarify the role of adenosine and its receptors in cancer [5–7]. The expression of the  $A_3$  adenosine receptor ( $A_3\text{AR}$ ), which is one of four subtypes of the adenosine receptor family, has been reported in several human tumor cell lines including leukemia (Jurkat T, HL-60), melanoma (A375), and astrocytoma (ADF) [8–12]. In particular, there is a rising interest in the involvement of  $A_3\text{AR}$ s in CRC as  $A_3\text{AR}$  protein expression has been reported for various colon cancer cell lines, including Caco-2, HCT-116, CCL-228, DLD-1, and HT-29 [13–15]. Merighi et al. have shown that caffeine leads to hypoxia-inducible factor-1 (HIF-1) protein accumulation and increased vascular endothelial growth factor (VEGF) expression through  $A_3\text{AR}$  stimulation in HT-29 cells under hypoxic conditions [16]. According to Sakowicz-Burkiewicz et al., treatment with the  $A_3\text{AR}$  agonist IB-MECA (1  $\mu\text{M}$ ) results in an  $A_3\text{AR}$ -dependent growth promoting effect in HT-29 cells. In contrast, IB-MECA causes cell apoptosis in HCT-116 cells, similarly in an  $A_3\text{AR}$  dependent manner [13].

High expression of  $A_3\text{AR}$  mRNA and protein has been reported in colon and breast carcinoma compared to adjacent nonneoplastic tissue by Madi et al. Remarkably, even higher levels of  $A_3\text{AR}$  mRNA have been found in lymph node metastases than in primary tumor tissue, suggesting  $A_3\text{AR}$ -overexpression as a marker for tumor progression [17]. Additionally, Gessi et al. studied  $A_3\text{AR}$  expression in colorectal cancer tissue samples of 73 patients and provided evidence that the  $A_3\text{AR}$  has the potential to be used as a diagnostic marker for colon cancer. The authors have shown  $\geq 2$ -fold increased  $A_3\text{AR}$  protein expression in primary colon carcinomas compared to normal mucosa and describe a tendency towards higher  $A_3\text{AR}$  expression in large adenomas compared to small adenomas. Therefore, the authors proposed a major role of the  $A_3\text{AR}$  in cancer aggressiveness [18]. Moreover, radioligand binding experiments using the  $A_3\text{AR}$  antagonist [ $^3\text{H}$ ]MRE 3008F20 and western blot analysis indicated that the  $A_3\text{AR}$  is the most abundant of all four adenosine receptor subtypes in colorectal cancer tissues as well as in colon cancer cell lines (Caco-2, DLD-1 and HT-29). On the contrary, RT-PCR experiments showed relatively

low levels of  $A_3\text{AR}$  mRNA in the mentioned colon cancer cell lines compared to mRNA levels of the other adenosine receptor subtypes [15]. As mRNA levels do not necessarily correlate with protein levels [19] and protein transcription is a prerequisite for targeted receptor imaging approaches such as PET imaging, protein expression data is the most relevant for this study.

The  $A_3\text{AR}$  antagonist [ $^{18}\text{F}$ ]FE@SUPPY has been presented as the first PET-tracer for  $hA_3\text{AR}$  imaging in 2008 by Wadsak et al. [20, 21]. First preclinical PET imaging using CHO-K1- $hA_3\text{AR}$  xenografts has shown promising results leading to further evaluation of this PET-tracer in oncology [22]. Besides [ $^{18}\text{F}$ ]FE@SUPPY and [ $^{18}\text{F}$ ]FE@SUPPY:2, only a few other PET-ligands have been proposed for  $A_3\text{AR}$  imaging, including carbon-11 labeled 1,2,4-triazolo[4,3-a]quinoxalin-1-one derivatives and bromine-76 labeled nucleoside ligands ([ $^{76}\text{Br}$ ]MRS3581 and [ $^{76}\text{Br}$ ]MRS5147) [23–25]. To our knowledge, no preclinical *in vivo* PET imaging has been reported for these  $A_3\text{AR}$  PET-ligands so far. In our preclinical study, we aimed to evaluate [ $^{18}\text{F}$ ]FE@SUPPY as a PET-tracer for human cancer using *in vitro* imaging and *in vivo* PET imaging in a CRC tumor model.

## 2. Methods

### 2.1. General

**2.1.1. Cell Culture.** HT-29 cells and CHO-K1 cells were purchased from ATCC. HT-29 cells were cultured in RPMI 1640 medium supplemented with 10% fetal calf serum, 2 mM L-glutamine, and 10  $\mu\text{g}/\text{mL}$  gentamicin sulfate. Human  $A_3$  adenosine receptor-expressing CHO-K1 cells (CHO-K1- $hA_3\text{AR}$ ) were purchased from PerkinElmer (ValiScreen<sup>®</sup> GPCR cell line) and were grown using Ham's F12 supplemented with 10% FCS, 2 mM L-glutamine, penicillin (100 U/M), streptomycin (100  $\mu\text{g}/\text{mL}$ ), and 0.4 mg/mL G418. Parental CHO-K1 cells were cultured likewise, but without selection antibiotics. Cells were maintained under standard conditions in a humidified incubator (37°C, 5%  $\text{CO}_2$ ).

**2.1.2. Animals.** Six-week-old male BALB/c mice (BALB/cAnNRj, Division of Laboratory Animal Science and Genetics, Himberg, Austria) were kept under conventional housing conditions, with food and water supply ad libitum and a 12 h day/night cycle. Male, immunodeficient CBI7-SCID mice (CB-17/Icr-Prkdc<sup>scid</sup>/Rj, Janvier Labs, France) of the same age were kept under specific pathogen-free conditions in individually ventilated cages. All animals were treated according to the European Union rules on animal care. The corresponding animal experiments were approved by the Austrian Ministry of Sciences (BMWFV-66.009/0031-WF/V/3b/2015, BMWFW-66.009/0029-WF/V/3b/2015).

**2.1.3. Tumor Grafting.** After 10 to 14 days upon arrival, CBI7-SCID mice were injected subcutaneously with  $2 \times 10^6$  HT-29 cells into one flank and  $2 \times 10^6$  CHO-K1 cells in the opposite flank ( $n = 9$ ). Body weight and tumor development

were monitored every second day by caliper measurement. The respective tumor volume was calculated according to the following equation: tumor volume ( $\text{mm}^3$ ) =  $d^2 \times D/2$  (where  $d$  is the shortest diameter and  $D$  the longest diameter). Animals were subjected to  $\mu\text{PET}$  imaging 10 days after inoculation, when tumors reached a volume of at least  $300 \text{ mm}^3$ . Tumor volume never exceeded  $1 \text{ cm}^3$ .

**2.1.4. Human Tissues.** Colorectal carcinoma tissue and adjacent healthy colon tissue were obtained directly after tumorectomy from two patients after full informed consent and quick-frozen in 2-methylbutane ( $-40^\circ\text{C}$ ). Tissue was sliced into  $16 \mu\text{m}$  slices using a microcryotome (Thermo Scientific Microm HM 560) and stored at  $-80^\circ\text{C}$  until usage. Depending on the sample size, 3 to 4 different regions were defined and analyzed by means of autoradiography and immunohistochemistry.

## 2.2. Characterization of Binding and Target Expression

**2.2.1. Competitive Binding Assay.** Competitive binding assays were performed using  $\text{hA}_1\text{AR}$ ,  $\text{hA}_{2A}\text{AR}$ , or  $\text{hA}_3\text{AR}$  expressing cell membranes ( $18.5 \text{ ng}/\mu\text{L}$ ,  $16.7 \text{ ng}/\mu\text{L}$ , or  $1.7 \text{ ng}/\mu\text{L}$  final protein concentration, resp.) and  $1.7 \text{ nM}$  [ $^3\text{H}$ ]DPCPX ( $K_D = 1.7 \text{ nM}$ ),  $50 \text{ nM}$  [ $^3\text{H}$ ]CGS21680 ( $K_D = 23 \text{ nM}$ ), or  $0.4 \text{ nM}$  [ $^{125}\text{I}$ ]AB-MECA ( $K_D = 0.78 \text{ nM}$ ) as the respective radioligands (all purchased from PerkinElmer, Inc. Waltham, USA). The assay was performed according to the manufacturer's instructions in a final volume of  $500 \mu\text{L}$ . Increasing concentrations of test compounds were added, whereby the concentration of dimethyl sulfoxide (DMSO) in final assay volume remained  $\leq 10\%$  ( $\text{hA}_1\text{AR}$  and  $\text{hA}_{2A}\text{AR}$  assay) and  $\leq 1\%$  in the  $\text{hA}_3\text{AR}$  assay. Nonspecific binding was determined using  $1 \mu\text{M}$  DPCPX ( $\text{hA}_1\text{R}$  assay),  $1 \mu\text{M}$  SCH-442,416 ( $\text{hA}_{2A}\text{R}$  assay), or  $10 \mu\text{M}$  I-AB-MECA ( $\text{hA}_3\text{AR}$  assay). Filtration through GF/B filters (Whatman®, presoaked in 0.1% PEI or 0.5% BSA) was performed using a cell harvester (Brandel®), and receptor-bound radioactivity was determined via gamma counting (2480 Wizard<sup>2</sup>, PerkinElmer) or liquid scintillation counting (Hidex 300 SL).  $\text{IC}_{50}$  fitted binding curves were generated using the GraphPad Software 5.0, and  $K_i$  values were calculated using the Cheng-Prusoff equation.

**2.2.2. Flow Cytometry.** For the flow cytometric evaluation of  $\text{hA}_3\text{AR}$  expression, single-cell suspensions of HT-29 cells ( $2 \times 10^5$  per tube) were fixed and permeabilized using Cytotfix/Cytoperm™ kit (BD Biosciences). Cells were incubated with mouse monoclonal anti-human  $\text{A}_3\text{AR}$  ( $100 \mu\text{L}$  of  $4 \mu\text{g}/\text{mL}$  in PBS + 2% FCS, Abnova H00000140-M01) or mouse IgG2b kappa isotype control ( $100 \mu\text{L}$  of  $4 \mu\text{g}/\text{mL}$  in PBS + 2% FCS, eBioscience™ 14-4732-85) for 1 h at  $4^\circ\text{C}$ . Following a washing step, bound primary antibodies were detected with rabbit anti-mouse IgG FITC ( $100 \mu\text{L}$  of  $40 \mu\text{g}/\text{mL}$  in PBS + 2% FCS, Dako F0261) for 30 min at  $4^\circ\text{C}$  in the dark. Samples were analyzed on a FACSCalibur™ flow cytometer (BD Bioscience), whereby 10,000 single cells were recorded.

**2.2.3. Western Blot.** Cell lysates were prepared from  $75 \text{ cm}^2$  cell culture flasks when cells reached 80% confluency using radioimmunoprecipitation assay (RIPA) buffer and protease inhibitor cocktail according to the manufacturer's instructions. Tissue lysates from HT-29 xenografts were prepared according to a standard protocol using RIPA buffer (according to sample size approx. 4 times of lysis buffer), protease inhibitor, and Ultra-Turrax® for homogenization. The protein concentration of cell lysates was determined using Pierce™ BCA Protein Assay Kit (Thermo Scientific), and  $20 \mu\text{g}$  protein per well was loaded onto TGX™ precast gels (Bio-Rad). After gel electrophoresis (200 V, 30 min), proteins were transferred to nitrocellulose membranes (Amersham™ Protran™ Premium  $0.2 \mu\text{m}$  NC, GE Healthcare Life Sciences) via semidry blotting (80 mA per gel). Membranes were incubated with rabbit polyclonal anti- $\text{A}_3\text{AR}$  (Santa Cruz Biotechnology, Inc. sc-13938) (1:750, 2 h, RT) and further incubated with goat anti-rabbit IgG HRP conjugate (1:5000, 1 h, RT). Detection was performed using the dedicated kit (SuperSignal West Pico Chemiluminescent Substrate detection kit, Thermo Scientific), and chemiluminescence imaging was conducted (Bio-Rad VersaDoc™ Imaging System).

## 2.3. In Vitro Imaging

**2.3.1. Immunofluorescence Microscopy.** HT-29 cells were seeded on chamber slides ( $3 \times 10^5/\text{mL}$ ,  $200 \mu\text{L}$  per well, 8 well slides) and incubated at  $37^\circ\text{C}$  until 50% confluency was reached. Cells were then fixed (4% paraformaldehyde in PBS, 15 min,  $4^\circ\text{C}$ ), permeabilized (0.2% Triton X in PBS, 2 min, room temperature (RT)), and blocked (2% FCS in PBS, 30 min, RT). Mouse monoclonal anti-human  $\text{A}_3\text{AR}$  (Abnova H00000140-M01) and mouse IgG2b kappa isotype control (eBioscience 14-4732-85) were used 1:50 in PBS + 2% FCS and incubated for 1 h at RT. Cells were washed three times with PBS and incubated with the secondary antibody (rabbit anti-mouse IgG FITC, Dako F0261) for 1 h at RT. After washing, cells were incubated with DAPI (1:5000) for 10 min at RT, and subsequently, slides were embedded with an aqueous mounting medium (Fluoromount™, Sigma F4680). Slides were recorded on an Axioplan II fluorescence microscope (Carl Zeiss Microscopy).

**2.3.2. Autoradiography.** Tissue slices were thawed and reconstituted in assay buffer (50 mM Tris-HCl pH 7.4, 100 mM NaCl, 1 mM EDTA, 1% BSA, 1 unit adenosine deaminase/100 mL) for 30 min at RT. Radiosynthesis of [ $^{18}\text{F}$ ]FE@SUPPY was performed as previously described and the product was physiologically formulated (EtOH/0.9% saline 10/90) [20]. Tissue slices were incubated with  $50 \text{ kBq}$  [ $^{18}\text{F}$ ]FE@SUPPY ( $40\text{--}200 \text{ GBq}/\mu\text{mol}$ ) in  $100 \mu\text{L}$  assay buffer for 1 h at RT. Slices were thoroughly washed with ice-cold wash buffer (50 mM Tris-HCl pH 7.4), dried, and exposed to a phosphor screen overnight. The readout of the phosphor storage screen was performed on a Cyclone Phosphor Imager (Perkin Elmer), and data analysis was performed using OptiQuant® Software as previously described [26]. Statistical testing was performed using GraphPad Prism 5.0 Software. Differences among groups (colorectal cancer

versus healthy colon) were analyzed using a two-tailed, unpaired Student's *t*-test with Welch's correction.

**2.3.3. Immunohistochemistry.** Vicinal cryosections of colorectal carcinoma and healthy colon tissue were stained to identify regions with hA<sub>3</sub>AR expression following a standard protocol. In brief, cryosections were fixed (96% ethanol, 10 min), permeabilized (0.2% Triton X-100 in PBS, 5 min), and blocked using Bloxall™ Blocking Solution and a dedicated avidin/biotin blocking kit (Invitrogen, Thermo Fisher Scientific). Additionally, sections were incubated with goat serum (1:10 in PBS) to reduce nonspecific binding. Rabbit polyclonal anti-A<sub>3</sub>AR (1:100, ab203298; Abcam) was used 1:100 in PBS + 0.1% BSA for 1 h in a humid, dark chamber. Purified rabbit IgG (Life technologies) was used as an isotype control likewise. Cryosections were washed 3 times for 5 min (PBS + 0.1% Tween-20) and incubated with biotinylated anti-rabbit IgG (1:200, PBS + 5% goat serum) for 30 min. After washing, further detection was performed with the Vectastain® ABC kit (Vector Laboratories) according to the manufacturer's instructions. DAB substrate kit (Abcam) was used as a chromogen to detect peroxidase, and haematoxylin was used for counterstaining of cell nuclei. Immunohistochemically stained slides were acquired on an automated TissueFAXS microscope system (TissueGnostics, Vienna, Austria) at a 5-fold and 20-fold magnification.

#### 2.4. Tracer Stability in Mice

**2.4.1. In Vitro Stability Tests.** Stability of [<sup>18</sup>F]FE@SUPPY was tested against mouse liver microsomes, mouse S9 fraction, and mouse plasma (BD Sciences). Amount of intact tracer (%) was determined after 5, 10, 20, 40, 60, and 120 min using an Agilent series 1100/1200 HPLC system connected to a radioactivity detector (Raytest, Ramona Star) (*n* = 2 in triplicate). The assay was conducted as previously described for respective rat and human enzymes [27].

**2.4.2. Ex Vivo Blood Stability.** Radiosynthesis was performed as described elsewhere [20] and the product was processed as follows: ethanol was totally evaporated and the dry product was again physiologically formulated in 1.5–2 mL Tween-20/EtOH/0.9% saline 1/9/90 to obtain activity concentrations of approximately 1 GBq/mL. Healthy BALB/c mice were injected with 18 ± 2 MBq (molar activity = 70–200 GBq/μmol) retroorbitally and sacrificed after 5, 10, 20, 40, and 70 min (*n* = 3 for each time point). Blood samples were collected and immediately precipitated using acetonitrile/methanol (10:1) and centrifuged (12,000 rpm, 5 min, 4°C). The obtained supernatants were subjected to radio-HPLC as previously described [22].

**2.5. Biodistribution.** Ex vivo biodistribution of [<sup>18</sup>F]FE@SUPPY was assessed 70 min after tracer application in BALB/c mice. Radioactivity was determined using a gamma counter (2480 Wizard<sup>2</sup>, PerkinElmer), organs were wet-weighted, and percentage of injected dose per gram of organ was calculated (%ID/g).

**2.6. In Vivo Imaging.** Xenograft-bearing CB17-SCID mice were anesthetized using isoflurane (2.5%) mixed with oxygen (1.5 L/min) to avoid movement during the imaging. Blocking agents (2 mg/kg BW FE@SUPPY or MRS1523) or the respective vehicle control (Tween-20/EtOH/0.9% physiological saline 1/9/90) was administered retroorbitally 2 min prior to the radiotracer administration (*n* = 3 per group). Subsequently, the animals received another retroorbital injection of 17.42 ± 4.5 MBq [<sup>18</sup>F]FE@SUPPY into the venous plexus of the opposite eye. With a minor delay after the application of the radiotracer (2–3 min), mice were placed into the field of view of the scanner (μPET/CT Inveon, Siemens Medical Solution, Knoxville, USA), and dynamic imaging was performed for 60 min to follow tracer distribution. Vital parameters (respiration, body temperature) were continuously monitored using a dedicated monitoring unit (bioVet; m2m imaging, Cleveland, OH, USA) to ensure the depth of anesthesia and wellbeing of the animals. Retroorbital application volumes did not exceed 100 μL per application.

### 3. Results and Discussion

**3.1. Characterization of Binding and Target Expression.** Affinity and selectivity of FE@SUPPY and its potential metabolites upon cleavage by carboxylesterases, DFE@SUPPY, and FE@SUPPY:11 [28] were determined in competitive binding assays. FE@SUPPY has been first described by Li et al., who reported a *K<sub>i</sub>* value of 4.22 ± 0.7 nM for human A<sub>3</sub>AR. However, this study only provided the selectivity ratio towards rat A<sub>1</sub>AR (rA<sub>1</sub>AR/hA<sub>3</sub>AR = 7400) [29]. Here, we confirmed the affinity of FE@SUPPY towards the human A<sub>3</sub>AR (*K<sub>i</sub>* = 6.02 ± 0.4 nM, *n* = 3) and demonstrated its selective hA<sub>3</sub>AR binding compared to the other human adenosine receptors. Moreover, the respective theoretical metabolites show little affinity for the hA<sub>3</sub>AR, supporting the potential of FE@SUPPY as a ligand for human *in vivo* application (Table 1).

The human colorectal adenocarcinoma cell line (HT-29) was characterized regarding its hA<sub>3</sub>AR protein expression using flow cytometry and western blot. Flow cytometric analysis resulted in mean fluorescence intensity (ΔMFI) of 53.6 ± 22 in three independent experiments (Figure 1). Additionally, A<sub>3</sub>AR protein expression in HT-29 cells was determined by western blot (Figure 8) (western blot results are discussed separately below). This is in line with previous studies, which reported A<sub>3</sub>AR expression for this cell line as well [13, 15]. Thus, HT-29 cells were subsequently chosen for tumor graft experiments.

**3.2. In Vitro Imaging.** Fluorescence microscopy of HT-29 cells showed cell membrane-specific staining, pointing at the expression of hA<sub>3</sub>AR on the cell surface, which is typical for GPCRs (Figure 2).

In all investigated regions of the two CRC patients, [<sup>18</sup>F]FE@SUPPY accumulation was higher in colorectal carcinoma tissue slices than in healthy colon tissue slices of the same individual (for detailed analysis see supplementary (available here)). In 5 of 7 regions, a ≥2.3-fold higher binding

TABLE 1: Affinity and selectivity data of FE@SUPPY and metabolites towards adenosine receptor subtypes ( $n = 3-5$  in triplicate; amount of DMSO never exceeded 1% of total assay volume in hA<sub>3</sub>AR assay; DMSO was added up to 10% in hA<sub>1</sub>AR and hA<sub>2A</sub>AR assay; \* $n = 2$  in triplicate; exact  $K_i$  value could not be determined due to limited solubility).

| Compound    | hA <sub>1</sub> AR | hA <sub>2A</sub> AR | hA <sub>3</sub> AR | hA <sub>1</sub> /hA <sub>3</sub> AR | hA <sub>2A</sub> /hA <sub>3</sub> AR |
|-------------|--------------------|---------------------|--------------------|-------------------------------------|--------------------------------------|
| FE@SUPPY    | 4.03 ± 1.0 μM      | 1.72 ± 0.4 μM       | 6.02 ± 0.4 nM      | 669                                 | 285                                  |
| DFE@SUPPY   | 5.46 ± 0.4 μM      | 37.13 ± 16 μM       | 2.58 ± 1.2 μM      | 324                                 | 112                                  |
| FE@SUPPY:II | ≥57 μM*            | 5.86 ± 0.8 μM       | 2.80 ± 1.4 μM      | ≥20                                 | 2                                    |

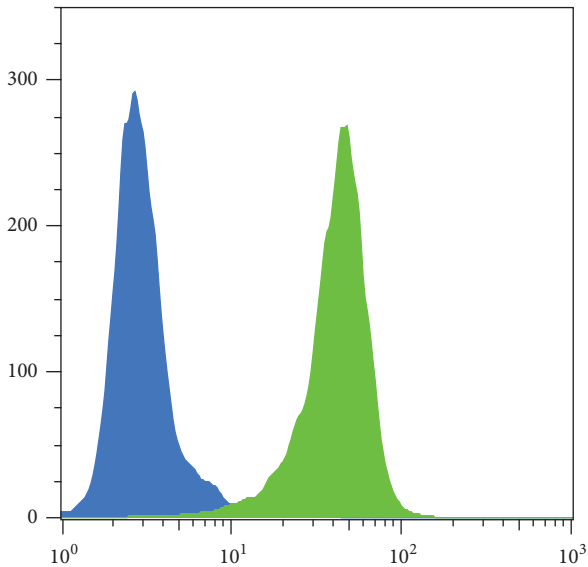


FIGURE 1: Flow cytometric analysis of HT-29 cells revealed expression of hA<sub>3</sub>AR protein (green). The isotype control did not show fluorescence signal (blue).

of [<sup>18</sup>F]FE@SUPPY was found ( $P < 0.05$ ). This finding is in accordance with Gessi et al., who reported similar ratios by means of [<sup>3</sup>H]MRE 3008F20 binding [18]. Regions with high accumulation of [<sup>18</sup>F]FE@SUPPY corresponded to regions with high hA<sub>3</sub>AR expression identified by immunohistochemistry (Figure 3).

3.3. *Tracer Stability in Mice.* [<sup>18</sup>F]FE@SUPPY exhibited high stability in mouse plasma, as 92.6 ± 0.7% of intact tracer could still be detected after 120 min of incubation at 37°C. *In vitro* stability tests against mouse liver homogenates (S9 fraction) and purified mouse liver microsomes showed 66.9 ± 6.7% and 31.4 ± 7.8% intact tracer after 120 min, respectively. *Ex vivo* blood stability analysis demonstrated more rapid degradation of [<sup>18</sup>F]FE@SUPPY *in vivo* than that observed in *in vitro* testing as only 2.2 ± 0.4% intact [<sup>18</sup>F]FE@SUPPY could be determined after 70 min (Figure 4). This data indicates higher metabolism in mice compared to rats described in previously conducted studies, where 25.8 ± 5.3% intact tracer was found in plasma after 60 min [22]. However, these data could also be mimicked by the fact that intact [<sup>18</sup>F]FE@SUPPY is rapidly cleared from blood hepatobiliary (into the bile fluid, compare

Figures 5 and 7), and the equilibrium in blood is therefore shifted to the metabolites.

3.4. *Biodistribution.* Biodistribution was assessed 70 min after tracer application in healthy BALB/c mice and revealed a high accumulation of radioactivity in fat-rich regions (brown adipose tissue, BAT) likely due to the tracer’s lipophilicity [30]. Regarding the emunctory organs, liver showed the highest accumulation (14.57 ± 0.20% ID/g), followed by the kidneys (2.67 ± 0.24% ID/g). The additional analysis of body liquids pointed at a mainly hepatobiliary excretion of [<sup>18</sup>F]FE@SUPPY, as the highest amount was found in bile fluid (162.78 ± 37.51% ID/g). The amount of radioactivity in the kidneys and urine (43.33 ± 9.23% ID/g) suggests the excretion of the hydrophilic radioactive metabolite, 2-[<sup>18</sup>F]fluoroethanol [31], which was already proposed by Haeusler et al. [28]. The circulating radioactivity in blood was low after 70 min (1.6 ± 0.1% ID/g). This finding is in accordance with the results obtained by the *ex vivo* blood analysis. Moreover, pronounced accumulation of [<sup>18</sup>F]FE@SUPPY was found in A<sub>3</sub>AR rich tissues such as the heart (1.13 ± 0.04% ID/g) and lung (1.50 ± 0.23% ID/g). A similar biodistribution pattern was observed for rats in a previously conducted study [20]. [<sup>18</sup>F]FE@SUPPY accumulation in the brain was low after 70 min (0.23 ± 0.03% ID/g) (Figure 5).

3.5. *In Vivo Imaging.* μPET imaging of the mouse xenograft model revealed high uptake of [<sup>18</sup>F]FE@SUPPY in the emunctory organs, which was again most pronounced in the liver (SUV = 6.68 ± 0.80). Low standardized uptake values were observed in tumor masses of both HT-29 and CHO-K1 xenograft tumors (SUV = 0.23 ± 0.06 and 0.25 ± 0.33), respectively. There was no difference between CHO-K1 xenografts, which served as a negative control (human A<sub>3</sub>AR negative), and HT-29 xenografts. Moreover, significant blocking could not be achieved (Figure 6). The affinity of FE@SUPPY for the mouse A<sub>3</sub>AR is uncertain but is expected to be lower than that for the human A<sub>3</sub>AR due to the known species differences. The lack of adequate rodent models, mainly due to the low affinity of most hA<sub>3</sub>AR ligands to the rodent A<sub>3</sub>AR, was already recognized by Yamano et al. who proposed a humanized mouse model [32]. Specific uptake was therefore not expected in mouse tissues. Interestingly, a significant influence of the blocking was observed in BAT (decrease in uptake) and lung (increase in uptake). However, the data is based on a set of three individuals in each group, and displacement was not performed in the same individuals.

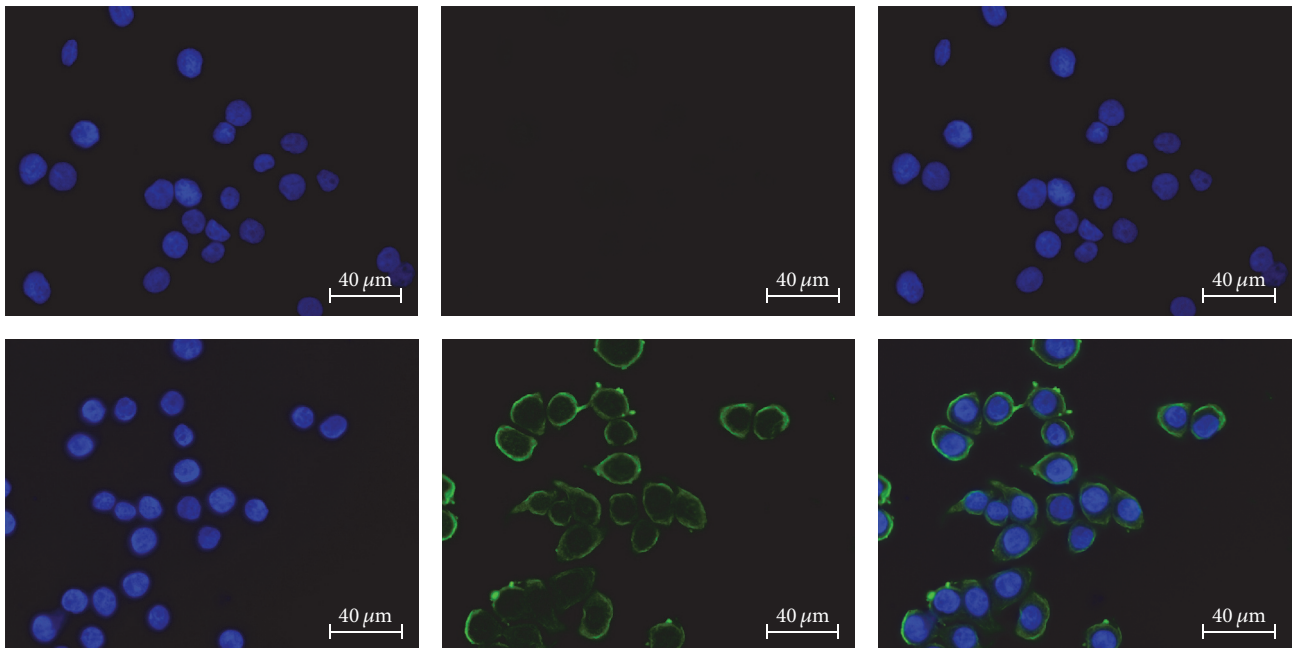


FIGURE 2: Immunofluorescent staining of HT-29 cells; left: DAPI, middle: FITC, right: merge. Upper row: mouse isotype control, lower row: anti-human A<sub>3</sub>AR staining.

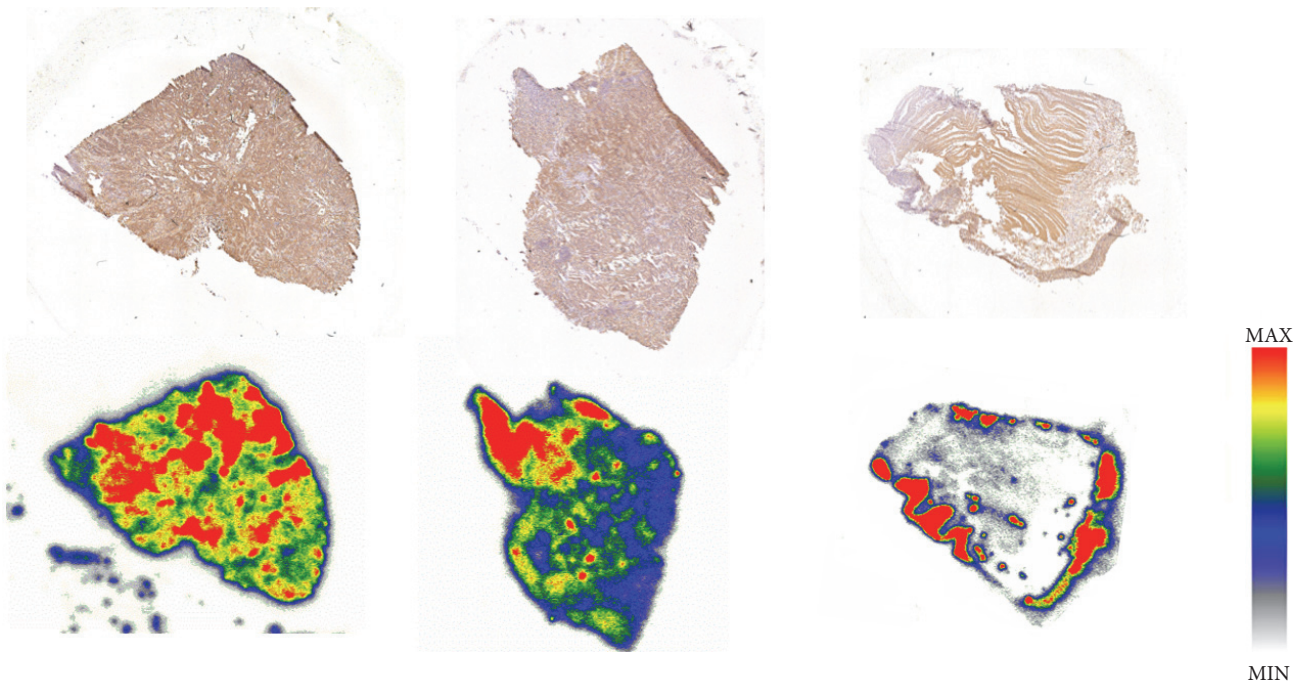


FIGURE 3: Upper row: immunohistochemical staining of hA<sub>3</sub>AR. Lower row: autoradiographic analysis of the corresponding vicinal tissue slices using [<sup>18</sup>F]FE@SUPPY. Left and center: colon cancer tissue, right: healthy colon tissue.

Since tumor uptake in the chosen model was insufficient and not blockable, this phenomenon was not investigated any further.

For a detailed analysis of the pharmacokinetics, volumes of interest were also generated for mouse body liquids including blood, urine, and bile fluid (Figure 7). The radioactivity

in blood was generally low ( $SUV = 1.21 \pm 0.11$ ) compared to the body liquids, urine ( $SUV = 8.86 \pm 3.44$ ), and bile fluid ( $21.85 \pm 10.63$ ), showing the highest accumulation of [<sup>18</sup>F]FE@SUPPY, which is in line with the biodistribution experiments. The mentioned standardized uptake values refer to baseline conditions.

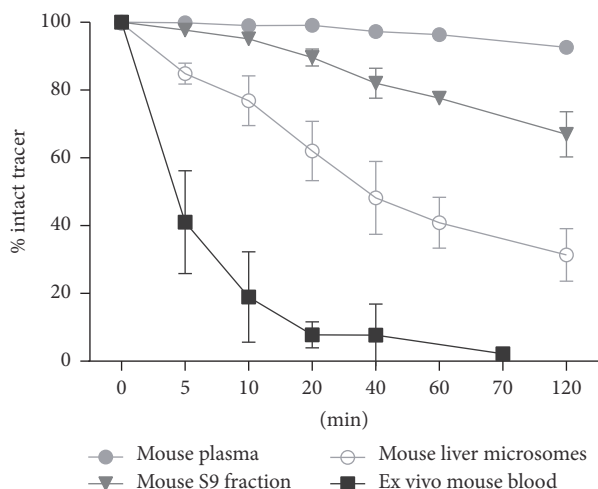


FIGURE 4: *In vitro* stability and *ex vivo* blood stability of [ $^{18}\text{F}$ ]FE@SUPPY.

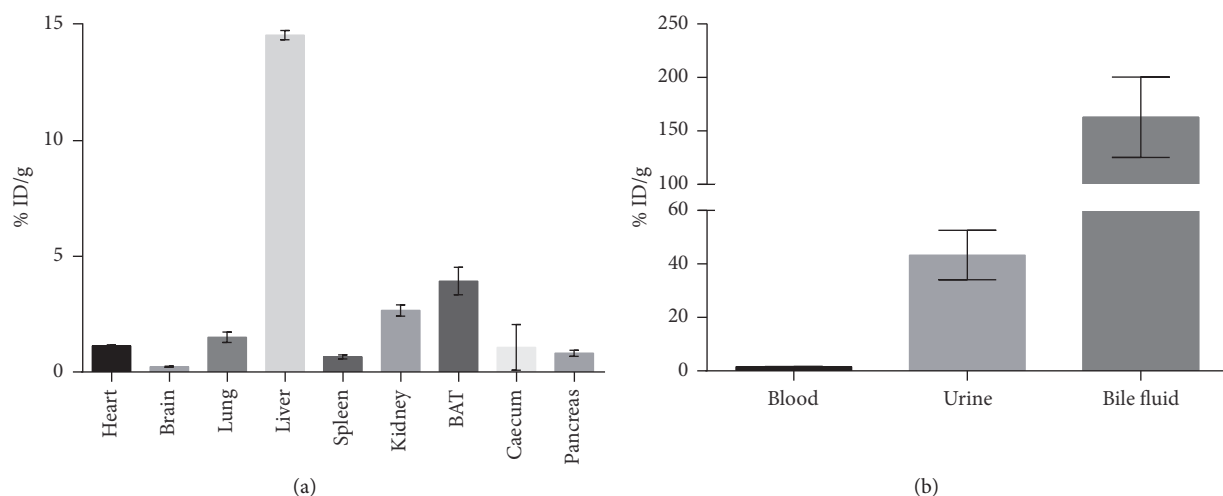


FIGURE 5: Biodistribution of [ $^{18}\text{F}$ ]FE@SUPPY in healthy BALB/c mice ( $n = 3$ ). (a) shows biodistribution in organs. (b) shows accumulation in body liquids.

Adenosine concentrations of  $\sim 0.5 \mu\text{M}$  have been proposed in HT-29 tumors grown as xenografts [4]. Even though adenosine displays only intermediate affinity for the  $A_3\text{AR}$  ( $\sim 1 \mu\text{M}$  at the rat  $A_3\text{AR}$  [33]), the PET-tracer would have to compete with the endogenous ligand for  $A_3\text{AR}$  occupancy. This may decrease accumulation of [ $^{18}\text{F}$ ]FE@SUPPY in the xenografts. However, more importantly, despite the fact that western blot analysis demonstrated h $A_3\text{AR}$  expression in HT-29 cells, h $A_3\text{AR}$  protein could not be detected in tissue lysates derived from HT-29 xenografts. This indicates that the human receptor is poorly conserved in mice upon tumor graft (Figure 8). To our knowledge, this phenomenon has not been described in literature so far but has tremendous impact on *in vivo* imaging. PET imaging is only feasible if an abundant amount of the target is available, as only nanomolar or even lower concentrations of PET-tracers are applied.

#### 4. Conclusion

We found a favorable binding profile of [ $^{18}\text{F}$ ]FE@SUPPY displaying high affinity for the human  $A_3\text{AR}$  besides low affinity for the other human adenosine receptor subtypes. Autoradiography showed  $\geq 2.3$ -fold higher uptake in human CRC compared to adjacent healthy colon tissues. First *in vivo* studies using HT-29 xenografts showed insufficient tumor uptake. After initial high expression rates of the  $A_3\text{AR}$  in the HT-29 cells, tumor masses, derived from HT-29 xenografts, revealed low target expression. The receptor was not conserved in the xenograft, which hampered the PET imaging strategy. An additional drawback of the used mouse model is the unfavorable pharmacokinetics of the PET-tracer [ $^{18}\text{F}$ ]FE@SUPPY in mice. It is questionable how accurate xenograft models in immunocompromised mice are to study the role of human  $A_3\text{AR}$ s in cancer. Despite all efforts, *in vivo*

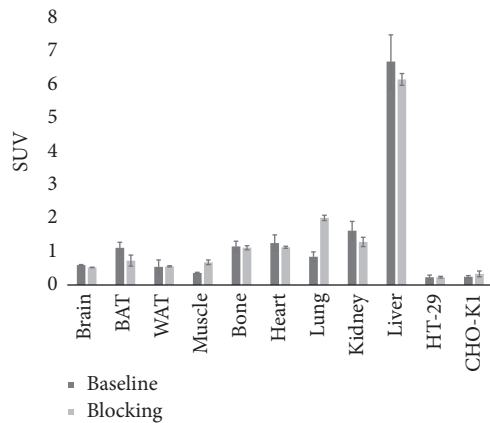


FIGURE 6:  $\mu$ PET-imaging was performed for 60 min. Activity concentration of [ $^{18}$ F]FE@SUPPY in organs of interest is expressed as standardized uptake value (SUV). Blocking experiments, shown in the figure, were performed using unlabeled FE@SUPPY. Blocking experiments using MRS1523 provided the same outcome and are not shown in the figure.

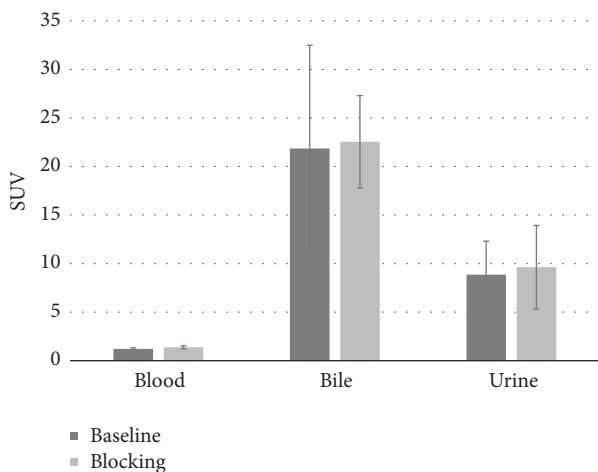


FIGURE 7:  $\mu$ PET-imaging was performed for 60 min. Activity concentration of [ $^{18}$ F]FE@SUPPY in body liquids is expressed as standardized uptake value (SUV). Blocking experiments, shown in the figure, were performed using unlabeled FE@SUPPY. Blocking experiments using MRS1523 provided the same outcome and are not shown in the figure.

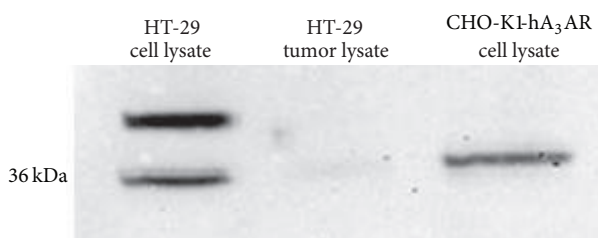


FIGURE 8: Western blot analysis of HT-29 cell lysate and tissue lysate derived from HT-29 xenograft tumors. CHO-K1-hA<sub>3</sub>AR cell lysate was loaded as a positive control. An additional band of unknown identity was detected in HT-29 cell lysate.

visualization of the A<sub>3</sub>AR has not been successful to date and deeper understanding of A<sub>3</sub>AR function is still missing.

## Conflicts of Interest

The authors declare that they have no conflicts of interest.

## Acknowledgments

This work was supported by the Austrian Science Fund (FWF P26502-B24, M. Mitterhauser) and was performed with the support of the Molecular Imaging Cluster of the Medical University of Vienna, Austria. J. Fazekas-Singer was supported by Grant CCHD W1205-B09 awarded to Dr. E. Jensen-Jarolim. The authors want to thank Petra Furlinger for her collaboration in the autoradiography experiments and Markus Zeilinger for his support in statistics.

## Supplementary Materials

Table S1: binding values of FE@SUPPY are expressed as fmol/mm<sup>2</sup> tissue. (*Supplementary Materials*)

## References

- [1] Global Burden of Disease Cancer C, "The global burden of cancer 2013," *JAMA Oncology*, vol. 1, no. 4, pp. 505–527, 2015.
- [2] L. Fass, "Imaging and cancer: a review," *Molecular Oncology*, vol. 2, no. 2, pp. 115–152, 2008.
- [3] B. B. Fredholm, A. P. Ijzerman, K. A. Jacobson, K. Klotz, and J. Linden, "International Union of Pharmacology. XXV. Nomenclature and classification of adenosine receptors," *Pharmacological Reviews*, vol. 53, no. 4, pp. 527–552, 2001.
- [4] J. Blay, T. D. White, and D. W. Hoskin, "The extracellular fluid of solid carcinomas contains immunosuppressive concentrations of adenosine," *Cancer Research*, vol. 57, no. 13, pp. 2602–2605, 1997.
- [5] S. Merighi, P. Mirandola, K. Varani et al., "A glance at adenosine receptors: Novel target for antitumor therapy," *Pharmacology & Therapeutics*, vol. 100, no. 1, pp. 31–48, 2003.
- [6] S. Gessi, S. Merighi, V. Sacchetto, C. Simioni, and P. A. Borea, "Adenosine receptors and cancer," *Biochimica et Biophysica Acta (BBA) - Biomembranes*, vol. 1808, no. 5, pp. 1400–1412, 2011.
- [7] P. A. Borea, S. Gessi, S. Merighi, and K. Varani, "Adenosine as a multi-signalling guardian angel in human diseases: when, where and how does it exert its protective effects?" *Trends in Pharmacological Sciences*, vol. 37, no. 6, pp. 419–434, 2016.
- [8] S. Gessi, K. Varani, S. Merighi et al., "Pharmacological and biochemical characterization of A<sub>3</sub> adenosine receptors in Jurkat T cells," *British Journal of Pharmacology*, vol. 134, no. 1, pp. 116–126, 2001.
- [9] S. Merighi, P. Mirandola, D. Milani et al., "Adenosine receptors as mediators of both cell proliferation and cell death of cultured human melanoma cells," *Journal of Investigative Dermatology*, vol. 119, no. 4, pp. 923–933, 2002.
- [10] S. Merighi, A. Benini, P. Mirandola et al., "A<sub>3</sub> adenosine receptors modulate hypoxia-inducible factor-1 $\alpha$  expression in human A375 melanoma cells," *Neoplasia*, vol. 7, no. 10, pp. 894–903, 2005.

- [11] S. Gessi, K. Varani, S. Merighi et al., "A3 adenosine receptors in human neutrophils and promyelocytic HL60 cells: A pharmacological and biochemical study," *Molecular Pharmacology*, vol. 61, no. 2, pp. 415–424, 2002.
- [12] M. L. Trincavelli, D. Tuscano, M. Marroni et al., "A3 adenosine receptors in human astrocytoma cells: Agonist-mediated desensitization, internalization, and down-regulation," *Molecular Pharmacology*, vol. 62, no. 6, pp. 1373–1384, 2002.
- [13] M. Sakowicz-Burkiewicz, A. Kitowska, M. Grden, I. Maciejewska, A. Szutowicz, and T. Pawelczyk, "Differential effect of adenosine receptors on growth of human colon cancer HCT 116 and HT-29 cell lines," *Archives of Biochemistry and Biophysics*, vol. 533, no. 1-2, pp. 47–54, 2013.
- [14] E. Polycarpou, L. B. Meira, S. Carrington, E. Tyrrell, H. Modjtahedi, and M. A. Carew, "Resveratrol 3-O-d-glucuronide and resveratrol 4'-O-d-glucuronide inhibit colon cancer cell growth: evidence for a role of A3 adenosine receptors, cyclin D1 depletion, and G1 cell cycle arrest," *Molecular Nutrition & Food Research*, vol. 57, no. 10, pp. 1708–1717, 2013.
- [15] S. Gessi, S. Merighi, K. Varani et al., "Adenosine receptors in colon carcinoma tissues and colon tumoral cell lines: focus on the A3 adenosine subtype," *Journal of Cellular Physiology*, vol. 211, no. 3, pp. 826–836, 2007.
- [16] S. Merighi, A. Benini, P. Mirandola et al., "Caffeine inhibits adenosine-induced accumulation of hypoxia-inducible factor-1 $\alpha$ , vascular endothelial growth factor, and interleukin-8 expression in hypoxic human colon cancer cells," *Molecular Pharmacology*, vol. 72, no. 2, pp. 395–406, 2007.
- [17] L. Madi, A. Ochaion, L. Rath-Wolfson et al., "The A3 adenosine receptor is highly expressed in tumor versus normal cells: Potential target for tumor growth inhibition," *Clinical Cancer Research*, vol. 10, no. 13, pp. 4472–4479, 2004.
- [18] S. Gessi, E. Cattabriga, A. Avitabile et al., "Elevated expression of A3 adenosine receptors in human colorectal cancer is reflected in peripheral blood cells," *Clinical Cancer Research*, vol. 10, no. 17, pp. 5895–5901, 2004.
- [19] A. Koussounadis, S. P. Langdon, I. H. Um, D. J. Harrison, and V. A. Smith, "Relationship between differentially expressed mRNA and mRNA-protein correlations in a xenograft model system," *Scientific Reports*, vol. 5, Article ID 10775, 2015.
- [20] W. Wadsak, L.-K. Mien, K. Shanab et al., "Preparation and first evaluation of [18F]FE@SUPPY: a new PET tracer for the adenosine A3 receptor," *Nuclear Medicine and Biology*, vol. 35, no. 1, pp. 61–66, 2008.
- [21] W. Wadsak, L.-K. Mien, K. Shanab et al., "Radiosynthesis of the adenosine A3 receptor ligand 5-(2-[18F]fluoroethyl) 2,4-diethyl-3-(ethylsulfanylcarbonyl)-6-phenylpyridine-5-carboxylate ([18F]FE@SUPPY)," *Radiochimica Acta*, vol. 96, no. 2, pp. 119–124, 2008.
- [22] D. Haeusler, C. Kuntner, L. Nics et al., "[18F]FE@SUPPY: a suitable PET tracer for the adenosine A3 receptor? An in vivo study in rodents," *European Journal of Nuclear Medicine and Molecular Imaging*, vol. 42, no. 5, pp. 741–749, 2015.
- [23] M. Mitterhauser, D. Haeusler, L. Mien et al., "Automatisation and First Evaluation of [18F]FE@SUPPY:2, an Alternative PET-Tracer for the Adenosine A3 Receptor: A Comparison with [18F]FE@SUPPY," *The Open Nuclear Medicine Journal*, vol. 1, no. 1, pp. 15–23, 2009.
- [24] M. Gao, A. C. Gao, M. Wang, and Q.-H. Zheng, "Simple synthesis of new carbon-11-labeled 1,2,4-triazolo[4,3-a]quinoxalin-1-one derivatives for PET imaging of A3 adenosine receptor," *Applied Radiation and Isotopes*, vol. 91, pp. 71–78, 2014.
- [25] D. O. Kiesewetter, L. Lang, Y. Ma et al., "Synthesis and characterization of [76Br]-labeled high-affinity A3 adenosine receptor ligands for positron emission tomography," *Nuclear Medicine and Biology*, vol. 36, no. 1, pp. 3–10, 2009.
- [26] C. Philippe, D. Haeusler, F. Fuchshuber et al., "Comparative autoradiographic in vitro investigation of melanin concentrating hormone receptor 1 ligands in the central nervous system," *European Journal of Pharmacology*, vol. 735, no. 1, pp. 177–183, 2014.
- [27] L. Nics, C. Vranka, M. Hendl, D. Haeusler, K. H. Wagner, K. Shanab et al., "In-vitro stability of [18F]FE@SUPPPY and [18F]FE@SUPPY:2 against human liver-microsomes and human plasma," *Nuklearmedizin*, vol. 50, 2011.
- [28] D. Haeusler, L. Nics, L.-K. Mien et al., "[18F]FE@SUPPY and [18F]FE@SUPPY:2 - metabolic considerations," *Nuclear Medicine and Biology*, vol. 37, no. 4, pp. 421–426, 2010.
- [29] A.-H. Li, S. Moro, N. Forsyth, N. Melman, X.-D. Ji, and K. A. Jacobson, "Synthesis, CoMFA analysis, and receptor docking of 3,5-diacetyl-2,4-dialkylpyridine derivatives as selective A3 adenosine receptor antagonists," *Journal of Medicinal Chemistry*, vol. 42, no. 4, pp. 706–721, 1999.
- [30] C. Vranka, L. Nics, K.-H. Wagner, M. Hacker, W. Wadsak, and M. Mitterhauser, "LogP, a yesterday's value?" *Nuclear Medicine and Biology*, vol. 50, pp. 1–10, 2017.
- [31] J. Pan, M. Pourghasian, N. Hundal et al., "2-[18F]Fluoroethanol and 3-[18F]fluoropropanol: Facile preparation, biodistribution in mice, and their application as nucleophiles in the synthesis of [18F]fluoroalkyl aryl ester and ether PET tracers," *Nuclear Medicine and Biology*, vol. 40, no. 6, pp. 850–857, 2013.
- [32] K. Yamano, M. Inoue, S. Masaki, M. Saki, M. Ichimura, and M. Satoh, "Generation of adenosine A3 receptor functionally humanized mice for the evaluation of the human antagonists," *Biochemical Pharmacology*, vol. 71, no. 3, pp. 294–306, 2006.
- [33] K. A. Jacobson, H. O. Kim, S. M. Siddiqi, M. E. Olah, G. L. Stiles, and D. K. J. E. Von Lubitz, "A3-adenosine receptors: Design of selective ligands and therapeutic prospects," *Drugs of the Future*, vol. 20, no. 7, pp. 689–699, 1995.

## Research Article

# Fluorine-19 Magnetic Resonance Imaging and Positron Emission Tomography of Tumor-Associated Macrophages and Tumor Metabolism

Soo Hyun Shin,<sup>1</sup> Sang Hyun Park,<sup>1</sup> Se Hun Kang,<sup>2</sup> Seung Won Kim,<sup>1</sup>  
Minsun Kim,<sup>1</sup> and Daehong Kim<sup>1</sup>

<sup>1</sup>Molecular Imaging Branch, Division of Convergence Technology, National Cancer Center, Ilsanro-ro 323, Ilsandong-gu, Goyang 10408, Republic of Korea

<sup>2</sup>Animal Molecular Imaging Unit, Research Institute, National Cancer Center, Ilsanro-ro 323, Ilsandong-gu, Goyang 10408, Republic of Korea

Correspondence should be addressed to Daehong Kim; [dkim@ncc.re.kr](mailto:dkim@ncc.re.kr)

Received 22 July 2017; Revised 31 October 2017; Accepted 14 November 2017; Published 5 December 2017

Academic Editor: Sundaresan Gobalakrishnan

Copyright © 2017 Soo Hyun Shin et al. This is an open access article distributed under the Creative Commons Attribution License, which permits unrestricted use, distribution, and reproduction in any medium, provided the original work is properly cited.

The presence of tumor-associated macrophages (TAMs) is significantly associated with poor prognosis of tumors. Currently, magnetic resonance imaging- (MRI-) based TAM imaging methods that use nanoparticles such as superparamagnetic iron oxide and perfluorocarbon nanoemulsions are available for quantitative monitoring of TAM burden in tumors. However, whether MRI-based measurements of TAMs can be used as prognostic markers has not been evaluated yet. In this study, we used positron emission tomography (PET) with <sup>18</sup>F-2-fluoro-2-deoxy-D-glucose (<sup>18</sup>F-FDG) as a radioactive tracer and fluorine-19- (<sup>19</sup>F-) MRI for imaging mouse breast cancer models to determine any association between TAM infiltration and tumor metabolism. Perfluorocarbon nanoemulsions were intravenously administered to track and quantify TAM infiltration using a 7T MR scanner. To analyze glucose uptake in tumors, <sup>18</sup>F-FDG-PET images were acquired immediately after <sup>19</sup>F-MRI. Coregistered <sup>18</sup>F-FDG-PET and <sup>19</sup>F-MR images enabled comparison of spatial patterns of glucose uptake and TAM distribution in tumors. <sup>19</sup>F-MR signal intensities from tumors exhibited a strong inverse correlation with <sup>18</sup>F-FDG uptake while having a significant positive correlation with tumor growth from days 2 to 7. These results show that combination of <sup>19</sup>F-MRI and <sup>18</sup>F-FDG-PET can improve our understanding of the relationship between TAM and tumor microenvironment.

## 1. Introduction

Many types of tumors with poor prognosis are characterized by dense infiltration of tumor-associated macrophages (TAMs) [1–3]. Crosstalk between TAMs and tumor cells through anti-inflammatory cytokines such as interleukin-10 contributes to various aspects of tumor progression by activities such as promoting tumor angiogenesis [4–6], supporting destruction of basal extracellular matrix [7, 8], and facilitating metastasis [9]. Thus, TAMs have been drawing attention as key diagnostic, prognostic, and therapeutic targets for characterization and treatment of tumors [10–12].

Several imaging methods have been developed for noninvasive analysis of distribution and quantification of TAMs in tumors. One of these methods is the nanoparticle-based

magnetic resonance imaging (MRI) cell-tracking method, which exploits the high phagocytic activity of macrophages to passively label them with nanoparticles through intravenous administration. Superparamagnetic iron oxide (SPIO) nanoparticles and perfluorocarbon (PFC) nanoemulsions are widely used as TAM-labeling contrast agents. With SPIO nanoparticles, TAMs are visualized as hypointense spots on T2-weighted MR images. These nanoparticles have a high potential for clinical translation owing to their approval by the Food and Drug Administration (e.g., Feraheme) [13, 14]. Upon fluorination with PFC nanoemulsions, TAMs are visualized as “hot spots” by fluorine-19- (<sup>19</sup>F-) MRI [15–18]. Because of the lack of <sup>19</sup>F atoms in biological tissues, <sup>19</sup>F-MRI confirms the presence of TAMs once <sup>19</sup>F signals

are detected; it also enables a simple quantification process, because the number of  $^{19}\text{F}$  spins is linearly correlated with the corresponding MR signal intensity.

While both SPIO and PFC have been shown to be effective for monitoring and quantifying TAMs, whether TAM burden quantified through these nanoparticle-based methods is associated with tumor development has yet to be examined. To investigate the prognostic implications of MRI-based TAM monitoring, another imaging modality designed for observing tumor behavior may be concurrently used, along with histopathological analysis. We hypothesized that positron emission tomography (PET) with  $^{18}\text{F}$ -2-fluoro-2-deoxy-D-glucose ( $^{18}\text{F}$ -FDG) as a radioactive tracer can serve such a purpose, since it is widely practiced as a clinical routine for staging tumor malignancy through measurement of tumor glucose uptake [19]. Simultaneous MRI tracking of TAMs and  $^{18}\text{F}$ -FDG-PET imaging of tumor metabolism might help determine the prognostic potential of MRI-based TAM tracking and provide new insights to understanding tumor physiology.

Here, we report the preliminary results from combining  $^{19}\text{F}$ -MRI and  $^{18}\text{F}$ -FDG-PET for monitoring TAM infiltration and tumor metabolism. The feasibility of spatial correlation of TAM distribution and glucose metabolism patterns was investigated, and significant correlations were observed between  $^{19}\text{F}$ -MR signal intensity and PET parameters. Overall, we demonstrate that combination of  $^{19}\text{F}$ -MR-based TAM tracking and  $^{18}\text{F}$ -FDG-PET imaging could provide opportunities for noninvasive yet precise profiling of tumor microenvironment and behavior.

## 2. Materials and Methods

**2.1. Preparation of PFC Emulsion.** PFC nanoemulsions were synthesized in accordance with a previous protocol, with a minor modification [20]. Lutrol F68 (60 mg/mL; BASF, Ludwigshafen, Germany) was dissolved in phosphate buffered saline (PBS; Gibco, Waltham, MA). Perfluoro-15-crown-5-ether (60% w/v; Oakwood Chemicals, Estill, SC) was thoroughly mixed into this solution using a micromixer. The mixture was emulsified by sonication in ice-cold water in a pulsed mode (2 s run and 2 s off) at 1.5 W for 10 min using a sonicator (Sonicator 3000; Misonix, Farmingdale, NY). In the last 2-3 cycles of sonication, 1,1'-dioctadecyl-3,3,3'-tetramethylindocarbocyanine perchlorate (DiI; 4  $\mu\text{l}$ /mL; Molecular Probes, Eugene, OR) was added for fluorescence. The resultant emulsions were then filter-sterilized through 0.45 and 0.2  $\mu\text{m}$  filters (Sartorius Stedim, Aubagne, France) and stored at 4°C until use. The size and polydispersity index of the PFC nanoemulsions were determined to be 160 nm and 0.08, respectively, using dynamic light scattering (Malvern Zetasizer, Worcestershire, UK).

**2.2. Animal Models.** All animal experiments were performed in accordance with the guidelines of the Institutional Animal Care and Use Committee (approval number, NCC-15-249) of the National Cancer Center, Korea. 4T1 mouse breast cancer

cells (American Type Culture Collection, Manassas, VA) were cultured in Roswell Park Memorial Institute-1640 medium (Hyclone, Logan, UT) supplemented with 10% fetal bovine serum (Cellgro, Tewksbury, MA) and 1% antibiotic solution (Gibco) at 37°C in a 5%-CO<sub>2</sub> incubator. For establishing a 4T1-tumor model,  $5 \times 10^5$  cells were suspended in 100  $\mu\text{l}$  of 5 mg/mL Matrigel (Corning, Corning, NY) and subcutaneously injected into the left and right flanks of 6-week-old female Balb/c mice (Japan SLC, Hamamatsu, Japan). Tumors ( $n = 16$ ) were grown until they reached a size of 50–100 mm<sup>3</sup>. The mice were intravenously given 200  $\mu\text{l}$  of the PFC nanoemulsions 48 h before the first MRI and  $^{18}\text{F}$ -FDG-PET scan.

**2.3. In Vivo MRI.** MR images were acquired using a 7T scanner (BioSpec 70/20 USR; Bruker, Billerica MA) and a custom-made  $^1\text{H}/^{19}\text{F}$ -double-tune 35 mm volume coil. A custom-built animal bed was used for transferring mice to the PET scanner without altering their posture. The mice were sedated with 2% isoflurane in 100% oxygen, and their respiration rates were monitored during imaging. Anatomical proton MR images were acquired using the rapid acquisition with relaxation enhancement (RARE) sequence. T2-weighted images were acquired with the following parameters: repetition time (TR), 2600 ms; echo time (TE), 30 ms; slice thickness (ST), 1 mm; RARE factor, 4; number of acquisitions (NA), 2; matrix size, 256  $\times$  192; and field of view (FOV), 3.5  $\times$  2.5 cm. For  $^{19}\text{F}$  image acquisition, the fast low angle shot sequence was used with the following parameters: TR, 100 ms; TE, 2.5 ms; ST, 2 mm; NA, 256; receiver bandwidth, 25 kHz; FOV, 3.5 cm  $\times$  2.5 cm; and matrix size, 64  $\times$  48. A reference tube containing 6 mg/mL PFC nanoemulsions entrapped in acrylamide gel was placed next to the mice for tumor signal normalization. The mice were imaged 2 (day 2) and 7 (day 7) days after administration of the PFC nanoemulsions.  $^{19}\text{F}$ -MR images were acquired only on day 2.

**2.4. PET/CT and Image Analysis.** In order to maintain the orientation of the mice, PET/CT images were acquired immediately after MRI. The mice were fasted for 6 h before PET/CT. They were anesthetized with 2% isoflurane in 100% oxygen. Body temperature was maintained throughout the imaging procedure using a heating lamp and pad.  $^{18}\text{F}$ -FDG was prepared by an automated module (NEPTIS® Nx3 system, ORA, Philippeville, Belgium) using fluoride-18 generated by our on-site cyclotron (RDS-111, Siemens, Munich, Germany). The mice were intravenously injected with 18.5 MBq of  $^{18}\text{F}$ -FDG 40 min before PET. PET-CT fusion images were acquired through a three-dimensional acquisition mode (eXplore VistaCT, GE, Fairfield, CT) using the following X-ray parameters for CT: 250  $\mu\text{A}$  tube current and 40 kV voltage for 6 min; resolution, 200  $\mu\text{m}$ ; and number of projections, 360. For PET images, the mice passed through the 6 cm diameter  $\times$  4.6 cm deep FOV of PET detector, and the voxel size of the reconstructed images was 0.3875  $\times$  0.3875  $\times$  0.775 mm. The images were acquired for 9 minutes per bed position and reconstructed by iterative reconstruction using the two-dimensional ordered subset

expectation maximization method (32 subsets, 2 iterations). Normalization and scatter and attenuation correction were also applied for PET images. The images were normalized to standardized uptake values (SUVs) using the following formula:  $SUV = \text{decay-corrected mean tissue activity concentration (Bq/ml)} / [\text{injected dose (Bq)} / \text{body weight (g)}]$ .  $SUV_{\max}$  was measured as the maximum SUV in a given region of interest. Percentage injected dose per gram tissue (% ID/g) was calculated as follows:  $[\text{mean tumor activity concentration (Bq/ml)} / (\text{injected dose (Bq)} \times \text{density of a tumor (g/ml)})] \times 100\%$ . All image analyses were performed using the OsiriX imaging software (Pixmeo SARL, Bernex, Switzerland).

**2.5. Histological Examination and Immunofluorescence Staining.** The mice were euthanized upon completion of imaging experiments. Tumors were excised, fixed in 4% paraformaldehyde (Sigma Aldrich, St. Louis, MO) for 24 h, embedded in paraffin blocks, and cut into 4  $\mu\text{m}$  thick sections for hematoxylin and eosin (H&E) staining. The H&E-stained sections were imaged using the Aperio Scan Scope XT system (Leica Biosystems, Heidelberg, Germany) at 200x magnification.

For immunofluorescence staining, the fixed tumors were frozen in the optimal cutting temperature compound at  $-80^{\circ}\text{C}$  and cut into 6  $\mu\text{m}$  thick sections using a Cryotome. Fluorescein isothiocyanate- (FITC-) conjugated rat anti-mouse F4/80 antibody (AbCam, Cambridge, MA) was used for staining macrophages. The stained sections were observed with a fluorescence microscope (Axio Observer.Z1, Zeiss, Germany).

**2.6. Statistical Analysis.** All statistical data were analyzed using GraphPad Prism 5 (GraphPad Software, La Jolla, CA). Correlations among  $^{19}\text{F}$ -MRI signal intensities, tumor volume, and PET parameters (including SUV,  $SUV_{\max}$ , and percentage injected dose per gram tissue [% ID/g]) were analyzed by Pearson's correlation coefficient analysis. Absolute correlation coefficients  $\geq 0.5$  were considered as indicating strong correlation [21]. A  $p$  value  $< 0.05$  was considered to be statistically significant.

### 3. Results and Discussion

$^{19}\text{F}$ -MRI and  $^{18}\text{F}$ -FDG-PET images were first acquired 2 days after administration of PFC nanoemulsions (Figure 1).  $^{19}\text{F}$ -MR signals were detected not only from tumors but also from naturally macrophage-rich tissues such as the spleen and bone marrow (Figure 1(b)). Coregistration of proton MR images and their corresponding PET images demonstrated tumor glucose metabolism in the same slices in which TAMs were visualized in  $^{19}\text{F}$ -MR images (Figure 1(d)). While  $^{18}\text{F}$ -FDG-PET signals appeared to be homogeneously distributed in tumors,  $^{19}\text{F}$  signals exhibited relatively heterogeneous intratumoral distribution, with higher signals emanating from the periphery of tumors. This difference in spatial distribution was further highlighted by the histogram findings, which revealed different frequency distributions of  $^{19}\text{F}$  signals

and consistent SUV distribution between the left and right tumors (Figures 1(c) and 1(e)).

Proton MRI and  $^{18}\text{F}$ -FDG-PET were repeated on day 7, and the imaging data were coregistered (Figure 2). In PET images, SUV hypointensities were observed at the centers of tumors, which corresponded to hyperintense signals observed in T2-weighted MR images (Figures 2(b) and 2(c)). Considering a previous study that reported an association between necrosis and high-intensity signals on T2-weighted MR images [22], it is likely that the colocalization of low SUVs and hyperintense T2-weighted MR signals observed in the present study represents the formation of a necrotic core. This possibility was further supported by the histological findings, which revealed hypocellularity at the center of tumor sections and intact cell morphology at the periphery (Figures 2(d)–2(f)).

The findings of immunofluorescence staining—performed to confirm that the  $^{19}\text{F}$ -MR signals represent TAMs—demonstrated the colocalization of DiI with PFC nanoemulsions and F4/80-positive cells (Figure 3). While significant proportions of TAMs were labeled with PFC nanoemulsions, unlabeled TAMs were also detected (Figure 3(c)). This partial labeling of TAMs is consistent with the findings of previous studies [17, 23]. Further studies are needed to identify methods for achieving full saturation of endogenous macrophages with PFC nanoemulsions for more accurate quantification of TAMs.

$^{19}\text{F}$ -MR signal intensities from tumors measured on day 2 were correlated with tumor volume and various PET parameters (Table 1). Tumor  $^{19}\text{F}$ -MR signal intensities measured on day 2 exhibited significantly strong correlations with tumor volume measured on day 7 ( $r = 0.626$ ;  $p < 0.01$ ) and tumor growth between days 2 and 7 ( $r = 0.624$ ;  $p < 0.01$ ; Figures 4(a) and 4(d)). All PET parameters measured on day 7 exhibited strong negative correlations with  $^{19}\text{F}$ -MR signal intensities measured on day 2 (SUV:  $r = -0.666$ ,  $p < 0.005$ ; % ID/g:  $r = -0.681$ ,  $p < 0.005$ ; and  $SUV_{\max}$ :  $r = -0.663$ ,  $p < 0.01$ ; Figures 4(b), 4(c), and 4(e)). Changes in PET parameters over time were also correlated with  $^{19}\text{F}$ -MR signal intensity in a similar manner as the measurements on day 7—changes in SUV ( $r = -0.519$ ,  $p < 0.05$ ) and % ID/g ( $r = -0.510$ ,  $p < 0.05$ ) exhibited strong negative correlations (Figure 4(f)) with  $^{19}\text{F}$ -MR signal intensity. There was no correlation between  $^{19}\text{F}$ -MR signal intensity and any of the measurements recorded on day 2 or change in  $SUV_{\max}$  ( $|r| < 0.2$ ,  $p > 0.5$ ).

Considering the protumoral activities of TAMs, we initially hypothesized that  $^{19}\text{F}$ -MR signal intensity would be positively correlated with all of the parameters evaluated in the present study. While the positive correlation of  $^{19}\text{F}$ -MR signal intensity with tumor volume and growth can be explained by the effects of TAMs on tumor development, the negative correlation between  $^{19}\text{F}$ -MR signal intensity and PET measurements recorded on day 7, which often serve as indicators of tumor malignancy, seem to be paradoxical. A possible explanation for this inverse correlation is the decrease in average tumor metabolism due to the formation of the necrotic core, which was observed in PET/MR images acquired on day 7 as well as in histological

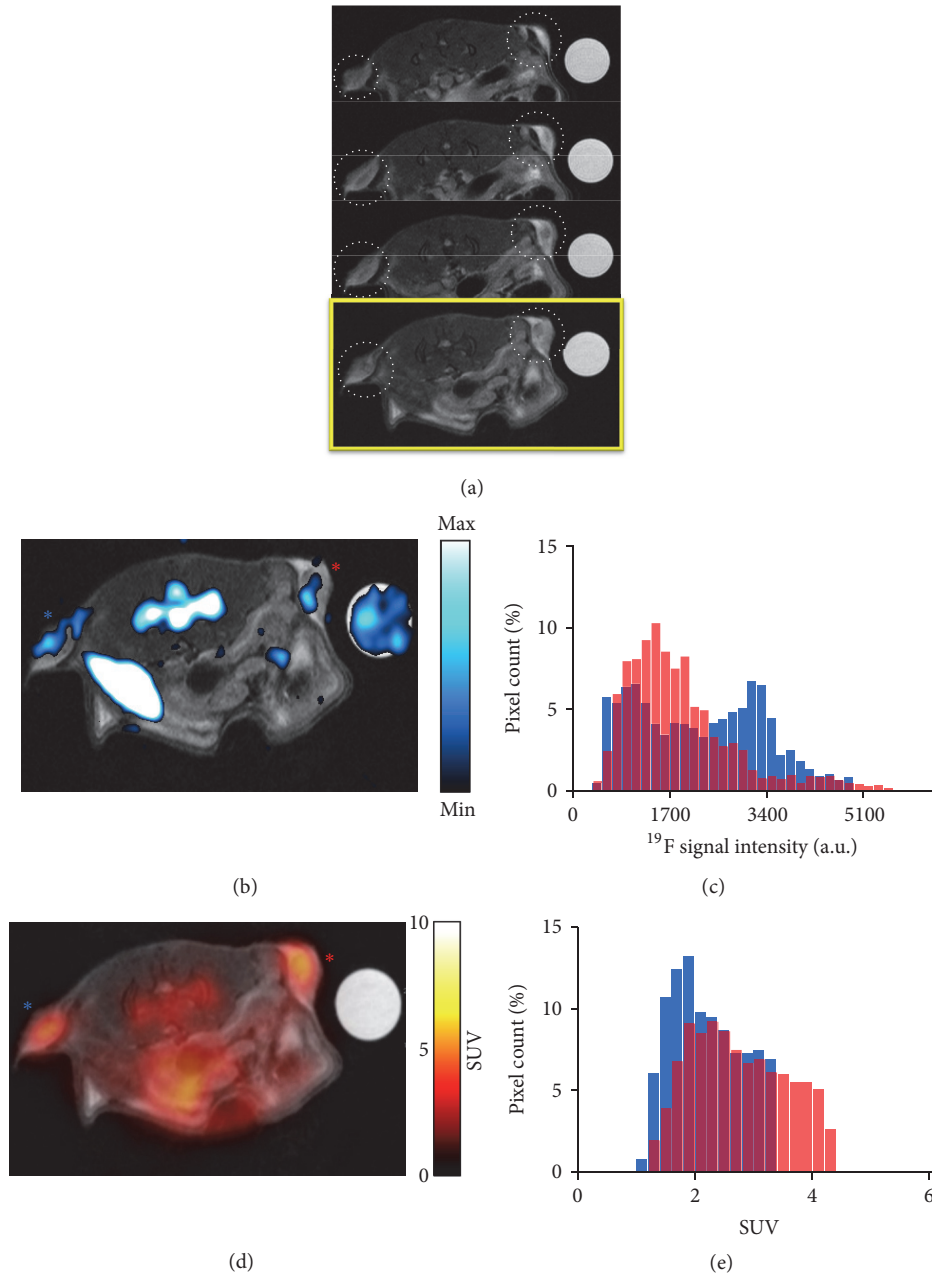


FIGURE 1: *In vivo*  $^{19}\text{F}$ -MRI and PET and histogram analysis on day 2. (a) Serial  $^1\text{H}$  MR image slices with tumors indicated with dotted white circles. The last slice in yellow box is the slice that is coregistered with corresponding  $^{19}\text{F}$ -MR image and  $^{18}\text{F}$ -FDG-PET image in (b) and (d), respectively. (b) Superimposition of an anatomical proton MR image and its corresponding  $^{19}\text{F}$ -MR image.  $^{19}\text{F}$  signals are detected not only from tumors, but also from the bone marrow, the spleen, and a reference tube placed on the right side of the mouse. (c) Histogram of  $^{19}\text{F}$  pixel intensities from left and right tumors. Blue and red are from left (blue asterisk) and right (red asterisk) tumors in (b). (d) Coregistration of the same anatomical MR image as that used in image A and its corresponding  $^{18}\text{F}$ -FDG-PET image. Blue and red are from left (blue asterisk) and right (red asterisk) tumors in (d).  $^{19}\text{F}$ , fluorine-19; MRI, magnetic resonance imaging; PET, positron emission tomography; 2-FDG, fluoro-2-deoxy-D-glucose; SUV, standardized uptake value.

specimens (Figure 2). It is widely known that aggressive tumors often outgrow their blood supply, upon which their central regions are exposed to chronic ischemia, which ultimately leads to necrosis. In breast cancer, formation of such necrotic cores is associated with an accelerated

clinical course and poor prognosis [24, 25]. Similarly, the formation of necrotic zones in breast tumor models used in this study—visualized as decreased  $^{18}\text{F}$ -FDG uptake at the center of tumors—might represent the aggressiveness and malignancy of tumors. To investigate this possibility,

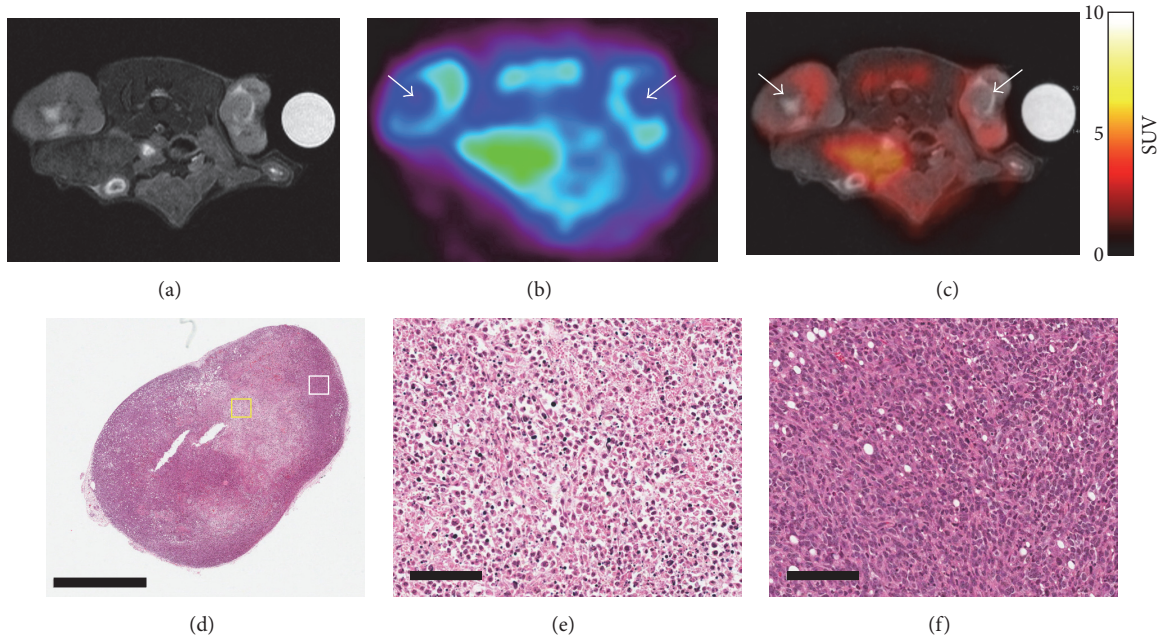


FIGURE 2: PET-MRI and histological findings on day 7. (a) Axial MR image of a mouse and (b) the corresponding PET image were merged. (c) The coregistered MR-PET image shows overlapping of low SUV regions and high MR signal regions in tumors (white arrow in (b) and (c)). (d) Overview of an H&E-stained section of a tumor excised after PET-MRI (scale bar: 2 mm). (e) High-magnification view of the central region of the H&E-stained section (indicated by a yellow box in (d); scale bar: 100  $\mu\text{m}$ ); fragmented nuclei and disrupted cell morphology are observed, along with hypocellularity. (f) High-magnification view of the peripheral region of the tumor (white box in (d); scale bar: 100  $\mu\text{m}$ ); cell morphology and nuclei are intact, while the cells are densely packed. PET, positron emission tomography; MRI, magnetic resonance imaging; SUV, standardized uptake value; H&E, hematoxylin and eosin.

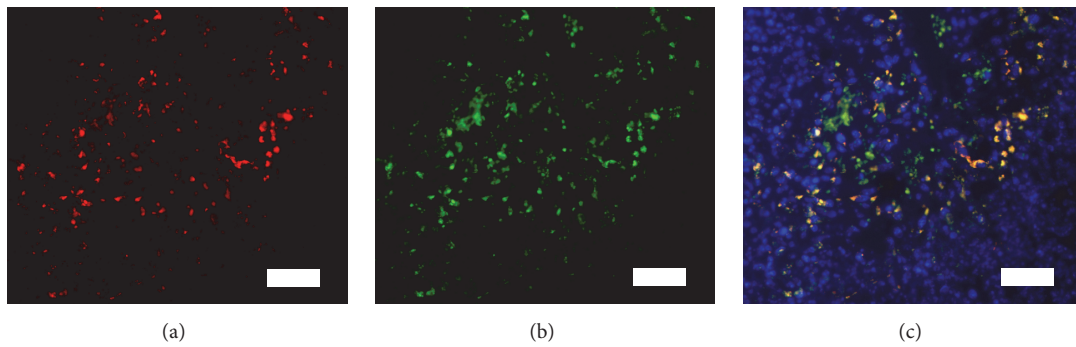


FIGURE 3: Immunofluorescence staining of TAMs reveals colocalization of TAMs and PFC nanoemulsions (scale bar: 50  $\mu\text{m}$ ). (a) DiI on PFC nanoemulsions. (b) FITC on F4/80 antibodies. (c) Merged images of DAPI, DiI, and FITC staining showing colocalization of TAMs and PFC nanoemulsions (yellow); TAMs that are not labeled with PFC nanoemulsions are also observed (green). TAM, tumor-associated macrophage; PFC, perfluorocarbon; DiI, 1,1'-dioctadecyl-3,3,3',3'-tetramethylindocarbocyanine perchlorate; FITC, fluorescein isothiocyanate; DAPI, 4',6'-diamidino-2-phenylindole.

tumor models with the same genetic background but different degrees of malignancies should be evaluated by imaging along with rigorous histopathological analysis.

The lack of correlation between  $^{19}\text{F}$ -MR signal intensity and PET parameters measured on day 2 should also be noted. A previous histopathological study had reported that immune-cell infiltration and  $^{18}\text{F}$ -FDG-PET SUV are not significantly correlated [26]. Nevertheless, there is a possibility that varying the timing of monitoring will generate different results. Using both SPIO and PFC labeling, Makela

et al. showed that distribution of TAMs varies significantly on the basis of tumor size at the time of monitoring [17]. Future studies should evaluate whether the characteristics of TAMs, too, change along with their intratumoral distribution over time. It should also be determined if any correlation exists between  $^{19}\text{F}$ -MR signal intensity and PET parameters concurrently measured at a later time point in tumor growth.

The combination of proton MRI and PET has been widely studied, with the aim of gaining a comprehensive understanding of tumor physiology and differentiating

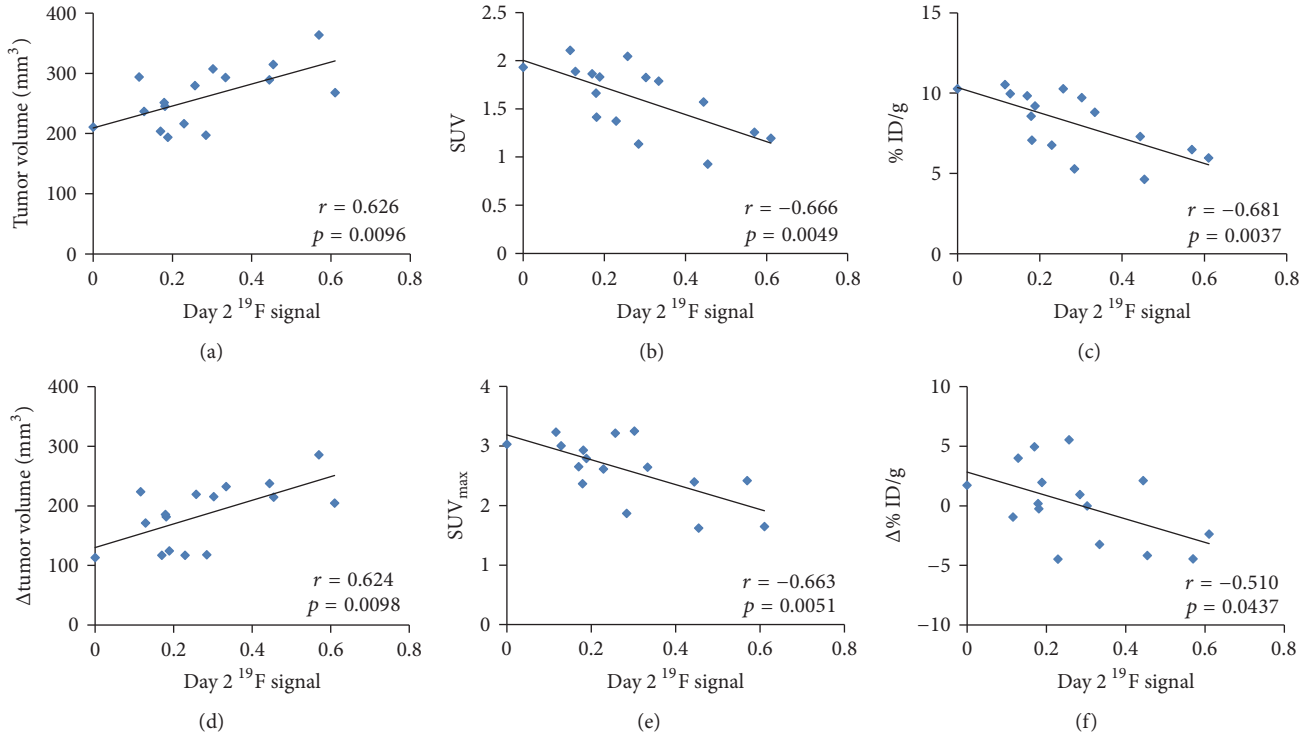


FIGURE 4: Correlation of  $^{19}\text{F}$ -MR signal intensity with tumor growth and PET parameters. (a) Tumor volume, (b) SUV, and (c) % ID/g measured on day 7 as functions of  $^{19}\text{F}$ -MR signal intensities measured on day 2. (d) Change in tumor growth from day 2 to day 7, (e)  $\text{SUV}_{\max}$  measured on day 7, and (f) change in % ID/g from day 2 to day 7 as functions of  $^{19}\text{F}$ -MR signal intensities measured on day 2.  $^{19}\text{F}$ , fluorine-19; MR, magnetic resonance; PET, positron emission tomography; SUV, standardized uptake value; % ID/g, percentage injected dose per gram tissue;  $\text{SUV}_{\max}$ , maximum SUV.

TABLE 1: Correlation of  $^{19}\text{F}$  signal on day 2 with tumor volume, PET parameters, and their changes over time.

| Parameters                            | $r$     | $p$    |
|---------------------------------------|---------|--------|
| $\Delta(\text{day 7} - \text{day 2})$ |         |        |
| Tumor volume                          | 0.6242  | 0.0098 |
| SUV                                   | -0.519  | 0.0393 |
| $\text{SUV}_{\max}$                   | -0.1818 | 0.5004 |
| % ID/g                                | -0.510  | 0.0437 |
| Day 2                                 |         |        |
| Tumor volume                          | -0.1684 | 0.533  |
| SUV                                   | 0.155   | 0.567  |
| $\text{SUV}_{\max}$                   | -0.163  | 0.547  |
| % ID/g                                | 0.1269  | 0.6396 |
| Day 7                                 |         |        |
| Tumor volume                          | 0.626   | 0.0096 |
| SUV                                   | -0.666  | 0.0049 |
| $\text{SUV}_{\max}$                   | -0.663  | 0.0051 |
| % ID/g                                | -0.681  | 0.0037 |

PET, positron emission tomography; SUV, standardized uptake value;  $\text{SUV}_{\max}$ , maximum SUV; % ID/g, percentage injected dose per gram tissue.

tumor subtypes by monitoring various aspects of the tumor microenvironment [27]. Several MR parametric methods, such as chemical exchange saturation transfer imaging,

dynamic contrast enhanced MRI, and apparent diffusion coefficient mapping, have been used for measuring tumor acidosis, perfusion, and necrosis [28–30]. In terms of  $^{18}\text{F}$ -FDG-PET, a myriad of analytic approaches, including texture analysis, are being studied for better assessment of glucose metabolism patterns and enhanced characterization of tumors [31]. Considering these developments in both MRI and PET approaches for tumor characterization, it is envisioned that our knowledge of tumor microenvironment would be further enriched through the combination of these two imaging modalities.

To the best of our knowledge, the present study is the first to use a combination of  $^{19}\text{F}$ -MRI and  $^{18}\text{F}$ -FDG-PET. Owing to the simplicity of its quantification process and image interpretation,  $^{19}\text{F}$ -MRI has been suggested as a useful tool for quantitative monitoring of TAMs. The parametric potential of  $^{19}\text{F}$ -MRI TAM tracking has been suggested in a previous study, which had reported that the  $^{19}\text{F}$ -MR signal intensity observed in the colon of an inflammatory bowel disease model was correlated with a high chance of developing dysplasia [16]. Unlike SPIO nanoparticles, PFC nanoemulsions do not affect the proton spin of adjacent water molecules; this allows simultaneous measurement of other MR parameters, such as those mentioned above, for further analysis of the tumor microenvironment [20, 32]. Thus,  $^{19}\text{F}$ -MRI tracking of TAMs in conjunction with  $^{18}\text{F}$ -FDG-PET

is expected to be a valuable bimodal platform that provides complementary information for comprehensive monitoring of the tumor microenvironment.

Yet, several concerns regarding PFC-based TAM tracking remain to be overcome. In most  $^{19}\text{F}$ -MRI-based TAM-tracking studies, including the present one, TAMs are passively labeled by PFC nanoemulsions, without targeting any specific moieties on the cells. It should be noted that not all TAMs are protumorigenic, and labeling both tumor-promoting and tumor-antagonizing TAMs would compromise the goal of tumor characterization. Therefore, for precise profiling of tumors, the phenotype of fluorinated TAMs should be analyzed, and methods for noninvasive differentiation of tumor-promoting and tumor-antagonizing TAMs should be developed. Another concern is that fluorination of TAMs with PFC nanoemulsions might affect the phenotype and physiology of these cells. In several studies, PFC nanoemulsions have been shown to preserve the original function and differentiation potential of various cell types, including hematopoietic [33, 34], neural [35], and mouse-mesenchymal [36] stem cells. Similar studies should be conducted to investigate the influence of PFC labeling on TAM characteristics. The recently reported intrinsic effects of SPIO nanoparticles on altering TAM polarization also emphasize the need for such investigations [37].

The sensitivity and resolution of  $^{19}\text{F}$ -MRI should also be improved. In this study, the correlations between  $^{19}\text{F}$ -MR signal and  $^{18}\text{F}$ -FDG-PET parameters were only done in tumor-by-tumor basis. To further examine the usefulness of combining  $^{19}\text{F}$ -MRI and  $^{18}\text{F}$ -FDG-PET in characterizing tumor heterogeneity, a voxel-by-voxel analysis in a tumor as well as correlation to corresponding histology should be performed. For these analyses to be precise, the spatial resolution of  $^{19}\text{F}$ -MRI should be improved without compromising the current sensitivity.

#### 4. Conclusion

In summary, preliminary results from combining  $^{19}\text{F}$ -MRI and  $^{18}\text{F}$ -FDG-PET suggest that  $^{19}\text{F}$ -MRI tracking of TAMs might aid the characterization of tumors and prediction of tumor development. Comparison of intratumoral distribution of TAMs and the spatial pattern of tumor glucose uptake revealed several degrees of heterogeneity in the tumor microenvironment. A significant positive correlation was observed between  $^{19}\text{F}$ -MR signal intensity and subsequent tumor growth, while inverse correlations were observed between  $^{19}\text{F}$  signal intensity and  $^{18}\text{F}$ -FDG-PET parameters. These results together suggest that  $^{19}\text{F}$ -MRI tracking of TAMs could potentially be used for tumor characterization and that, in combination with  $^{18}\text{F}$ -FDG-PET, this method could further expand our understanding of the heterogeneous tumor microenvironment and its impact on tumor prognosis. Since TAMs are becoming popular as significant therapeutic targets for cancer treatment, the combination of  $^{19}\text{F}$ -MRI and  $^{18}\text{F}$ -FDG-PET might also serve as a platform for assessment of therapeutic response.

#### Conflicts of Interest

The authors declare that there are no conflicts of interest regarding the publication of this article.

#### Authors' Contributions

Soo Hyun Shin and Sang Hyun Park are co-first authors and contributed equally to this study.

#### Acknowledgments

The authors are grateful to Soyeon Jeon for her support with MRI data acquisition. This study was supported by National Cancer Center, Korea (NCC 1510030-3).

#### References

- [1] A. Mantovani, B. Bottazzi, F. Colotta, S. Sozzani, and L. Ruco, "The origin and function of tumor-associated macrophages," *Trends in Immunology*, vol. 13, no. 7, pp. 265–270, 1992.
- [2] J. W. Pollard, "Tumour-educated macrophages promote tumour progression and metastasis," *Nature Reviews Cancer*, vol. 4, no. 1, pp. 71–78, 2004.
- [3] F. Balkwill, K. A. Charles, and A. Mantovani, "Smoldering and polarized inflammation in the initiation and promotion of malignant disease," *Cancer Cell*, vol. 7, no. 3, pp. 211–217, 2005.
- [4] S. F. Schoppmann, P. Birner, J. Stöckl et al., "Tumor-associated macrophages express lymphatic endothelial growth factors and are related to peritumoral lymphangiogenesis," *The American Journal of Pathology*, vol. 161, no. 3, pp. 947–956, 2002.
- [5] L. Bingle, C. E. Lewis, K. P. Corke, M. Reed, and N. J. Brown, "Macrophages promote angiogenesis in human breast tumour spheroids in vivo," *British Journal of Cancer*, vol. 94, no. 1, pp. 101–107, 2006.
- [6] R. D. Leek, C. E. Lewis, R. Whitehouse, M. Greenall, J. Clarke, and A. L. Harris, "Association of macrophage infiltration with angiogenesis and prognosis in invasive breast carcinoma," *Cancer Research*, vol. 56, no. 20, pp. 4625–4629, 1996.
- [7] E. Y. Lin, V. Gouon-Evans, A. V. Nguyen, and J. W. Pollard, "The macrophage growth factor CSF-1 in mammary gland development and tumor progression," *Journal of Mammary Gland Biology and Neoplasia*, vol. 7, no. 2, pp. 147–162, 2002.
- [8] J. Wyckoff, W. Wang, E. Y. Lin et al., "A paracrine loop between tumor cells and macrophages is required for tumor cell migration in mammary tumors," *Cancer Research*, vol. 64, no. 19, pp. 7022–7029, 2004.
- [9] E. Y. Lin, A. V. Nguyen, R. G. Russell, and J. W. Pollard, "Colony-stimulating factor 1 promotes progression of mammary tumors to malignancy," *The Journal of Experimental Medicine*, vol. 193, no. 6, pp. 727–739, 2001.
- [10] Y. Luo, H. Zhou, J. Krueger et al., "Targeting tumor-associated macrophages as a novel strategy against breast cancer," *The Journal of Clinical Investigation*, vol. 116, no. 8, pp. 2132–2141, 2006.
- [11] C. H. Ries, M. A. Cannarile, S. Hoves et al., "Targeting tumor-associated macrophages with anti-CSF-1R antibody reveals a strategy for cancer therapy," *Cancer Cell*, vol. 25, no. 6, pp. 846–859, 2014.

- [12] K. Movahedi, S. Schoonooghe, D. Laoui et al., "Nanobody-based targeting of the macrophage mannose receptor for effective in vivo imaging of tumor-associated macrophages," *Cancer Research*, vol. 72, no. 16, pp. 4165–4177, 2012.
- [13] H. E. Daldrup-Link, D. Golovko, B. Ruffell et al., "MRI of tumor-associated macrophages with clinically applicable iron oxide nanoparticles," *Clinical Cancer Research*, vol. 17, no. 17, pp. 5695–5704, 2011.
- [14] Y.-Y. I. Shih, Y.-H. Hsu, T. Q. Duong, S.-S. Lin, K.-P. N. Chow, and C. Chang, "Longitudinal study of tumor-associated macrophages during tumor expansion using MRI," *NMR in Biomedicine*, vol. 24, no. 10, pp. 1353–1360, 2011.
- [15] A. Balducci, Y. Wen, Y. Zhang et al., "A novel probe for the non-invasive detection of tumor-associated inflammation," *Oncotarget*, vol. 2, no. 2, Article ID e23034, 2013.
- [16] S. H. Shin, D. K. Kadayakkara, and J. W. M. Bulte, "In vivo <sup>19</sup>F MR imaging cell tracking of inflammatory macrophages and site-specific development of colitis-associated dysplasia," *Radiology*, vol. 282, no. 1, pp. 194–201, 2017.
- [17] A. V. Makela, J. M. Gaudet, and P. J. Foster, "Quantifying tumor associated macrophages in breast cancer: a comparison of iron and fluorine-based MRI cell tracking," *Scientific Reports*, vol. 7, Article ID 42109, 2017.
- [18] J. W. M. Bulte, "Hot spot MRI emerges from the background," *Nature Biotechnology*, vol. 23, no. 8, pp. 945–946, 2005.
- [19] R. J. Shaw, "Glucose metabolism and cancer," *Current Opinion in Cell Biology*, vol. 18, no. 6, pp. 598–608, 2006.
- [20] S. H. Shin, E.-J. Park, C. Min et al., "Tracking perfluorocarbon nanoemulsion delivery by <sup>19</sup>F MRI for precise high intensity focused ultrasound tumor ablation," *Theranostics*, vol. 7, no. 3, pp. 562–572, 2017.
- [21] Z. Ram, Z. R. Cohen, S. Harnof et al., "Magnetic resonance imaging-guided, high-intensity focused ultrasound for brain tumor therapy," *Neurosurgery*, vol. 59, no. 5, pp. 949–955, 2006.
- [22] T. Uematsu, "MR imaging of triple-negative breast cancer," *Breast Cancer*, vol. 18, no. 3, pp. 161–164, 2011.
- [23] R. B. Van Heeswijk, M. Pellegrin, U. Flögel et al., "Fluorine MR imaging of inflammation in atherosclerotic plaque in vivo," *Radiology*, vol. 275, no. 2, pp. 421–429, 2015.
- [24] R. E. Jimenez, T. Wallis, and D. W. Visscher, "Centrally necrotizing carcinomas of the breast: a distinct histologic subtype with aggressive clinical behavior," *The American Journal of Surgical Pathology*, vol. 25, no. 3, pp. 331–337, 2001.
- [25] R. D. Leek, R. J. Landers, A. L. Harris, and C. E. Lewis, "Necrosis correlates with high vascular density and focal macrophage infiltration in invasive carcinoma of the breast," *British Journal of Cancer*, vol. 79, no. 5-6, pp. 991–995, 1999.
- [26] N. Avril, M. Menzel, J. Dose et al., "Glucose metabolism of breast cancer assessed by <sup>18</sup>F-FDG PET: Histologic and immunohistochemical tissue analysis," *Journal of Nuclear Medicine*, vol. 42, no. 1, pp. 9–16, 2001.
- [27] J. Schmitz, J. Schwab, J. Schwenck, Q. Chen, L. Quintanilla-Martinez, M. Hahn et al., "Decoding intratumoral heterogeneity of breast cancer by multiparametric," *Cancer Research*, vol. 76, no. 18, pp. 5512–5522, 2016.
- [28] D. L. Longo, A. Bartoli, L. Consolino et al., "In vivo imaging of tumor metabolism and acidosis by combining PET and MRI-CEST pH imaging," *Cancer Research*, vol. 76, no. 22, pp. 6463–6470, 2016.
- [29] S. Metz, C. Ganter, S. Lorenzen et al., "Multiparametric MR and PET imaging of intratumoral biological heterogeneity in patients with metastatic lung cancer using voxel-by-voxel analysis," *PLoS ONE*, vol. 10, no. 7, Article ID e0132386, 2015.
- [30] M. A. Zahra, K. G. Hollingsworth, E. Sala, D. J. Lomas, and L. T. Tan, "Dynamic contrast-enhanced MRI as a predictor of tumour response to radiotherapy," *The Lancet Oncology*, vol. 8, no. 1, pp. 63–74, 2007.
- [31] M. Soussan, F. Orlhac, M. Boubaya et al., "Relationship between tumor heterogeneity measured on FDG-PET/CT and pathological prognostic factors in invasive breast cancer," *PLoS ONE*, vol. 9, no. 4, Article ID e94017, 2014.
- [32] E. Bible, F. Dell'Acqua, B. Solanky et al., "Non-invasive imaging of transplanted human neural stem cells and ECM scaffold remodeling in the stroke-damaged rat brain by (<sup>19</sup>F)- and diffusion-MRI," *Biomaterials*, vol. 33, no. 10, pp. 2858–2871, 2012.
- [33] B. M. Helfer, A. Balducci, Z. Sadeghi et al., "<sup>19</sup>F MRI tracer preserves in vitro and in vivo properties of hematopoietic stem cells," *Cell Transplantation*, vol. 22, no. 1, pp. 87–97, 2013.
- [34] L. E. Duinhouwer, B. J. M. Van Rossum, S. T. Van Tiel et al., "Magnetic resonance detection of CD34+ cells from umbilical cord blood using a <sup>19</sup>F label," *PLoS ONE*, vol. 10, no. 9, Article ID e0138572, 2015.
- [35] P. Boehm-Sturm, M. Aswendt, A. Minassian et al., "A multi-modality platform to image stem cell graft survival in the naïve and stroke-damaged mouse brain," *Biomaterials*, vol. 35, no. 7, pp. 2218–2226, 2014.
- [36] G. Muhammad, A. Jablonska, L. Rose, P. Walczak, and M. Janowski, "Effect of MRI tags: SPIO nanoparticles and <sup>19</sup>F nanoemulsion on various populations of mouse mesenchymal stem cells," *Acta Neurobiologiae Experimentalis*, vol. 75, no. 2, pp. 144–159, 2015.
- [37] S. Zanganeh, G. Hutter, R. Spitler et al., "Iron oxide nanoparticles inhibit tumour growth by inducing pro-inflammatory macrophage polarization in tumour tissues," *Nature Nanotechnology*, vol. 11, no. 11, pp. 986–994, 2016.